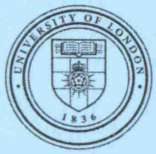

UNIVERSITY OF LONDON THESIS

Degree PhD Year 2008 Name of Author RASSAT, Anais Marie Melanie

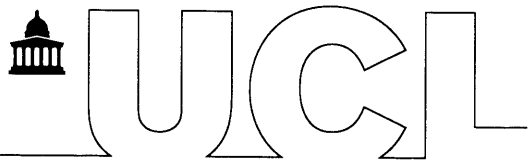

Cosmological Probes of Gravity

Anaïs Marie Mélanie Rassat

Thesis submitted for the Degree of Doctor of Philosophy
of the University of London

Department of Physics & Astronomy
UNIVERSITY COLLEGE LONDON

October 2007

ProQuest LLC
789 East Eisenhower Parkway
P.O. Box 1346
Ann Arbor, MI 48106-1346

I, Anaïs Marie Mélanie Rassat, confirm that the work presented in this Thesis is my own. Where information has been derived from other sources, I confirm that this has been indicated in the Thesis.
I specifically note some major contributions from third parties:

- I am co-author for Erdoğdu (a) *et al.* (2006) and Erdoğdu (b) *et al.* (2006), in which I have helped verify code and calculations. The bulk of the work was not done by me.

- The parameterisation of galaxy redshift distributions in Chapters 3 and 4 were fitted by Pirin Erdoğdu

- The computer codes for computing the galaxy auto-correlation function in Chapters 3 and 4 were written jointly with Filipe Abdalla (UCL). Figure 3.4 was produced using calculations made by Filipe Abdalla.

- Chapter 6 is also presented in Rassat, Land, Lahav & Abdalla (2007). The computer codes for computing the theoretical ISW signal in Chapter 6 were written jointly with Kate Land (Oxford). The code for calculating the preferred axis ('Axis of Evil') was written by Kate Land. Figures 6.3-6.9 were produced by Kate Land.

- For the work presented in Chapter 7, I acknowledge the use of *icosmo*, a code written by Alexandre Réfrégier (CEA, Saclay) which calculates the Fisher forecasts from the Weak Lensing. I have adapted *icosmo* to produce forecasts from the ISW effect and for the Minimalist Modified Gravity (MMG) growth parameter γ.

A Manou, qui croit au progrès.

To Manou, who believes in progress.

"Tout ce que j'ai reçu jusqu'à présent pour le plus vrai et assuré, je l'ai appris des sens, ou par les sens; or j'ai quelquefois éprouvé que ces sens étaient trompeurs, et il est de la prudence de ne se fier jamais entièrement à ceux qui nous ont une fois trompés."

"All that I received until now for truest and ensured, I learnt it from the senses, or by the senses; however I sometimes found that these senses were misleading, and it is wise never to trust entirely those who once misled us."

— Descartes

ABSTRACT

This Thesis is concerned with two cosmological probes of linear gravity. The first relates to Large Scale Structure (LSS) in the Universe, probed by galaxy surveys. The second to temperature anisotropies of the Cosmic Microwave Background (CMB), probed by the Wilkinson Microwave Anisotropy Map (WMAP). Both probe the matter and dark energy distributions in the Universe and can be used to test general relativity.

The first part of this Thesis (Chapters 2 to 4) is concerned with the analysis of galaxy clustering in redshift space. The second part (Chapters 5 to 7) is concerned with the Integrated Sachs-Wolfe (ISW) effect using LSS-CMB cross-correlations.

Chapter 1 introduces the cosmological theory and overviews the subsequent chapters. Chapter 2 gives a review of recent results from the 2 Micron All-Sky Survey (2MASS) and its Redshift Survey (2MRS). It includes work published in Erdoğdu (a) *et al.* (2006) and Erdoğdu (b) *et al.* (2006). Chapter 3 quantifies the clustering of 2MRS galaxies in redshift space. Chapter 4 uses results from Chapter 3 to constrain cosmological parameters. A selection of work from Chapters 3 and 4 will shortly become available in Rassat et al. (2008), entitled 'Redshift Space Analysis of 2MRS'.

Chapter 5 overviews the late-time Integrated Sachs-Wolfe effect (ISW) and cross-correlations between the LSS and the CMB. Chapter 6 is also published in Rassat *et al.* (2007), entitled "Cross-correlation of 2MASS and WMAP3: Implications for the Integrated Sachs-Wolfe effect". It investigates a detection of the ISW effect and correlations which may affect statistical isotropy in the CMB ('Axis of Evil'). Chapter 7 uses the ISW effect to forecast constraints on dark energy parameters and general modifications of gen-

eral relativity for the next generation of galaxy surveys, particularly the Dark UNiverse Explorer (DUNE) and the Dark Energy Survey (DES).

Chapter 8 presents the overall conclusions of this Thesis. Chapter 9 discusses possible extensions to this work.

ACKNOWLEDGEMENTS

I am indebted to Ofer Lahav, my supervisor, for all his help and innumerable discussions. I am grateful to everyone I have discussed this work with, particularly Niayesh Afshordi, Sarah Bridle, Filipe Abdalla, Eduardo Cypriano, Carlo Contaldi, Kate Land, Dragan Huterer, Tom Jarrett, Alexandre Réfrégier, Adam Amara, Chris Blake, Jochen Weller, Jiayu Tang, Shaun Thomas and Saleem Zaroubi. I thank Sarah Bridle for her encouragement and for being a role model.

I have been lucky to have been hosted by many institutions during my Ph.D.; for these travels I am grateful to the UCL Graduate School, the department of Physics & Astronomy, the Astrophysics group and my supervisor for funding. Many thanks to the Anglo-Australian Observatory, Fermilab and Saclay CEA who also financially aided this travel. I am grateful to the Royal Astronomical Society for making two Young Astronomers' Meetings (YAM) possible. For joining in at Speakers' Corner and acheiving true grassroots outreach, I thank Joe Zuntz and Francisco Diego, as well as everyone at ULO for their enthusiasm and for teaching me how to use a telescope.

For friendship, coffee and philosophical arguments, I thank Eduardo Cypriano, Antonio Hales and Chris Lintott. I thank my office mates and the graduate social life which made UCL a great place to evolve in, especially for the fun in the Isle of Wight, West Sussex and Wales. I hope we can all meet up in France next time.

I am indebted to everyone who put up with me during my nomadic months, with special thanks to the Kilburn Crew. Neil and Christian, thank you for being truly extraordinary friends over the past eight years. I am very lucky to have you. A million thanks to my sister Marie for generously providing flats, mobile phones and transportation. I thank my father for proof-reading this Thesis. Most of all, I thank my parents for their education, their support and vision of life, and Manou, for always being there.

CONTENTS

List of Figures

LIST OF TABLES

CHAPTER 1

INTRODUCTION

Summary

In this Chapter I give an overview of the current cosmological model and the theoretical framework necessary to understand the work presented in this Thesis. In Section 1.9 I present the overall structure of this Thesis.

1.1 Birth of Observational Cosmology

Data: today's *Golden Age* of cosmology is just that, the golden age of data. Immanuel Kant had none when he postulated in 1755 that there should exist other *Island Universes* outside our own Galaxy the Milky Way. Observational evidence confirming his speculation, came only 170 years later when Edwin Hubble investigated Cepheid variables residing in nebulæ. The Cepheid variables act as *standard candles* - stars whose intrinsic luminosity follows a known trend (Pigott 1785). By measuring their observed luminosity, Hubble estimated their distances from us (Hubble 1925). These nebulæ were originally thought to be substructures within our Milky Way, but the measured distances showed the nebulæ were much further than expected and were in fact large conglomerates of stars, separate from our own spiral home. For the first time - this is 1925! - humankind realised the Milky Way was just one of many, many galaxies. From then on, thanks to the construction and development of ground based telescopes, multi-wavelength detectors and space missions, cosmology matured from a data-starved field to an observational

science determined to investigate the framework recently provided by Einstein's theory of general relativity. Observational cosmology was born.

1.2 Birth of the Standard Cosmological Model

In the last century, cosmological observations have led us to revise our understanding of the Universe, which was thought, even by Einstein, to be static. For the equations of general relativity to describe a static universe, Einstein introduce the famous cosmological constant Λ*. In the 1930s, Edwin Hubble and Milton Humason discovered the distance of galaxies from us was correlated to their measured redshift, implying the Universe was expanding (Hubble & Humason 1931). In this case there was no need for a cosmological constant and Einstein set the cosmological constant to zero. In 1965, Penzias and Wilson accidentally discovered an unexplained extremely uniform radiation observed from all directions†. Dicke *et al.* (1965) knew this was the signature of a hot phase in the early Universe. A few years later, Wagoner, Fowler & Hoyle (1967) calculated the expected light element abundance expected in an expanding Universe for which the background radiation today was the observed 3K. It matched that measured in the local Universe. All this was mounting evidence for the new Big Bang model which stated that space and time in our Universe were not immutable, but had a *beginning*.

The 20th century hosted major cosmological revolutions, and the last twenty years have been extremely animated. In the early 1990s, the NASA's COBE mission (Bennett, Smoot & Kogut 1990) precisely measured the Cosmic Microwave Background (CMB) on the entire sky. It was found to be extremely uniform - to one part in the 10^5, which was consistent with the Big Bang model. Interestingly, the CMB also presented extremely small temperature fluctuations which were thought to be related to density fluctuations in the early Universe. Overdense regions in the early Universe eventually grew through gravitational instability. This mechanism is thought to explain the formation of galaxies and galaxy clusters that we see in the Universe today. Then in the same decade, evidence mounted that the cosmological constant might be different to zero (Efstathiou, Sutherland & Maddox 1990). Several groups (Riess *et al.* 1998; Perlmutter *et al.* 1998; Schmidt

*See Section 1.5.4

†See http://www.bell-labs.com/project/feature/archives/cosmology/

et al. 1998) showed using supernovæ data that the Universe was not only expanding, but *accelerating*, requiring $\Lambda \neq 0$. In 2003 another cosmic microwave background space mission - WMAP (Bennett *et al.* 2003) - measured the geometry of the Universe to be most probably Euclidean (flat). This, with other corroborating data sets, led to the birth of a standard cosmological model: an isotropic, homogeneous and flat Universe composed of baryons, dark matter and a mysterious dark energy driving the accelerated expansion of the Universe.

In Section 1.3 I overview the theoretical framework of general relativity in which the standard cosmological model exists. In Section 1.4 I overview some problems with the Big Bang model which were solved by the theory of Inflation. In Section 1.5 I describe the major components of the Universe. Sections 1.6 and 1.7 are more technical reviews of statistical and observational tools used in modern cosmology. In Section 1.8 I discuss some alternative models that also attempt to explain current observations and are widely debated today. In Section 1.9 I present the overall structure of this Thesis.

1.3 Friedman-Robertson-Walker Model

In this Section I describe the equations that govern the dynamics of an isotropic and homogeneous universe.

1.3.1 General Relativity

Einstein introduced the revolutionary idea of a *space-time event*. An event is a unique point of space-time, defined by 3 spatial coordinates (r, θ, ϕ) and one temporal coordinate t. Space-time is then defined as the set of all events, and is described by a four-dimensional manifold characterized by a metric. General relativity states that a non-trivial mass distribution will imply non-trivial curvature on the manifold.

The Cosmological Principle states that on large spatial scales ($> 100h^{-1}$Mpc), the Universe is homogeneous (i.e., uniform in composition and density) and isotropic (i.e., has no preferred direction). Isotropy is verified by the apparent uniformity of the cosmic microwave background. On small scales we know from observation (and our existence) that the Universe is not homogeneous. On larger scales homogeneity is impossible to

prove from the CMB observation only, simply because we observe from only one point in space. In order to infer homogeneity from isotropy, it is necessary to combine isotropy with the Copernican principle. Studies have also tried to infer homogeneity from LSS (Wu, Lahav & Rees 1999; Lahav 2000), though these have a theoretical limitation due to the fact that the high redshift Universe is more homogeneous because younger.

In this Thesis I assume the Universe is homogeneous and isotropic. The metric of such a universe is described by the Friedman-Robertson-Walker (FRW) line element:

$$ds^2 = dt^2 - a^2(t)\left[\frac{dr^2}{1-kr^2} + r^2 d\theta^2 + r^2 \sin^2\theta d\phi^2\right], \tag{1.1}$$

where I use the signature $(+---)$, where the speed of light is defined as $c \equiv 1$.

1.3.2 The Expanding Universe

The scale factor $a(t)$ in Equation 1.1 defines the distance between two objects in the Universe, which changes due to the expansion of the Universe. It is normalized so that today, $a(t_0) = 1$. Due to this expansion, an object emitting light at a wavelength λ_{emit} will be observed with a different wavelength λ_{obs}. The change in wavelength defines the redshift parameter z:

$$1 + z \equiv \frac{\lambda_{emit}}{\lambda_{obs}}. \tag{1.2}$$

For an expanding universe, $\lambda_{emit} > \lambda_{obs}$, i.e., the wavelength is shifted towards longer and redder wavelengths, hence the term *red*shift. In an FRW model, the redshift is related to the scale factor by:

$$1 + z = \frac{a(t_{obs})}{a(t_{emit})}. \tag{1.3}$$

1.3.3 The Geometry of the Universe

The factor k in Equation 1.1, relates to the geometry of the Universe which can be one of three cases:

1. $k = 0$: flat or Euclidean, parallel light rays remain parallel.
2. $k < 0$: open or hyperbolic, parallel light rays eventually diverge.
3. $k > 0$: closed or spherical, parallel light rays eventually converge.

1.3.4 Dynamics of an Isotropic and Homogeneous Universe

The dynamics of an isotropic and homogeneous Universe are described by the Friedman equations:

$$\left(\frac{\dot{a}}{a}\right)^2 + \frac{k}{a^2} = \frac{8\pi G}{3}\rho_{\rm tot}\,, \tag{1.4}$$

$$\frac{2\ddot{a}}{a} + \left(\frac{\dot{a}}{a}\right)^2 + \frac{k}{a^2} = -8\pi G p\,, \tag{1.5}$$

where $\rho_{\rm tot}$ is the total energy density in the Universe.

The Hubble parameter defining the expansion of the Universe is given by:

$$H(t) = \frac{\dot{a}(t)}{a(t)}\,, \tag{1.6}$$

and its value today is given by $H_0 = 100h\,{\rm km\,s^{-1}Mpc^{-1}}$. The critical density is defined by $\rho_{\rm crit} = \frac{3H_0^2}{8\pi G}$ so that the first Friedman Equation (1.4) can be rewritten:

$$\frac{k}{a^2H_0^2} + 1 = \frac{\rho_{\rm tot}}{\rho_{\rm crit}} \equiv \sum_i \Omega_i\,, \tag{1.7}$$

where $\Omega_i = \frac{\rho_i}{\rho_{\rm crit}}$ and

$$\rho_i = \rho_{\rm m}, \rho_\Lambda, \rho_{\rm rad} \cdots\,, \tag{1.8}$$

which correspond to the densities of matter (m), the cosmological constant (Λ) and any other component of the Universe. The densities are defined so that $\rho_{\rm tot} = \sum_i \rho_i$.

From Equation 1.7, we note:

$$\frac{k}{H_0^2a^2} = \sum_i \Omega_i - 1\,, \tag{1.9}$$

i.e., the sign of k, or the overall geometry of the Universe, is determined by the sign of $\left(\sum_i \Omega_i - 1\right)$. By letting $\Omega_k = -\frac{k}{H_0^2a^2}$, this is equivalent to writing:

$$\sum_i \Omega_i + \Omega_k = 1\,. \tag{1.10}$$

The sum here includes the energy densities of matter (m), dark energy (Λ), curvature (k), radiation (*rad*) and any new type of energy density can be added to the equation. In this Thesis, I use the term Λ to refer to the cosmological constant or a dynamical dark energy, so that Ω_Λ or $\Omega_{\rm DE}$ are used interchangeably (see Section 1.6.4).

1.3.5 Age of the Universe

The lookback times is defined as the difference in time between an event which happened at a redshift z and today. It is given by:

$$\Delta t = \frac{1}{H_0}\int_0^z \frac{(1+z)^{-1}dz}{\sqrt{(1+z)^2(1+\Omega_m^0 z - z(2+z)\Omega_\Lambda^0)}}\,. \tag{1.11}$$

This is the general equation for a Universe composed of matter, a cosmological constant and arbitrary curvature. To find the age of the Universe one simply sets the upper limit of integration to $z = \infty$, although this ignores the early era of radiation domination in the Universe.

1.4 Inflation and the Big Bang Problems

There are four problems with the Big Bang model which eventually were solved by a theory brought forward by Guth & Tye (1980); Guth (1981), which suggests the very early Universe was subject to a phase of accelerated expansion, or *inflation*. For a review see Lahav & Liddle (2004). Here, I briefly review the main problems with the Big Bang model, and how they are solved by inflation.

Horizon Problem

The temperature fluctuations in the CMB, first measured by COBE (Bennett *et al.* 1990) were of the order $\Delta T/T \sim 2.10^{-5}$ at 10 degrees angular scales on the sky. Yet the size of the causal horizon on the sky corresponds to ~ 1 degree. These observations suggested that regions that were causally disconnected were somehow of exactly the same temperature. This is called the horizon problem.

The early inflationary period solves this problem: our whole observable Universe was inflated from a very small region at early times, so that all regions of the CMB we see today were all in causal contact in the early Universe.

Flatness Problem

A second problem is related to the geometry of the Universe and the fact that flat geometry is an unstable case. For the Universe to be flat today, i.e. $\Omega_k = 0$ then the value

of Ω_k in the very early Universe must have been exactly zero. It is the fine tuning of this scenario which is the flatness problem.

Inflation solves this initial condition problem. Whatever the initial curvature of the Universe it is smoothed out by the accelerated expansion.

Monopole Problem

Supermassive magnetic monopoles are expected from Grand Unified Theories (GUT). The prediction of their relic abundance is in contradiction with the fact that they have never been observed. With inflation, their number density was diluted in the very early Universe.

The Seeds of Structure

The CMB is extremely uniform in temperature suggesting the early Universe was homogeneous, yet today we observe very inhomogeneous Large Scale Structure. During inflation quantum fluctuations grow to astrophysical scales are the seeds of structure formation. Inflation also predicts these fluctuations should be Gaussian, which is what is observed in the CMB.

1.5 Components in the Universe

The Standard Model of Cosmology was born from observational evidence that the Universe was correctly described by the equations of general relativity. It stated what the Universe *could* be composed of, but not exactly what it was. The search to pinpoint exactly what the relative components of the Universe are, has been stimulated in the last decades by the large amount of available data. Studies of the CMB, large scale structure, along with other probes such as type Ia supernovæ have compelled us to endorse the ΛCDM model, today's *concordance cosmology*.

In this Section I describe the components of our Universe: baryons ($\sim 4\%$), dark matter ($\sim 22\%$) and a mysterious dark energy ($\sim 74\%$). These relative densities are those accepted as concordance cosmology today (and may change sooner or later!).

1.5.1 Baryonic Matter ($\sim 4\%$)

Humans, planets, stars, most things we *see* in the Universe are made of baryonic matter. Baryons encompass protons, neutrons and anything consisting of three quarks. They constitute what one might call *normal* matter. Primordial baryons were produced in the first 100 seconds following the Big Bang, when the Universe was hot and dense. The process in which they were formed is called Big Bang Nucleosynthesis (BBN) and is basically the same thermonuclear mechanism that fuels stars, except that it only produced very light elements.

The measured cosmic abundance of light elements shows that the Universe is made of approximately 74% Hydrogen (^{1}H), 26% Helium (^{4}He), 3.10^{-5} Deuterium (^{2}H) and 10^{-9} Lithium (^{7}Li). This is in accordance with prediction from the Big Bang. All other chemical elements we find on earth today and which comprise the building blocks of organic life (carbon, oxygen, etc ...) were formed much later in the core of stars. Their abundance is negligible on cosmic scales.

Baryons themselves are a subdominant quantity in the Universe, and as such, are not the norm. From the latest measurements of acoustic oscillations in the CMB (see Section 1.7), baryons are found to account for only 4% of the energy density of the Universe, or using the nomenclature of Equation 1.10, $\Omega_b \simeq 0.04$.

1.5.2 Dark Matter ($\sim 22\%$)

However present baryons are in our local environment, the dominant form of matter is now accepted to be an invisible, collisionless *dark matter*. This is the 'CDM' in ΛCDM, which stands for Cold Dark Matter. The two main pieces of evidence for this are observational anomalies on large scales.

Evidence for Dark Matter

Zwicky (1933) was the first to highlight the problem of a "missing mass" by studying the velocities of galaxies in the Coma cluster. On the scale of galaxies, discrepancies were found in the orbital velocities of HII regions. Spiral galaxies (see Section 1.5.3) rotate in a quasi-plane and the velocities of stars and material within the galaxy is a function

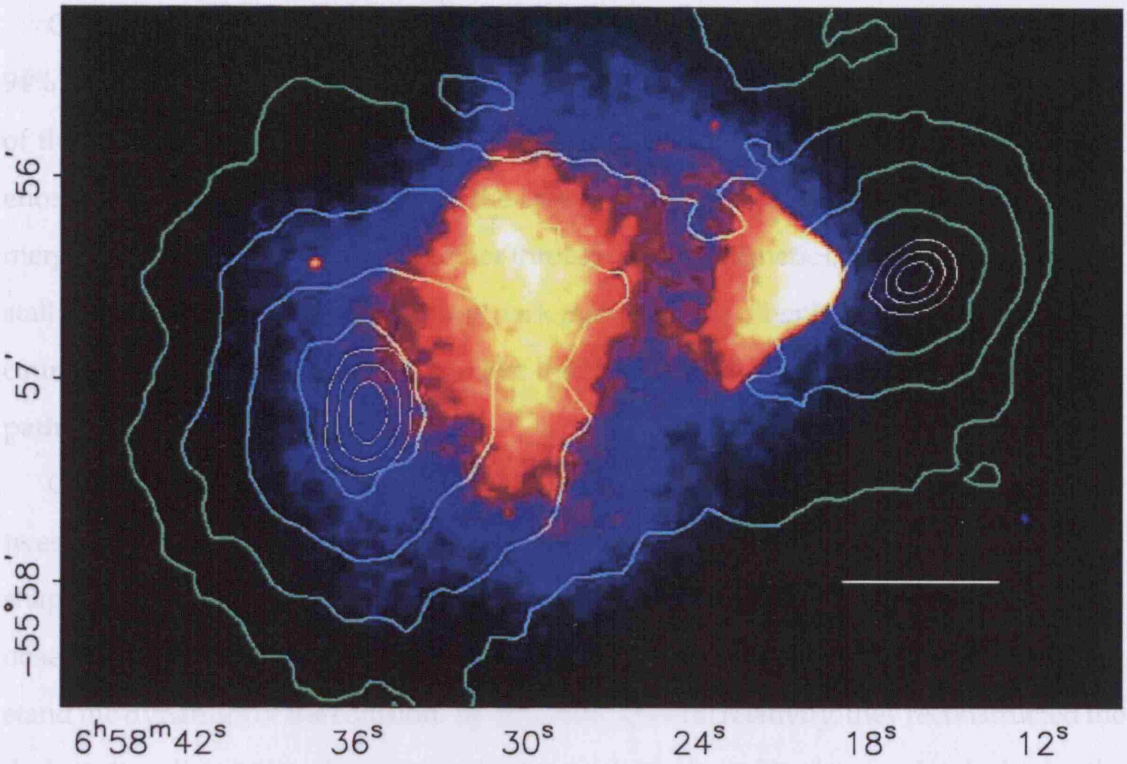

Figure 1.1: *from Clowe* et al. *(2006)*: X-ray image of the *Bullet* cluster (yellow, red and blue). The X-rays trace the plasma, i.e. the baryonic mass in the cluster. The overlaid green (solid) contours correspond to the weak lensing mass density reconstruction. These contours are obtained from measuring the weak lensing (assuming general relativity) of background galaxies (not shown in this image). The central white (dashed) contours show the 68.3%, 95.5%, 99.7% confidence limits on the centre of the mass. This is consistent with what is expected if the clusters are formed of baryonic plasma and collisionless dark matter.

of their distance from the centre. This velocity is expected to fall with radius following $v_{\rm orb} \propto r^{-1/2}$. The velocities of HII regions were measured from emission lines by Rubin *et al.* (1985) and were actually found to be constant with radius. This problem disappears if the matter within the galaxy extended beyond the visible disk of the galaxy.

The key property of dark matter is that it is collisionless. It only interacts with baryonic matter through gravity, and does not interact electromagnetically. Playing pool or snooker with dark matter billiard balls would be quite tricky, as they would never impact. Two dark matter billiard balls travelling towards one another would simply pass through each other.

Clusters of galaxies are thought to be made of $5-15\%$ of baryonic plasma and $84-94\%$ dark matter (the mass of stars in galaxies is estimated to be a mere 1%). Because of this, a merger between galaxies is the ideal scenario to check for behavioural differences between both components. In the case of a merger, the baryonic matter from each merging galaxy would interact together through electromagnetic collisions, which would stall its propagation. The collisionless dark matter on the other hand would continue its course unaffected by the impact, just like the billiard balls would continue their original path.

Clowe, Gonzalez & Markevitch (2004) and Clowe *et al.* (2006) studied a merger between two clusters, known together as the *Bullet* cluster because of the characteristic shape of the X-ray emission (see Figure 1.1). The advantage of the *Bullet* cluster, is that the observed merger is occurring in the plane of the sky, making it easier to study and understand the dynamics of the collision. By assuming general relativity, they reconstructed the dark matter distribution by measuring the weak lensing of background galaxies by the foreground cluster (see Section 1.7). The reconstructed centres of mass are plotted as the central white (dashed) contours in Figure 1.1, where the background galaxies have been removed from the image. The green (solid) contours correspond to the weak lensing mass density contours. What this study shows is that the bulk of the mass is distributed in two separate agglomerations, which are dissociated from the baryonic matter (in red, yellow and blue). This coincides with what is expected if the clusters are formed of baryonic plasma and collisionless dark matter. Alternative models such as MOND (see Section 1.8) fail to predict these observations without massive neutrinos of the order $\sum m_\nu \simeq 1\text{eV}$.

Can Dark Matter be Baryonic?

It is true that a small proportion of dark matter may be in the form of dark baryons, i.e. objects which are too faint to be detected or do not emit light, such as brown dwarfs or black holes (e.g., MAssive Compact Halo Objects - MACHOs). However, the energy density of baryons is constrained from the primordial abundances of light elements predicted from Big Bang Nucleosynthesis. Today, the search for dark matter is in the form of *non-baryonic* or *exotic* matter.

Massive Neutrinos as Hot Dark Matter

There is also evidence both from solar neutrino experiments (Totsuka & The Super-KAMIOKANDE Collaboration 1998) and large scale structure surveys (Lesgourgues & Pastor 2006) that a small amount of dark matter is *hot*, in the form of neutrinos. Conservative upper limits on the neutrino fraction from large scale structure surveys constrain the neutrino mass $\sum_i m_{\nu_i} < 2eV$, where i corresponds to the possible neutrino flavours μ, e or τ. This corresponds to a neutrino energy density $\Omega_\nu < 0.04$ (Seljak, Slosar & McDonald 2006; Elgarøy & Lahav 2006).

1.5.3 Galaxies

Together baryons and dark matter form galaxies: self gravitating conglomerates of stars (1%), baryonic plasma (5-15%) and dark matter (84-94%). The current largest all-sky survey (2MASS, see Chapter 2, Jarrett 2004) catalogued over 1 million of them out to a redshift of $z \sim 0.07$. Future survey like the Dark UNiverse Explorer (DUNE, see Chapter 7 Réfrégier *et al.* 2006) will image over 3 billion galaxies out to a mean redshift $z \sim 1$.

Galaxy Morphological Types

Hubble (1936) was the first to classify galaxies according to their morphology, and provided the well known *tuning fork* diagram, of which I show an example in Figure 1.2. Hubble originally thought elliptical galaxies (left of the *tuning fork*) were younger galaxies which later evolved into more structured spiral galaxies (both right branches of the *tuning fork*). This is now thought to be wrong, and to some extent the opposite is true: when two spiral galaxies merge, they will eventually form a larger elliptical galaxy, though even today galaxy evolution is not well understood. One of the main goals of modern cosmology is to understand how galaxies and large scale structure evolve with time and environment.

Unfortunately, Hubble's original misnomer remained and elliptical galaxies are sometimes referred to as *early type* galaxies and spiral as *late type* galaxies. Although there are many subdivisions within elliptical and spiral galaxies, in this Thesis I am only concerned with the broader division and refer to both elliptical and lenticular ($S0$) galaxies as *early*

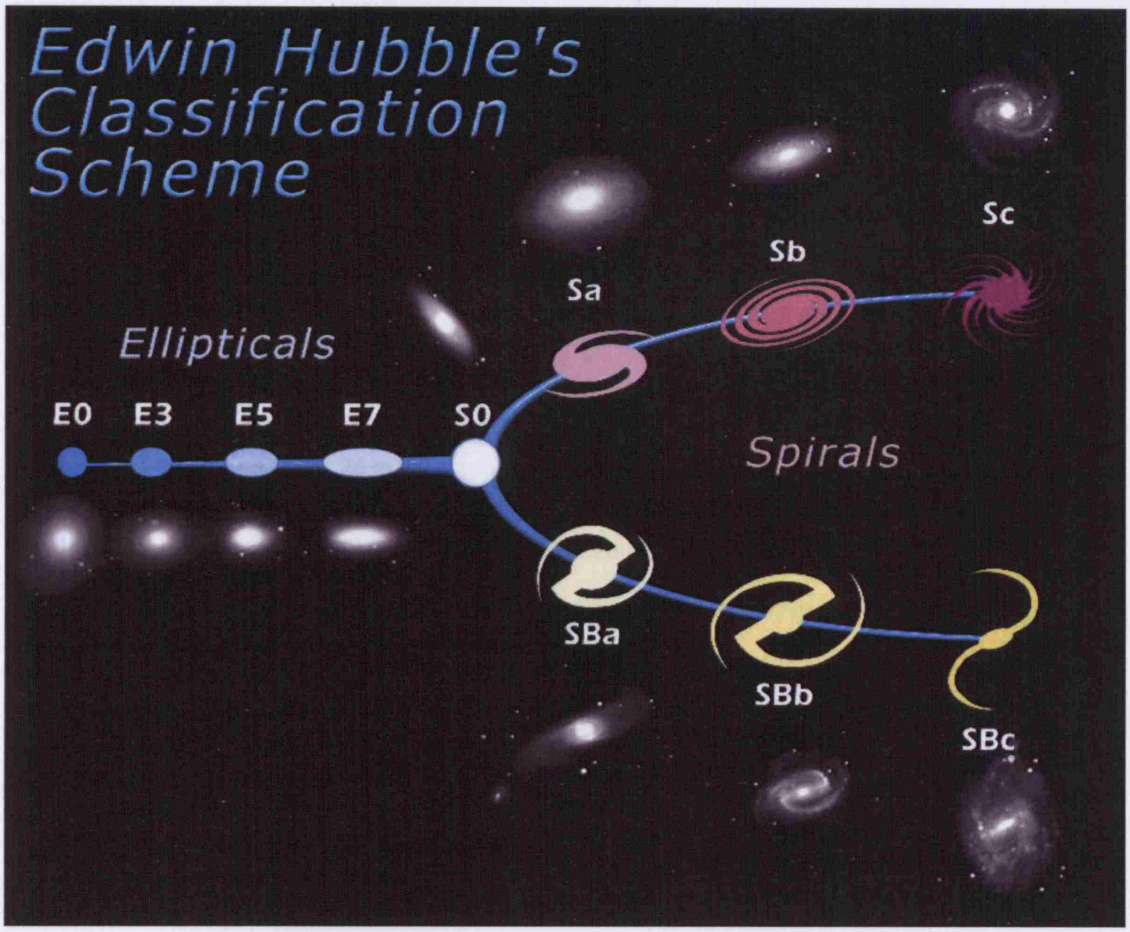

Figure 1.2: Example of a Hubble tuning fork diagram, which was the first classification of galaxy morphology. Elliptical (E0, E3, E5, E7) and lenticular (S0) galaxies are on the left hand, and spirals are on the right hand side. Spiral galaxies divide into standard spirals (Sa, Sb, Sc) and barred spirals (SBa, SBb, SBc). *(credit: NASA)*

type and any type of spiral or irregular as *late type*. Our Galaxy, the Milky Way, is a spiral galaxy, probably a type Sb or Sc.

Morphological classification also reflects more fundamental properties of the galaxies. Hubble & Humason (1931) were the first to notice that early types tend to live in the centre of clusters and late types at the periphery. Dressler (1980) was the first to quantify this trend as a dependence on density (see Chapter 4 for a study of this in the 2MRS survey). Galaxy spectra are also different for separate morphological types. In the optical and Near Infra Red (NIR) early type galaxies tend to be redder and late types bluer, due to their star forming regions. This makes it possible to segregate them by applying colour cuts. Sodré & Cuevas (1994) and Madgwick *et al.* (2003) used principal component

analysis on separate galaxy spectra (galaxy spectra from Kennicutt (1992) and the 2dF Galaxy Survey respectively) as a means of morphological classification. This is useful as visual morphological classification is time consuming and prone to human error. Instead Artificial Neural Networks (ANN) can be used (Naim *et al.* 1995; Lahav *et al.* 1995) or classification can be done by combining human effort, as in a new on-line project called *Galaxy Zoo*[‡] (open to astronomers and amateurs alike) which sets out to classify over a million SDSS galaxies visually.

1.5.4 Dark Energy ($\sim 74\%$)

Einstein initially introduced a cosmological constant to describe a static universe. When he realized the Universe was expanding, he set it to zero, saying it was the *"biggest mistake of* [his] *life"*. The cosmological constant came back in fashion in the early nineties, when measurements of the matter density Ω_m were lower than the critical density of 1 (Efstathiou, Sutherland & Maddox 1990). Inflationary scenarios predicted that the Universe should be flat, i.e. $\Omega_k = 0$. These measurements suggested something was missing in the equations, which could just be the cosmological constant.

Quantum field theory also predicted a cosmological constant as a natural by-product, which can be interpreted as vacuum energy. Vacuum energy means that the minimal energy state of empty space is not null. Space then has a vacuum density and a pressure. The special characteristic of vacuum energy is that it has a *negative* pressure, and would cause the Universe to accelerate.

In the 1990s, type Ia supernovæ data suggested the Universe was accelerating. This, with the low value of Ω_m, suggested there was an extra energy component in the Friedman equation, or a cosmological constant. This is the Λ in ΛCDM. Although the missing energy component was originally thought to be a cosmological *constant*, it can also be spatially and temporally varying, and is then called dark energy or quintessence.

The term dark energy, is a more general term to describe a mysterious (i.e. *dark*) energy which can explain both the acceleration of the Universe and the missing energy. A Universe with matter and curvature for example, will account for the missing energy, but not the acceleration.

[‡]See http://galaxyzoo.org/

The equation of state of dark energy is given by:

$$p = w\rho \,. \tag{1.12}$$

where p is the pressure and ρ is the density. A value $w = -1$ corresponds to a cosmological constant. The parameter w can take any value with $w < -1/3$ to explain the acceleration of the Universe. In Section 1.6.4, I discuss some of the effects of dark energy on observable quantities in the Universe, and in Section 1.7, cosmological probes of dark energy, in particular the Integrated Sachs-Wolfe (ISW) effect, which I investigate in Chapter 5, 6 and 7 of this Thesis.

1.5.5 Curvature

In general relativity, geometry or curvature also contributes to the stress-energy tensor and as such has an energy density in the same way matter and dark energy do.

As I described in Section 1.3, the geometry of the Universe can either be flat, hyperbolic or spherical. Photons always travel along geodesics, which are dictated by the geometry, so that the apparent size of distant objects is dependent on the curvature of the Universe. Acoustic oscillations in the CMB power spectrum (see Section 1.7.1), combined with measurement of the matter energy density, suggest the Universe we live in is flat, or using the nomenclature in Equation 1.10, $\Omega_k = 0$, which is what is predicted by inflation (Guth & Tye 1980; Guth 1981).

1.6 Observable Quantities

Equations 1.4 and 1.5 describe the global dynamics of an isotropic and homogeneous Universe. However the Universe is not homogeneous on all scales; if it were there would not be the structure we observe today in clusters and galaxies (and even in our bodies). After the Big Bang the Universe was extremely smooth but hosted very small fluctuations. No matter how small these fluctuations were, they eventually grew by attracting surrounding matter through *gravitational instability*, which was the agent of structure formation. One of the main goals of modern cosmology is to understand the seeds of structure formation.

The quantities Ω_i given in Section 1.3 denote the energy densities of each component of the Universe and are only zeroth order properties. In order to quantify fluctuations, we need to consider first order deviations from a smooth Universe.

In this Section I give an overview of the two point statistical tools useful to measure the fluctuations in cosmic fluids. In particular I define the matter power spectrum $P(k)$ in Section 1.6.1. In Sections 1.6.2 through to 1.6.4, I describe the normalization of the matter power spectrum, as well as non-linear and quintessence corrections. The matter power spectrum is related to the observable galaxy power spectrum by the bias b_g, which I introduce in Section 1.6.5, in the context of linear theory and the halo model. Finally, for data on a sphere, it is useful to consider the angular two-point functions, either in spherical harmonic or in real angular space. I define these angular correlation functions in Section 1.6.6.

1.6.1 The Matter Power Spectrum P(k)

The matter power spectrum describes the fluctuations of the matter distribution. It is defined by:

$$\left\langle \delta(\vec{k})\delta^*(\vec{k'}) \right\rangle = (2\pi)^3 \delta^3(\vec{k} - \vec{k'}) P(k) \,, \tag{1.13}$$

where δ represents the Fourier transform of the matter overdensities:

$$\delta(\vec{r}) = \frac{\rho(\vec{r}) - \bar{\rho}}{\bar{\rho}} \,, \tag{1.14}$$

and the mean density of the Universe is $\bar{\rho}$.

The initial power spectrum is assumed to be of the form:

$$P(k)_{init} \propto k^n \,. \tag{1.15}$$

The power spectrum today can be obtained by assuming the initial power spectrum has evolved according to:

$$P(k, z) \propto P_{\rm init}(k) T^2(k) D^2(z) \,. \tag{1.16}$$

Where $D(z)$ is the linear growth factor. The quantity $T(k)$ is the transfer function, and is a solution to Boltzman's equations which describes the way in which each component in the Universe interact with each other.

1.6.2 Normalization of the Power Spectrum

The matter power spectrum is usually normalized by considering the variance σ_R^2 of the mass contrast smoothed over a sphere of radius R. The radius of the sphere is chosen by convention as $R = 8h^{-1}\mathrm{Mpc}$, so that $\sigma_8 \simeq 1$ from galaxy counts (Groth & Peebles 1977). Current model dependent estimates from combined CMB and LSS analysis show that $\sigma_8 \simeq 0.75$ (Spergel *et al.* 2006). The normalization is taken so that:

$$\sigma_8^2 = \sigma^2_{R=8h^{-1}\mathrm{Mpc}} = \frac{4\pi}{(2\pi)^3}\int \tilde{W}^2(k)P(k)k^2dk\,, \tag{1.17}$$

$$\tilde{W}(k) = \frac{3}{(kR)^3}\left[\sin(\mathrm{kR}) - \mathrm{kRcos(kR)}\right]\,, \tag{1.18}$$

where $\tilde{W}(k)$ is the Fourier transform of a 3-dimensional sphere.

1.6.3 Non-Linear Power Spectrum

The linear power spectrum is modified by motion of matter due to gravity at small scales. Peacock & Dodds (1994) proposed an analytic reconstruction of the non-linear power spectrum, which characterizes large fluctuations (i.e., $|\delta| \sim 1$). They showed the dimensionless form of the power spectrum $\Delta^2(k) \propto k^3P(k)$ transforms as:

$$\Delta^2_{\mathrm{NL}}(k) = f_{\mathrm{NL}}\left(\Delta^2_{\mathrm{L}}(k_{\mathrm{L}})\right)\,, \tag{1.19}$$

$$k_{\mathrm{L}} = \left[1 + \Delta^2_{\mathrm{NL}}(k_{\mathrm{NL}})^{-1/3}\right]k_{\mathrm{NL}}\,, \tag{1.20}$$

where the subscripts L refer to linear quantities and NL to non-linear quantities. The fitting formula f_{NL} is given by:

$$f_{\mathrm{NL}}(x) = x\left[\frac{1 + 0.2\beta x + (Ax)^{\alpha\beta}}{a + (Ax)^{\alpha}g^3(\Omega)/(11.68\sqrt{x})}\right]\,, \tag{1.21}$$

where $g(\Omega)$ is the growth function, and depends on cosmological parameters.

1.6.4 Quintessence Correction

When the equation of state of dark energy is given by $w \neq -1$, the quantity Ω_Λ no longer corresponds to the energy density of a cosmological constant but to a general form of dark energy or *quintessence*. Contrarily to the cosmological constant, quintessence is a spatially inhomogeneous and time evolving cosmic fluid (though there exist forms of dark energy which are not spatially inhomogeneous such as the Chapylgin gas).

Quintessence will remain smooth on small scales (where $k \gg k_Q$), however on large scales ($k \ll k_Q$), it will cluster and therefore contribute to the energy density and pressure perturbations. On linear scales, both the transfer function $T(k)$ and the growth factor $g(a) \equiv D/a$ will be affected by these perturbations. The general effect of the quintessence perturbations will be to increase large scale power in the CMB (Weller & Lewis 2003).

Quintessence Approximations and Nomenclature in this Thesis:

In this Thesis, I am mainly concerned with a Universe with $w = -1$. In Chapter 7, I consider slight deviations from $w = -1$ in order to calculate the Fisher forecasts. For small deviations from $w = -1$ the corrections to the transfer function and the growth factor are negligible (see details in Chapter 7), and so quintessence corrections to the transfer function and the growth factor are ignored in this Thesis (see Chapter 5 for details).

Quintessence will also introduce a correction to the non-linear mapping of the power spectrum. However, I am only concerned with linear effects in this Thesis, and do not include them.

Throughout this Thesis I use the terms Ω_Λ and $\Omega_{\rm DE}$ interchangeably; whether the component is a cosmological constant or quintessence is implicitly defined by the value of w.

1.6.5 Galaxy Bias and Halo Model

In this Section I describe the galaxy bias which relates the galaxy power spectrum with the matter power spectrum.

Linear Scale Independent Galaxy Bias:

If the galaxies we see, linearly trace the underlying matter distribution, then the galaxy power spectrum $P_g(k, z)$ is related to the matter power spectrum $P_m(k, z)$ by:

$$P_g(k, z) = b_g^2(z) P_m(k, z) \,, \tag{1.22}$$

which assumes the bias is scale independent but not necessarily constant with redshift. If the growth of structure is linear, the redshift and scale dependence of the power spectrum are independent and:

$$P_m(k, z) = D^2(z) P_m(k) \,. \tag{1.23}$$

Galaxy Bias in the Halo Model:

Another model exists which does not assume matter is continuously distributed in the Universe, called the Halo Model (see Cooray & Sheth (2002); Seljak (2000); Peacock & Smith (2000) for a good introduction). The Halo Model assumes that matter is concentrated in haloes, which may or may not host galaxies. Outside of haloes the density is null and only haloes above a certain threshold $M_H \geq M_{\rm cut}$ will host galaxies. The matter power spectrum can then be written as the sum of two terms:

$$P_m(k) = P^{1h} + P^{2h} \,, \tag{1.24}$$

where P^{1h} is the non-linear *intra*-halo term and P^{2h} the linear *inter*-halo term.

A halo is defined by its mean halo occupation number $\langle N|M\rangle$, which is the mean number of galaxies per halo of mass M. The halo population is defined by the halo mass function $n(M)$ which gives the expected number of haloes of a given mass M.

The bias in the Halo Model is defined by:

$$P^{2h} = b_g^2 P^{\rm lin}_{\rm DM}(k) \,, \tag{1.25}$$

and:

$$b_g \equiv \int {\rm d}M n(M) b(M) \frac{\langle N|M\rangle}{\bar{n}_{\rm gal}} \,, \tag{1.26}$$

where $\bar{n}_{\rm gal}$ is the galaxy number density (i.e., the mean number of galaxies per halo), and $b(M)$ is a function of the mass of the halo.

Assumptions on the Galaxy Bias in this Thesis:

In this Thesis, I always assume the bias is linear and scale independent. Throughout this Thesis, I consider $b = b(z)$ following the Galaxy conserving model of Magliocchetti *et al.* (2000), except in Chapters 4 and 6 where I have assumed it to be constant; given the depth of the 2MRS and 2MASS surveys which are considered, this only introduces an error of about 1% on the bias. In Future work, I plan to extend analysis of the galaxy bias to the halo model.

1.6.6 Harmonic Power Spectra

Astronomical observations are projected on the celestial sphere, and it is easier and often more useful to the astronomer to record an object by spherical equatorial coordinates (RA, δ) or galactic coordinates (l, b) rather than Euclidean coordinates such as supergalactic coordinates (SGX, SGY, SGZ). In this Section I describe the two point statistics for decomposing fields on a sphere using either spherical harmonic decomposition or real space angular correlations.

Spherical Harmonic Decomposition:

When objects are distributed on a sphere, a natural basis in which to decompose their density field is defined by the spherical harmonics $Y_{\ell m}(\theta, \phi)$, which form an orthonormal set on the sphere. For example, the galaxy density field (or equivalently the temperature anisotropy field of the CMB), can be decomposed as:

$$\rho(\vec{r}) = \sum_{\ell=0}^{\infty} \sum_{m=-\ell}^{\ell} a_{\ell m} Y_{\ell m}(\theta, \phi) \,, \tag{1.27}$$

where $\theta = [0; \pi]$ and $\phi = [0; 2\pi]$ are the angular position of the galaxies on the celestial sphere where the term $a_{\ell m}$ corresponds to the spherical harmonic coefficients of the expansion.

The spherical harmonic two point Auto-Correlation Function (ACF) or spherical harmonic power spectrum is given by:

$$C(\ell) = \left\langle |a_{\ell m}|^2 \right\rangle \,. \tag{1.28}$$

Isotropy assures that $\left\langle |a_{\ell m}|^2 \right\rangle$ is a function of scale ℓ only and independent of phase m.

The decomposition of a field using 1.27 is only valid for data covering the whole sky. In the case of incomplete sky coverage, it is possible to recover the true underlying $C(\ell)$ using *pseudo-C(ℓ)* technique. This is described in Section 3.5.1 of Chapter 3.

Angular Correlation Function $w(\theta)$:

In the case where sky coverage is much smaller than 4π, it is often easier to measure correlations using the angular correlation function $w(\theta)$. The angular correlation function

is related to the ACF by:

$$w(\theta) = \frac{1}{4\pi}\left(\frac{\Delta\Omega}{N_g}\right)^2 \sum_{\ell=1}^{\infty}(2\ell+1)C(\ell)P_\ell(\cos\theta)\ . \tag{1.29}$$

The mean galaxy surface density is given by $\left(\frac{N_g}{\Delta\Omega}\right)$, and $P_\ell(\cos\theta)$ are the Legendre polynomials. This Equation can be inverted, to obtain the spherical harmonic power spectrum from the angular correlation function:

$$C(\ell) = 2\pi\left(\frac{N_g}{\Delta\Omega}\right)^2 \int_{-1}^{+1} w(\theta)P_\ell(\cos\theta)\mathrm{d}(\cos\theta)\ . \tag{1.30}$$

Both quantities $w(\theta)$ and $C(\ell)$ are equivalent in theory, though in practice $w(\theta)$ can only be accurately measured on small scales, beyond which Poisson noise will dominate. The $C(\ell)$ power spectrum has the highest signal on large scales so long as the survey used has all- or nearly all-sky coverage.

Cross-Correlations Function (CCF):

If two separate fields are correlated, their correlation can be measured by using the Cross-Correlation Function (CCF) or spherical harmonic cross-power spectrum:

$$C_{XY}(\ell) = \langle |X_{\ell m}Y^*_{\ell m}| \rangle\ , \tag{1.31}$$

where $X_{\ell m}$ and $Y_{\ell m}$ are simply the harmonic coefficients of each field and $C_{XY} = C_{YX}$.

In Chapters 3, 4 and 6, I give expressions for the linear theory prediction of the galaxy ACF. I use this to derive the galaxy bias and the matter density from the 2MRS and 2MASS galaxy surveys. In Chapters 5, 6 and 7, I present the linear theory predictions for the galaxy-temperature, as expected for the ISW effect (see Section 1.7.1). I use this to derive constraints on the dark energy parameters.

1.7 Cosmological Tools

In this Section I give a brief overview of the different cosmological tools which have together provided evidence to build the Standard Model of Cosmology. Combining cosmological tools breaks existing parameter degeneracies and also acts as independent confirmation of a general underlying model.

One of the most important cosmological tools which presents strong evidence for both the Big Bang and ΛCDM model is the Cosmic Microwave Background. In Section 1.7.1, I describe the main primary and secondary temperature anisotropies which can be used to constrain cosmology from the CMB. In Section 1.7.2, I describe the effects of gravitational lensing and how it is suited to the study of dark matter and galaxy formation. In Section 1.7.3, I overview how clusters counts can be used as a cosmological tool. In Section 1.7.4, I describe type Ia supernovæ and their role in determining the expansion history of the Universe, and inferring the presence of dark energy. In Section 1.7.5, I explain how the study of galaxy clustering can be related to cosmological parameters. In Section 1.7.6, I introduce the meaning of *cosmic variance*, an important statistical uncertainty in observational cosmology.

1.7.1 Cosmic Microwave Background (CMB)

The CMB is the background sea of photons which permeates the Universe with around 400 photons per cubic metre, and is often called the *primordial light*. After the Big Bang, the Universe was extremely hot and dense, so much so that the light elements were all ionized. The electrons of the ionized material constantly interacted with the photons through Compton scattering so that the photons and electrons were coupled. During this time the Universe is opaque, as photons could not travel far before interacting with electrons.

As the Universe expanded, the temperature dropped. When the Universe was about 300,000 years old, the temperature was low enough for neutral Hydrogen to form. This is called recombination: when protons and electrons combined to form neutral Hydrogen. After recombination the photons and electrons were no longer coupled and the Universe became transparent as photons were able to free-stream from what is called the *surface of last scattering*. These photons are the same we see today in the background radiation, and so represent a map of the very early Universe.

The CMB we observe today is extremely uniform - to one part in 10^5, which is evidence that the Universe is extremely isotropic on large scales. The CMB also presents small fluctuations or *temperature anisotropies*. These anisotropies are usually measured using the temperature-temperature ACF, defined by Equation 1.28 and where the har-

monic coefficients $a^T_{\ell m}$ are defined by:

$$\frac{\Delta T}{T}(\vec{r}) = \sum_{\ell=0}^{\infty} \sum_{m=-\ell}^{\ell} a^T_{\ell m} Y_{\ell m}(\theta, \phi) \, . \tag{1.32}$$

Some of these anisotropies are primordial, and enclose a wealth of information about the very early Universe; other anisotropies are due to secondary effects which occurred between the surface of last scattering and today - these contain information about the media through which the photons have travelled. Here I describe both the primary anisotropies and a few of the secondary anisotropies.

Primary Anisotropies

Primary temperature anisotropies in the CMB are due to effects at or just before the surface of last scattering.

- *The Sachs Wolfe Effect:*

  Before recombination the photons and electrons were coupled through Compton scattering. Baryons were clustered and as photons were coupled to baryons through electromagnetic radiation they were also clustered. After recombination, photons were able to free-stream, but first needed to climb out of the varying potential wells created by clustered baryons. The net effect of this was that underdense regions appeared as hotter regions in the CMB. This created power in the CMB temperature-temperature power spectrum on large scales and is called the Sachs-Wolfe effect (Sachs & Wolfe 1967).

- *Acoustic Peaks*

  Just before recombination, the fluctuations in the baryon-photon coupled fluid were subject to two competing effects: attractive gravity and repulsive pressure. These two effects meant the size of the fluctuations would oscillate and each subsequent oscillation corresponded to a different characteristic scales. These oscillations are frozen at recombination and we observe them as the consecutive peaks in the CMB temperature-temperature power spectrum.

- *Damping*

  Recombination did not occur instantaneously in the Universe, so that while some photons were free-streaming, others were still coupled to electrons and baryons and could 'random-walk' a certain distance. This had the effect of washing out anisotropies on small scales, and has a characteristic exponential damping tail; it is called *collisionless* or *Silk* damping (Silk 1967).

Secondary Anisotropies

Secondary temperature anisotropies in the CMB are due to effects between the surface of last scattering and the observer.

- *Early Integrated Sachs-Wolfe (eISW) effect*

  The early integrated Sachs-Wolfe effect is due to an effect shortly after recombination. At that time, the dynamics of the Universe are dominated by radiation. Gravitational potentials which are larger than the sound horizon, decay due to radiation. The energy from the gravitational potential decay is transfered to the photons, which are blueshifted. As the Universe expands the sound horizon grows, so that this effect takes place on larger and larger scales. At matter-radiation equality, gravitational potentials crossing the sound horizon no longer decay, and the eISW effect is no longer important. The eISW is *integrated* because the radiation era is not finite in time.

- *Late Time Integrated Sachs-Wolfe (ISW) Effect*

  The late-time integrated Sachs-Wolfe (ISW) effect is another secondary gravitational effect. It takes place long after the early ISW effect, when Large Scale Structure has formed in the Universe. As photons travel from the surface of last scattering they travel in and out of large scale gravitational potential wells, causing respectively blue- and redshifting of the photon. If these potential wells do not vary with time, the net effect will be null and the photon will emerge from the potential well unaffected by the large scale structure.

  However, if the potential wells vary with time, as in the case of a universe with curvature, or dominated by dark energy, the photon's wavelength will be affected

by LSS. This can also arise in alternative models of gravity The late-time ISW is therefore an *integrated* effect, because it depends on all the potential wells along the line of sight. This effect is expected to achromatic, i.e. independent of the measured wavelength of the photon and so should be measured in all CMB wavelength bands.

This effect is hard to measure in the CMB power spectrum as it is much smaller than the Sachs-Wolfe effect and on the sames scales, but can be measured in harmonic space by cross-correlating the CMB temperature with a tracer of the potential well such as a galaxy density field, i.e.:

$$C^{gT}(\ell) = \left\langle a^{g}_{\ell m} a^{*T}_{\ell m} \right\rangle . \tag{1.33}$$

On the assumption that the Universe is flat, and that general relativity is the correct prescription of gravity, a detection of the ISW effect is an independent signature of the presence of dark energy, making it a powerful tool in cosmology. There have been over ten claimed detections of the ISW effect (see Chapter 5 for a review of these), including Rassat *et al.* (2007) which I discuss in Chapter 6. In Chapter 7 I make forecasts on how well the ISW effect can constrain dark energy parameters. I make these predictions for cross-correlations of the CMB with the future generation of galaxy surveys such as the Dark Energy Survey (DES, Annis *et al.* 2005) and the Dark UNiverse Explorer (DUNE, Réfrégier *et al.* 2006).

- *Sunyaev-Zel'dovich (SZ) Effect*

  The Sunyaev-Zel'dovich (SZ) effect is a spectral distortion of the CMB caused by the inverse Compton scattering of photons as they travel though ionized gas (Sunyaev & Zeldovich 1980, or see Birkinshaw 1999 for a review). Large galaxy clusters have deep gravitational wells and the ability to keep material within it hot and ionized, and so cause the SZ effect.

  Given that the SZ effect is a frequency dependent effect, by probing the CMB in different wavelengths it is possible to detect clusters at any redshift from the SZ effect. This is extremely useful for detecting clusters that are otherwise invisible in the optical or infrared. It can also be used to probe modified gravity models

(Tang, Weller & Zablocki 2006). The SZ effect measures the total thermal energy of electrons residing in gravitational potential wells and so it is also possible to measure the mass estimates of clusters from it.

- *Gravitational Lensing of the CMB*

  Large Scale Structure in the Universe will distort space time, so that photons travelling from the surface of last scattering will be displaced from their original trajectory. The displacement is expected to smooth the acoustic peaks and add power at small scales in the temperature-temperature power spectrum. However these effects seem hard to distinguish from other anisotropies at similar scales. Alternatively, they could be measured in the CMB by considering the four point temperature correlation function, but this suffers from high statistical noise.

  One approach is to consider the cause of the lensing, the LSS as traced by a galaxy survey for example. One can calculate the three point function - of the displacement α (measured from the CMB two point function) with the potential well traced by the LSS, i.e. cross-correlate the two point temperature function with the galaxy field, by:

$$C^{\alpha g}(\ell) = \left\langle a^T_{\ell_1 m_1} a^T_{\ell_2 m_2} a^g_{\ell_3 m_3} \right\rangle \ . \tag{1.34}$$

  Smith, Zahn & Doré (2007) recently reported a 3.4σ detection of gravitational lensing of the CMB by foreground large scale structure, using WMAP data and NVSS radio surveys.

1.7.2 Gravitational Lensing

Even if the global geometry of the Universe is flat, inhomogeneities in the matter distribution of the Universe, mean there exists local distortions in space-time. As shown in the previous Section this can induce secondary anisotropies in the CMB. It will also affect the path of photons emitted from distant galaxies and travelling towards us, so that the image of a distant galaxy will be distorted through *gravitational lensing*.

Figure 1.3: This image of the Abell 2218 galaxy cluster was taken by the Hubble Wide field and Planetary Camera 2 in 2000. The large blurry elliptical galaxies form this massive cluster of galaxies, which acts as a gravitational lens in the Universe. This lensing effect distorts the image of the background images, seen as large concentric arcs in blue and red. The arcs are distorted images of galaxies which are 5 to 10 times further than the lensing cluster, and existed when the Universe was only a quarter of its ages. The gravitational lensing not only distorts the images but also magnifies them so that the background galaxies would otherwise be too faint to be detected without the foreground lens effect. This makes gravitational lensing an invaluable tool for studying high redshift galaxies and galaxy formation. As the shape of the arcs depend on the mass of the lens, it is also useful for the study dark matter distribution in clusters. *(Credit: NASA)*[**]

Strong Gravitational Lensing

If the lensing object and the image source are nearby (projected on the sky - not physically near), this can lead to a dramatic distortion and multiple images, as in this Hubble image of the Abell 2218 cluster (Kneib *et al.* 1996), shown in Figure 1.3.[**]

Studies of the shape of the arcs and of the position of the multiples images can yield information about the relative distance of the lens and the source and of the mass of the lens. Strong lensing also magnifies the background images, letting us see further in the

[**]For a breathtaking high resolution version of this image, see the Hubble website: http://imgsrc.hubblesite.org/hu/db/2000/07/images/b/formats/full_jpg.jpg

distant and past Universe. This makes strong lensing an invaluable tool for the study of high redshift galaxies and galaxy formation, as well as for studies of the dark matter distribution of the lensing object (see Fort & Mellier (1994) for a review).

Weak Gravitational Lensing or Cosmic Shear

In the weak limit, i.e. when the source and the lens are relatively distant on the sky, the effect is a slight distortion or ellipticity of the source image, of the order of a few percent. The effect is small in amplitude but will affect all observed galaxies and so can be studied statistically to yield cosmological information.

Weak lensing was detected for the first time in 2000 by four independent teams (Van Waerbeke *et al.* 2000; Kaiser, Wilson & Luppino 2000; Bacon, Refregier & Ellis 2000; Wittman *et al.* 2000) using independent data processing techniques and telescopes. Since then, there have been more detections using data from the Canada-France-Hawaii Telescope Legacy Survey (CFHTLS) Semboloni *et al.* (2006) and Hoekstra *et al.* (2006). However, the measurement of the ellipticity or shear of galaxies, is a difficult endeavour. It is greatly hindered by detector limitations and atmospheric distortions.

Nonetheless, the next generation of galaxy surveys such as DUNE (Réfrégier *et al.* 2006) and DES (Annis *et al.* 2005) are being conceived specifically with cosmic shear in mind, because weak lensing is predicted to be such a powerful tool with which to understand cosmology. DUNE is a space mission, expected to launch circa 2017, which will image the *entire sky* with Hubble Space Telescope (HST) image quality. As it is a satellite, it bypasses the impeding effects of atmospheric distortions. Cosmic shear measurements with DUNE are predicted to measure the equation of state of dark energy, w, down to a few percent.

Three dimensional lensing reconstructions or weak lensing tomography (Taylor *et al.* 2004; Massey *et al.* 2007) are also promising tools.

1.7.3 Cluster Counts

The galaxy cluster mass function and the spatial cluster correlation both depend on the dark energy density in the Universe through the growth of density perturbations and through the evolution of the volume element. Clusters are useful probes because their

number counts are very sensitive to cosmological parameters and their evolution depends only on dark matter and are independent of baryonic physics.

1.7.4 Type Ia Supernovæ

Type Ia supernovæ arise from material accretion on white dwarfs. White dwarfs are remnants of stars which have gone through a normal life cycle and can no longer sustain the temperature necessary for nuclear fusion of carbon and oxygen of which they are composed. This is because their maximum mass is dictated by the Chandrasekhar limit, about $1.4M_{\odot}$, where $M_{\odot}$ is the mass of our Sun. This upper mass limit arises from the electron degeneracy pressure, which is due to the Pauli exclusion principle. This states that no two identical fermions can be in the same quantum state.

If the white dwarf is confined in a binary system, it can slowly accrete material from its companion until its core reaches the temperature of carbon fusion. At this point the white dwarf enters a runaway reaction seen as a supernova explosion.

Although the details of supernovæ are not well understood, in particular it is not known if their characteristics are environmentally or redshift dependent, it is usually assumed that they behave as *standard candles* - just as the Cepheid stars which were used by Hubble to measure the redshift velocity relation. The idea is that if type Ia supernovæ always explode as they hit the Chandrasekhar limit, then it is not unreasonable to expect them to be a benchmark phenomenon. In nearby supernovæ , it was found that the rate with which the brightness of a supernova declines is proportional to its intrinsic luminosity. Thus by measuring the light curves of distant supernovæ , it is possible to measure their distance, and by obtaining a spectra one can compare their distance-redshift relation, which is highly dependent on cosmological parameters. Several groups, Riess *et al.* (1998); Perlmutter *et al.* (1998) and Schmidt *et al.* (1998), used the light curves of supernovæ to infer that the universe was expanding.

1.7.5 Galaxy Clustering

The acoustic oscillations present in the CMB power spectrum are also expected to exist in the galaxy power spectrum, and are referred to as Baryon Acoustic Oscillations (BAO).

The reason they are related is because fluctuations in the galaxy field are relics of primordial fluctuations in the CMB. Current galaxy surveys now probe the scales on which the BAO are expected and were recently detected by two independent teams and surveys (Eisenstein *et al.* 2005; Cole *et al.* 2005).

In this Thesis, I also study large scale galaxy clustering (Chapters 3 and 4). The clustering of local galaxies will include a distortion due to the peculiar velocities of galaxies, called 'redshift' distortions. This term was coined because the radial component of the peculiar velocities introduce an error in the estimation of galaxy redshifts. There exists an exact prescription for the galaxy redshift space power spectrum in spherical harmonics (see Chapter 3 for a detailed explanation and analysis using the all-sky 2MRS data).

1.7.6 Cosmic Variance

Cosmologists are disadvantaged compared to biologists, in that where biologists can experiment with cells in Petri dishes, cosmologists cannot experiment with the one Universe they have at their disposal. Any cosmological observation is then associated with a statistical uncertainty called *cosmic variance*, which arises from the inability to make several observations of the same 'type' of universe.

These incompressible error bars will be present in all observational quantitites such as the Fourier space and spherical harmonic power spectra $P(k)$ and $C(\ell)$. On large scales such quantities will be cosmic variance limited, i.e. when the error due to cosmic variance is larger than those from other sources (shot noise, instrumental noise, etc ...).

1.8 Alternative Models

A critic might question what is so admirable about the ΛCDM model. It requires 96% of the Universe to be dark, which is a delicate way of saying those 96% are poorly understood. Does this really show for a universal understanding of cosmological physics? Yes, this is the golden age of cosmology, flooded with data. Yes, we can *constrain* parameters to within a few percent, but is that useful if we do not understand what these parameters mean?

Luckily, the community is still divided over the infallibility of the Standard Cos-

mological Model. Much work is spent deriving alternative models and checking them against the stream of new data. Entire conferences are dedicated to the investigation of alternative approaches, and though none has to date been able to explain the integrity of cosmological observations, the mathematical advances and rise in awareness are promising and healthy. The challenge of the next generation of cosmological observations is either to confirm or disprove that Einstein's theory of general relativity is the simplest and most accurate way of describing gravity.

In this Section I give a brief overview of four types of alternative models. The first refute the fundamental assumption that the Universe is homogeneous, as an attempt to explain the accelerated expansion of the Universe. The second propose alterations to our model of gravity in order to explain large scale anomalies which call for dark matter. The third type investigate the consequences of non-trivial topology on isotropy. Finally, I discuss higher dimensional models which assume the Universe has more than three spatial dimensions.

Inhomogeneous Models

The cosmological principle states that the Universe has no preferred direction (isotropy) and no preferred place (homogeneity). This fundamental axiom is the very base of the Standard Cosmological Model. By removing the assumption that the Universe is homogeneous, it is possible to live in an accelerated Universe without dark energy (Alnes, Amarzguioui & Gron 2005). In this case, our local universe is found in an underdense region or bubble, and is gravitationally attracted to the surrounding denser regions, mimicking the effect of dark energy.

However, to reproduce the effects of the observed accelerated expansion, our place has to be extremely special: almost precisely in the centre of a spherically symmetric inhomogeneity and is disfavoured by some other authors (Ishibashi & Wald 2006).

Modified Gravities

Should the data fit the theory or the theory the data? When challenged with conflicting observations and theory, the scientist may take two different routes. The first is to look for issues with the observations, such as detection issues. This is the solution taken

by proponents of dark matter. In this case, the problem with the observation is that dark matter is invisible to the detectors. The second is to reconsider the theory. In the case of galaxy rotation curves, this is quite legitimate. General relativity and Newtonian theory had never been tested on scales beyond the solar system. Anomalies of galactic rotation curves might just point to a failure of our gravity model on these scales.

Milgrom proposed in 1981 a modified version of Newtonian dynamics to explain the galactic anomalies. MOdified Newtonian Dynamics (MOND) has a characteristic acceleration a_0 below which newtonian dynamics are modified to explain the observed orbital velocities of stars in galaxies. However, it cannot explain recent observations of the *Bullet* cluster without massive neutrinos of the order $\sum m_\nu \simeq 1\text{eV}$ (see Section 1.5.4).

Another type of modified gravity are the so called "f(R) theories" which modify the Lagrangian action. These arise in Grand Unified Theories (GUT) and superstring theory and can predict the same expansion history as ΛCDM (Fay, Nesseris & Perivolaropoulos 2007).

Topology

Several analyses of the large scale power in the CMB power spectrum have suggested a lack of statistical isotropy on very large scales (Eriksen *et al.* 2004; Land & Magueijo 2005*b*,*a*; Copi *et al.* 2006), as well as suppressed power on these scales. Lack of statistical isotropy means there is a preferred direction, and this direction has been nicknamed 'Axis of Evil'. I discuss this axis in more detail in Chapter 6. This axis may be due to non-trivial topology in the Universe.

The *geometry* of the Universe is a separate concept from that of topology. Topology relates to the *shape* of the Universe. A Universe can be flat and finite in size, it is then technically called a 'flat torus'. In this case, 'flat' describes the universe's geometry and 'finite' the universe's topology. Travelling to one side of this universe, one eventually reappears at the other side. This universe can be finite is all spatial dimensions, or only in one. If only one direction is finite, then there is exists a preferred direction in the Universe, and so statistical isotropy is broken. This model could also explain low power on large scales, if the finite dimension is of the same order of the scales probed by the CMB. Another model explaining the low power requires dodecahadron topology (Caillerie *et al.*

2007), though other work (Kunz *et al.* 2006) claims the CMB is compatible with an infinite Universe.

Higher Dimensional Theories

Kaluza was the first to take the liberty of adding an extra spatial dimension in Einstein's field equations. The idea was to add more degrees of freedom to the metric; in doing so he successfully unified electromagnetism and gravity. However, his model required physical quantities to be invariant with respects to the fifth dimension, which was not physically motivated until Klein suggested in 1925 that the fifth dimension may be compactified. From then on higher dimensional theories arose, in which our 4-dimensional Universe is merely a membrane (or *brane*) embedded in a higher dimensional bulk.

In these models, while electromagnetic radiation is confined to the brane, gravity interacts in all dimensions. This can solve several issues in gravitational physics. The first is that gravity is the weakest of the four forces, referred to as the hierarchy problem. In brane theory it is merely our perception of gravitational force which is weak, as we do not witness the rest of the gravitational force which radiates in higher dimensions. Dark matter could also be matter confined to another brane which can only communicate gravitationally with us, and dark energy can be explained by brane interactions. Ekpyrotic models, where the Big Bang is caused by two colliding branes, are also attractive explanations (though hard to verify).

The main argument against brane theories is that it has many degeneracies with the standard model of cosmology. Some models such as DGP (Dvali, Gabadadze & Porrati 2000) may already be ruled out as they cannot explain the expansion history of the Universe.

General Parameterisations of Modified Gravity

Instead of comparing specific alternative models to data, it is useful to find a general parametrization of gravity. In this way, one can search for general deviations from general relativity. In Chapter 7, I discuss a parametrization called *Minimalist Modified Gravity* in the context of the Integrated Sachs-Wolfe effect.

1.9 Structure of this Thesis

In this Thesis, I always work within the framework of general relativity. In Chapter 7, I introduce a general parametrization of gravity modification (Minimalist Modified Gravity), which also works within the framework of general relativity. When constraining parameters, I assume the geometry of the Universe is flat, though investigate how correlation signals will change with geometry. In each chapter, I define the fiducial model used.

Chapters 2 to 4 are related to the study of redshift space large scale galaxy clustering, focussing on the 2 Micron All-Sky Survey (2MASS) and the 2MASS Redshift Survey (2MRS). Chapters 5 to 7 focus on the study of the integrated Sachs-Wolfe (ISW) effect as a means of detecting dark energy in current and future galaxy surveys.

Chapter Overview:

- In Chapter 2, I give a review of the 2MASS, 2MRS and 6dF galaxy surveys and present recent key results regarding the LSS of the Universe.
- In Chapter 3, I quantify the clustering of 2MRS galaxies in the redshift space and search for non-Gaussian signatures in the spherical harmonic phase distribution.
- In Chapter 4, I use a maximum likelihood method to estimate the matter density Ω_m and the galaxy bias b_g from the 2MRS correlation functions. I also check for consistency of the galaxy field with a Gaussian random field.
- In Chapter 5, I give a detailed overview of the Integrated Sachs-Wolfe (ISW) effect and how it can be detected through cross-correlating a tracer of LSS with the CMB. I also discuss cosmic magnification and how it affects the ISW signal.
- In Chapter 6, I cross-correlate third year WMAP (WMAP3) data with the 2MASS galaxy survey, and report a 2σ detection of an ISW effect, compatible with $\Omega_\Lambda < 0.89$ (95% CL). I also investigate large scale "Axis of Evil" type anomalies in both WMAP3 and 2MASS data.

- In Chapter 7, I review the method of using the Fisher Information Matrix for parameter forecast and use the ISW effect to forecast errors on the dark energy parameters Ω_Λ and w, in particular for the future generation of galaxy surveys, the Dark Energy Survey (DES) and the Dark UNiverse Explorer (DUNE). I also investigate a general parametrization of gravity modification, Minimalist Modified Gravity (MMG) and forecast how well DES and DUNE will be able to measure discrepancies from general relativity.

- In Chapter 8, I present an overall discussion and conclusions about the work presented in this Thesis.

- In Chapter 9, I give an overview of future directions and extensions to the work presented in this Thesis.

- Appendices A and B give useful derivations of equations fundamental to this Thesis.

CHAPTER 2

THE 2 MICRON ALL-SKY SURVEY AND ITS REDSHIFT SURVEY

Summary

In this chapter I give a review of the 2 Micron All-Sky Survey (2MASS), the 2MASS Redshift Survey (2MRS) and the 6 degree Field Galaxy Survey (6dFGS) as well an overview of recent key results from these surveys regarding the Large Scale Structure (LSS) of the Universe. These include results published in Erdoğdu (a) *et al.* (2006), Erdoğdu (b) *et al.* (2006) and briefly overview results from Rassat *et al.* (2007). In Chapters 3 and 4 I redshift space analysis of 2MRS galaxy field. The results of Rassat *et al.* (2007) are discussed in detail in Chapter 6 and investigate correlations between the 2MASS galaxy field and the Cosmic Microwave Background (CMB).

2.1 Introduction

The 2 Micron All-Sky Survey (2MASS) is the first all-sky Near Infra-Red (NIR) survey since the Two Micron Sky Survey (TMSS) (Neugebauer & Leighton 1969) nearly thirty years ago. Since then, there has been substantial innovation in the world of Infra-Red (IR) detector technology. New IR sensitive array detectors can now detect objects 10^8 times fainter than those detected in the TMSS, so that 2MASS will catalogue 50 thousand times more celestial objects than the TMSS.

The main achievements of the 2MASS include:

- A map of the Milky Way nearly un-obscured by interstellar dust and which probes the true distribution of luminous mass and of the largest structures along the length of the Galaxy.
- The first all-sky photometric census of galaxies brighter than $K_s = 13.5$. Low Galactic extinction in the NIR means it probes galaxies down to low galactic latitudes as well as in the Zone of Avoidance (ZoA). This provides a robust tracer of the Large Scale Structure (LSS) in the local Universe.
- A thorough survey of objects which dominate the NIR: low luminosity stars, cool objects such as brown dwarfs and objects in dusty environments (e.g., globular clusters in the plane of the Milky Way).

To achieve this, 2MASS has uniformly scanned the sky using two purpose built 1.3m telescopes in the J (1.11 - 1.36μm), H (1.50 - 1.80μm) and K_s (2.00 - 2.32μm) bands. Observing in the northern hemisphere took place in Mount Hopkins (Arizona, USA), and at the CTIO (Chile) for the southern hemisphere. Data acquisition is finished since 2001 and the following data products are now publicly available:

1. A digital atlas of the sky containing 4 billion $8' \times 16'$ atlas images having $4''$ spatial resolution in each 3 wavelength bands.
2. A point source catalogue containing accurate position and fluxes for about 300 million stars and unresolved objects.
3. An eXtended Source Catalogue (XSC) containing positions and total magnitudes for more than 1.6 million galaxies and nebulae (see Figure 2.1).

For 2MASS galaxies brighter than $K_S = 12.2$, the 2MASS Redshift Survey (2MRS) is currently under way, obtaining spectroscopic redshifts for 100,000 galaxies over the entire sky. In Table 2.1, I compare the main specifications of the 2MASS XSC, 6dFGS and 2MRS galaxy surveys.

In Section 2.2, I describe the survey strategy for the XSC, and discuss the advantages of a NIR survey in Section 2.3. In Section 2.4, I give an overview of the most significant

	2MASS XSC	6dFGS	2MRS
Survey Area	All-Sky	$\delta < 0°$	All-Sky
		$\|b\| > 10°$	$\|b\| > 5°$
Limiting K_s Magnitude	13.5	12.75	12.2
Mean Redshift z	~ 0.07	~ 0.05	~ 0.03
Number of galaxies	> 1.6 Million	150k	100k
Redshift Estimation	Photo-z	Spectro-z	Spectro-z
Current Status	Complete since 2001	DR2 2005	DR2 2007
Galaxies Observed	100%	60%	32% ($K_s < 11.5$)

Table 2.1: Comparison of specifications for the 2MASS XSC (see Section 2.2), the 6dFGS (see Section 2.5) and the 2MRS galaxy surveys (see Section 2.5).

recent results of the XSC. The 2MASS Redshift Survey (2MRS) is described in Sections 2.5 and 2.6. In Section 2.7, I describe recent results from the 2MRS team.

2.2 The eXtended Source Catalogue (XSC)

The 2MASS survey strategy is to map the sky with overlapping strips or tiles of approximately $6° \times 8.5'$, such that every piece of the sky is observed a total of six times at $1.3s$ of integration per sample (Jarrett *et al.* 2000). Source detection is run by an algorithm based on the DAOPHOT find algorithm, whose threshold is chosen to assure complete detection of galaxies brighter than $K_s = 13.5$ and $J = 15$ mag. The extended source processor GALWORKS separates point sources from extended sources by analysing their point spread function. The final XSC contains over 1.6 million galaxies. Extended sources which are not galaxies are flagged according to their nature. Specifications of the 2MASS XSC are compared in Table 2.1 with those of the 6dFGS and the 2MRS galaxy surveys.

2.3 Advantages of a Near Infra-Red Survey

The NIR selection of galaxies is one of the main advantages of the 2MASS along with its all-sky uniform photometry. Galaxies selected in the NIR bands J, H and K_s are subject to

Figure 2.1: The Large Scale Structure of the Universe as measured by the 2MASS eXtended Source Catalogue (XSC), plotted in supergalactic coordinates. *(Credit: Two Micron All Sky Survey.)*

little Galactic and internal extinction. It has also been shown that their K correction and luminosity per unit stellar mass are nearly independent of galaxy type (Cowie *et al.* 1996). These intrinsic benefits of a NIR survey, along with the fact that the 2MASS photometry is measured with consistent aperture size and shapes for all three bands, make the 2MASS photometry extremely reliable. This provides a uniform catalogue and also helps rid the XSC of stellar contamination as galaxies and stars have different colours in $(J - K_s)$ and $(H - K_s)$ bands (Jarrett *et al.* 2000). As NIR light travels deeper through the plane of the Milky Way than optical light, there is less obscuration due to extinction along the Galactic plane. This means a NIR survey provides better sky coverage than an optical survey near the Galactic plane. Finally, galaxies selected in the NIR are dominated by older stellar populations, mostly K and M giants (Jarrett *et al.* 2000). The older stellar

populations are stable and are therefore robust tracers of mass.

2.4 Recent Results from the 2MASS XSC

In this Section, I highlight some recent results from the 2MASS XSC. I focus on results relating to Large Scale Structure (LSS) statistics and the integrated Sachs-Wolfe (ISW) effect. These are of specific interest to this Thesis. I discuss results from the 2MRS later in Section 2.7.

2.4.1 The K-band Luminosity Function

The galaxy Luminosity Function (LF) is fundamental to observational cosmology as well as to our understanding of galaxy formation. As a NIR survey with reliable photometry, 2MASS is an ideal catalogue from which to derive the K band luminosity function. This is because it has little Galactic and internal extinction and that its K correction and luminosity per unit stellar mass are independent of morphological type.

In order to establish the LF, it is necessary to have around 5000 galaxies with spectroscopic redshifts (Kochanek *et al.* 2001). These are available to the brightest 2MASS galaxies due to its overlap with redshift surveys. The redshifts are necessary to determine the absolute magnitudes of the galaxies from their apparent magnitudes. Because 2MASS is a shallow survey, the estimation of the absolute magnitude is insensitive to the cosmological model used. The low mean redshift also renders visual morphological classification possible, meaning a LF for both early and late type galaxies can be determined as well as for the total population.

Kochanek *et al.* (2001) determined the K-band LF using over 4000 galaxies from the 2MASS incremental release catalogue of extended sources with $\delta \geq 11°$ and $|b| > 20°$. The galaxies all have spectroscopic redshifts taken from ZCAT Huchra *et al.* (1992), and were also checked against those given by the Updated Zwicky Catalogue (Falco *et al.* 1999) of the CfA2 redshift survey (Geller & Huchra 1989). Galaxies in their analysis also have visually identified morphological types, one third of which were obtained from the RC3 catalogue of de Vaucouleurs, de Vaucouleurs & Corwin (1976), the rest were identified visually by the authors. The galaxies were separated into early types (all ellipticals and

S0+), and late types (all spirals and S0/a).

Kochanek *et al.* (2001) fit the Schechter LF, parametrized by:

$$\frac{dn}{dL} = \frac{n_*}{L_*}\Big(\frac{L}{L_*}\Big)^{\alpha} exp\Big(-\frac{L}{L_*}\Big)\,, \tag{2.1}$$

and found that early (e) and late (l) type galaxies have similar shaped luminosity functions, with $\alpha_e = -0.92 \pm 0.10$ and $\alpha_l = -0.87 \pm 0.09$. They also found that the late types slightly dominate the K-band luminosity density while the early type galaxies are brighter. The derived LF was using galaxies with magnitudes $7 \leq K_s \leq 11.25$ but was checked to be valid for $K_s \leq 18$.

Cole *et al.* (2001) also calculated the 2MASS luminosity function. They obtained spectroscopic redshift information by combining the 2MASS XSC with the 2 degree Field Galaxy Redshift Survey (2dFGRS), producing a NIR selected survey containing over 17,000 galaxy redshifts. They fitted the luminosity function and found $\alpha_{K_s} = -0.96 \pm 0.05$ for the K_s band which is compatible with the results from Kochanek *et al.* (2001). Cole *et al.* (2001) also fitted the luminosity function for the J band and found $\alpha_J = -0.93 \pm 0.04$.

2.4.2 Galaxy bias, Correlation Function and 3d Power Spectrum

The 3d power spectrum $P(k)$ which probes the 3d distribution of matter in the Universe is an essential statistic of the matter distribution in the Universe. It can be estimated directly from the angular correlation $w(\theta)$ if the redshift distribution $N(z)$ is known or assumed.

Allgood, Blumenthal & Primack (2001) estimated the 3d power spectrum for $\sim 500,000$ galaxies with $K_s < 14$ taken from the second data release of 2MASS. They found that the angular correlation function obeyed a power law on small scales,

$$w(\theta) \propto \theta^{\alpha}\,, \tag{2.2}$$

where $\alpha = -0.79$, which breaks down at $\theta \sim 1.7°$. This expected departure from a power law occurs at larger scales than in the angular correlation function measured from the SDSS and APM (Maddox *et al.* 1990*b*,*a*; Zehavi *et al.* 2004). As these are deeper surveys, this is what is expected assuming the surveys have the same underlying 3d power spectrum. Allgood, Blumenthal & Primack (2001) also found that 2MASS galaxies are 1.25 times more biased than SDSS galaxies, in accord with the expectation that elliptical galaxies are more clustered than spirals.

Maller *et al.* (2005) also measured the angular correlation function from which they constrained the matter density and linear galaxy bias. They found $\Omega_m h = 0.13 \pm 0.07$, $b = 1.1 \pm 0.2$ for an assumed value of $\sigma_8 = 1.0 \pm 0.09$. This corresponds to a linear distortion parameter $\beta \simeq \frac{\Omega_m^{0.6}}{b} \simeq 0.33 \pm 0.11$ †. Frith (2005) also constrained the linear galaxy bias and found $(\sigma_8 b)^2 = 1.39 \pm 0.10$ for $\Omega_m = 0.3$, or $\beta \simeq 0.31 \pm 0.01$ †.

2.4.3 The Clustering or LSS Dipole

A large part of the dipole in the Cosmic Microwave background is believed to be caused by our motion in the local Universe which is due to large scale inhomogeneities in the matter distribution. With an all-sky survey it is possible to measure our acceleration due to the LSS. On large scales and where $\delta \ll 1$, then the peculiar acceleration vector is given by:

$$\vec{g}(\vec{r}) = G\overline{\rho} \int_r^\infty \mathrm{d}^3\vec{r}'\,\delta(\vec{r}')\frac{\vec{r}' - \vec{r}}{|\vec{r}' - \vec{r}|^3} \,. \tag{2.3}$$

The mean matter density is given by $\overline{\rho}$ and the overdensity δ is defined by Equation 1.14. In linear theory, the acceleration is linearly related to the peculiar velocity field:

$$\vec{v}(\vec{r}) = \frac{H_0 f(\Omega_m)}{4\pi G\overline{\rho}}\vec{g}(\vec{r}) \,. \tag{2.4}$$

Maller *et al.* (2003) considered the 2MASS projected density field (compare with the dipole calculation byErdoğdu (a) *et al.* (2006), see Section 2.7). By comparing the clustering dipole to the CMB dipole they determine a best fit to the matter density $\Omega_m = 0.27 \pm 0.04$ and to the linear galaxy bias $b = 1.37 \pm 0.3$ (or $\beta = 0.33 \pm 0.10$ †).

2.4.4 Comparison with Gravity Field and Velocity Surveys

With redshift information and an all-sky survey, it is possible to derive the linear velocity field of the LSS. Pike & Hudson (2005) calculated the linear velocity field for 2MASS galaxies with public redshift data within $65h^{-1}Mpc$ ($K_s \leq 10.5$) and compared it to three published peculiar velocity datasets: the Spiral Field I band (which uses the Tully-Fisher relation to determine the distance to 836 spiral galaxies), the I band Surface Brightness Fluctuations (which has distances for 266 galaxies) and 59 type Ia supernovæ.

†See Chapter 4, Table 4.2 for comparisons between different values of β.

They find there is a good fit between these three datasets and the reconstructed 2MASS velocity field if $\beta = 0.49 \pm 0.04$ for a normalization of $\sigma_8 = 0.90$ (for $\sigma_8 = 0.75$, this corresponds to $\beta = 0.41 \pm 0.04$[†]). They also split the data into early (elliptical and S0) and late (spiral and irregular) type galaxies and find that early type galaxies are more biased than late types, with $b_e/b_l \simeq 1.6$.

2.4.5 The integrated Sachs-Wolfe Effect and Dark Energy

In Section 1.7.1 I described the late time Integrated Sachs-Wolfe effect (ISW), which is a secondary anisotropy in the Cosmic Microwave Background (CMB). This effect is hard to differentiate from primary CMB anisotropies and can be smaller than the cosmic variance at those scales. However, it is possible to detect this effect through cross-correlation between LSS and the CMB. In the a flat Universe dominated by dark energy or hyperbolic (open) curvature, large scale overdensities in the galaxy field will correspond to hot spots in the CMB - and a positive cross-correlation will be measured.

Afshordi *et al.* (2004) cross-correlated 4 magnitude cuts of 2MASS ($\Delta K_s = 0.5 mag$ over the range $12 < K_s < 14$) with 4 different first year WMAP maps (Q, V, W and the internal linear combination). In Rassat *et al.* (2007), I repeated the analysis using the new third year data release of WMAP (WMAP3).

Both studies found an achromatic signal, which is what is expected for the ISW effect. The signal was compatible with no correlation but preferred the ΛCDM model at the 2.5σ level (Afshordi *et al.* 2004) and 2σ Rassat *et al.* (2007). In Rassat *et al.* (2007), we used the ISW signal to constrain the dark energy density Ω_Λ, and found an upper limit $\Omega_\Lambda < 0.89$ (95% C.L.). Results from Rassat *et al.* (2007) are given in detail in Chapter 6.

2.5 The 2MASS Redshift Survey (2MRS) Survey Strategy

The 2MASS Redshift Survey is a spectroscopic all-sky galaxy survey based on the 2MASS XSC. Its aim is to map the three dimensional distribution of galaxies and dark matter in the local Universe out to approximately $85h^{-1}$Mpc. This means collecting spectroscopic redshifts for all 2MASS galaxies with $K_s < 12.2$ and $|b| > 5°$. The final redshift survey is

[†]See Chapter 4, Table 4.2 for comparisons between different values of β.

expected to contain around 100,000 galaxies. Specifications of the 2MRS, and the 6dFGS from which some of the spectra are taken, are compared in Table 2.1 with those of the 2MASS XSC.

The spectroscopic redshifts are obtained from various telescopes:

- In the southern Galactic hemisphere, redshifts are obtained as part of the 6 degree Field Galaxy Survey (6dFGS, Jones *et al.* 2005) which aims to collect spectra for 150,000 galaxies. Spectra for the 6dFGS are taken on the 1.2m Schmidt telescope in Siding Spring Observatory, Australia, using a multi-object fibre spectroscopic system. The fibres are positioned using an off telescope robotic fibre positioner. This can configure up to 150 fibres simultaneously on an interchangeable field plate unit. Figure 2.2 shows one of the two field plates used for 6dFGS. Four fibres are allocated to calibrate the telescope's position by locking onto guide stars. The spectra are obtained by using two Volume-Phase transmissive Holographic (VPH) gratings. In the blue, a 580V grating with wavelength range: $3900 - 5600\mathring{A}$ and in the red, a 425R grating with range: $5400 - 7500\mathring{A}$. Each field is observed in both V and R gratings that are later spliced together to obtain a single spectrum. The overlap between the red and blue spectra around the $5577\mathring{A}$ skyline is used as a calibration. A continuum is fitted to both the V and R spectra in order to match the levels. A package adapted from the Two degree Field Galaxy Survey (2dFGS), *RUNZ*, is used to extract redshifts from spectra, using a template matching technique.

- The 6dFGS only surveys areas with $|b| > 10°$, so for Galactic latitudes between $5° < |b| < 10°$, spectra are obtained from the Cerro Tololo Inter-american Observatory (CTIO).

- The galaxies in the northern Galactic hemisphere are being observed mainly by the Fred Lawrence Whipple Observatory (FLWO) 1.5m telescope in Arizona, USA. As there is no multi-fibre spectrograph there, the spectra are taken individually.

- Where spectra exist as part of other surveys (IRAS, SDSS, etc...) these are incorporated into the 2MRS.

Figure 2.2: The off-telescope robotic fibre positioner can configure up to 150 fibres on a field plate to be used on the 1.2m UK Schmidt telescope as part of the 6dFGS. A subset of redshifts obtained in the 6dFGS are used for the 2MRS catalogue. *(Photo taken at Siding Spring by A.R., 2005)*

2.6 2MRS Completeness and current phase releases

The 2MRS strategy is to survey the whole sky, but it will inevitably have regions of incompleteness due to unavoidable Galactic and extra-galactic foregrounds. Galactic foregrounds consist of stellar confusion along the plane of the Milky Way, and for this reason galaxies with Galactic longitude $|b| < 5°$ are not targeted. Galaxies in regions with high Galactic extinction (i.e. with $E(B-V) > 1$ based on the Schlegel, Finkbeiner & Davis (1998) extinction maps) are not targeted for spectroscopic redshifts.

Obscuration by nearby extragalactic objects such as the Large Magellanic Cloud (LMC) at ($275° < l < 284°$, $-37° < b < -30°$) and the Small Magellanic Cloud (SMC) at ($300° < l < 304°$, $-46° < b < -43°$) also contribute to incompleteness of the 2MRS.

The goal of the 2MRS is to be complete within these constraints down to a limiting magnitude of $K_s = 12.2$ mag. Currently the second data release is nearly complete with over 32,000 galaxies down to $K_s < 11.5$ and $|b| > 5°$ for which most galaxies also have visually classified morphological types. The catalogue is also complete down to $K_S < 11.75$ but with no coverage along $|b| < 10°$. About 100,000 galaxies are expected to make up the final catalogue.

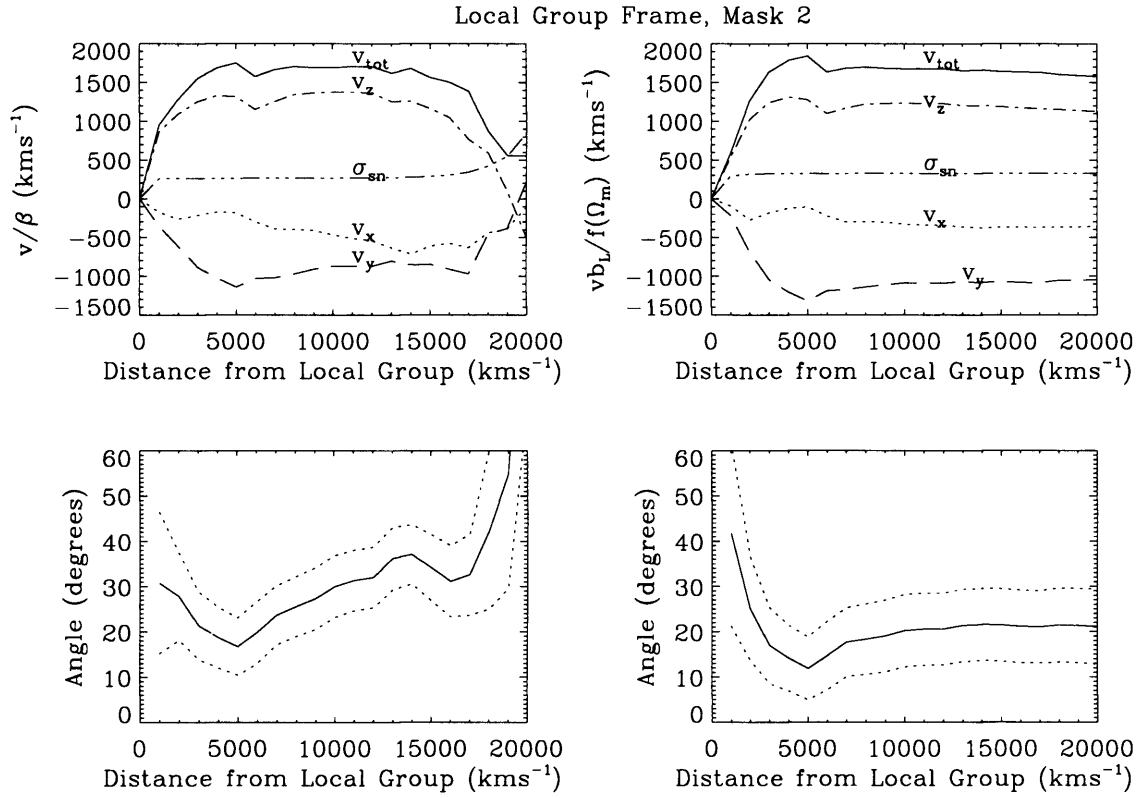

Figure 2.3: *from Erdoğdu (b)* et al. *(2006):* Top: The magnitudes and 3 Cartesian coordinates of the acceleration of the LG due to galaxies at a distance cz from the centre of the LG. Bottom: The misalignment angle between the clustering dipole and the CMB dipole. In the left-hand side, the calculation has been done in the number weighted scheme and in the right-hand side in the flux weighted scheme.

2.7 Recent Results from the 2MRS

In this Section, I highlight recent results from the 2MRS team, in particular recent results from Erdoğdu (a) *et al.* (2006) and Erdoğdu (b) *et al.* (2006), of which I am a co-author. These results use the first 2MRS data release.

2.7.1 The Clustering and LSS Dipole and its Evolution with Redshift

As discussed in Section 2.4.3, it is possible to obtain an estimate of the distortion parameter β by comparing the dipole which arises from LSS to the CMB dipole.

Using the three dimensional information available from the 2MRS it is possible to measure the convergence of the clustering dipole with redshift. Radial information also permits a precise calculation of the selection function of the survey.

Erdoğdu (a) *et al.* (2006) use the first 2MRS data release, which includes over 23,200 galaxies with extinction corrected magnitudes brighter than $K_s = 11.25$ to calculate the clustering dipole and misalignment angle with the CMB dipole as a function of redshift and an estimate of the distortion parameter β.

Erdoğdu (a) *et al.* (2006) calculate not only the number weighted dipole (where each galaxy contributes an equal amount to the dipole) but also the flux weighted dipole (where galaxies contribute to the dipole proportionally to their intrinsic flux). The latter requires the mass to light ratio to be relatively constant across galaxies in the survey (i.e. across different morphological types) which is a reasonable assumption for NIR selected galaxies (Cowie *et al.* 1996), though bias will change with morphological type.

The dipole can be calculated either in the Local Group (LG) frame (i.e. relative to the centre of the LG) or in the CMB frame. The results show that for the number weighted dipole, the calculation is more robust in the LG frame, whereas it does not fluctuate between methods for the flux-weighted dipole. Figure 2.3 shows the magnitude and 3 Cartesian components of the acceleration of the LG due to galaxies at a distance cz from the centre of the LG as well as the misalignment angle between the clustering dipole and the CMB dipole. The dotted lines indicate the 1σ errors due to shot noise. The left side shows results for the number weighted dipole and the right hand side for the flux weighted dipole. By comparing the clustering dipole to that measured from the CMB anisotropies, Erdoğdu (a) *et al.* (2006) find a value for the distortion parameter $\beta = 0.40 \pm 0.09$[†].

Figure 2.4 shows the direction in Galactic coordinates of the angle misalignment between the dipole calculated from LSS and the CMB dipole. The dipole seemingly converges by $60h^{-1}Mpc$.

2.7.2 The Density and Velocity Field Wiener Reconstructions

One of the original aims of the 2MRS is to map the three dimensional distribution of matter. Using linear theory to account for redshift distortions and assuming an underlying ΛCDM fiducial model, it is possible to reconstruct the matter density field using a Wiener filter (Fisher *et al.* 1995). Such a filter is an optimal estimator of an underlying field for

[†]See Chapter 4, Table 4.2 for comparisons between different values of β.

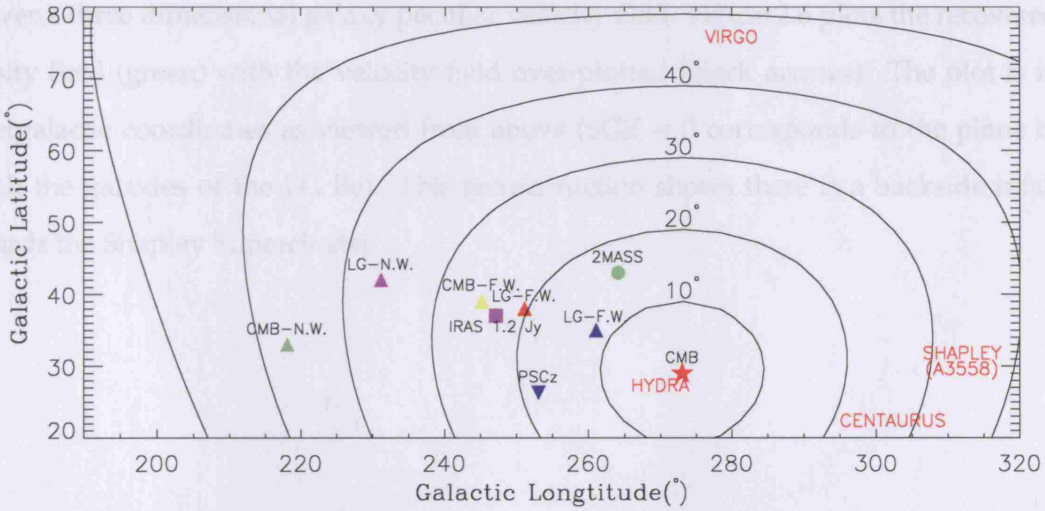

Figure 2.4: *from Erdoğdu (b)* et al. *(2006):* The triangles show the dipole directions at 13000 $\mathrm{km\,s^{-1}}$ derived in Erdoğdu (b) *et al.* (2006). The direction of the number weighted 2MRS dipole in the LG frame is shown in magenta (LG-N.W., $l = 231°$, $b = 42°$). The red triangle shows the direction of the flux weighted 2MRS in the LG frame (LG-F.W., $l = 251°$, $b = 38°$). The blue triangle shows the direction of the flux weighted 2MRS in the LG frame excluding Maffei 1, Maffei 2, M81, IC342 and Dwingeloo 1 (LG-F.W., $l = 261°$, $b = 35°$). The red star shows the CMB dipole direction ($l = 273°$, $b = 29°$). The green triangle is the number weighted LG dipole in the CMB frame (CMB-N.W., $l = 218°$, $b = 33°$); the yellow triangle is the flux weighted LG dipole in CMB frame (CMB-F.W., $l = 245°$, $b = 39°$). The green circle is the 2MASS dipole ($l = 264°$, $b = 43°$, Maller *et al.* 2003). The magenta square is the *IRAS* 1.2-Jy dipole ($l = 247°$, $b = 37°$, Webster, Lahav & Fisher 1997). The blue upside-down triangle is the *IRAS* PSCz dipole ($l = 253°$, $b = 26°$, Rowan-Robinson *et al.* 2000). Contours are drawn at constant misalignment angles. Also shown are the Virgo Cluster ($l = 280°$, $b = 75°$), the Hydra Cluster ($l = 270°$, $b = 27°$), the Centaurus Cluster ($l = 302°$, $b = 22°$) and A3558 ($l = 312°$, $b = 31°$).

which the cosmology is known. Erdoğdu (b) *et al.* (2006) reconstructed the 2MRS density field in thin redshift shells. The reconstructed density field at $cz = 6000$ km s^{-1} is plotted in Figure 2.5 and recovers the main structures and underdensities known in the local Universe. This particular shell probes the large overdensities, which manifests itself as a sharp peak in the 2MRS redshift distribution just below $z = 0.02$ (see Section 3.2 in Chapter 3).

From the density field, it is possible to reconstruct the linear velocity field and thus to recover a three dimensional galaxy peculiar velocity field. Figure 2.6 plots the recovered density field (green) with the velocity field over-plotted (black arrows). The plot is in supergalactic coordinates as viewed from above (SGZ = 0 corresponds to the plane in which the galaxies of the LG lie). This reconstruction shows there is a backside infall towards the Shapley Supercluster.

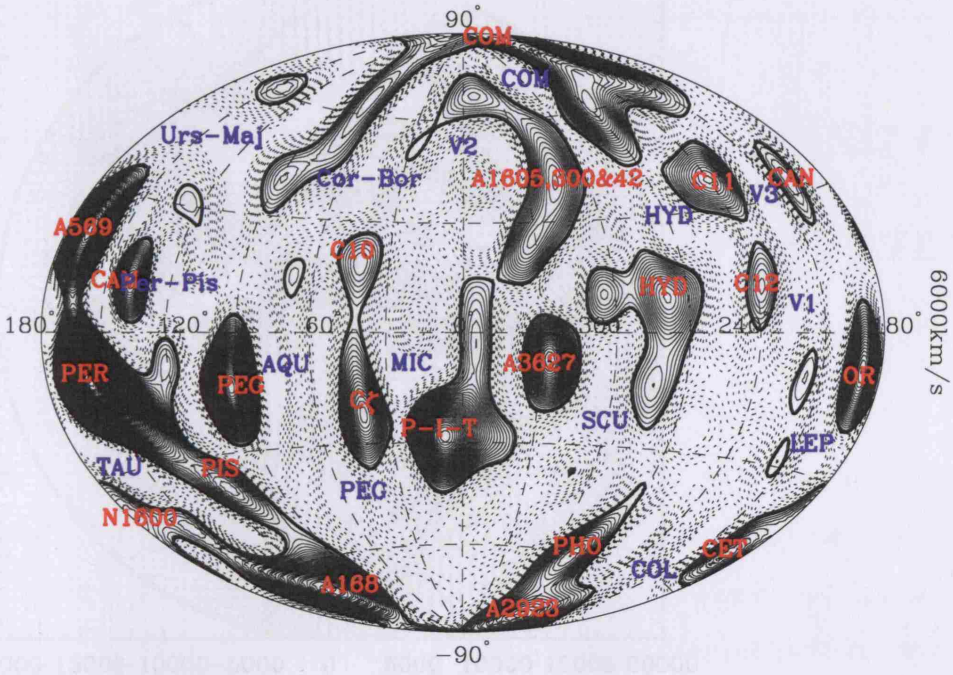

Figure 2.5: *from Erdoğdu (b)* et al. *(2006):* The Wiener Reconstructed density field of the 2MRS, evaluated at a thin shell at 6000 $\mathrm{km\,s^{-1}}$ for a fiducial concordance cosmology. The spacing of the density contours are $|\Delta\delta| = 0.1$. Solid lines indicate overdensities and dotted line underdensities. Shown in Galactic Aitoff coordinates. Known structures are recovered such as Abell 569 (A569), Perseus (Per), Pisces (Pis), and the Pavo-Indus-Telescopium (PIT) amongst others. There are large overdensities at this redshift, which reflects itself as a sharp peak in the 2MRS redshift distribution (see Section 3.2 in Chapter 3).

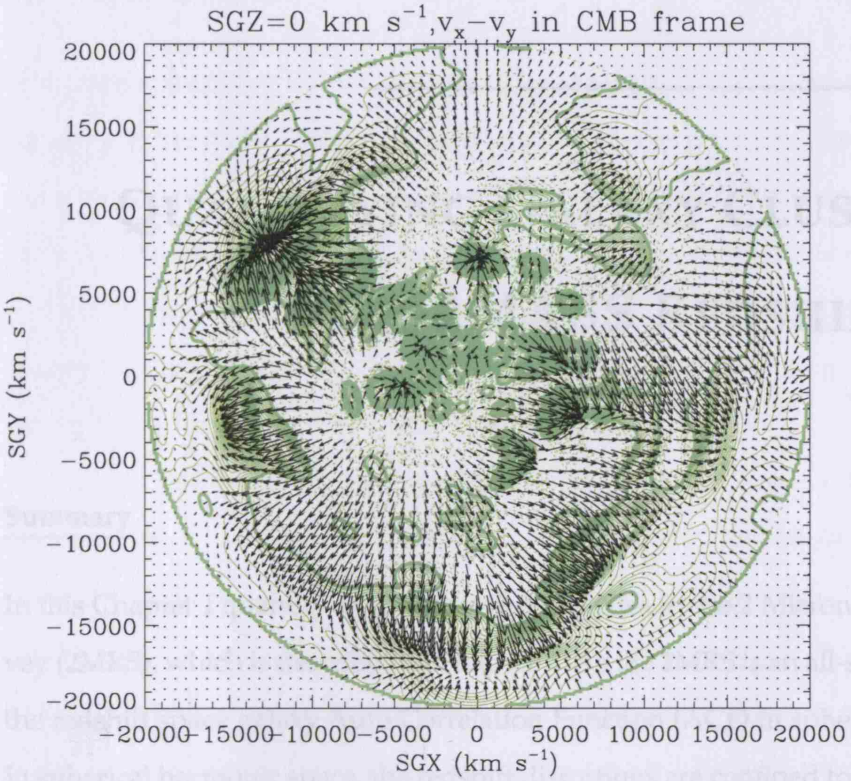

Figure 2.6: *from Erdoğdu (b)* et al. *(2006):* The Wiener reconstructed density and velocity field of the 2MRS in supergalactic coordinates at $SGZ = 0$, plotted in the CMB frame (as opposed to the LG frame). The spacing of the density contours is $|\Delta\delta| = 0.1$ with dashed lines representing underdense regions and solid lines overdense regions. Superimposed in black are the reconstructed three dimensional peculiar velocity field. The length of the arrows are about 300 km s^{-1} per cell. The main overdensities are Hydra-Centaurus (centre-left), Perseus-Pisces (centre-right), Shapley Concentration (upper left), Coma (upper-middle). This reconstruction shows there is a backside infall towards the Shapley Supercluster.

CHAPTER 3

QUANTIFYING GALAXY CLUSTERING IN THE 2MASS REDSHIFT SURVEY

Summary

In this Chapter I quantify the clustering of galaxies in the 2 Micron all-sky Redshift Survey (2MRS), which is described in Chapter 2. As the 2MRS is an all-sky survey, I calculate the redshift space galaxy Auto Correlation Function (ACF) in spherical harmonic space. In spherical harmonic space, the redshift distortions are confined to the radial dimension and there exists an exact prescription for calculating the linear theory redshift space ACF.

I also contrast two methods of maximum likelihood analysis, one which assumes the galaxy field is a Gaussian Random Field (GRF), and another which assumes the $C(\ell)$ quantities are Gaussian. Applying the latter to simulated galaxy GRFs, I show that this returns erroneous constraints on the matter density Ω_m, the linear galaxy bias b_g and the normalization σ_8.

Finally, I test whether the 2MRS galaxy field is compatible with a GRF. A simple test to quantify this is the check the phase distribution of the spherical harmonic coefficients ($a_{\ell m}$) with the Kuiper test. For a true GRF the phases are expected to follow a uniform distribution. I find the entire 2MRS sample is compatible with a GRF; I also apply the test to four separate redshift shells of the 2MRS with mean redshifts z = (0.005, 0.022, 0.039, 0.056). In this case the nearest (z=0.005) and furthest (z=0.056) shells show departures

from Gaussianity. This might be due to large scale structure and shot noise. The central shells are compatible with a GRF, though may still be non-Gaussian in a way that is not detected by the Kuiper test.

3.1 Introduction

The current cosmological model cannot be authoritative if we do not have good understanding of the local Universe. Studies of local cosmography should endeavour to inform not only about global cosmological parameters but also about the representativity of data samples with respects to other sampled regions of the Universe. In this sense, and assuming galaxies trace the underlying distribution of dark matter, an all-sky galaxy survey will give representative information about the distribution of luminous and dark matter in the local Universe, even if it is shallow in redshift.

In this Chapter, I use the 2 Micron All-Sky Redshift Survey (2MRS), a subset of the near infrared selected eXtended Source Catalogue (XSC) (Jarrett 2004) with spectroscopic redshifts. Galaxies in the 2MRS are selected in the K_S band which is 5 to 10 times less sensitive to Galactic dust than the B band (Maller *et al.* 2005). The means it is possible to have greater sky coverage than in an optical survey and more completeness along the plane of our Galaxy. Because the 2MRS is a nearly all-sky survey, the most legitimate correlation statistic to use is the angular power spectrum obtained from a spherical harmonic decomposition, which is ideal for decomposing fields on a sphere. The angular power spectrum permits an effective comparison between the galaxy catalogue and a cosmological model.

Moreover, the 2MRS contains spectroscopic redshift information which means it is possible to probe the Dark Matter distribution through the large scale linear redshift distortions of the observed galaxy density field. By decomposing the galaxy density field in spherical harmonics (see Section 3.3), the redshift distortions are confined to the radial dimension (Fisher, Scharf & Lahav 1994*b*; Heavens & Taylor 1995), meaning one can separate the matter density real space and redshift space contribution to the angular power spectrum.

These linear redshift distortions are modulated by the distortion parameter $\beta \simeq \frac{\Omega_m^\gamma}{b_g}$,

which is a function of the matter density Ω_m and the linear galaxy bias b_g, and $\gamma \sim 0.60$. The 2MRS galaxies are selected in the K_s band and therefore tend to be composed of older stellar populations. Their luminosities, because more stable than in star forming galaxies, are robust tracers of mass. Given its sky coverage, the 2MRS is an ideal survey for probing redshift distortions. These redshift distortions are ideal probes for exploring the Dark Matter distribution in the local Universe. In addition, morphological types of 2MRS galaxies have been visually identified by John Huchra of the 2MRS team. I present constraints on Ω_m and the b_g, as well as an analysis for separate morphological types in Chapter 4.

In Section 3.2, I describe the 2MASS data and its redshift survey. In Section 3.3, I describe the theoretical framework of linear redshift distortions and spherical harmonic decomposition in redshift space. In Section 3.4 I discuss the effect of potential non-linear redshift distortions. In Section 3.5, I recapitulate how to estimate the angular power spectrum of a nearly all-sky redshift survey. In Section 3.6, I indicate how to extract cosmological information from the redshift distortions and the angular power spectrum using a Gaussian likelihood function; I stress what assumptions this implies about the underlying galaxy density field. In Section 3.7, I test the compatibility of the 2MRS galaxy distribution with an isotropic Gaussian Random Field (GRF), by checking the uniformity of the harmonic phase distribution. I also briefly discuss, a test for detecting a lognormal distribution. In Section 3.8, I discuss these results.

3.2 The 2MASS Redshift Survey (2MRS)

In this Section, I summarize the 2 Micron All-Sky Redshift Survey (2MRS) data set, which is a spectroscopic subsample of the 2 Micron All-Sky Survey (2MASS). The selection criteria presented here are used in the analysis done in this chapter and also in Chapter 4.

3.2.1 2MASS and its Redshift Survey

The 2 Micron All-Sky Redshift Survey (2MRS) is the densest all-sky redshift survey to date. Galaxies targeted for spectroscopic redshift are selected from the 2 Micron All

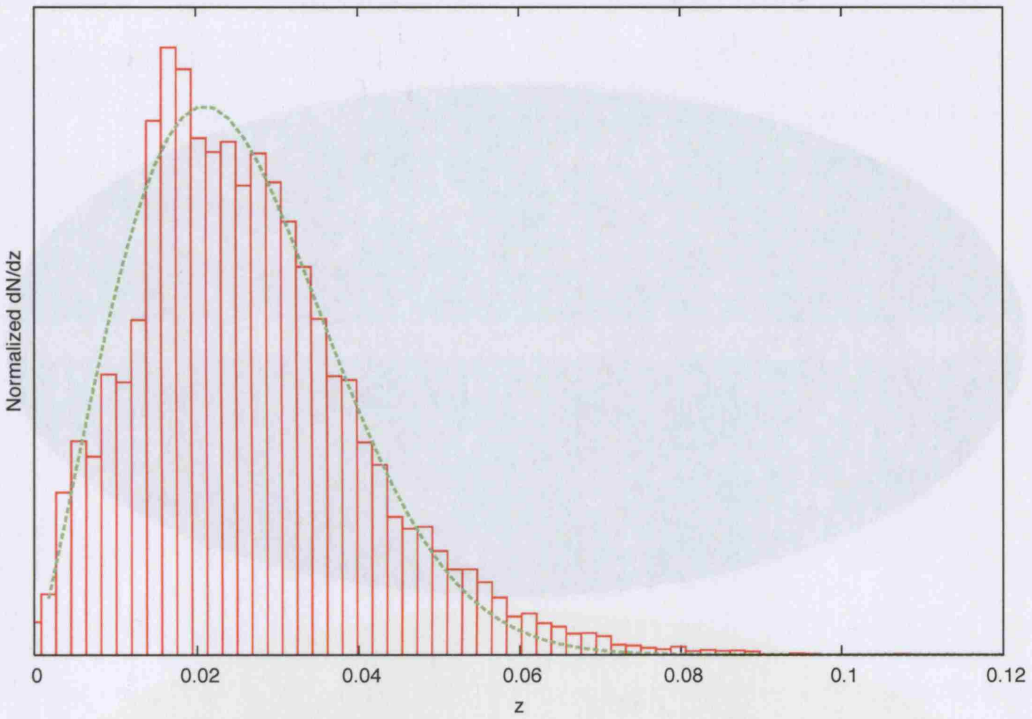

Figure 3.1: The redshift distribution of the 2MRS for all galaxies with $K_s < 11.5$ and $|b| > 5°$. The mean redshift is $z \sim 0.027$. The dip at $z \sim 0.01$ and the sharp peak at $z \sim 0.02$ correspond to the Local Void and structure such as Perseus-Pisces, the Pavlo-Indus-Telescopium and the Abell cluster 569 (see Figure 2.5 in Chapter 2).

Sky Survey (2MASS) eXtended Source Catalogue (XSC), which is complete down to an isophotal K_s magnitude of 13.75 (Huchra *et al.* 2005). The 2MASS All-Sky Data Release XSC is now publicly available[†] and contains positions and photometry in the three infrared survey bandpasses (J, H and K) for 1,647,599 objects. Further details about the 2MASS and the 2MRS are given in Chapter 2.

3.2.2 Selection Criteria for this Analysis

In this analysis, the primary selection criterion is the extinction corrected isophotal magnitude K_s. I select all galaxies with $K_s < 11.5$ for which the 2MRS has spectroscopic redshifts (i.e. for all galaxies with galactic latitude $|b| > 5°$). This corresponds to the second data release of the 2MRS. Galaxies in regions with extinction $E(B-V) > 1$ are not targeted for spectroscopic redshift (based on extinction maps of Schlegel, Finkbeiner

[†]http://irsa.ipac.caltech.edu/applications/2MASS/PubGalPS/

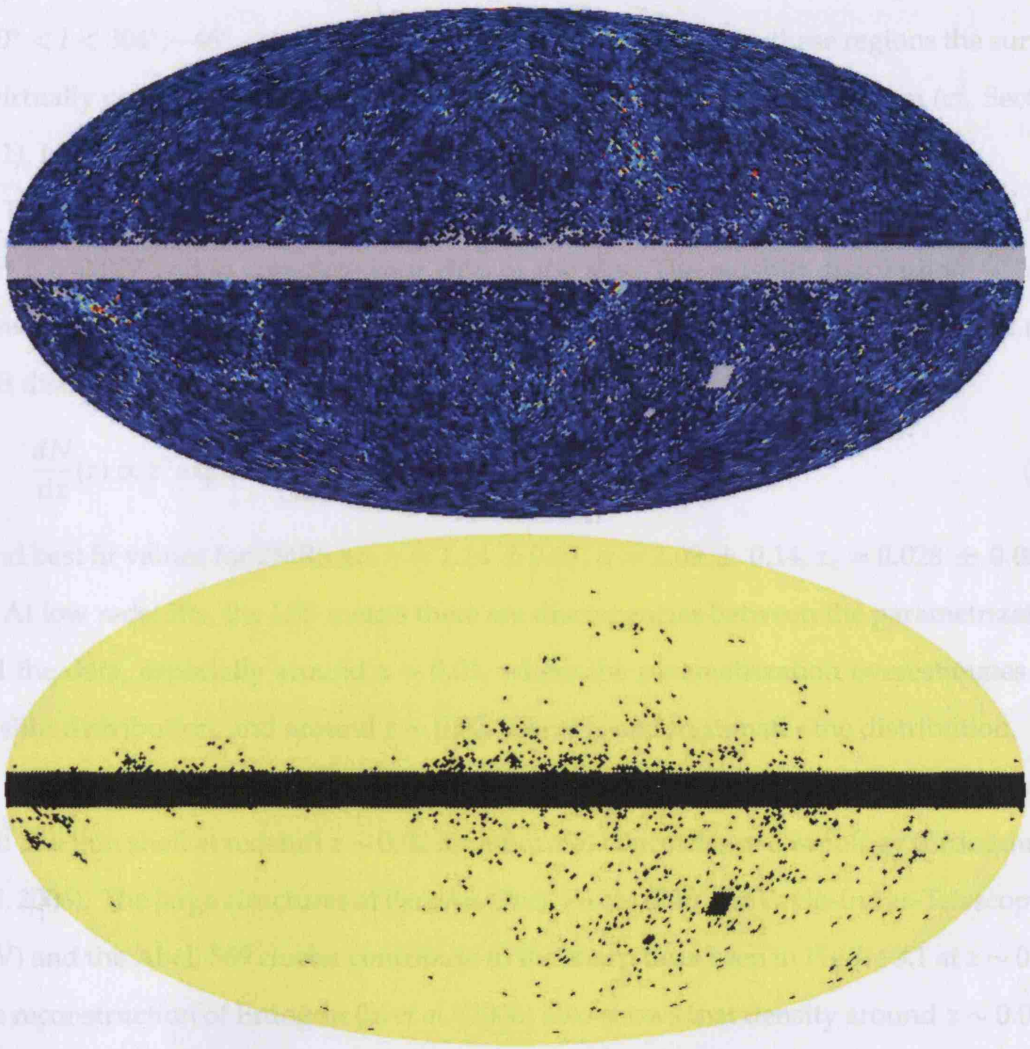

Figure 3.2: *TOP*:The 2MRS galaxy distribution, shown in Mollweide projection of Galactic Coordinates. The 2MRS catalogue is complete on 89% of the sky down to a magnitude limit of $K_s < 11.5$. Incomplete sky coverage is due to foregrounds such as: confusion in the region of the Galactic Plane ($|b| < 5°$); obscuration due to extinction (the survey has no spectroscopic data where $E(B-V) > 1$, based on the extinction maps of Schlegel, Finkbeiner & Davis 1998); obscuration by nearby extragalactic objects such as the Large Magellanic Cloud (LMC) at ($275° < l < 284°$,$-37° < b < -30°$) and the Small Magellanic Cloud (SMC) at ($300° < l < 304°$,$-46° < b < -43°$). Regions of incompleteness are indicated in grey. *BOTTOM*: The Mollweide projection in Galactic Coordinates of the sky coverage of the 2MRS. Yellow (light) regions indicate completeness and black regions incomplete regions of the survey.

& Davis 1998). The catalogue suffers from incompleteness in the region of the Large Magellanic Cloud ($275° < l < 284°; -37° < b < -30°$) and the Small Magellanic Cloud ($300° < l < 304°; -46° < b < -43°$). On other regions apart from these regions the survey is virtually complete. When calculating the galaxy angular power spectrum (cf. Section 3.5.1), I take into account these regions of incompleteness.

This analysis therefore uses 30833 galaxies with spectroscopic redshifts and mean redshift $z = 0.027$ and is complete over 89% of the sky. The redshift distribution $\frac{dN}{dz}(z)$ is shown in Figure 3.1 (histogram), where the solid line is the parametrization of the redshift distribution given by:

$$\frac{dN}{dz}(z) \propto z^{\gamma} \exp\left[-\left(\frac{z}{z_c}\right)^{\alpha}\right] . \tag{3.1}$$

I find best fit values for 2MRS are $\gamma = 1.14 \pm 0.07$, $\alpha = 2.09 \pm 0.14$, $z_c = 0.028 \pm 0.0016$.

At low redshifts, the LSS means there are discrepancies between the parametrization and the data, especially around $z \sim 0.01$, where the parametrization overestimates the redshift distribution, and around $z \sim 0.02$, where it underestimates the distribution.

Figure 2.5 in Chapter 2 shows the Wiener reconstructed density field of 2MRS evaluated at a thin shell at redshift $z \sim 0.02$ for a fiducial concordance cosmology (Erdoğdu (b) *et al.* 2006). The large structures of Perseus (Per), Pisces (Pis), the Pavlo-Indus-Telescopium (PIV) and the Abell 569 cluster contribute to the sharp peak seen in Figure 3.1 at $z \sim 0.02$. The reconstruction of Erdoğdu (b) *et al.* (2006) also shows that density around $z \sim 0.01$ is dominated by the Local Void, a large underdensity. This probably corresponds to the dip seen in Figure 3.1 at $z \sim 0.01$.

I discuss the effects of errors in the estimation of the selection function, and how these propagate in the cosmological parameter estimation in Section 4.5.

The large scale distribution of galaxies in the 2MRS survey can be seen in Figure 3.2 in Mollweide projection of Galactic Coordinates, pixelized using HEALPix (Gorski *et al.* 2005). The grey areas indicate regions of incompleteness in the catalogue, where spectroscopic redshifts are not available and represent only 11% of the sky. The bottom map shows the mask used in Section 3.5.1 to calculate the corrections to the spherical harmonics which arise from incomplete sky coverage.

3.3 Linear Theory Galaxy Auto-Correlation Function (ACF)

In this Section, I present the formalism for the Auto-Correlation Function (ACF) both in real space (Section 3.3.1) and with linear redshift distortions (Section 3.3.2), which takes into account the spectroscopic information of 2MRS. In the following, the subscript r refers to real space quantities, whereas the subscript z refers to those that are redshift distorted. In Section 3.3.3, I note that it is possible to recover the ACF projected on the sphere (i.e. without redshift distortions) by setting a constant radial weighting.

3.3.1 Radially Weighted Galaxy Auto-Correlations Function

One can decompose the *projected* galaxy density field of an *all-sky* survey using an angular decomposition in spherical harmonics:

$$\rho(\hat{\mathbf{r}}) = \sum_{\ell=0}^{+\infty} \sum_{m=-\ell}^{\ell} a_{\ell m} Y_{\ell m}(\hat{\mathbf{r}}) \,. \tag{3.2}$$

Where $Y_{\ell m}(\hat{\mathbf{r}}) = Y_{\ell m}(\theta, \varphi)$ represent the set of orthonormal spherical harmonics which span the sphere and the $a_{\ell m}$'s are the spherical harmonic coefficients. The spherical coordinates θ and φ are related to the Galactic coordinates by: $\theta = b + \frac{\pi}{2}$ and $\varphi = l$.

When the radial information of galaxy positions are known through the spectroscopic redshifts, one can decompose the *radially weighted* density field using the decomposition:

$$\rho(\mathbf{r}) = \sum_{\ell=0}^{+\infty} \sum_{m=-\ell}^{\ell} a_{\ell m} f(r) Y_{\ell m}(\hat{\mathbf{r}}) \,, \tag{3.3}$$

where $f(r)$ is an arbitrary radial weighting function, and the actual values of the harmonic coefficients in Equation 3.3 are different than those in Equation 3.2 and depend on the choice of $f(r)$. The radial weighting functions can be taken as spherical Bessel functions $j_\ell(x)$ which form an orthonormal set (Fisher *et al.* 1995; Heavens & Taylor 1995). However, in Section 3.7, I am interested in separating the data into different redshift shells, which is one of the reasons I have chosen the weighting shells as Gaussian distributions.

For a given discrete density distribution, the coefficients can be determined by direct summation over the galaxy angular positions:

$$a^{\rho}_{\ell m} = \sum_{i=1}^{N_g} f(r_i) Y^{\star}_{\ell m}(\theta_i, \varphi_i) \,, \tag{3.4}$$

where the sum is over all galaxies in the survey; (θ_i, φ_i) correspond to the angular position of each galaxy; r_i to the galaxy's distance from the observer and ρ denotes the density (as opposed to overdensity). The above harmonic coefficients are related to the galaxy *overdensity* coefficients by:

$$a^{\delta}_{\ell m} = \frac{a^{\rho}_{\ell m}}{\int \mathrm{d}r r^2 \phi(r) f(r)} , \tag{3.5}$$

where δ represents the overdensity:

$$\delta(\mathbf{r}) = \frac{\rho(\mathbf{r}) - \bar{\rho}}{\bar{\rho}} , \tag{3.6}$$

and $\int \mathrm{d}r r^2 \phi(r) f(r)$ denotes the effective number of galaxies per steradian per radially weighted shell. When $f(r) = 1$, I note that $\int \mathrm{d}r r^2 \phi(r) = N_g/\Omega$, i.e. the number of galaxies per steradian in all of 2MRS (see Section 3.3.3 for further comments on constant radial weighting).

The harmonic coefficients are not rotationally invariant quantities. It is the spherical harmonic overdensity power spectrum that one can compare with linear theory predictions (Peebles 1980; Scharf *et al.* 1992). The power spectrum is related to the harmonic coefficients by:

$$C_{\delta\delta}(\ell) = \left\langle |a^{\delta}_{\ell m}|^2 \right\rangle = 4\pi b_g^2 \int \mathrm{d}k \, \frac{\Delta^2(k)}{k} \, |W^r_{\delta}(k)|^2 , \tag{3.7}$$

where the angled brackets imply an averaging over many realizations of the field and:

$$\Delta^2(k) = \frac{4\pi}{(2\pi)^3} k^3 P(k) , \tag{3.8}$$

$$W^r_{\delta}(k) = \int \mathrm{d}r \, \Theta(r) j_{\ell}(kr) D , \tag{3.9}$$

$$\Theta(r) = \frac{r^2 \phi(r) f(r)}{\int \mathrm{d}r \, r^2 \phi(r) f(r)} . \tag{3.10}$$

The power spectrum $P(k)$ is defined by $\left\langle \tilde{\delta}(\mathbf{k}) \tilde{\delta}(\mathbf{k}') \right\rangle = (2\pi)^3 P(k) \delta^3(\mathbf{k} - \mathbf{k}')$.

The linear growth factor, $D = D(z)$, is the growing solution of the linear perturbation equation:

$$\ddot{\delta}_k + 2\left(\frac{\dot{a}}{a}\right)\dot{\delta}_k - 4\pi G \rho \delta_k = 0 , \tag{3.11}$$

where δ_k is the Fourier mode of the overdensity, ρ is the density and $\dot{} \equiv \mathrm{d}/\mathrm{d}t$.

It can be expressed as:

$$D(z) \propto H(a) \int^{a(z)} \frac{da'}{(a'H(a'))^3} , \tag{3.12}$$

where it is normalized such that $D(0) = 1$. This equation is only valid for certain values of the dark energy parameter of state ($w = -1, -1/3$). Note that we've normalized the selection function such that $\int dr r^2 \phi(r) f(r)$ denotes the effective number of galaxies per steradian per radially weighted shell, which is useful to express the shot noise later in this section. However since I further divide the term $\phi(r)f(r)$ by $\int dr r^2 \phi(r) f(r)$ the theory is that for the galaxy *overdensity* ACF (and not density ACF).

Throughout this chapter, I assume the 2MRS galaxy bias does not evolve with redshift, which is motivated by the limited redshift range of the 2MRS survey. For deeper surveys this should not be assumed, and the general form of Equation 3.7 is:

$$C_{\delta\delta}(\ell) = \left\langle |a^{\delta}_{\ell m}|^2 \right\rangle = 4\pi \int dk \frac{\Delta^2(k)}{k} |W^r_{\delta}(k)|^2 , \tag{3.13}$$

where the bias is implicitly expressed in the density window function:

$$W^r_{\delta}(k) = \int dr b_g^2 \Theta(r) j_\ell(kr) D , \tag{3.14}$$

where $b_g = b_g(z)$. For deeper surveys, the redshift dependence of the bias should be taken into account wherever it appears, i.e. in the cross-correlation between shells, etc.

Inhomogeneities in the galaxy density field, mean galaxies are subject to peculiar velocities, as well as velocities from the Hubble flow. The peculiar velocities of galaxies will introduce redshift distortions, which on linear scales will enhance structure along the line of sight. This will add power to the power spectrum on large scales. The linear theory correction term to the power spectrum is discussed below.

3.3.2 Redshift Distortions as a Cosmological Probe

Redshift distortions are a radial distortion of the galaxy density field due to the peculiar velocities of galaxies. This distortion occurs because the observed spectroscopic redshift z_{obs} is a sum of two quantities:

$$z_{obs} = z_h + z_{\vec{v}\cdot\vec{r}} , \tag{3.15}$$

where z_h is the Hubble redshift due to the general expansion of the Universe and $z_{\vec{v}\cdot\vec{r}}$ is the redshift due to the radial component of the peculiar velocity of the galaxy, which arises due to local inhomogeneities in the density field. A reconstruction of the density field in redshift space will therefore be disparate to a reconstruction in real space.

In linear theory, galaxies will infall towards the centre of overdensities on large scales. The redshift distortion is an effect due to the radial component of the peculiar velocity field. The peculiar velocity component which is transversal to the line of sight will not result in any distortions. However, along the line of sight, measured redshifts will include the radial component of the peculiar velocity so that structure will appear enhanced on large (linear) scales. This will result in an increase of power in the ACF.

To account for this added power, it is necessary to add a correction term to the product $\phi(r)f(r)$ in Equation 3.7. Following Fisher, Scharf & Lahav (1994*b*), I Taylor expand the product to first order:

$$f(r)\phi(r) \simeq f(r)\phi(r) + \frac{\mathrm{d}(f(r)\phi(r))}{\mathrm{d}r}[U(\mathbf{r}) - \mathbf{V}_{obs}.\hat{\mathbf{r}}] \,, \tag{3.16}$$

where $U(\mathbf{r}) = \mathbf{v}(\mathbf{r}) \cdot \hat{\mathbf{r}}$ is the radial component of the peculiar velocity field and $\mathbf{V}_{obs}$ is the velocity of an observer defined in the same reference frame as $\mathbf{v}(\mathbf{r})$.

This leads to a redshift distortion correction term in the radially weighted ACF:

$$C_{\delta\delta}(\ell) = \left\langle |a_{\ell m}|^2 \right\rangle = 4\pi b_g^2 \int \mathrm{d}k \, \frac{\Delta^2(k)}{k} \, |W_\delta^r(k) + \beta W_\delta^z(k)|^2 \,. \tag{3.17}$$

The term

$$W_\delta^z(k) \;=\; \frac{1}{k}\int \mathrm{d}r \, \frac{\mathrm{d}\left[\phi(r)f(r)\right]}{\mathrm{d}r} j'_\ell(kr) \,, \tag{3.18}$$

is the redshift distortion contribution to the measured ACF (cf. Fisher, Scharf & Lahav (1994*b*) for the derivation) and $\beta = \frac{f_g(z)}{b_g}$ is the distortion term and $f_g(z) = \frac{\mathrm{dln}D(z)}{\mathrm{dln}a(z)}$ is the growth factor.

Padmanabhan *et al.* (2006) showed that this could be re-written (also see Appendix A for the full derivation):

$$W_\delta^z(k) = \int \mathrm{d}r\phi(r)f(r)\left(A_\ell j_\ell(kr) - B_\ell j_{\ell-2}(kr) - D_\ell j_{\ell+2}(kr)\right) \,, \tag{3.19}$$

where:

$$A_\ell = \frac{(2\ell^2 + 2\ell - 1)}{(2\ell + 3)(2\ell - 1)} \,, \tag{3.20}$$

$$B_\ell = \frac{\ell(\ell-1)}{(2\ell+1)(2\ell-1)}\,, \tag{3.21}$$

$$D_\ell = \frac{(\ell+1)(\ell+2)}{(2\ell+1)(2\ell+3)}\,. \tag{3.22}$$

When calculating the dipole contribution, it is necessary to include a correction term due to the rocket effect (i.e. some of the dipole arises from our motion relative to the large scale structure), which can be done by adding the following term to Equation 3.18:

$$W^z_{\ell=1}(k) = -\frac{1}{k}\int_0^\infty \mathrm{d}r r^2 \frac{\mathrm{d}[\phi(r)f(r)]}{\mathrm{d}r}\frac{\delta_{\ell 1}}{3}\,. \tag{3.23}$$

This can also be integrated by parts, which simplifies to:

$$W^z_{\ell=1}(k) = \frac{2}{3k}\int_0^\infty \mathrm{d}r r\phi(r)f(r)\delta_{\ell 1}\,. \tag{3.24}$$

The total galaxy window including redshift distortions can then be rewritten:

$$W^{r+z}_\ell(k) = W^r(k) + \beta W^z(k)\,, \tag{3.25}$$

$$= W^r_\ell(k) + \beta\left(A_\ell W^r_\ell(k) + B_\ell W^r_{\ell-2}(k) + D_\ell W^r_{\ell+2}(k) + W^z_{\ell=1}\right)\,. \tag{3.26}$$

So that the ACF with redshift distortions is:

$$C_{\delta\delta}(\ell) = 4\pi b_g^2 \int dk \frac{\Delta^2(k)}{k}|W^{r+z}(k)|^2\,. \tag{3.27}$$

I am interested in Chapter 4 in constraining the matter density Ω_m and the galaxy bias b_g from the redshift space ACF. The parameters are constrained by a combination of the real space correlation function and the redshift distortions. The ACF dependence on Ω_m will affect both the shape of the matter power spectrum and the redshift distortion, modulated by $\Omega_m^0.6$.. The bias also affects the ACF in two ways, it will change the overall normalization (and is degenerate with σ_8 on linear scales - see Section 4.3), and modulates the redshift distortion by $1/b_g$.

In this analysis I chose four Gaussian weighting functions (cf. Section 3.5). As these shells physically overlap I need to take account of cross-correlation functions (CCF) between different shells. Let i and j be labels of different shells, then the CCF will be given by:

$$C^{ij}_{\delta\delta}(\ell) = \left\langle a^i_{\ell m} a^{*j}_{\ell m}\right\rangle = 4\pi b_g^2 \int dk \frac{\Delta^2(k)}{k}|W^{r+z}_i(k)||W^{r+z}_j(k)|\,, \tag{3.28}$$

and the ACF is given for $i = j$.

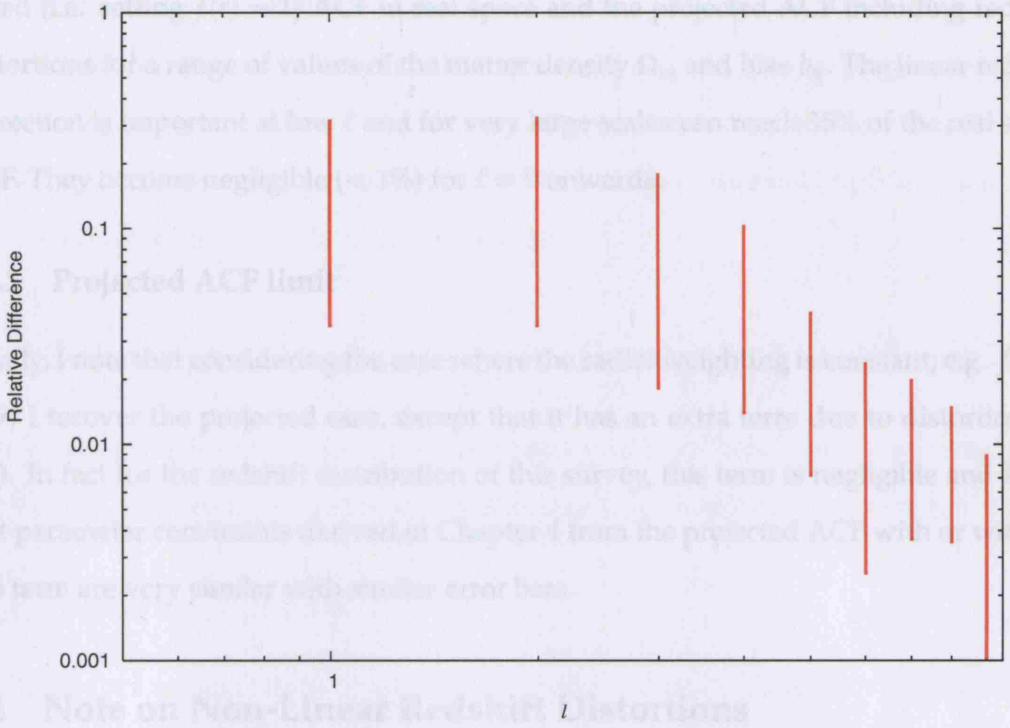

Figure 3.3: The relative difference between the real space projected ACF (Equation 3.7) and the redshift space projected ACF (Equation 3.17) for a range of values of the matter density Ω_m and bias b_g. The relative difference can reach 35% on large scales, but becomes negligible ($< 1\%$) from $\ell = 9$ onwards.

Due to the discreteness of the field, the data will include power due to shot noise which I must include in the theory both in the ACF and the CCF. Even when considering the *cross*-correlation, there will still be a shot noise term as galaxies can physically belong to both shells. This shot noise term for the CCF is given by:

$$C_{SN}^{ij} = \left\langle a_{\ell m}^{i} a_{\ell m}^{*j} \right\rangle_{SN} = \frac{\int_0^\infty \mathrm{d}r r^2 \phi(r) f^i(r) f^j(r)}{\int_0^\infty \mathrm{d}r r^2 \phi(r) f^i(r) \int_0^\infty \mathrm{d}r r^2 \phi(r) f^j(r)} , \tag{3.29}$$

where $f^i(r)$ is the weighting function corresponding to different shells. The shot noise term for the ACF is given for $i = j$. In the ACF case, this corresponds to $/Omega/N_g$, i.e. the inverse of the number of galaxies per steradian.

In all calculations, I use Equation 3.27 to calculate the ACF for $\ell < 10$ after which I use the small angle approximation given by:

$$C_{gg}(\ell) = b_g^2 \int \mathrm{d}r \, \frac{\Theta^2}{r^2} \, D^2 P \left(\frac{\ell + 1/2}{r} \right) . \tag{3.30}$$

In Figure 3.3, I plot the absolute relative difference range between the real or pro-

jected (i.e. setting $f(r) = 1$) ACF in real space and the projected ACF including redshift distortions for a range of values of the matter density Ω_m and bias b_g. The linear redshift correction is important at low ℓ and for very large scales can reach 35% of the real space ACF. They become negligible ($< 1\%$) for $\ell = 9$ onwards.

3.3.3 Projected ACF limit

Finally, I note that considering the case where the radial weighting is constant, e.g. $f(r) = 1\ \forall r$, I recover the projected case, except that it has an extra term due to distortions in $\phi(r)$. In fact for the redshift distribution of this survey, this term is negligible and I find that parameter constraints derived in Chapter 4 from the projected ACF with or without this term are very similar with similar error bars.

3.4 Note on Non-Linear Redshift Distortions

Peculiar velocities will induce line of sight distortions on all scales. As discussed above on linear scales, this will have the effect of compressing structures along the line of sight, which will add power to the galaxy power spectrum. On non-linear scales, the effect will be to dilute structures along the line of sight (Hamilton 1998), resulting in the 'Finger of God' (FoG) structures, so-called because they create the illusion that structures are all pointing towards the observer.

While linear distortions can be corrected for exactly, non-linear distortions must be corrected 'by hand'. By identifying clusters which are subject to FoG effects and compressing them (Gramann *et al.* 1994), which eliminates the distortion. The FoG identification can be performed using a *friends of friends* algorithm with a window function elongated in the radial direction (Ramella *et al.* 1989).

The translinear regime (the transition between the linear and non-linear regime) can be corrected with several phenomenological prescriptions such as the assumption of random isotropic pairwise velocity dispersion, which was first proposed by Peebles (1976) and has been implemented either with Gaussian (Peacock & Dodds 1994; Heavens & Taylor 1995) or exponential (Fisher *et al.* 1994*a*; Hamilton 1995) velocity components. Others have dealt with the translinear regime using the Zel'dovich approximation (Fisher &

Nusser 1996; Taylor & Hamilton 1996).

In this work, I assume that non-linear effects are negligible. This may be over-optimistic as it has been suggested that non-linear effects can be important up to scales of $\sim 20h^{-1}Mpc$ (Hamilton 1998), i.e. those probed by the 2MRS. I discuss potential implications of non-linearities on the results of Chapter 4 in Section 4.7.

3.5 Estimation of the Galaxy Auto-Correlation Function for 2MRS

In this Section, I discuss estimation of the galaxy ACF for both real (or projected) and radially weighted cases, including corrections due to incomplete sky coverage.

3.5.1 Partial Sky Coverage

The spherical harmonic decomposition described in Equation 3.2 and 3.4 makes the fundamental assumption that the survey is complete over the whole sky. This is because the decomposition depends on the $Y_{\ell m}$'s forming an orthonormal set, which they only do on a sphere.

Due to our position in the Universe (i.e. hosted by a galaxy), it is impossible to obtain a completely all-sky survey. There will always be some obscuration and confusion along the galactic bulge and plane; other close-by galaxies like the LMC and the SMC will introduce incompleteness.

Even though the 2MRS is in the advantageous position of being a nearly all-sky survey with 89% of the sky covered, the missing 11% will affect the power spectrum C_ℓ and the $a_{\ell m}$ coefficients in the following way:

1. The density power spectrum C_ℓ will be subject to a loss of power on all scales, proportional to the fractional sky coverage

2. If the underlying C_ℓ's are independent (e.g., as in a Gaussian random field, cf. Section 3.7.1, where I investigate if this is plausible for 2MRS), incomplete sky coverage will make adjacent multipoles correlated. The size $\Delta\ell$ of the correlation (or "power leakage") can be determined analytically.

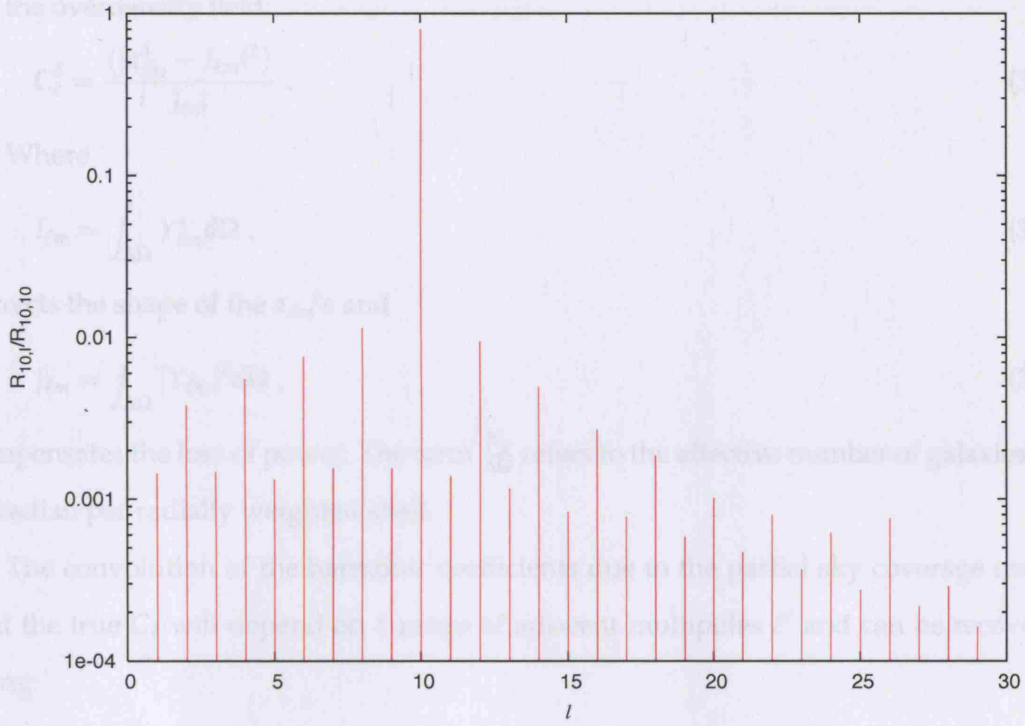

Figure 3.4: The mixing matrix $R_{\ell,\ell'}$ for multipoles $\ell = 10$ as a function of ℓ', indicating the range of multipoles correlated due to partial sky coverage.

3. The structure of the $a_{\ell m}$'s will change. Again, if the underlying field is a Gaussian random field, the phases of the true $a_{\ell m}$'s will be independently drawn from a uniform random distribution. The $a_{\ell m}$'s measured in a partial sky survey will no longer be independent and therefore will not be uniformly distributed.

If the regions of the sky over which the survey is not complete are known, it is possible to correct the effect on the estimators C_ℓ and $a_{\ell m}$'s using a pseudo-C_ℓ estimator. In this sense, it is better to slightly overestimate regions of the sky that are incomplete, rather than underestimate them, as this permits a better estimation of the true C_ℓ's and $a_{\ell m}$'s. I note that for larger sky cuts, it may be more optimal to use a quadratic maximum likelihood to estimate the large scale power spectrum rather than the pseudo-C_ℓ estimator (Efstathiou 2004).

For an incomplete sky survey (Peebles 1993, Wall & Jenkins 2004, Blake *et al.* 2007), an estimator of the C_ℓ is, for the density field:

$$C_\ell^\rho = \frac{\left\langle |a_{\ell m}^\rho - \frac{N_g}{\Delta\Omega} I_{\ell m}|^2 \right\rangle}{J_{\ell m}}, \tag{3.31}$$

for the overdensity field:

$$C_\ell^\delta = \frac{\langle |a_{\ell m}^\delta - I_{\ell m}|^2 \rangle}{J_{\ell m}} \,. \tag{3.32}$$

Where

$$I_{\ell m} = \int_{\Delta\Omega} Y_{\ell m}^* d\Omega \,, \tag{3.33}$$

corrects the shape of the $a_{\ell m}$'s and

$$J_{\ell m} = \int_{\Delta\Omega} |Y_{\ell m}|^2 d\Omega \,, \tag{3.34}$$

compensates the loss of power. The term $\frac{N_g}{\Delta\Omega}$ refers to the effective number of galaxies per steradian per radially weighted shell.

The convolution of the harmonic coefficients due to the partial sky coverage means that the true C_ℓ will depend on a range of adjacent multipoles ℓ' and can be recovered using:

$$C_\ell = \sum_{\ell'} R_{\ell,\ell'} C_{\ell'} \,, \tag{3.35}$$

where the mixing matrix $R_{\ell,\ell'}$ is determined from the angular power spectrum W_ℓ of the survey window function:

$$R_{\ell,\ell'} = \frac{2\ell'+1}{4\pi} \sum_{\ell''} (2\ell''+1) W_{\ell''} \begin{pmatrix} \ell & \ell' & \ell'' \\ 0 & 0 & 0 \end{pmatrix} \,, \tag{3.36}$$

where the last term in Equation 3.36 is a Wigner 3-j symbol and

$$W_\ell = \frac{\sum_{m=-\ell}^{\ell} |I_{\ell m}|^2}{2\ell+1} \,, \tag{3.37}$$

(see, Hivon *et al.* 2002, Deligny *et al.* 2004, Blake *et al.* 2007).

I find the convolution function from the 2MRS sky coverage is sharply peaked for all multipoles ℓ considered in the analysis, and is less than 1% for $\ell \neq \ell'$. I plot the mixing matrix $R_{\ell,\ell'}$ for multipoles $\ell = 10$ in Figure 3.4. It is representative of the mixing matrix for all multipoles covered in this analysis. There exists an even/odd pattern in the mixing matrix, which may either be due to the symmetry of the mask around $b = 0°$ or could be the result of a numerical artifact.

Therefore I assume correlations between multipoles are negligible and do not account for them. I do correct for loss of power and for change of structure in the harmonic coefficients by using Equation 3.32 when estimating the power spectrum.

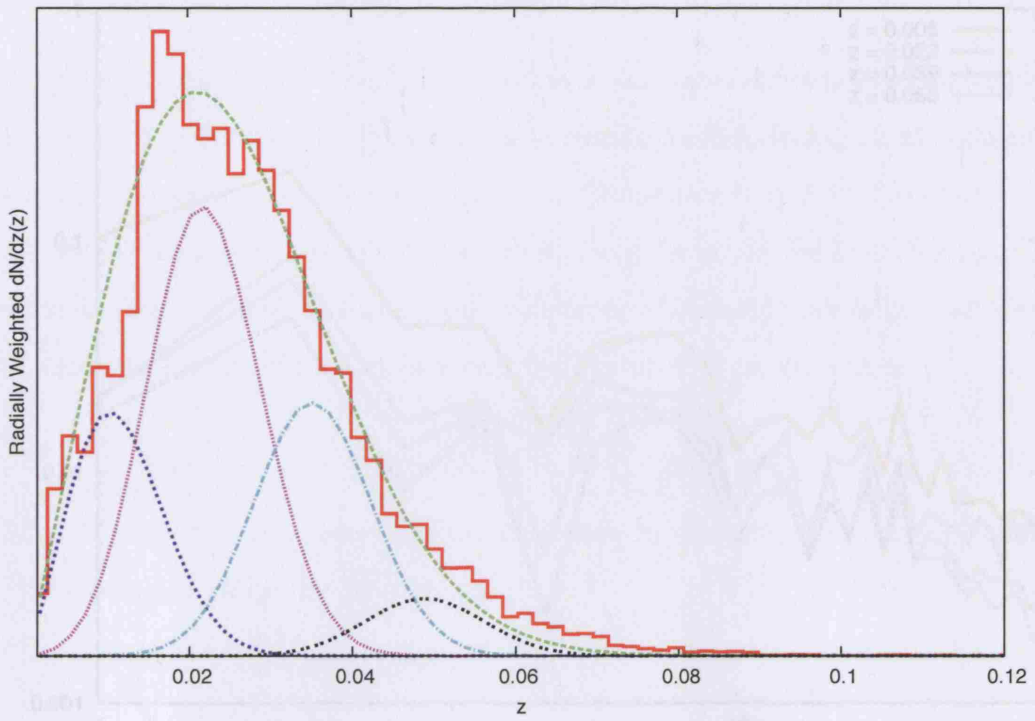

Figure 3.5: The redshift distribution $\frac{dN}{dz}(z)$ for the 2MRS. The red histogram represents 2MRS data, the green solid line the best fit given by Equation 3.1. The four overlapping shells are the weighted redshift distributions $f(z)\frac{dN}{dz}(z)$ where $f(z)$ are Gaussians with mean $\mu_z = (0.005,\ 0.022,\ 0.039,\ 0.056)$ and dispersion $\sigma_z = 0.008$.

3.5.2 Projected and radially weighted case

In this analysis, I consider the projected and radially weighted auto-correlation functions which I obtain from direct summation over the galaxy angular and radial positions of the 2MRS, using Equation 3.4. For the projected case I simply set $f(r) = 1\ \forall r$. In both cases, the estimates for the harmonic coefficients require modifications due to incomplete sky coverage, which I discussed in Section 3.5.1.

For the radially weighted case, I chose four Gaussian weighting function given by $f(z) = f(r)\frac{dr}{dz}$ each with mean $\mu_z = (0.005,\ 0.022,\ 0.039,\ 0.046)$ and standard deviation $\sigma_z = 0.008$. In Figure 3.5 I show the 2MRS redshift distribution $\frac{dN}{dz}(z)$ used in the projected case, and the weighted redshift distribution for each of the four shells.

The radially weighted / redshift space ACF for the four Gaussian radial shells considered in this analysis are plotted in Figure 3.6. In Chapter 4, I constrain cosmological parameters using all four shells simultaneously (i.e., by calculating the covariances be-

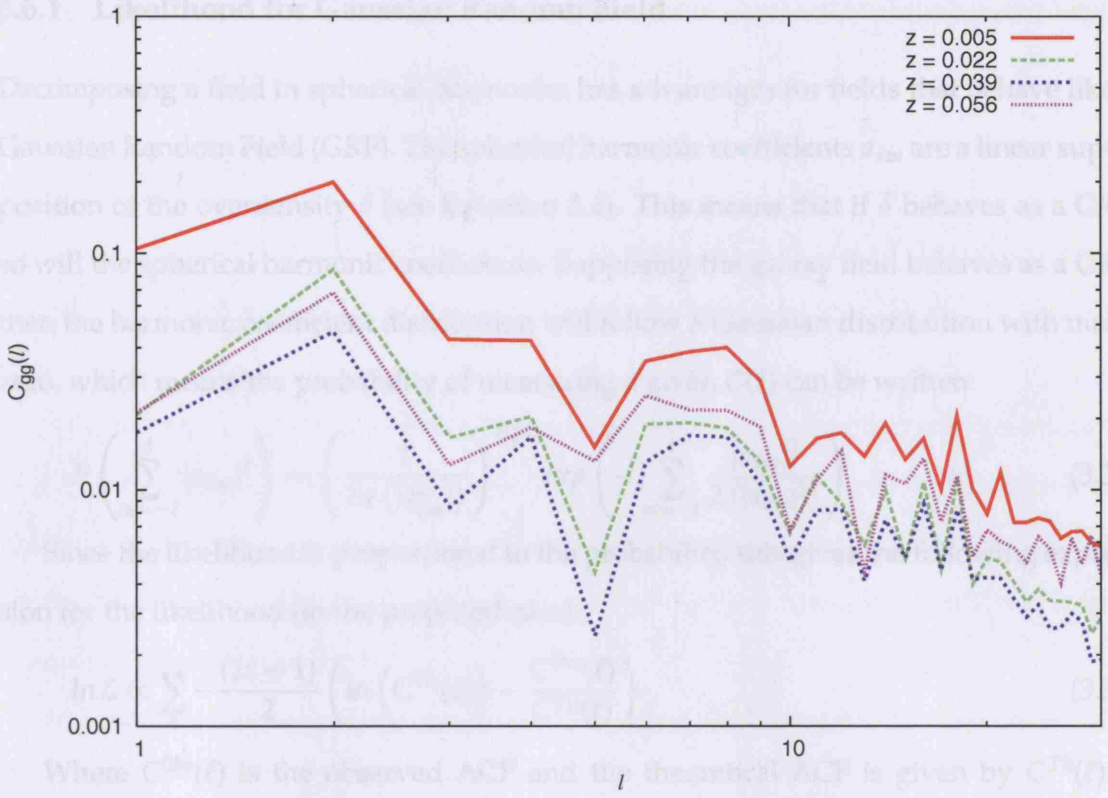

Figure 3.6: The 2MRS galaxy overdensity auto-correlation function for each radially weighted shell. The mean redshift of each Gaussian weighting shell were chosen to be $\mu_z = (0.005, 0.022, 0.039, 0.056)$.

tween the shells). Constraints are also presented using the two central shells only, which I justify in Section 3.7.

3.6 Choice of Likelihood and Assumptions on the underlying field

In this Section, I present the likelihood equation I use for parameter estimation done in Chapter 4, stressing that it fundamentally assumes that the galaxy density field behaves as a Gaussian random field (GRF). Using a toy model of a GRF, I illustrate how applying an incorrect likelihood affects determination of cosmological parameters.

3.6.1 Likelihood for Gaussian Random Field

Decomposing a field in spherical harmonics has advantages for fields that behave like a Gaussian Random Field (GRF). The spherical harmonic coefficients $a_{\ell m}$ are a linear superposition of the overdensity δ (see Equation 3.4). This means that if δ behaves as a GRF, so will the spherical harmonic coefficients. Supposing the galaxy field behaves as a GRF, then the harmonic coefficient distribution will follow a Gaussian distribution with mean zero, which means the probability of measuring a given $C(\ell)$ can be written:

$$P\left(\sum_{m=-\ell}^{\ell}|a_{\ell m}|^2\right) = \left(\frac{1}{2\pi\left\langle|a_{\ell m}^2|\right\rangle}\right)^{\frac{2\ell+1}{2}} exp\left(-\sum_{m=-\ell}^{\ell}\frac{|a_{\ell m}|^2}{2\left\langle|a_{\ell m}|^2\right\rangle}\right) . \tag{3.38}$$

Since the likelihood is proportional to the probability, this gives the following expression for the likelihood (in the projected case):

$$\ln\mathcal{L} \propto \sum_{\ell} -\frac{(2\ell+1)}{2}\left(\ln\left(C^{\rm Th}(\ell)\right) - \frac{C^{\rm 0bs}(\ell)}{C^{\rm Th}(\ell)}\right) . \tag{3.39}$$

Where $C^{0bs}(\ell)$ is the observed ACF and the theoretical ACF is given by $C^{Th}(\ell) = C_{\delta\delta}(\ell) + C_{\rm SN}$, where $C_{\rm SN}$ is the signal due to shot noise. When considering several radially weighted shells where cross-correlations between shells are not negligible, the likelihood is expressed as (see Bucher, Moodley & Turok 2002):

$$\ln\mathcal{L} \propto \sum_{\ell} -\frac{(2\ell+1)}{2}\left(\ln|\mathrm{A}| + \mathrm{Tr}(\mathrm{A}^{-1}\mathrm{C}^{\rm Obs})\right) . \tag{3.40}$$

Where elements of the covariance matrix A are defined as:

$$A_{ij}(\ell) = C^{ij}_{\delta\delta}(\ell) + C^{ij}_{SN} . \tag{3.41}$$

Equations 3.39 and 3.40 implicitly assume that the harmonic coefficients follow a Gaussian distribution (they are equivalent to Equation (14) in Fisher, Scharf & Lahav 1994*b*).

3.6.2 Problems with Assuming a Non-Gaussian Likelihood with a Gaussian Random Field

I also consider a likelihood which does not assumes that the harmonic coefficients follow a Gaussian distribution but instead that the C_ℓs do. In this case the likelihood is written:

$$\ln\mathcal{L} = -\frac{1}{2}\chi^2 = \sum_{\ell}\left(\frac{C^{\rm Obs}(\ell) - C^{\rm Th}(\ell)}{\sigma(C(\ell))}\right)^2 , \tag{3.42}$$

where the error on $C(\ell)$ is derived using the four point function of the harmonic coefficients (see Appendix B for the derivation) which leads to:

$$\sigma(C(\ell)) = \left\langle C^2(\ell) \right\rangle = \sqrt{\frac{2}{f_{sky}(2\ell+1)}} C(\ell) \,, \tag{3.43}$$

where the value of $C(\ell)$ can be taken to be the observed ($C^{Obs}(\ell)$) or theoretical values ($C_{\delta\delta}(\ell) + C_{SN}$) of the ACF. Equation 3.42 implicitly assumes that the $C(\ell)$ quantity is Gaussian.

As a toy model, I consider the projected angular power spectrum of a galaxy field, in a flat universe with $\Omega_m = 0.30$, $h = 0.70$, $n = 1.0$ and $b_g \frac{\sigma_8}{0.75} = 1.50$. I make many realizations of this universe, drawn assuming the harmonic coefficients are Gaussian; i.e., I independently draw real and imaginary parts of each harmonic coefficient from a Gaussian with variance $C_\ell/2$.

In Table 3.1, I report estimates of Ω_m and b_g using likelihood function which assume that:

1. **Gaussian $a_{\ell m}$:** The harmonic coefficients $a_{\ell m}$ follow a Gaussian distribution, i.e. I use Equation 3.39 to estimate the likelihood.

2. **Gaussian C_ℓ:** The power coefficients C_ℓ follow a Gaussian distribution, i.e. I use Equation 3.42 to estimate the likelihood.

In the top part of Table 3.1, the correct normalization is used in the likelihood calculation ($\sigma_8 = 0.75$), in the bottom part of Table 3.1 I use a different normalization ($\sigma_8 = 0.90$). In both cases, the likelihood using the Gaussian $a_{\ell m}$ assumption returns the correct value for Ω_m while the product $b_g\sigma_8$ remains constant ($0.75 \cdot 1.49 \simeq 0.90 \cdot 1.25$), whereas the likelihood using the Gaussian C_ℓ assumption returns erroneous values for both Ω_m and b_g, and in fact barely differentiates between $\sigma_8 = 0.75$ and $\sigma_8 = 0.90$. The error bars for the invalid likelihood are also much larger.

In Section 3.7.1, I test whether the 2MRS data are compatible with a GRF. The test can detect non-Gaussianities that affect the phase distribution, but cannot guarantee that the field *is* Gaussian. Indeed the only complete test of non-Gaussianity is to verify that each moment $\mu_n = \langle(\delta - \langle\delta\rangle)^n\rangle = 0$ for $n > 2$, i.e. that all moments apart from the mean and the variance are zero.

	(i) Gaussian $a_{\ell m}$	(ii) Gaussian C_ℓ
$\sigma_8 = 0.75$		
b_g	1.50 ± 0.085	1.30 ± 0.20
Ω_m	0.35 ± 0.16	0.46 ± 0.19
$\sigma_8 = 0.90$		
b_g	1.25 ± 0.049	1.31 ± 0.23
Ω_m	0.31 ± 0.089	0.49 ± 0.16
Input Values	$b_g = 1.50$; $\sigma_8 = 0.75$;	$\Omega_m = 0.30$

Table 3.1: The mean of the best fit values for b_g and Ω_m for 40 Gaussian random field simulations with input parameters $b_g = 1.50$, $\Omega_m = 0.30$ and $\sigma_8 = 0.75$. Values are given when the likelihood estimator implicitly assumes (i) the $a_{\ell m}$ distribution is Gaussian and (ii) the C_ℓ distribution is Gaussian. In the top part, the best fit values were calculated using the correct σ_8 normalization ($\sigma_8 = 0.75$), in the bottom part I used $\sigma_8 = 0.9$. When assuming the $a_{\ell m}$ distribution is Gaussian, the product $\sigma_8 b_g$ is constant, and Ω_m is unaffected by the assumed value of the normalization.

To some extent, we know the 2MRS will present some non-Gaussianity. Applying the Gaussian likelihood analysis to a 2MRS type N-body simulation would quantify the effect of non-Gaussianities in the analysis. This will be done in future work.

3.7 Testing assumptions about the underlying field

In this Section, I test the assumption that the underlying overdensity field of 2MRS behaves like a GRF in harmonic space.

This can be done by checking whether the real and imaginary parts of the spherical harmonics follow a Gaussian distribution. For each multipole ℓ, the expected distribution is a Gaussian with variance $C_\ell/2$. However, on the large scales I am considering, cosmic variance makes it difficult to asses the non-Gaussianity in this way.

Another way to test the GRF assumption, is to inspect the phase distribution of the spherical harmonics. The 1 point function of the phases of the harmonic decomposition

is expected to follow a uniform distribution for a statistically isotropic GRF. I test this for the projected field both before and after applying harmonic coefficient corrections due to partial sky coverage (as described in Section 3.5.1). By doing so, I am interested in testing the effect of the sky coverage correction.

I also test the phase distribution for each radially weighted shell. This time I perform the test after the spherical harmonics have been corrected for the partial sky coverage. This test is aimed at finding departures from Gaussianity in the 2MRS dataset, and identifying which redshift shells they may be attributed to.

Finally, I describe how to test if the overdensity field is better described by a lognormal distribution.

3.7.1 Testing the Gaussian Random Field Hypothesis

The calculation of the likelihood assumes that the galaxy density field is a statistically isotropic GRF. Such a field requires that the real and imaginary parts of the harmonic coefficients $a_{\ell m}$ are independent and drawn from a Gaussian distribution with variance $C_\ell/2$. This is equivalent to the moduli $|a_{\ell m}|$ being drawn from a Rayleigh distribution and the phases $\phi_{\ell m}$ being drawn from a random uniform distribution.

In the following Section, I test if the uniformity of the phases of the galaxy overdensity distribution is consistent with a uniform distribution. The phases in a spherical harmonic decomposition are not rotationally invariant and analysing the data in a different coordinate system will yield different values of the $a_{\ell m}$'s and the phases. However, one of the motivations is to analyse how the corrections due to partial sky coverage affect the phase distribution. The actual frame in which the phases are calculated are not that important, as long as phases before and after correction are calculated in the same frame.

I test the uniformity of phases for multipoles $1 \leq \ell \leq 15$, considering only phases with $m \geq 1$. I omit phases where $m = 0$ as these will always have $\phi = 0\ [\pi]$ since $a_{\ell 0} = \mathcal{R}(a_{\ell 0})$. Phases with $m < 0$ are implicitly included in the analysis by the fact that $a^*_{\ell m} = (-1)^m a_{\ell -m}$, for real valued fields. I divide the multipole space into three groups: $1 \leq \ell \leq 5$, $6 \leq \ell \leq 10$ and $11 \leq \ell \leq 15$, following Chiang, Naselsky & Coles (2006). The $a_{\ell m}$'s (corrected for sky coverage) for the projected galaxy field for these three groups are plotted in Figures 3.7, 3.8 and 3.9.

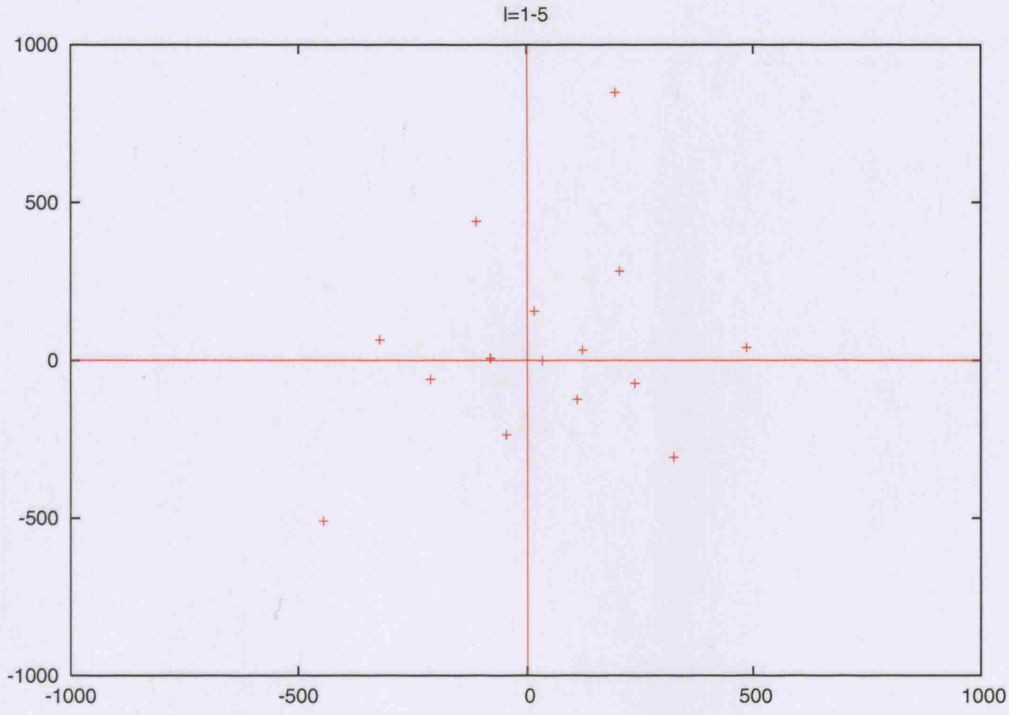

Figure 3.7: The $a_{\ell m}$ harmonic coefficients for the projected overdensity field after corrections for partial sky coverage $1 \leq \ell \leq 5$ for $m \geq 1$ are plotted on the complex plane, where the y-axis corresponds to the imaginary part and the x-axis to the real part of the spherical harmonic coefficient.

If the phase distribution is uniform, there should be approximately the same number of harmonic coefficients in each quadrant of Figures 3.7, 3.8 and 3.9.

To test the uniformity of the phases, I use the Kuiper Statistic, which is a variant of the Kolmorov-Smirnov test used for the case of cyclic data (Chiang, Naselsky & Coles 2006). The Kuiper statistic is defined by:

$$D_{\pm} = max_{\ 0<\phi<2\pi} \pm (S_N(\phi) - P(\phi)) \,, \tag{3.44}$$

where $S_N(\phi)$ is the cumulative probability distribution of the sample and $P(\phi)$ is the theoretical probability, in the case of uniform phase distribution over $[0 : 2\pi]$ $P(\phi) = \frac{\phi}{2\pi}$.

The significance level α is given by:

$$\alpha = Q_{Kuiper}(V(\sqrt{N} + 0.155 + 0.24/\sqrt{N})) \,, \tag{3.45}$$

where

$$Q_{Kuiper}(\lambda) = 2 \sum_{j=1}^{\infty} (4j^2\lambda^2 - 1)e^{-2j^2\lambda^2} \,, \tag{3.46}$$

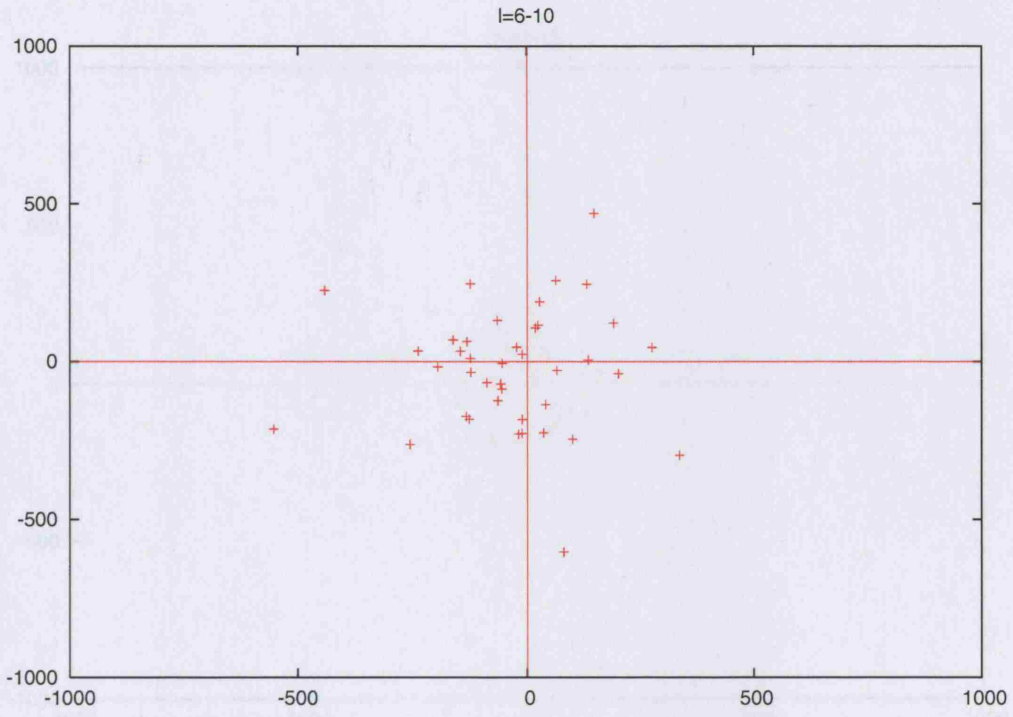

Figure 3.8: The $a_{\ell m}$ harmonic coefficients for the projected overdensity field after correction for partial sky coverage for $6 \leq \ell \leq 10$ for $m \geq 1$ are plotted on the complex plane, where the y-axis corresponds to the imaginary part and the x-axis to the real part of the spherical harmonic coefficient.

and $V = D_+ + D_-$ and N is the number of data points (Press *et al.* 1992).

The significance levels for different scales and 2MRS redshift shells are given in Table 3.2. Considering first the harmonic coefficients in the projected ACF case (columns 1 and 2). For all scales, the significance increases when the harmonic coefficients are corrected for sky coverage using Equation 3.32. In the projected (and corrected) case, the significance is always larger than 93.0% whichever scales are considered, and is equal to 95.0% over scales $\ell = 1 - 15$.

This suggests phase correlations due to incomplete sky coverage are successfully removed when the correction described in Equation 3.32 is used. Although this does not certify that the data is a statistically isotropic GRF, it does show that its phase distribution is consistent with one. Using Equation 3.39 for the likelihood is therefore at the least self consistent.

However, any large data set will tend towards the Gaussian limit, following the cen-

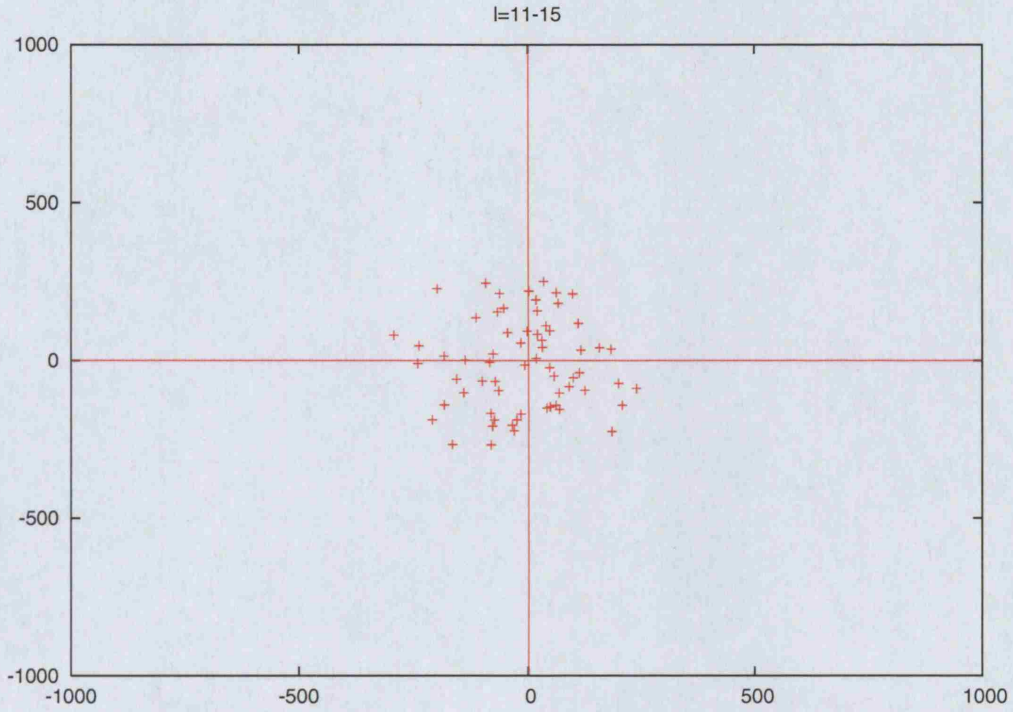

Figure 3.9: The $a_{\ell m}$ harmonic coefficients for the projected overdensity field after corrections for partial sky coverage for $11 \leq \ell \leq 15$ for $m \geq 1$ are plotted on the complex plane, where the y-axis corresponds to the imaginary part and the x-axis to the real part of the spherical harmonic coefficient.

	Projected Uncorrected for sky coverage	Projected Corrected for sky coverage	$\mu_z =$ 0.005	$\mu_z =$ 0.022	$\mu_z =$ 0.039	$\mu_z =$ 0.056
$1 \leq \ell \leq 5$	99.9	100.0	99.6	98.0	95.4	95.3
$6 \leq \ell \leq 10$	47.5	99.7	88.8	99.9	97.8	85.5
$11 \leq \ell \leq 15$	82.0	93.7	51.8	91.5	99.99	79.4
$1 \leq \ell \leq 10$	89.4	95.8	82.8	97.5	98.7	67.5
$1 \leq \ell \leq 15$	58.4	95.0	45.3	83.5	96.1	65.0

Table 3.2: The significance level $\alpha(\%)$ of agreement with a uniform phase distribution of the 2MRS galaxy distribution. Phases on scales $1 \leq \ell \leq 5$ agree to 99.9% with a uniform phase distribution, whereas phases on scales $6 \leq \ell \leq 10$ agree to only 47.5% with a uniform phase distribution.

tral limit theorem. As I have already split the data into four Gaussian redshift shells, I can consider each separately, to investigate whether they are independently compatible with a GRF.

I consider the phase distributions (corrected for sky coverage) of the four radially weighted shells. These shells are chosen and described in Section 3.5.2 and the results for them reported in columns 3 to 6. The central shells, i.e. those centered on $\mu_z = (0.022, , 0.039)$, present significance levels greater than 97% for multipole ranges $\ell = 1 - 10$ and greater than 83.0% and 96.1% respectively for multipole ranges $\ell = 1 - 15$. These shells are therefore compatible with a statistically isotropic GRF.

However, the two extreme shells show departure from a statistically isotropic GRF. For the nearest shell, centered on $\mu_z = 0.005$, the agreement drops to 45.3% on scales $\ell = 1 - 15$. and for the furthest shell, centered on $\mu = 0.056$, the agreement falls to 65.0% on scales $\ell = 1 - 15$. This might be due to the presence of non-linear structure (the closest shell probes the Local Void, the furthest begins to probe Shapley) or due to low signal to noise (in the furthest shell).

Again, although we cannot certify which redshift bins are definitely statistically isotropic GRFs, we can assure that the nearest and furthest bins are *not*. This might be due to non linear local structure in the nearest shell and for the furthest shell shot noise predominance (which follows Poisson statistics) or large scale structure (the Shapley superstructure is probed at these redshifts). For consistency, I should exclude these from the Gaussian likelihood analysis in Chapter 4.

The likelihood I use for the parameter estimation (Equations 3.39 and 3.40) assumes the field behaves as a statistically isotropic GRF and so in Section 6.7 I chose to perform the maximum likelihood analysis on two data sets in order to probe how this affects the parameter estimation.. The first is on all radially weighted shells, the second only on the central shells, i.e. excluding those which are not statistically isotropic GRFs. In Section, 4.3, I presented constraints on Ω_m and b_g with and without data that is not compatible with a GRF (i.e., considering all four radial shells, or only the two central shells).

3.7.2 Testing the Lognormal Field Hypothesis

In the previous Section, I discussed the fact that the 2MRS is not a statistically isotropic GRF in certain redshift shells. It is possible to test if the density field is described by a lognormal probability distribution by considering the normalized overdensity field:

$$\Delta(\hat{\mathbf{r}}) = 1 + \delta(\hat{\mathbf{r}}) \,, \tag{3.47}$$

where as before, $\rho(\hat{\mathbf{r}})$ describes the galaxy density distribution and $\delta(\hat{\mathbf{r}})$ the galaxy overdensity defined by Equation 3.6. The normalized overdensity is defined so that $\langle\Delta\rangle = 1$ and $\Delta(\hat{\mathbf{r}}) > 0$ is always true.

Following the notation of Kayo, Taruya & Suto (2001), if Δ is a lognormal field, its probability distribution function (PDF) will be of the form:

$$P_{\rm LN}(\Delta) = \frac{1}{\sqrt{2\pi\sigma_1^2}\Delta} \exp\left[-\frac{\left(\ln\Delta + \frac{\sigma_1^2}{2}\right)^2}{2\sigma_1^2}\right] \,. \tag{3.48}$$

The lognormal field is described by a single parameter σ_1 that is related to the variance of Δ by:

$$\sigma_1^2 = \ln\left\langle\Delta^2\right\rangle \,. \tag{3.49}$$

Preliminary tests on the 2MRS overdensity field, suggest it is well described by a lognormal distribution. If this is the case, this should be reflected in the choice of the likelihood function.

In Chapter 4, I perform a maximum likelihood method which assumes the underlying 2MRS galaxy field behaves as a GRF. An extension of this work which is not presented in this Thesis, is currently under way and uses a lognormal likelihood.

3.8 Discussion

The second data release of the 2MASS Redshift Survey (2MRS) is complete down to a K_s magnitude of 11.5 for galactic latitudes of $|b| > 5°$. It contains over 30k galaxies with mean spectroscopic redshifts out to a mean redshift ~ 0.3. Its relatively shallow depth compared to deep surveys like SDSS and 2dF is a trade-off for having 90% sky coverage.

As the 2MRS is nearly all-sky, I calculate the galaxy Auto Correlation Function (ACF) in spherical harmonic space. With the spectroscopic redshift information, I calculate the radially weighted ACF which includes power due to redshift distortions.

In spherical harmonic space, the redshift distortions are confined to the radial dimension and there an exact prescription for the linear theory redshift space ACF. The linear redshift distortions are modulated by the distortion parameter $\beta = \Omega_m^{0.6}/b_g$, while Ω_m and b_g will affect the shape and normalization of the real space matter power spectrum $P(k)$. I show in Chapter 4 that it is in fact the $\sigma_8 b_g$ normalization which is constrained.

I estimate the 2MRS galaxy ACF in real and redshift space using pseudo-C_ℓs in order to account the for lack of sky coverage along the Galactic plane as well as around the large and small Magellanic clouds. The redshift space ACFs are calculated using four Gaussian redshift shells, which use the spectroscopic redshift information of 2MRS.

In preparation for the maximum likelihood analysis presented in Chapter 4, I contrast two forms of likelihood functions from the literature. The first assumes that the galaxy density field behaves as a Gaussian Random Field (GRF). The second that the $C(\ell)$s from the ACF are Gaussian, which is non-Gaussian in the galaxy field. I show there are serious problems with applying a non-Gaussian likelihood to a GRF. Applying this non-Gaussian likelihood to simulated galaxy GRFs, I show it is not possible to recover the fiducial model, and that the normalization $b_g\sigma_8$ is especially prone to errors.

Another relevant test to do would be to test problems with applying a Gaussian likelihood function to a non-Gaussian random field. In future work, I plan to do this using N-body simulations.

In Chapter 4 I use a maximum likelihood method, which assumes the galaxy density field is a GRF. I test the compatibility of the 2MRS galaxy field with a GRF using the Kuiper test. This tests whether the phase distribution of the spherical harmonic coefficients are compatible with a uniform distribution, as expected in a GRF. I find the entire 2MRS sample is compatible with a GRF. However, when considering separate redshift shells in the data, this is no longer the case. The nearest (mean redshift $z = 0.005$) and furthest (mean redshift $z = 0.056$) are not compatible with a GRF. Erdoğdu (b) *et al.* (2006) reconstructed the linear density field of 2MRS using a Wiener filter (see Chapter 2) and confirmed that in the nearest shell, structure is dominated by the Local Void which may

explain these results. In the furthest shell this could be attributed to large scale structure and shot noise in the furthest shell.

The phase distributions of the two central shells (mean redshifts $z = 0.022, 0.039$) are compatible with those of GRFs, though can still be non-Gaussian in a way that is not detected by the Kuiper test.

Preliminary work also shows that the 2MRS galaxy field can be described by a lognormal distribution. In future work, I plan to investigate problems with applying a Gaussian likelihood function to a lognormal field, as well as repeat the analysis presented in Chapter 4 with a lognormal likelihood.

CHAPTER 4

CONSTRAINING COSMOLOGICAL PARAMETERS WITH THE 2MASS REDSHIFT SURVEY

Summary

In this Chapter I constrain cosmological parameters using the real and redshift space spherical harmonic Auto Correlation Function (ACF) of the 2 Micron all-sky Redshift Survey (2MRS). I use a maximum likelihood method to estimate the matter density Ω_m and the scale independent, linear galaxy bias b_g. The analysis is done in spherical harmonic space, for which there exists an exact prescription of the redshift space distortions. Performing the analysis in redshift space - as opposed to real space, reduces errors on Ω_m by a factor of 5 and on b_g by a factor of 2. The unmarginalised best fit constraints are $\Omega_m = 0.23 \pm 0.06$ and $b_g(\frac{\sigma_8}{0.75}) = 1.06^{+0.06}_{-0.05}$. This is equivalent to a distortion parameter $\beta = 0.39 \pm 0.08$ and is consistent with results in the literature.

The likelihood function I use in this Chapter assumes the galaxy field is a Gaussian Random Field. In Chapter 3 I found that some redshift shells in 2MRS presents clear signatures of non-Gaussianity. For consistency, I remove these shells from the analysis and find little difference in the best fit values of Ω_m and b_g, and a slight increase in the error bars. Non-Gaussianities that are not detected by the test I used may still be present in the data.

I also separate 2MRS galaxies by visually classified morphological type; I use a broad distinction between early (49%, elliptical and lenticular) and late types (51%, spiral). I show that early types tend to reside in dense regions and late types in the field. This is true whichever scale is considered and means each population has its own bias. Using the spherical harmonic analysis in redshift space, I find that $b_{\rm g}^{\rm early}/b_{\rm g}^{\rm late} \sim 1.30 \pm 0.11$.

4.1 Introduction

The 2MASS Redshift Survey (2MRS) is the densest all-sky spectroscopic redshift survey with over 30,000 galaxies covering almost 90% of the sky. Although it contains twenty times less galaxies than SDSS, it benefits from nearly all-sky coverage. For an all sky survey, spherical harmonics are the natural basis in which to calculate the galaxy Auto Correlation Function (ACF). In this basis there exists an exact prescription for the linear redshift distortions.

The 2MRS is therefore ideal to probe cosmology in redshift space. The redshift space ACF contains information about cosmology through the matter power spectrum $P(k)$ and through the redshift distortion parameter $\beta = \Omega_m^{0.6}/b_{\rm g}$. As the 2MRS galaxies are Near Infra Red (NIR) selected, they trace older stellar populations. This also makes 2MRS a robust tracer of mass and galaxy bias. In this Chapter, I use a maximum likelihood method to estimate the matter density Ω_m and the scale independent, linear galaxy bias $b_{\rm g}$ from the real and redshift space 2MRS galaxy ACF.

In the previous Chapter, I discussed problems with using a non-Gaussian likelihood on a Gaussian Random Field (GRF). I found that applying such a likelihood on simulated GRFs meant I could not recover the input cosmology. Here, I use a Gaussian likelihood function, and so for consistency first checked for any departures from Gaussianity in the galaxy field. To do this I investigated the phase distribution of the spherical harmonics coefficients. The phase distribution in a GRF is expected to be a uniform distribution. In Section 3.7, I found that the nearest 2MRS redshift shell and the furthest were not compatible with uniform phase distributions, and so were non-Gaussian. This may be due to the large Local Void which dominates the nearest shell (Erdoğdu (b) *et al.* 2006), and to large scale structure such as Shapley or shot noise dominance in the furthest shell.

In addition, morphological types of 2MRS galaxies have been visually identified by John Huchra of the 2MRS team. In this Chapter I use the broad distinction between early (elliptical and lenticular) and late (spiral) types. I use this to identify morphological dependence on density, i.e. to investigate whether early and late type galaxies have a tendency to live in denser environments or in the field. If this is the case, then their clustering is different and so their biases should also be. I perform the redshift distortion analysis on separate galaxy morphological types to check if the bias results are the same for different morphological types.

The 2MRS data used in the analysis in this Chapter is described in detail in Section 3.2 in the previous chapter. In Section 4.2, I define the fiducial model and priors used in this analysis. In Section 4.3, I present constraints on the matter density Ω_m and the galaxy bias b_g for the projected (real space) and radially weighted (redshift space) ACFs. In Section 4.4, I compare these results with other work on 2MASS and 2MRS. In Section 4.5, I investigate the errors in the estimation of the selection function from the redshift distribution and how these propagate into the cosmological parameter estimation. In Section 4.6, I investigate properties of different morphological types in the 2MRS data set, notably their environmental dependence and their relative bias. In Section 4.7, I discuss the implications of our results for biasing in the local Universe.

4.2 Choice of Fiducial Model and Priors

In this analysis, I focus on how to constrain the matter density Ω_m in the local Universe and the linear scale independent galaxy bias b_g. As I have discussed in Section 3.6, I assume, by the choice of likelihood, that the underlying matter field traced by the galaxies in 2MRS is a homogeneous and statistically isotropic Gaussian random field. I discuss a specific way to test this in Section 3.7. This method consists in quantifying the compatibility of the harmonic phase distribution with a uniform distribution, and was proposed by Chiang, Naselsky & Coles (2006) with regards to the CMB. I also assume the galaxy distribution in the 2MRS is well described by the linear regime, and that non-linear redshift distortions such as Finger of God effects are negligible.

This analysis also requires assumptions about other cosmological parameters, which

I fix prior to constraining Ω_m and b_g. Based on inflation, I assume the Universe is flat and therefore that $\Omega_\Lambda = 1 - \Omega_m$. I also assume the spectral index to have the Harrisson-Zeldovich value of $n = 1$ (although some inflationary models and the recent WMAP3 data suggest that $n \simeq 0.95$). Based on the HST key project, I take for the Hubble parameter $h = 0.7$. For the baryon density, I assume $\Omega_b = 0.04$.

The normalization of the power spectrum, parameterised by σ_8 (see Section 1.6.1), is still highly uncertain, with reported values in the range $\sigma_8 \simeq 0.75$ (e.g. WMAP3 results) to $\sigma_8 \simeq 1.0$ (Massey *et al.* 2005). I fix $\sigma_8 = 0.75$ and solve for the linear, scale independent and redshift invariant bias b_g. I note that in linear theory it is product $b_g\sigma_8$ that is constrained, I check this using simulations in Section 4.3, so it is easy to scale the results for any preferred value of σ_8.

In principle, one should marginalise over the prior associated with each parameter, which will widen the constraints obtained. However, this analysis aims to:

1. find out if a redshift space analysis can return constraints on Ω_m compatible with the standard cosmological model

2. for a fixed cosmological model, find what the associated near infrared galaxy bias b_g is.

4.3 Constraints on Ω_m and b_g

In this Section I show constraints on Ω_m and b_g which I obtain from considering the radially weighted (or redshift space) ACFs. The redshift space ACF depends on these cosmological parameters through the matter power spectrum $P(k)$ and the redshift distortion, which is modulated by the distortion parameter $\beta = \Omega_m^{0.6}/b_g$. The matter density Ω_m will affect the shape of the matter power spectrum and the amplitude of the distortion. The galaxy bias b_g will affect the overall normalization as well as the amplitude of the redshift distortion.

Because the bias modulates the overall normalization, it is degenerate with σ_8, as both act as normalizations in the calculation of the ACF. In order to quantify this degeneracy, I constrain Ω_m and b_g using the real space ACF for two values of σ_8. For $\sigma_8 = 0.75$, the best

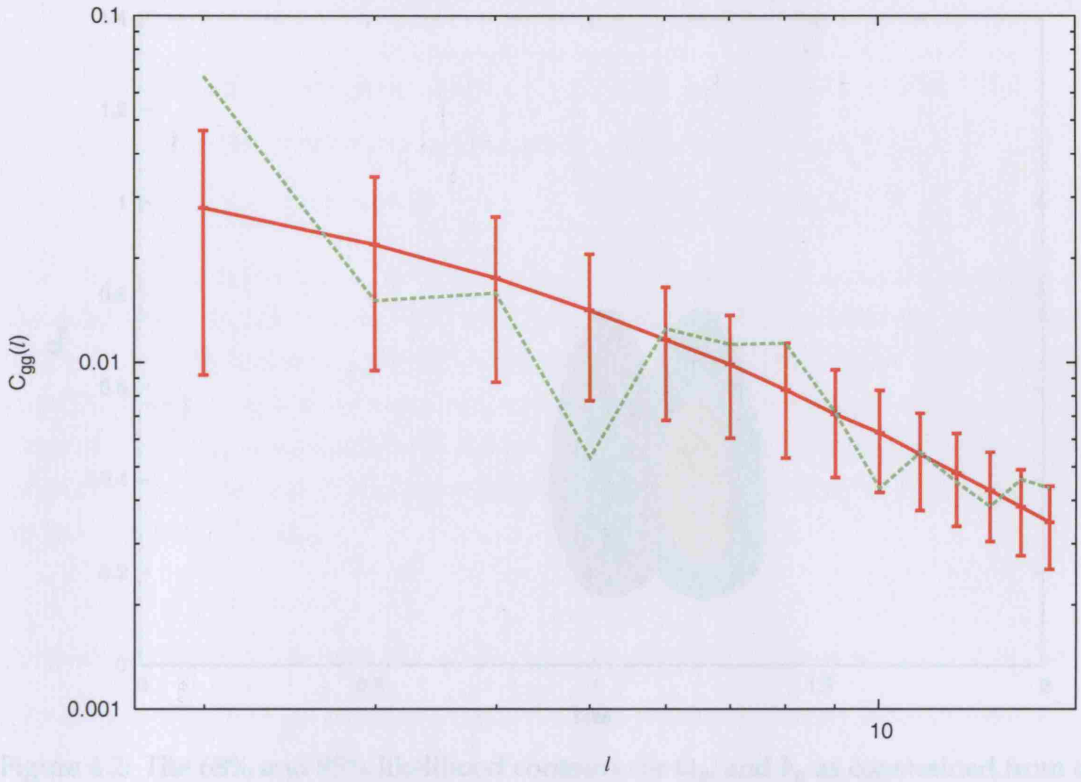

Figure 4.1: The 2MRS projected galaxy overdensity auto-correlation function (green line). Overlaid is the best fit linear theory prediction (red line) with Gaussian error bars and shot noise.

fit value of the bias is $b = 1.22^{+0.09}_{-0.08}$ and for $\sigma_8 = 0.90$, the best fit value is $b = 1.02 \pm 0.07$. I find the best fit value for $\Omega_m = 0.37^{+0.22}_{-0.15}$ is independent of the value of σ_8. This confirms that in linear theory, what is actually constrained is the product $\sigma_8 b_g$. The real space ACF, which I obtain by setting $f(r) = 1$, is plotted in Figure 4.1 with the best fit linear theory prediction. The 68% and 95% likelihood contours for Ω_m and b_g for the projected case, are plotted in Figure 4.2 with $\sigma_8 = 0.75$ corresponding to the right-hand contours and $\sigma_8 = 0.90$ corresponding to the left-hand contours.

In Section 3.5.2, I described the four Gaussian weighting functions which I use to estimate the radially weighted ACFs. By including a radial weighting it is possible to measure the redshift space ACF instead of the real space ACF.

The redshift space ACF for the four Gaussian radial shells considered in this analysis are plotted in Figure 3.6 in Chapter 3. I constrain Ω_m and b_g using all fours shells simultaneously, by calculating the covariance between each shell. I also consider constraints

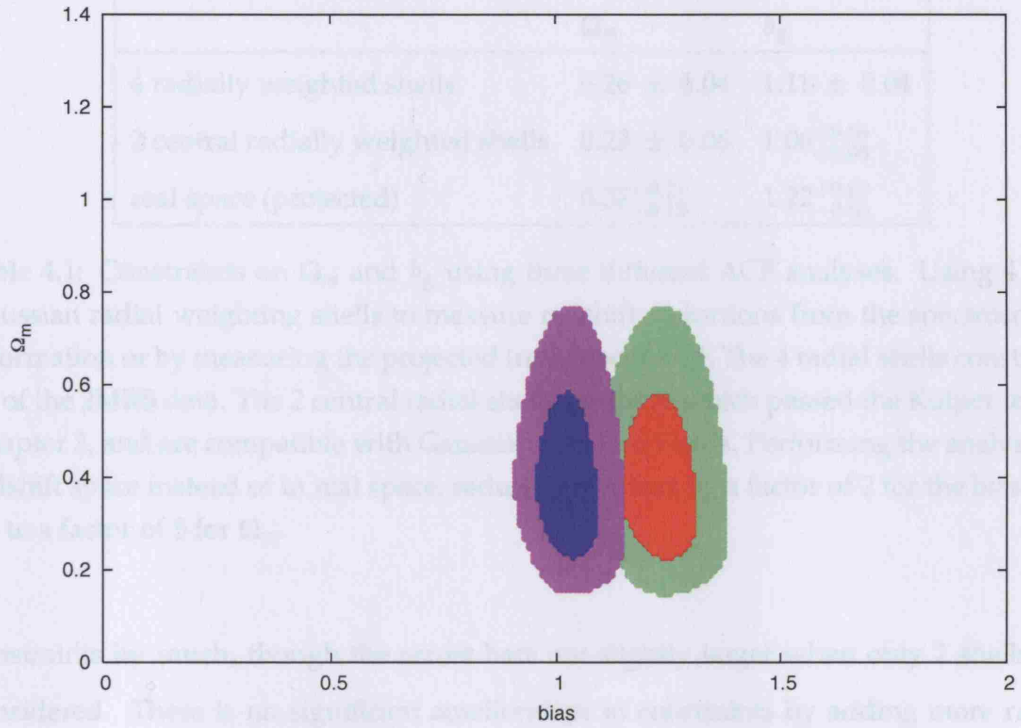

Figure 4.2: The 68% and 95% likelihood contours for Ω_m and b_g as constrained from the projected (real space) ACF of the 2MASS Redshift Survey. The left contours are for a high value of σ_8 ($\sigma_8 = 0.90$) and the right hand contours for a lower value ($\sigma_8 = 0.75$), showing that in linear theory it is the product $\sigma_8 b_g$ which is constrained; the constraint on Ω_m is unaffected by a change in the input values of σ_8.

from the two central shells only; I justify this in Section 3.7.1. In Chapter 3 I tested the phase distribution of each redshift shell using the Kuiper test and found the nearest and furthest shells were not compatible with a GRF phase distribution. The two central shells were compatible with a GRF, though they may present non-Gaussianities not detected by the Kuiper test.

I perform the redshift space analysis with (4 shells) and without (2 shells only) those which present non-Gaussianities, as well as performing the analysis in real space (projected). The results for the three analyses are reported in Table 4.1 as well as in Figure 4.3 where I have fixed $\sigma_8 = 0.75$.

Including available spectroscopic information through redshift distortions reduces error bars on b_g by a factor of 2 and on Ω_m by up to a factor of 5, when comparing with the real space analysis. Removing the non-Gaussian shells does not change the best fit

	Ω_m	b_g
4 radially weighted shells	0.26 ± 0.04	1.11 ± 0.04
2 central radially weighted shells	0.23 ± 0.06	$1.06^{+0.06}_{-0.05}$
real space (projected)	$0.37^{+0.21}_{-0.15}$	$1.22^{+0.09}_{-0.08}$

Table 4.1: Constraints on Ω_m and b_g using three different ACF analyses. Using 4 or 2 Gaussian radial weighting shells to measure redshift distortions from the spectroscopic information or by measuring the projected (real space) ACF. The 4 radial shells constitute all of the 2MRS data. The 2 central radial shells are those which passed the Kuiper test in Chapter 3, and are compatible with Gaussian Random Fields. Performing the analysis in redshift space instead of in real space, reduces error bars by a factor of 2 for the bias and up to a factor of 5 for Ω_m.

constraints by much, though the errors bars are slightly larger when only 2 shells are considered. There is no significant amelioration in constraints by adding more radial shells. Considering four shells instead of 2 only improves errors bars by 0.02 for Ω_m and 0.01 for b_g.

In the redshift space analysis, removing the non-Gaussian shells, the best fit value of the distortion parameter is $\beta = 0.39 \pm 0.08$.

4.4 Comparison with other results from linear theory

These results are in complete agreement with other linear theory analysis of 2MRS data. Erdoğdu (a) *et al.* (2006) estimated the acceleration of the Local Group using both a flux and number weighted Large Scale Structure (LSS) dipole in linear theory. Comparison with known value of the CMB dipole yields a constraint on $\beta = \frac{\Omega_m^{0.6}}{b_g} \simeq 0.40 \pm 0.09$ which is the same constraint returned by our analysis.

Other linear theory analyses have been done on all of 2MASS. These are harder to compare with 2MRS analysis as they do not trace galaxy populations with the same magnitude limit or redshift distribution, but they both trace the NIR population, so I quote recent constraints on Ω_m and the galaxy bias from 2MASS for comparison. Maller *et al.* (2003) also analysed the LSS dipole, this time from over 700,000 2MASS galaxies with $K < 13.57$, replacing galaxies with $|b| > 7°$ along the galactic plane and $|b| > 12°$ around

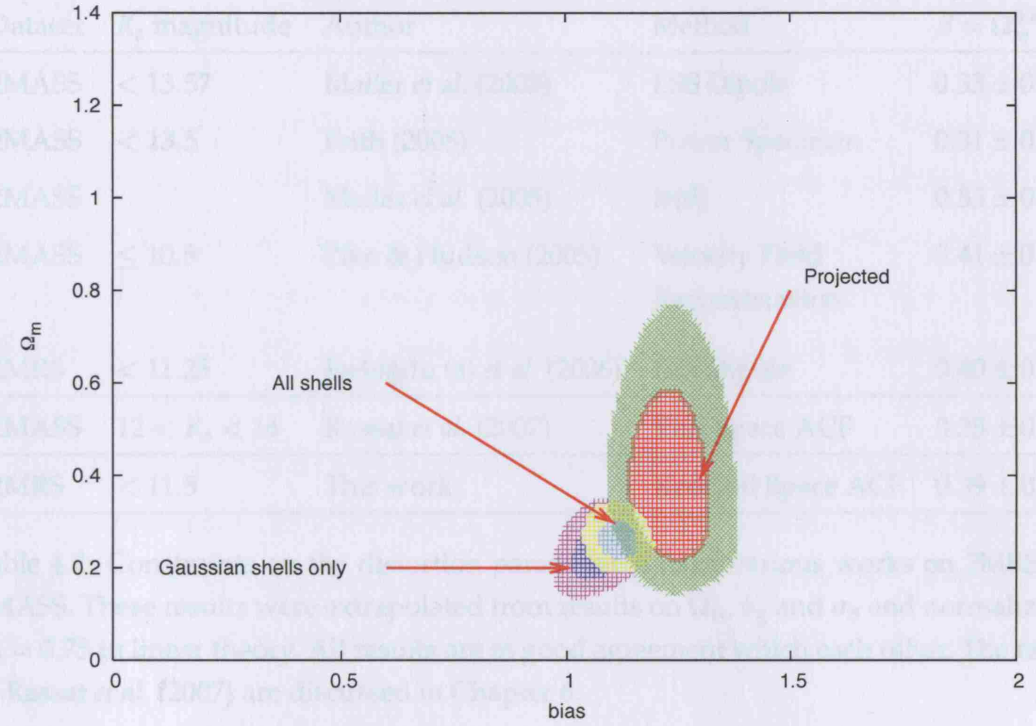

Figure 4.3: The 68% and 95% likelihood contours for Ω_m and b_g for three different analyses, one of which considers only the real space projected ACF and the other two include distortions in redshift space. Performing the analysis in redshift space as opposed to real space, reduces error bars by a factor of 2 for the bias and up to a factor of 5 for Ω_m. *All Shells* corresponds to four redshift shells, described by Gaussian redshift distributions, but not necessarily compatible with a Gaussian Random Field (GRF). In Chapter 3, I found that the nearest and furthest of these redshift shells were not compatible with a GRF and so remove them from the analysis names *Gaussian shells only*. This last analysis is consistent with using a Gaussian likelihood function. Best fit values are reported in Table 4.1.

the galactic bulge ($360 > l > 330°$ and $0 < l < 30°$) with mock galaxies. They found that for $\Omega_m = 0.27 \pm 0.04$, $b_g = 1.37 \pm 0.30$. Maller *et al.* (2005) used the angular power spectrum $w(\theta)$ to measure the bias and found $b_g\sigma_8 = 1.1 \pm 0.20$. For a lower value of $\sigma_8 = 0.75$ this gives $b_g\left(\frac{\sigma_8}{0.75}\right) = 1.47 \pm 0.20$ for $\Omega_m h = 0.13 \pm 0.07$. Frith (2005) measured the linear bias for over 500,000 2MASS galaxies with $K_s < 13.5$ and $|b| > 20°$ and found that for $\Omega_m = 0.30$, $(\sigma_8 b_g)^2 = 1.36 \pm 0.10$ (or $\sigma_8 b_g = 1.17 \pm 0.05$). They assumed a delta prior on the matter density Ω_m, resulting in an overall small error on β. Finally in Rassat *et al.* (2007), I analysed the galaxy ACF for 2MASS galaxies with $12 < K_s < 14$ and found that for $\Omega_m = 0.30$, $b_g = 1.40 \pm 0.03$. This was done for all of the 2MASS eXtended Source

Dataset	K_s magnitude	Author	Method	$\beta = \Omega_m^{0.6}/b_g$
2MASS	< 13.57	Maller *et al.* (2003)	LSS Dipole	0.33 ± 0.10
2MASS	< 13.5	Frith (2005)	Power Spectrum	0.31 ± 0.01 *
2MASS		Maller *et al.* (2005)	$w(\theta)$	0.33 ± 0.11
2MASS	≤ 10.5	Pike & Hudson (2005)	Velocity Field Reconstruction	0.41 ± 0.04
2MRS	< 11.25	Erdoğdu (a) *et al.* (2006)	LSS Dipole	0.40 ± 0.09
2MASS	$12 < K_s < 14$	Rassat *et al.* (2007)	Real Space ACF	0.35 ± 0.01 *
2MRS	< 11.5	This work	Redshift Space ACF	0.39 ± 0.08

Table 4.2: Constraints on the distortion parameter β from various works on 2MRS and 2MASS. These results were extrapolated from results on Ω_m, b_g and σ_8 and normalized to $\sigma_8 = 0.75$ in linear theory. All results are in good agreement which each other. The results of Rassat *et al.* (2007) are discussed in Chapter 6.

* These results do not assume an error on Ω_m.

Catalogue (XSC) in real space and with a likelihood that assumed the $C(\ell)$s are Gaussian. I had also fixed a delta function prior on the value of the matter density to $\Omega_m = 0.30$ so that the errors on β from this analysis are small compared to other results which varied or marginalised over Ω_m.

I report all these results in Table 4.2. To ease comparison, I quote the equivalent value of the distortion parameter $\beta = \Omega_m^{0.6}/b$, where I have normalized the product $b_g\sigma_8$ for $\sigma_8 = 0.75$. All values are in agreement within the quoted 68% error bars. Two authors return low error bars, (including our work described in Chapter 4), as they only assume errors in the bias, and have a delta function prior on Ω_m.

4.5 Propagation of Errors from dN/dz(z)

Here I consider how errors on the selection function estimation may affect parameter constraints. I consider errors of the selection function which are due to:

1. formal (statistical) errors on the parameterisations of $\frac{dN}{dz}(z)$
2. redshift distortions/LSS which will affect the statistical significance of $\phi(r)$.

First I investigate the propagation of formal errors, i.e. errors on the parameters in Equation 3.1 which quantify the redshift distribution. I vary each parameter to within $\pm 1\sigma$ of its best fit values and have found which combination affects the $\frac{dN}{dz}(z)$ distribution the most. Figure 4.4 illustrates how these formal errors affect the estimation of the redshift distribution. I propagate this uncertainty into the cosmological parameter estimation and find that results on the best fit bias is only affected at the 10% level with $b_g \in [1.06; 1.18]$, whereas the best fit values for the matter density fluctuate by over 40% with $\Omega_m \in [0.12 - 0.41]$.

Using the 'raw' measured $\frac{dN}{dz}(z)$ might bypass this effect which is due to its parameterisation. However the aim of measuring $\frac{dN}{dz}(z)$ is to measure a statistically representative gauge of the galaxy radial distribution of the universe by inferring the selection function from it. The 'raw' redshift distribution should be representative of an underlying distribution.

I check how representative our measure of $\frac{dN}{dz}(z)$ is. To do this, I consider errors in the estimation of the selection function which come from the finite nature of the 2MRS survey. Because the survey is finite, it cannot be a true statistical representation of the Universe. A way to look at this is to consider only part of the 2MRS sample: for example, to consider only data in the northern or southern hemisphere. If the selection functions estimated from each data set separately are very different, then how representative are they of the underlying 'true' selection function? To test this, I compare the redshift distribution of 2MRS galaxy sample estimated from the northern and southern galactic hemisphere (Figure 4.5). I compare these to the estimation of the selection function from the ensemble of the survey (Equation 3.1 with best fit parameters described in Section 3.2). I plot this in Figure 4.5 and find that errors induced from this will more or less encompassed by formal errors of the $\phi(r)$ parameterisation.

4.6 Galaxy Bias for Separate Morphological Populations

Almost all 2MRS galaxies with $|b| > 10^\circ$ have been visually classified by morphological type. In this Section I investigate if there exists morphological trends in the 2MRS large scale structure by separating 2MRS galaxies into two distinct types: elliptical and lenticu-

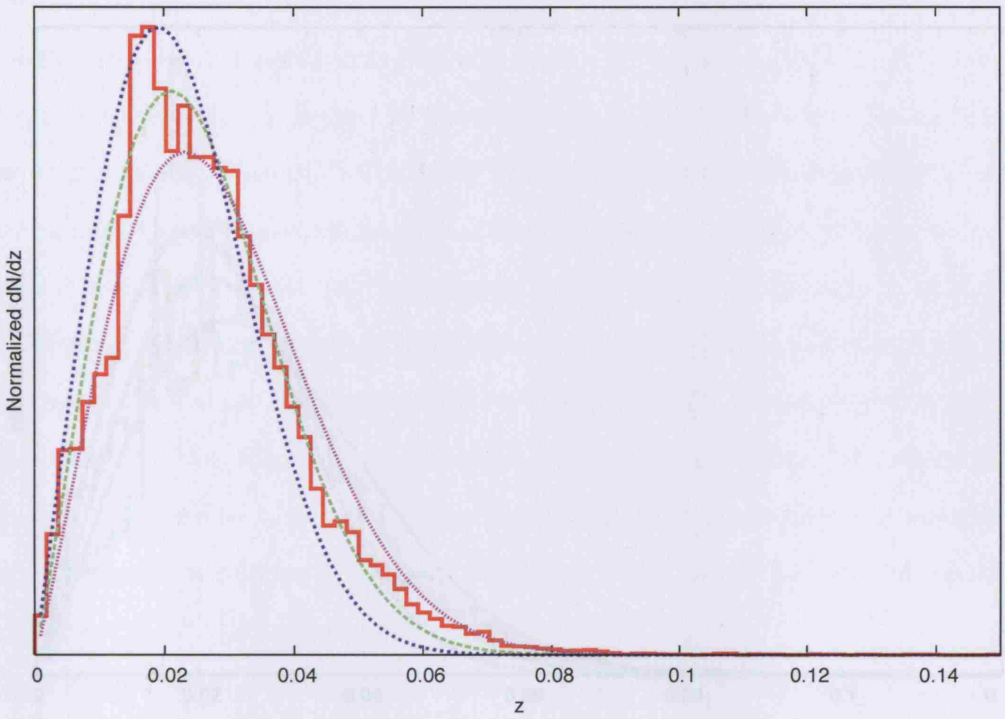

Figure 4.4: The effect of formal 68%CL errors on the parameterisation of the redshift distribution using Equation 3.1. The green line is the fit using the best fit parameters, the blue dotted line a combination of parameters within 1σ errors that decreases the mean redshift the most and the pink line the combination of parameters that increases the mean redshift the most. The red histogram is the $\frac{dN}{dz}(z)$ estimated from all of 2MRS. These propagate into the cosmological parameter estimation and vary best fit bias estimates by $\sim 10\%$ and Ω_m estimates by $\sim 40\%$.

lar (early type) galaxies and spiral (late type) galaxies. These galaxies have been visually classified by John Huchra of the 2MRS team. I quantify the environmental dependence of morphological type on density. Early type galaxies tend to lie in denser regions than late types, suggesting their bias to dark matter is different. In Section 4.6.2 I perform the spherical harmonic analysis for both early and late galaxy types.

4.6.1 Morphological Types in 2MRS

Dressler (1980) first showed that there existed a relationship between galaxy density and galaxy morphological type. He found that increasing density corresponded to an increase in early type population and a decrease in late type population. Because of this environmental dependence, the galaxy bias is expected to be different for different morphological

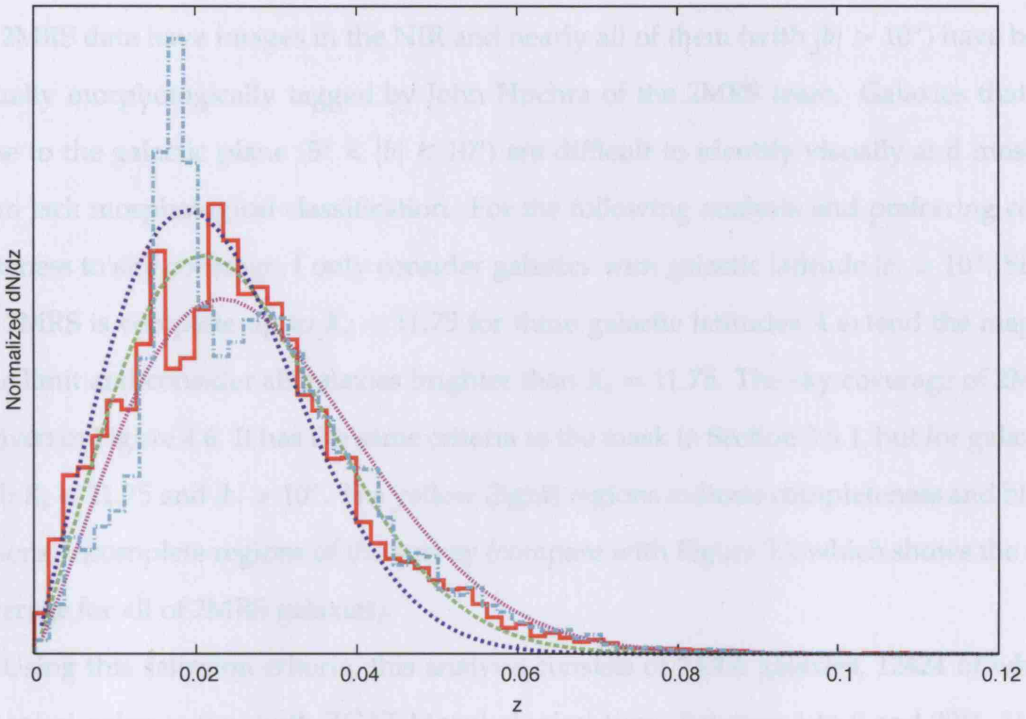

Figure 4.5: The effect of clustering in the local Universe on $\frac{dN}{dz}(z)$. The blue histogram is for galaxies in the southern hemisphere and the red histogram for galaxies in the northern hemisphere. The lines are the same as in Figure 4.4.

Figure 4.6: The Mollweide projection in Galactic Coordinates of the sky coverage of the 2MRS, for the analysis done for separate morphological types (compare with Figure 3.2). Yellow (light) regions indicate completeness and black regions incomplete regions of the survey.

types.

2MRS data have images in the NIR and nearly all of them (with $|b| > 10°$) have been visually morphologically tagged by John Huchra of the 2MRS team. Galaxies that lie close to the galactic plane ($5° < |b| < 10°$) are difficult to identify visually and most of them lack morphological classification. For the following analysis and preferring completeness to sky coverage, I only consider galaxies with galactic latitude $|b| > 10°$. Since the 2MRS is complete up to $K_s < 11.75$ for these galactic latitudes, I extend the magnitude limit and consider all galaxies brighter than $K_s = 11.75$. The sky coverage of 2MRS is given in Figure 4.6. It has the same criteria as the mask in Section 3.5.1, but for galaxies with $K_s < 11.75$ and $|b| > 10°$. The yellow (light) regions indicate completeness and black regions, incomplete regions of the survey (compare with Figure 3.2 which shows the sky coverage for all of 2MRS galaxies).

Using this selection criteria, this analysis consists of 24306 galaxies, 12424 of which are spiral galaxies (i.e. with ZCAT Morphological types between 1 to 9 and 20)*, 11490 are elliptical or lenticular galaxies (i.e. with ZCAT Morphological types between -7 to 0), less than 400 of these are irregular, peculiar, unclassifiable galaxies or QSOs.

The 2MRS catalogue contains only slightly more late (51%) than early (49%) type galaxies. This high proportion of early type galaxies is characteristic of the NIR selection.

Another way to determine galaxy morphological type is by analying the galaxy spectra. Cole *et al.* (2001) and Madgwick *et al.* (2003) determined morphological types in a subset of the 2MASS XSC, by analysing the spectra using Principal Component Analysis (PCA). They considered the part of the 2MASS XSC which overlapped with the (blue-band selected) 2dF Galaxy Survey (2dFGS). This joint sample (hereafter XSC-2dF) provided an infrared catalogue with over 17,000 galaxy spectra. A PCA analysis estimated that 62% of the XSC-2dF sample was composed of early types, and 38% of late types.

The fractional population of XSC-2dF is difficult to compare with the fractional population in the 2MRS for several reasons. The first is that 2MRS is the very low redshift part of the 2MASS XSC. The XSC-2dF also discards part of the 2MASS XSC which is not targeted in the 2dFGS. It would be interesting to analyse the spectra of 2MRS galaxies

*http://www.cfa.harvard.edu/ huchra/zcat/zcom.htm

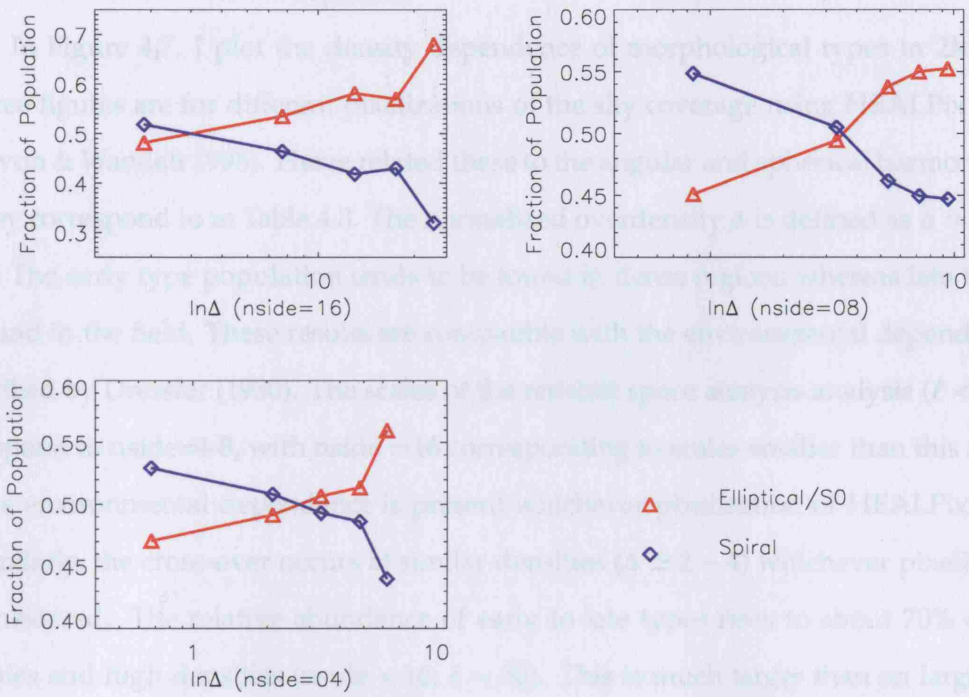

Figure 4.7: The fraction of galaxies as a function of density $\ln\Delta = \ln(1+\delta)$, for early and late type galaxies. This reflects the environmental dependence of morphological types in the 2MRS galaxy distribution, for three different HEALPix pixelizations of the data. Elliptical and lenticular (or early type, red triangle) galaxies are found in denser regions, where spiral galaxies (or late type, blue square) tend to be in the field. The angular scales corresponding to each pixelization scheme is shown in Table 4.3. The trend is the same whichever pixelization is used.

nside	Number of pixels	Angular size of pixels [deg^2]	Average scale (ℓ)
4	192	208	12
8	768	52	24.5
16	3072	13	50

Table 4.3: Approximate conversions between HEALPix parameter nside, the pixelization, the angular size of each pixel and the corresponding spherical harmonic scale, for nside = 4, 8 and 16. This is useful for understanding the scales considered in Figure 4.7.

and see if the fractional populations obtained from visual classifications are the same as those determined from the spectra.

In Figure 4.7, I plot the density dependence of morphological types in 2MRS. The three figures are for different pixelizations of the sky coverage using HEALPix (Gorski, Hivon & Wandelt 1998). I have related these to the angular and spherical harmonic scales they correspond to in Table 4.3. The normalized overdensity Δ is defined as $\Delta = 1 + \delta$.

The early type population tends to be found in dense regions whereas late types are found in the field. These results are compatible with the environmental dependence described by Dressler (1980). The scales of the redshift space analysis analysis ($\ell < 30$) correspond to nside=4-8, with nside =16 corresponding to scales smaller than this analysis. The environmental dependence is present whichever pixelization of HEALPix is used. Similarly, the cross-over occurs at similar densities ($\Delta \simeq 2 - 4$) whichever pixelization is considered. The relative abundance of early to late types rises to about 70% on small scales and high densities (nside = 16; $\ell \sim 50$). This is much larger than on larger scales (nside = 4, 8; $\ell \sim 12,\ 24.5$), where the relative abundance is never greater than 57%. This suggests the morphological dependence changes with scale, but seems constant within the scale range of this analysis.

4.6.2 Galaxy Bias per Morphological Type in the 2MRS

I fit the redshift distribution for the early and late type galaxies using the parametric expression given by Equation 3.1. I find that for early type galaxies $\gamma = 1.20^{+0.10}_{-0.17}$, $\alpha = 2.20^{+0.10}_{-0.17}$, $z_c = 0.029 \pm 0.06$ and for late type galaxies $\gamma = 1.17^{+0.10}_{-0.20}$, $\alpha = 2.17^{+0.10}_{-0.20}$, $z_c = 0.024^{+0.005}_{-0.004}$. For the same magnitude limit of $K_s = 11.75$, the late type galaxies have a slightly shallower distribution (mean redshift $z = 0.022$) than early type galaxies (mean redshift $z = 0.027$).

In Figure 4.8, I show the 68% and 95% likelihood contour levels for the matter density Ω_m and b_g for early and late types. The best fit values are quoted in Table 4.4. Early type galaxies prefer a higher value of Ω_m as well as a higher value for the galaxy bias ($b_g = 1.42^{+0.08}_{-0.06}$, $\Omega_m = 0.43^{+0.11}_{-0.09}$) than late types do. This is what is expected if early types reside in higher density (i.e. more clustered) regions. For the late type galaxies, the best fit cosmological parameters are $b_g = 1.08^{+0.04}_{-0.06}$, $\Omega_m = 0.33^{+0.09}_{-0.08}$.

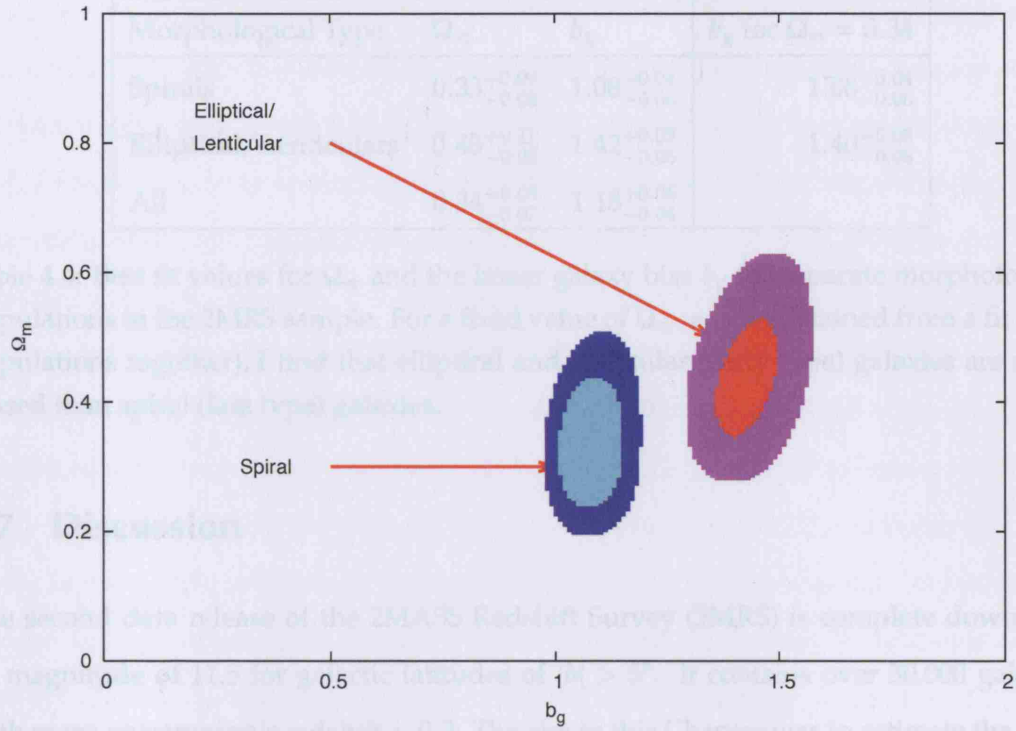

Figure 4.8: The 68% and 95% likelihood contours for Ω_m and the linear galaxy bias b_g for separate morphological populations in the 2MRS sample. The left contours are for late type galaxies and the right for early type galaxies. The best fit values of the parameters are reported in Table 4.4.

When considering all galaxies together (but still using the mask shown in Figure 4.6), the best fit values are $\Omega_m = 0.34^{+0.08}_{-0.07}$ and $b_g = 1.18^{+0.06}_{-0.04}$. These best fit values for Ω_m are different than those quoted in Table 4.1, where a different sky mask was used ($|b| > 5°$ instead of $|b| > 10°$). This difference may be due to effects from the sky cut, or perhaps to incompleteness along the galactic plane around $5° < |b| < 10°$.

If I fix the value of Ω_m to the best fit value of the entire sample, i.e. $\Omega_m = 0.34^{+0.08}_{-0.07}$, then the relative bias is $b_g^{\rm early}/b_g^{\rm late} \simeq 1.30 \pm 0.11$. This is quite similar to results from Collister & Lahav (2005) who tested the halo model using galaxies from the 2dFGS. They derived the halo occupation using the 2dF Percolation-Inferred Galaxy Group (2PIGG) catalogue. They found a relative bias of $b_g^{\rm early}/b_g^{\rm late} \simeq 1.4$. Madgwick *et al.* (2003) also analysed 2dFGS galaxies in redshift space and found a relative bias $b_g^{\rm early}/b_g^{\rm late} \simeq 1$. Pike & Hudson (2005) used morphological types of 2MASS galaxies and found a relative bias of $b_{\rm early}/b_{\rm late} = 1.60$.

Morphological Type	Ω_m	b_g	b_g for $\Omega_m = 0.34$
Spirals	$0.33^{+0.09}_{-0.08}$	$1.08^{+0.04}_{-0.06}$	$1.08^{+0.04}_{-0.06}$
Elliptical/Lenticulars	$0.43^{+0.11}_{-0.09}$	$1.42^{+0.08}_{-0.06}$	$1.40^{+0.08}_{-0.06}$
All	$0.34^{+0.08}_{-0.07}$	$1.18^{+0.06}_{-0.04}$	

Table 4.4: Best fit values for Ω_m and the linear galaxy bias b_g for separate morphological populations in the 2MRS sample. For a fixed value of $\Omega_m = 0.34$ (obtained from a fit to all populations together), I find that elliptical and lenticular (early type) galaxies are more biased than spiral (late type) galaxies.

4.7 Discussion

The second data release of the 2MASS Redshift Survey (2MRS) is complete down to a K_s magnitude of 11.5 for galactic latitudes of $|b| > 5°$. It contains over 30,000 galaxies with mean spectroscopic redshift ~ 0.3. The aim in this Chapter was to estimate the dark matter density Ω_m and the linear galaxy bias b_g in the local Universe.

I constrain these cosmological parameters using the real and redshift space Auto Correlation Function (ACF) of the 2MRS. I use a maximum likelihood method to estimate the matter density Ω_m and the scale independent, linear galaxy bias b_g. The analysis is done in spherical harmonic space, for which there exists an exact prescription of the redshift space distortions (Scharf 1993, Fisher, Scharf & Lahav 1994*b*, Heavens & Taylor 1995).

I fit the 2MRS ACF using a fiducial model inspired by the ΛCDM concordance cosmology. Based on inflation, I assume a flat Universe so that $\Omega_\Lambda = 1 - \Omega_m$. I assume the spectral index to have the Harrison-Zeldovich value of n=1. Based on the HST project I take the Hubble parameter to be $h = 0.7$. For the baryon density I assume $\Omega_b = 0.04$. I fix the normalization of the power spectrum to $\sigma_8 = 0.75$ and note that in linear theory I constrain the product $\sigma_8 b_g$ so that our results can be scaled to the appropriate value of σ_8 if needed.

Performing the analysis in redshift space - as opposed to real space, reduces errors on Ω_m by a factor of 5 and on b_g by a factor of 2. The unmarginalised best fit constraints are $\Omega_m = 0.26 \pm 0.04$ and $b_g = 1.11 \pm 0.04$.

In Chapter 3, I estimated the galaxy auto-correlation function using direct summa-

tion over the angular position of galaxies and corrected for partial sky coverage using pseudo-C_ℓs. In order to estimate Ω_m and b_g I use a Gaussian likelihood function which fundamentally assumes the galaxy density field behaves as a Gaussian Random Field (GRF). I tested this assumption in Chapter 3 by investigating if the phases of the $a_{\ell m}$'s are compatible with a random uniform distribution (as they should be in the case of a GRF). Because the phases are cyclic, I use the Kuiper test, which is a variant of the Kolmorov-Smirnov test used for the case of cyclic data (Chiang, Naselsky & Coles 2006).

I find that the lowest (centered on $z = 0.005$) and the highest (centered on $z = 0.056$) redshift bins are not compatible with a GRF. Erdoğdu (b) *et al.* (2006) reconstructed the linear density field of 2MRS using a Wiener filter (see Chapter 2) and confirmed that in the nearest shell, structure is dominated by the Local Void which may explain these results. In the furthest shell, the 2MRS begins to probe the Shapley Supercluster which may account for the non-Gaussianity, or dominance of shot noise. I note that the shells which 'pass' the Kuiper statistic may be non-Gaussian in ways not detected by the test.

For consistency, I remove these non-Gaussian redshift shells from the analysis. I find that performing the analysis with or without them does not change the best fit values by much, though the error bars increase. Considering only the central redshift shells, the best fit values are $\Omega_m = 0.23 \pm 0.06$ and $b_g = 1.06^{+0.06}_{-0.05}$. This low value of the matter density is agrees with recent results from the 2 degree Field Galaxy Survey (2dFGS) which constrained $0.19 < \Omega_m < 0.27$ at the 95% CL. This is equivalent to a distortion parameter $\beta = 0.39 \pm 0.08$ and is consistent with other work using 2MRS data (Erdoğdu (a) *et al.* 2006), and 2MASS data (Frith 2005, Maller *et al.* 2003, Maller *et al.* 2005, Rassat *et al.* 2007).

In the projected case (i.e. discarding the spectroscopic information and calculating the real space ACF), I find the best fit values of $\Omega_m = 0.37^{+0.21}_{-0.15}$ and $b_g = 1.22^{+0.09}_{-0.08}$. By performing the analysis in redshift space, I decrease error bars by a factor of 2 for b_g and a factor of 5 for Ω_m, giving the constraints: $\Omega_m = 0.23 \pm 0.06$ and $b_g = 1.06^{+0.06}_{-0.05}$. The best fit values of 2MRS are equivalent to a distortion parameter of $\beta = 0.39 \pm 0.08$, which is compatible with results in recent literature.

As discussed in Section 3.4, the present analysis assumes Finger of God effects are negligible and that the galaxy distribution in the 2MRS is well described by the linear regime. Hamilton (1998) suggests that such non-linearities may exist even up to scales

of $\sim 20h^{-1}Mpc$, i.e. scales which are probed by the 2MRS survey. Such non-linear effects may induce non-Gaussianities which will increase error estimations on the power spectrum. Non-linear redshift distortions will also decrease power on non-linear scales, which will effect the estimation of both the bias and matter density, if the linear regime has been assumed. A comparison analysis with non-linear effects included would help identify such issues.

Finally, I investigate different morphological types in the 2MRS dataset. I make a broad distinction between early (elliptical and lenticular) and late (spiral) galaxies. The 2MRS catalogue contains only slightly more late (51%) than early (49%) type galaxies. This high proportion of early type galaxies is characteristic of the NIR selection. Cole *et al.* (2001) and Madgwick *et al.* (2003) determined morphological types in a subset of the 2MASS XSC, by analysing the spectra using Principal Component Analysis (PCA). Their analysis applied to about 17,000 galaxies with spectroscopic redshifts, which I call the XSC-2dF sample. A PCA analysis of the spectra of the joint XSC-2dF sample estimated that 62% of the XSC-2dF sample was composed of early types, and 38% of late types. Both these studies suggest NIR samples are dominated by early type galaxies. It is not clear why their fractional populations are different; this might be due to the different redshifts sampled or the fact that 2dF is a blue band survey.

It is well known that morphological types have a strong dependence on environmental density (Dressler 1980). I find that early types galaxies in the 2MRS are found preferentially in dense regions, and late types in the field. This dependence is present at least on scales ranging from $\ell = 12 - 50$ and implies 2MRS galaxies follow the same trend as galaxies studied by Dressler (1980) in clusters. For the largest scales considered ($\ell = 12 \rightarrow 24.5$), the relative abundance of early types reaches 57% in the densest regions, 47% in the field. On smaller scales ($\ell = 50$), the difference is much larger, and early types account for 70% of galaxies in dense regions. The environmental dependence seems to evolve with scale, but is stable on the scales considered in this analysis.

Finally, I constrain Ω_m and b_g for early and late type galaxies separately. The relative bias is $b_g\text{early}/b_g^{\text{late}} = 1.30 \pm 0.11$, i.e. I find that early type galaxies - which tend to be found in denser environment - are more biased than late type galaxies - which tend to be present in the field. These results reflect those of Collister & Lahav (2005) who tested the

halo model using galaxies from the 2dFGS. They found a relative bias of $b_g^{\rm early}/b_g^{\rm late} \simeq 1.4$. Madgwick *et al.* (2003) also analysed 2dFGS galaxies in redshift space and found a relative bias $b_g^{\rm early}/b_g^{\rm late} \simeq 1$. Pike & Hudson (2005) used morphological types of 2MASS galaxies and found a relative bias of $b_{\rm early}/b_{\rm late} = 1.60$. In future work, I intend to repeat this analysis in the framework of the halo model.

CHAPTER 5

THE LATE-TIME INTEGRATED SACHS-WOLFE (ISW) EFFECT

Summary

In this Chapter, I give an overview of the late-time Integrated Sachs-Wolfe effect (ISW) and how it can be detected through cross-correlating a tracer of Large Scale Structure (LSS) with the Cosmic Microwave Background (CMB). I overview the linear theory prediction in spherical harmonic space and discuss redshift evolution of the signal and its dependence on cosmological parameters. In a flat universe there is a strong degeneracy in the (w, Ω_Λ) plane. The ISW signal is also degenerate in the $(\Omega_k, \Omega_\Lambda)$ plane for a cosmological constant. I also discuss the cosmic magnification (or magnification bias) and how it affects the ISW signal measurement. For the redshift ranges considered in this Thesis ($z \in [0; 2]$), the contribution of the cosmic magnification to the LSS-CMB cross-correlation is negligible.

5.1 Introduction

As discussed in Section 1.7.1, the Integrated Sachs-Wolfe (ISW) effect is due to the decay of gravitational potential wells. It can be split into two parts: the *early* ISW and the *late*-time ISW effects. The early ISW effect occurs shortly after recombination during the radiation era (see Section 1.7.1). The late-time ISW effect occurs much later, and is due to

the gravitational potentials of Large Scale Structure (LSS) [and of Dark Energy if one is considering a fluid with perturbations].

The late-time ISW effect probes the rate of linear structure formation and provides powerful independent evidence of the presence of dark energy, curvature or deviations from General Relativity on large scales. To do so, it requires large scale probes of both temperature anisotropies in the Cosmic Microwave Background (CMB) and of inhomogeneities in the LSS. As the ISW signal is expected to be an achromatic signal, the cross-correlation can be measured across different CMB bands and for tracers of mass measured in different wavelengths, thus minimizing detections of a spurious signal. Deep surveys permit investigation of the evolution of the ISW signal and mean the cosmological model can be probed more precisely.

With the advent of large galaxy surveys and with conclusive CMB measurements returned by the Wilkinson Microwave Anisotropy Probe (WMAP), it is becoming an authoritative probe of the standard cosmological model which has the potential to help us understand the nature of dark energy or highlight inconsistencies in General Relativity.

In Section 5.2, I explain the origin of the late-time ISW effect. In Section 5.3, I present the linear theory prediction for cross-correlating LSS and the CMB in spherical harmonic space. In Section 5.4, I show how the ISW signal evolves with redshift. In Section 5.5, I present the ISW cosmological parameter dependence, notably on the galaxy bias b_g, the dark energy density Ω_Λ and equation of state parameter w, as well as the curvature of the Universe. In Section 5.6 I discuss cosmic magnification (or magnification bias) and how it affects the late-time ISW signal measurement. In Section 5.7 I briefly overview how the ISW effect can be used to probe the dark energy parameters.

5.2 The Origin of the late-time ISW Effect

The gravitational potential of the LSS will distort space-time so that a photon travelling through it will be subject to a gravitational blueshift on entry of the potential well, and redshift on exit. If the potential does not change during the travel time of the photon, then the net effect of the gravitational redshift will be null: the photon will emerge unaffected by LSS. This is always the case on linear scales in an Einstein-de Sitter Universe.

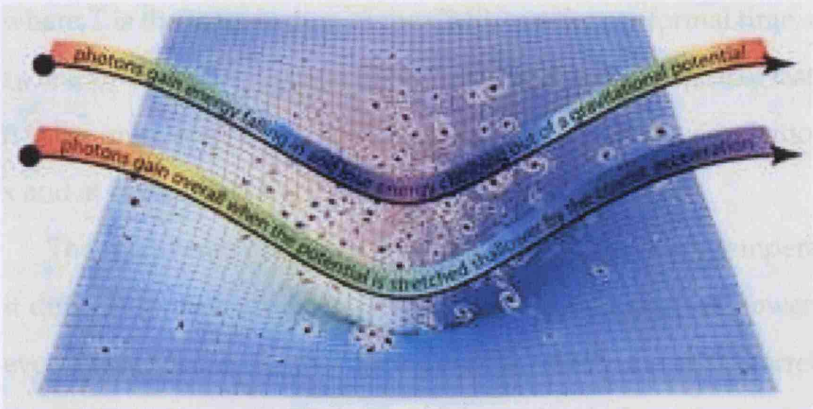

Figure 5.1: An illustration of the late-time Integrated Sachs-Wolfe (ISW) effect. Photons travel (from the left of the image) towards the observer (right) through LSS potential wells. The photons at the top of the image travel through large scale structure in an Einstein-de Sitter ($\Omega_m(z) = 1,\ \forall\ z$) universe and emerge from the LSS potential well with the same redshift as on entry. The photons at the bottom of the illustration travel through the LSS in an accelerating universe ($\Omega_\Lambda > 0$) in which large scale potential wells decay. In this scenario the photon exits bluer than on entry, because it has gained energy. This effect can be detected through cross-correlations of tracers of Large Scale Structure (LSS) with the Cosmic Microwave Background (CMB). *(© Institute of Physics and IOP Publishing Limited 2006.)*

If, however, these large scale potential wells vary with time, as they would in the presence of dark energy or curvature, the photon will emerge from the LSS gravitational field, either red- or blue-shifted depending on whether the potentials grow or decay respectively. This is illustrated in Figure 5.1. Photons travel (from the left of the image) towards the observer (right) through LSS potential wells. The photons at the top of the image travel through large scale structure in an Einstein-de Sitter universe and emerge from the LSS potential well with the same redshift as on entry. The photons at the bottom of the illustration travel through the LSS in an accelerating universe in which large scale potential wells decay and exit bluer than on entry.

For photons travelling from the surface of last scattering (CMB), the varying gravitational potential of LSS will create secondary temperature anisotropies which will add power to the temperature-temperature angular power spectrum C_{TT}. The power added on large scales is:

$$\left(\frac{\Delta T}{T}\right)_{ISW} = -2\int_{\eta_L}^{\eta_0} \Phi'((\eta_0 - \eta)\hat{\mathbf{n}}, \eta)d\eta\ , \tag{5.1}$$

where T is the temperature of the CMB, η is the conformal time, defined by $d\eta = \frac{dt}{a(t)}$ and η_0 and η_L are the conformal times today and at the surface of last scattering respectively; $\hat{\mathbf{n}}$ is the unit vector along the line of sight; $\Phi(\mathbf{x}, \eta)$ is the gravitational potential at position $\mathbf{x}$ and at conformal time η and $\Phi' \equiv \frac{\partial \Phi}{\partial \eta}$.

The relative amplitude of the ISW signal to primary temperature anisotropies make it difficult to measure from the temperature-temperature power spectrum alone. However, Crittenden & Turok (1996) proposed using the cross-correlation between LSS and the CMB to detect the ISW effect independently from the intrinsic CMB fluctuations. A significant decay in the gravitational potentials will produce large scale hot spots in the CMB. The gravitational potentials will tend to host an overdensity of galaxies, so a positive correlation between the CMB and the galaxy distribution is expected.

This positive correlation is also expected in open universes (Kamionkowski 1996; Kinkhabwala & Kamionkowski 1999), whereas a negative correlation will occur in closed universes where the gravitational potentials of LSS grow. The Sunyaev-Zel'dovich effect also produces a negative correlation, but this is expected on smaller scales ($\ell > 20$ for $z \approx 0.07$, see Afshordi *et al.* 2004).

In the currently favoured cosmological model, it is believed that the Universe has recently ($z < 1$) become dominated by dark energy, and since the ISW effect depends directly on the growth of structure, this makes the ISW effect an evident probe of the cosmological model. Alternative models of gravity can predict ISW signatures (Carroll *et al.* 2005, Song, Sawicki & Hu 2006), but these will also affect distance measurements (e.g., supernovæ). Measuring the ISW effect can therefore help break the degeneracy. I discuss this in more detail in Section 7.7

5.3 Cross-Correlation of Galaxy and Temperature Anisotropy Fields

In this Section I give an overview of current claimed detections (Section 5.3.1) of the ISW signal; these are also summarized in Table 5.1. I discuss some issues regarding these claimed detections in Section 5.3.2. In Section 5.3.3 I present the formalism for detecting the ISW through cross-correlation of the CMB and LSS by using a spherical harmonic decomposition of the temperature anisotropy and density fields.

5.3.1 Current Claimed ISW Detections

The first cross-correlations between the Cosmic Microwave Background Explorer (COBE) CMB map and tracers of LSS (hard X-ray background and radio sources) did not reveal any significant detections (Boughn & Crittenden 2002, 2003). However, there have since been a number of reported detections of late-time ISW from cross-correlating the first-year WMAP data (WMAP1) with: radio sources (Nolta *et al.* 2004; Boughn & Crittenden 2004, 2005); the hard X-ray background (Boughn & Crittenden 2004, 2005); the Sloan Digital Sky Survey (SDSS) (Fosalba, Gaztañaga & Castander 2003, Padmanabhan *et al.* 2005); the 2 Micron All Sky Survey (2MASS) (Afshordi *et al.* 2004); the APM Galaxy Survey (Fosalba & Gaztañaga 2004). Gaztañaga, Manera & Multamaki (2006) used a combination of the above data sets, which cover all LSS wavelengths and a redshift range $z \in [0; 1]$.

Recently, the third-year WMAP data (WMAP3) was correlated by Cabre *et al.* (2006) with the fourth SDSS data release (DR4), and they detected a significant positive cross-correlation, while Giannantonio *et al.* (2006) cross-correlated WMAP3 with high redshift SDSS quasars and found a 2σ detection. In Rassat *et al.* (2007), we cross-correlated the 2MASS galaxy survey with WMAP3 and found a 2σ detection. I describe the results from Rassat *et al.* (2007) in Chapter 6. The above cross-correlations were all performed in angular or spherical harmonic space. McEwen *et al.* (2006) used a directional spherical wavelet analysis and found a positive detection at the 3.9σ level. These claimed detections are summarized in Table 5.1. Below I discuss existing issues in the claimed detections.

5.3.2 Discussion on Current Claimed ISW Detections

In this Section I discuss two main issues regarding the claimed ISW detections. The first relates to the interpretation of the ISW signal and to the claim that they are independent detections of dark energy. The second to the fact that several studies use the ISW effect to constrain Ω_Λ, they report best fit values of the dark energy density which are higher than that of concordance cosmology. I discuss how this may be an even bigger problem when considering the galaxy bias. Another large scale correlation exists, called cosmic magnification, see Section 5.6 for a full discussion of this effect.

Author	CMB	LSS Tracer	Wavelength	Claimed Detection
Boughn & Crittenden (2002)	COBE	NVSS	Radio	No
Boughn & Crittenden (2003)		XRB	X-ray	No
Fosalba *et al.* (2003)		SDSS DR1	Optical	2σ (low z) 3.6σ (high z)
Boughn & Crittenden (2005)		XRB &	X-ray &	Tentative$(2.5-3\sigma)$
Boughn & Crittenden (2004)		NVSS	Radio	Tentative $(2-3\sigma)$
Afshordi *et al.* (2004)	WMAP1	2MASS	NIR	2.5σ
Nolta *et al.* (2004)		NVSS	Radio	$2.2\ \sigma$
Fosalba & Gaztañaga (2004)		APM	Optical	2.5σ
Padmanabhan *et al.* (2005)		SDSS LRG	Optical	2.5σ
Gaztañaga *et al.* (2006)		Combination	All	2σ $(>3\sigma^{*})$
Cabre *et al.* (2006)		SDSS DR4	Optical	$>2\sigma$
McEwen *et al.* (2006)		NVSS	Radio	3.9σ
Giannantonio *et al.* (2006)	WMAP3	SDSS Quasars	Optical	2σ
Rassat *et al.* (2007)**		2MASS	NIR	2σ

Table 5.1: An overview of current ISW detections (and non-detections) using three different probes of the CMB temperature anisotropies (COBE, WMAP1, WMAP3) with maps of large scale structure surveyed over a range of wavelengths including x-rays, optical, NIR and radio.

* Combined with supernovæ data, these provide a 3σ detection.

** See Chapter 6.

Interpretation and Independence of Detections

All claimed ISW detection are low in significance. The detections range from 2 to 2.5σ (apart from two studies McEwen *et al.* (2006) and Padmanabhan *et al.* (2005), which I discuss in the following point). What is at first striking from Table 5.1, is that there seems to exist a subjective change in the interpretation of the cross-correlations. Boughn & Crittenden (2004, 2005) were the first to claim a detection using radio and x-ray sources as tracers of LSS. The detection using x-ray sources is actually one of the highest detections (2.5-3σ), yet the authors interpret the result as a tentative detection of the ISW effect. Most of the other detections (apart from McEwen *et al.* 2006 and Padmanabhan *et al.* 2005) present lower significance, yet seem confident that their detection is *a*) significant, *b*) due to dark energy, and *c*) independent confirmation of the presence of dark energy.

To some extent the interpretation of the significance is largely context dependent. In 2002, Boughn & Crittenden (2002) found that the measured cross-correlation signal of x-rays and radio sources with COBE was consistent with no correlation. They used this lack of signal to put an upper limit on the energy density of the cosmological constant and found $\Omega_\Lambda < 0.74$ at the 95% CL.

Only a few year later Afshordi *et al.* (2004) cross-correlated 2MASS galaxies with WMAP1 data. Although the measured signal is compatible with no cross-correlation (which they state), it was also possible to compare it with the predicted ΛCDM ISW signal. This leads to a 2.5σ significance, even though the data is compatible with no-correlation at the 1σ level. Had Boughn & Crittenden (2002) used this approach, would they also have reported a detection? In Chapter 6 I confirm the results of Afshordi *et al.* (2004) using 2MASS galaxies with the new WMAP3 data. I argue that although both approaches are valid, one is a model *independent* interpretation (the data are consistent within 1σ of no correlation), the other is model *dependent* (if there is an ISW signal due to $\Omega_\Lambda = 0.70$, then the data prefers this to no correlation).

In this case the detection is *not* an independent detection of dark energy for two reasons. The first is that it a priori assumes the signal is due to a dark energy component. By fixing the curvature of the Universe to $\Omega_k = 0$, an important case where the ISW is expected is omitted. An ISW detection which assumes a flat geometry cannot claim to be a totally independent detection of dark energy.

The second reason is the one I explain in Chapter 6 and briefly above. The interpretation of the cross-correlation in Afshordi *et al.* (2004) and Rassat *et al.* (2007) a priori assume that there is an ISW signal. The analysis then consists of quantifying the significance of the detection and both find a significance in the range $[2-2.5\sigma]$. This figure should probably only be quoted alongside that of the cross-correlation being within 1σ of no correlation.

Another issue in these two studies (including Rassat *et al.* 2007) is the estimation method of the cross-correlation error bars. I discuss this in detail in Chapter 6.

Constraints on Ω_Λ from ISW Detections and Implications on the Galaxy Bias

Several studies of ISW use the signal to constrain the energy density of dark energy and find the best fit value is higher than that for concordance cosmology ($\Omega_\Lambda \simeq 0.70$).

Fosalba *et al.* (2003) cross-correlated SDSS galaxies with WMAP1 and found a best fit of $\Omega_\Lambda = 0.80^{+0.06}_{-0.11}$. Padmanabhan *et al.* (2005) cross-correlated SDSS LRGs with WMAP1 and found a best fit value of $\Omega_\Lambda = 0.80^{+0.03}_{-0.06}$. Cabre *et al.* (2006) cross-correlated SDSS with WMAP3 and found a best fit value of $\Omega_\Lambda = 0.82^{+0.02}_{-0.03}$. In Rassat *et al.* (2007), I cross-correlated 2MASS galaxies with WMAP3 and constrain $\Omega_\Lambda < 0.89$ at 95%CL, with a best fit value of $\Omega_\Lambda = 0.85$ (see Chapter 6).

In Section 5.5, I explain that there exists a strong degeneracy between the galaxy bias b_g and the dark energy density Ω_Λ; both affect the amplitude of the signal. Padmanabhan *et al.* (2005) use this degeneracy to 'parameterise' the ISW signal, i.e. they assume concordance cosmology with $\Omega_\Lambda = 0.70$ and find what the associated LRG bias should be to match the observed signal. For multipoles ranges $\ell < 50$ they find bias values ranging from $b_g = 2.8 - 3.1 \pm 1.7$ and for scales $\ell < 400$, $b_g = 3.9 - 4.2 \pm 1.60$, though another study on the SDSS LRGs (Padmanabhan *et al.* 2006) suggests $b_g = 1.82 \pm 0.02$. The detection of Fosalba *et al.* (2003) also assumed a high bias value of $b_g = 2.4$ (which they fitted from the galaxy auto-correlation). If the bias were in fact lower, the inferred dark energy density would be larger than $\Omega_\Lambda = 0.80$.

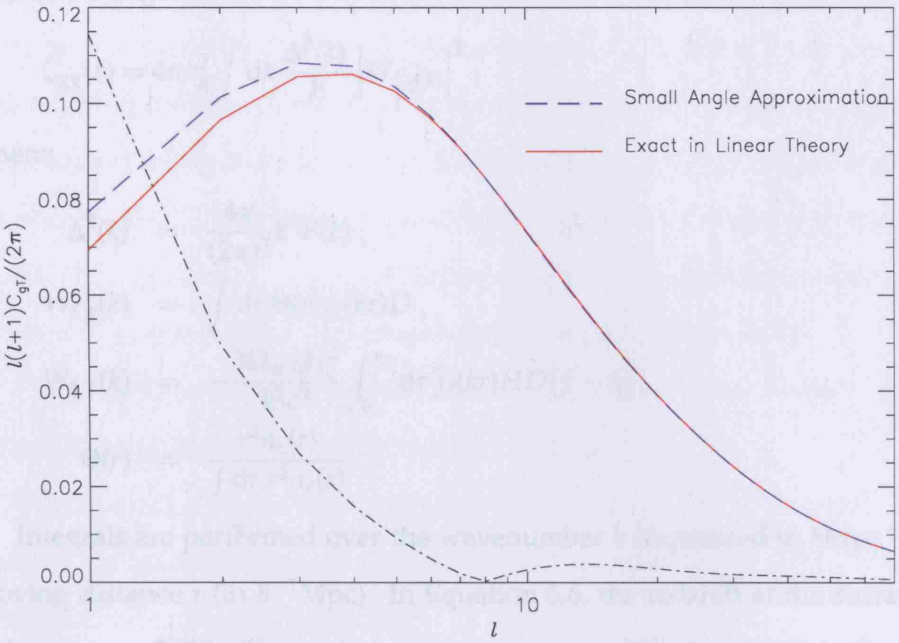

Figure 5.2: The expected cross-correlation from the exact equation in linear theory (Equation 5.2 - solid red line) and using a large-angle approximation for the Bessel function (Equation 5.12 - dashed blue line). These values are obtained using a fiducial model (flat universe with $\Omega_m^0 = 0.30$, $\Omega_b = 0.05$, $h = 0.70$, $\sigma_8 = 0.75$) and the 2MASS selection function for galaxies with $12 < K_{20} < 14$ (see Chapter 6). The black dot-dashed line is the absolute relative difference between the two. The difference is less than 1% from $\ell = 5$ onward, but is considerably larger for lower multipoles. For $\ell = 2$, for example, the difference is of order 10%. The multipole at which the small angle approximation begins to hold increases with the mean redshift of the survey.

5.3.3 Linear Theory Prediction for ISW

Here I present the linear theory prediction for the ISW signal in spherical harmonic space. In what follows, I use r as the comoving distance and implicitly as a label of redshift epoch z. They are related for a given cosmology by $\mathrm{d}r = \frac{c}{H(z)}\mathrm{d}z$, where c is the speed of light in vacuum. Thus, the growth factor $D(z)$, the growth function $f(z)$ (defined below) and the Hubble parameter $H(z)$ all have implicit dependences on r.

For the angular Cross-Correlation Function (CCF):

$$C_{gT}(\ell) = 4\pi b_g \int \mathrm{d}k \, \frac{\Delta^2(k)}{k} \, W_{\ell,g}(k) W_{\ell,T}(k) \, . \tag{5.2}$$

For the angular overdensity Auto-Correlation Function (ACF):

$$C_{gg}(\ell) = 4\pi b_g^2 \int \mathrm{d}k \, \frac{\Delta^2(k)}{k} \left| W_{\ell,g(k)} \right|^2 , \tag{5.3}$$

where:

$$\Delta^2(k) = \frac{4\pi}{(2\pi)^3} k^3 P(k) , \tag{5.4}$$

$$W_{\ell,g}(k) = \int \mathrm{d}r \, \Theta(r) j_\ell(kr) D , \tag{5.5}$$

$$W_{\ell,T}(k) = -\frac{3\Omega_{m,0}H_0^2}{k^2c^3} \int_0^{z_L} \mathrm{d}r \, j_\ell(kr) HD(f-1) , \tag{5.6}$$

$$\Theta(r) = \frac{r^2 n_c(r)}{\int \mathrm{d}r \, r^2 n_c(r)} . \tag{5.7}$$

Integrals are performed over the wavenumber k (expressed in $h\mathrm{Mpc}^{-1}$), and the comoving distance r (in $h^{-1}\mathrm{Mpc}$). In Equation 5.6, the redshift at the surface of last scattering is $z_L \sim 1089$. The matter power spectrum, $P(k)$, is related to the galaxy power spectrum through the linear bias b_g. The selection function, $n_c(r)$ is related to the redshift distribution by:

$$\int dr r^2 n_c(r) = \int \frac{dN(z)}{dz} dz . \tag{5.8}$$

The linear growth factor, $D(z)$, is the growing solution of the linear perturbation equation:

$$\ddot{\delta_k} + 2\left(\frac{\dot{a}}{a}\right)\dot{\delta_k} - 4\pi G\rho\delta_k = 0 , \tag{5.9}$$

where δ_k is the Fourier mode of the overdensity, ρ is the density and $\dot{} \equiv \mathrm{d}/\mathrm{d}t$.

It can be expressed as:

$$D(z) \propto H(a) \int^{a(z)} \frac{\mathrm{d}a'}{(a'H(a'))^3} , \tag{5.10}$$

where it is normalized such that $D(0) = 1$. Note that the above integral from of the growth factor is only valid for certain values of w ($w = -1, -1/3$), though comparing it the solution from the differential equation, I find it varies by less than 3% for $z \in [0;2]$ for the values of w considered in this Chapter. In Chapter 7, I consider small deviations around a fiducial value $w = -1$ in order to calculate the Fisher matrix, and in this case the difference between the numerical solution and the solution from Equation 5.10 is smaller than the numerical accuracy. For quintessence ($w \neq -1$), dark energy will also cluster

on large scales. I discuss how this affects the growth factor in Section 5.5.3. The growth function f is given by $f(z) \equiv \frac{d\ln D(z)}{d\ln a(z)}$. In Chapters 3, 4 and 6, I use the approximation $f(z) \simeq \Omega_m^{0.6}(z)$ (Peebles (1993), their Equation 5.120) in which case the dependence on the cosmological constant density is contained in the factor $\Omega_m(z)$ (Lahav *et al.* 1991; Wang & Steinhardt 1998). There is also dependence on the ratio of neutrino to total mass density $f_\nu = \Omega_\nu/\Omega_m$ (Kiakotou, Elgaroy & Lahav 2007), but in this analysis I assume $f_\nu = 0$. In all other Chapters I derive $f(z)$ directly from the growth factor $D(z)$.

The Hubble constant is parameterised by $H_0 = 100h$ km s^{-1} Mpc^{-1} and $j_\ell(kr)$ is the spherical Bessel function of the 1st kind of order ℓ.

These equations are exact in linear theory, and for $\ell > 10$ I replace them with the small angle approximation or *Limber* equation (Afshordi *et al.* 2004), which arise from the Bessel function approximation:

$$\lim_{\ell->\infty} j_\ell(x) = \sqrt{\frac{\pi}{2\ell+1}}\,\delta(\ell+\frac{1}{2}-x)\,. \tag{5.11}$$

Equations 5.2 and 5.3 then simplify to:

$$C_{gT}(\ell) = \frac{-3b_g H_0^2\Omega_{m,0}}{c^3(\ell+1/2)^2}\int \mathrm{d}r\,\Theta D^2 H[f-1]P\left(\frac{\ell+1/2}{r}\right)\,, \tag{5.12}$$

$$C_{gg}(\ell) = b_g^2\int \mathrm{d}r\,\frac{\Theta^2}{r^2}\,D^2 P\left(\frac{\ell+1/2}{r}\right)\,, \tag{5.13}$$

Reducing the number of integrals significantly reduces computation time. In Figure 5.2 I compare the CCF using the equation exact in linear theory (Equation 5.2) with its small angle approximation (Equation 5.12) for the 2MASS galaxy survey which has a mean redshift of $z \sim 0.07$ (cf. Chapter 6). The difference is less than 1% from $\ell = 5$ upward. However, for lower multipoles the difference is more important; for example, at $\ell = 2$ it is of order 10%. The small angle approximation makes the assumption that $kr \sim (\ell + 1/2)$. From this we see that for deeper surveys, the small angle approximation will begin to hold at a higher multipole. One should therefore check at which multipole the *Limber* equation begins to hold for a given galaxy population.

5.4 Redshift Evolution of the ISW Signal

The ISW effect is a probe of the rate of structure formation in the Universe, expressed by the growth factor term $[f(z) - 1]$ in the temperature kernel (Equation 5.6). From this term

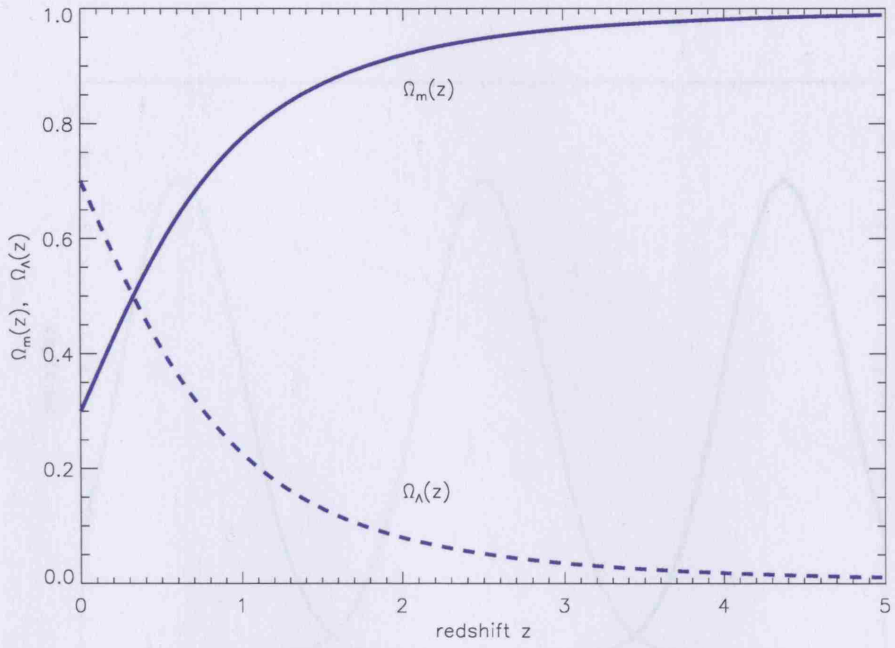

Figure 5.3: The redshift evolution of the matter and dark energy density for a concordance cosmology $\Omega_m^0 = 0.30$, $h = 0.70$ at $z = 0$ in a flat Universe.

it is clear that if $f(z) = 1\ \forall z$ (e.g., in an Einstein de-Sitter universe) there is no ISW signal expected. In a general universe, most models predict $\Omega_m(z) = 1$ at high redshifts and so the ISW is only expected to be present a low redshifts where $\Omega_m(z) \neq 1$. Figure 5.3 shows the redshift dependence of the matter and dark energy density in a flat Universe with $\Omega_m^0 = 0.30$ and $\Omega_\Lambda^0 = 0.70$. The dark energy density begins to dominate at late times but is not insignificant at high redshift ($z \sim 1 - 2$). This shows that the strength of the ISW signal will drop with redshift.

In Figure 5.4, the redshift evolution of the spherical harmonic cross-correlation signal expected from the ISW effect is plotted for a fiducial model. The redshift distributions of the LSS tracers are described by Gaussian distributions with dispersion 0.02 and mean redshifts 0.10 (green), 0.40 (red), 0.70 (blue). As expected the signal decreases with increasing redshift. The peak of the signal also moves to higher multipoles as the angular size of the largest structures decreases with redshift. The ISW signal is usually plotted in units of $\ell(\ell+1)C_{gT}(\ell)/(2\pi)(\mu K)$, and in Figure 5.5 I plot the redshift evolution of the ISW signal as unit-less $C_{gT}(\ell)$, so that one can appreciate the decay of the signal with redshift.

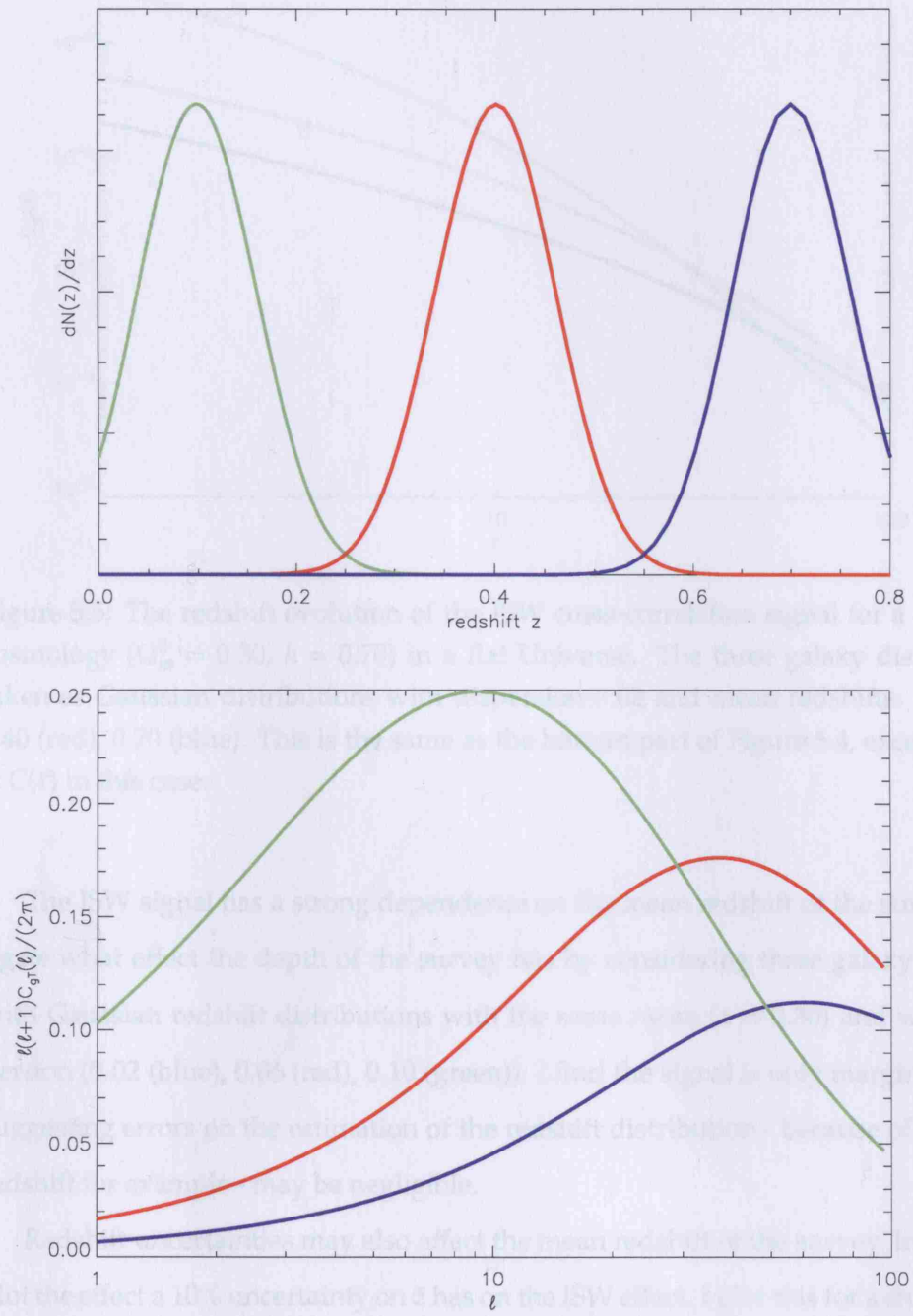

Figure 5.4: The redshift evolution of the ISW cross-correlation signal for a concordance cosmology ($\Omega_m^0 = 0.30$, $h = 0.70$) in a flat Universe. The three galaxy distribution are taken as Gaussian distributions with dispersion 0.02 and mean redshifts: 0.10 (green), 0.40 (red), 0.70 (blue).

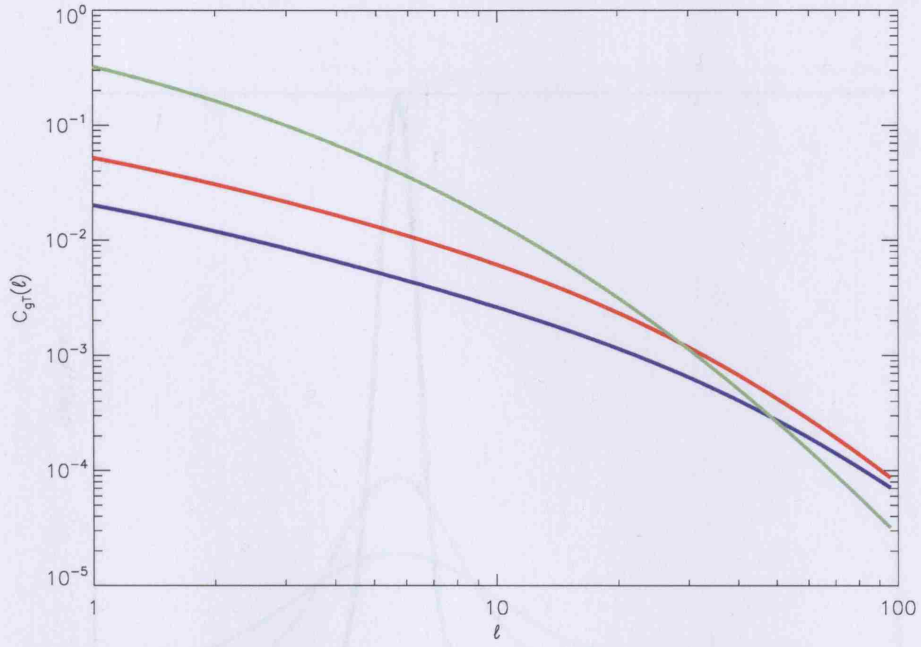

Figure 5.5: The redshift evolution of the ISW cross-correlation signal for a concordance cosmology ($\Omega_m^0 = 0.30$, $h = 0.70$) in a flat Universe. The three galaxy distribution are taken as Gaussian distributions with dispersion 0.02 and mean redshifts: 0.10 (green), 0.40 (red), 0.70 (blue). This is the same as the bottom part of Figure 5.4, except the y-axis is $C(\ell)$ in this case.

The ISW signal has a strong dependence on the mean redshift of the survey. I investigate what effect the depth of the survey has by considering three galaxy populations with Gaussian redshift distributions with the same mean ($z = 0.30$) and widening dispersion (0.02 (blue), 0.06 (red), 0.10 (green)). I find the signal is only marginally affected suggesting errors on the estimation of the redshift distribution - because of photometric redshift for example - may be negligible.

Redshift uncertainties may also affect the mean redshift of the survey. In Figure 5.7, I plot the effect a 10% uncertainty on $\bar{z}$ has on the ISW effect. I plot this for a shallow survey with $\bar{z} = 0.10$ (top part of Figure 5.7) and a deeper survey with $\bar{z} = 0.50$ (bottom part of Figure 5.7). Errors on the mean redshift of the survey have the potential to propagate errors into parameter estimation.

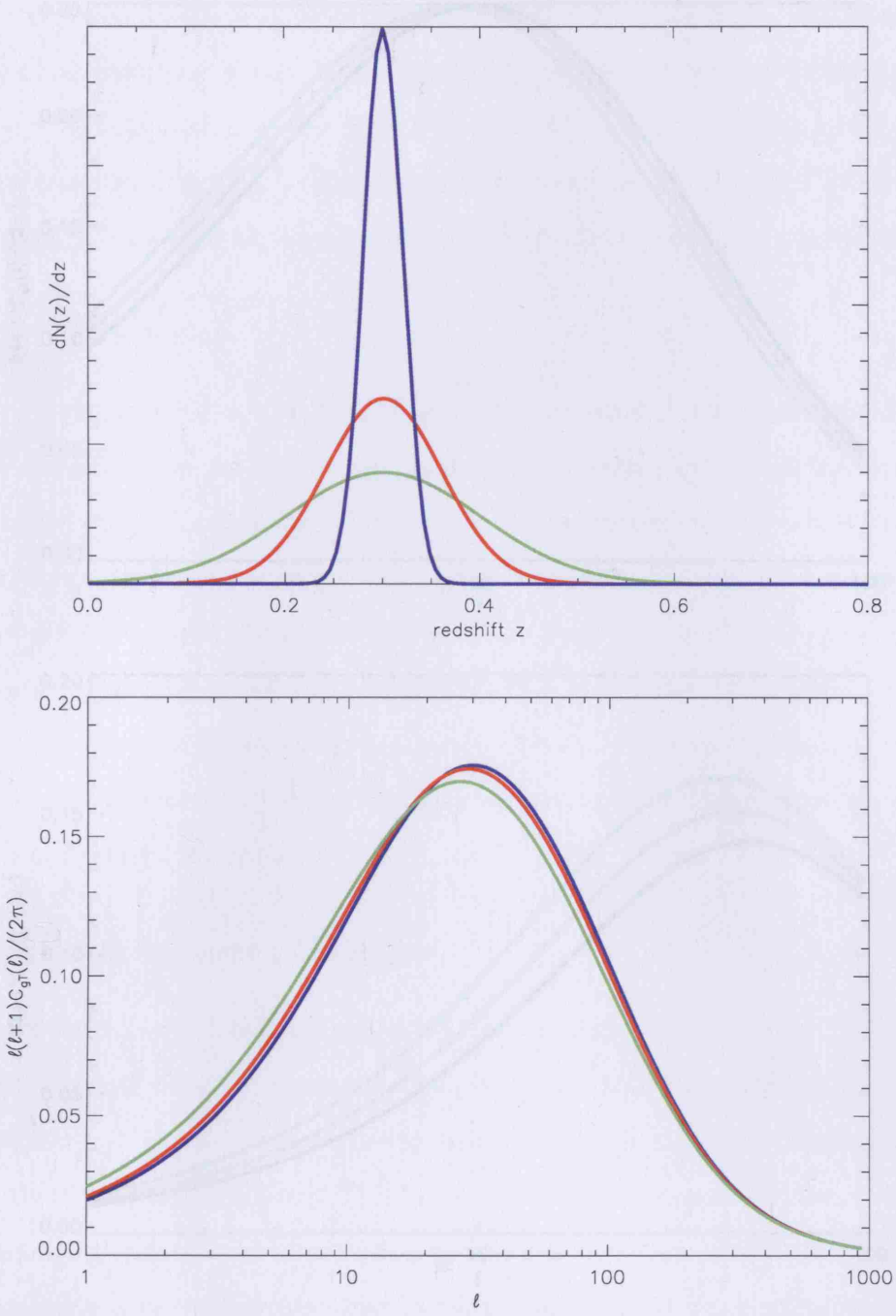

Figure 5.6: *Top:* The predicted ISW signal for three galaxy populations with the same mean redshift (0.30) but varying redshift range for a fiducial cosmology (flat, $\Omega_m^0 = 0.30$, $h = 0.70$). *Bottom:* The three galaxy distributions have Gaussian redshift distributions with mean redshift 0.30 and dispersion: 0.02 (blue), 0.06 (red), 0.10 (green).

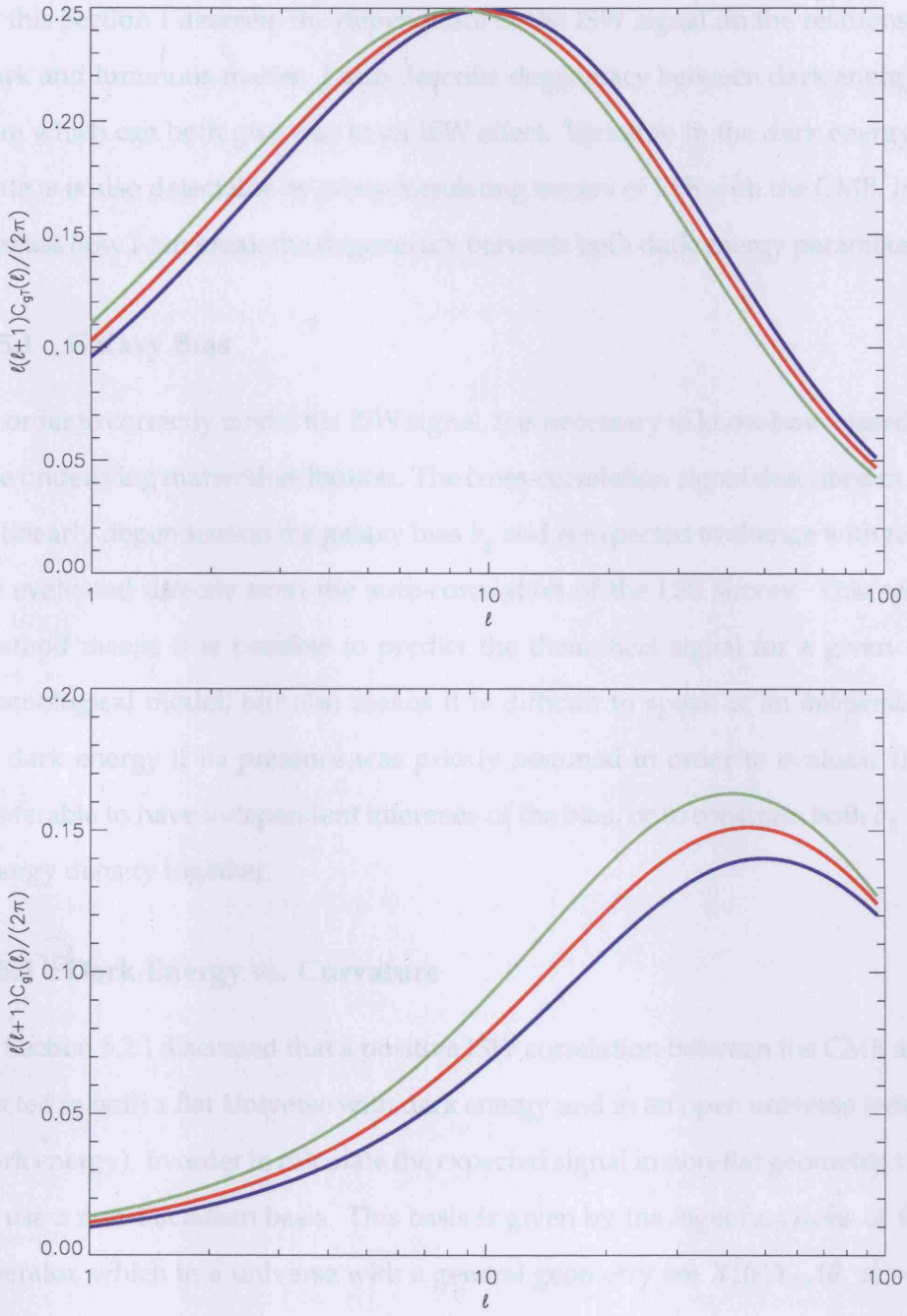

Figure 5.7: *Top:* The predicted ISW signal for three galaxy populations with 10% variation on the mean redshift $z = 0.10$, but with the same dispersion for fiducial cosmology (flat, $\Omega_m^0 = 0.30$, $h = 0.70$). *Bottom:* The predicted ISW signal for three galaxy populations with 10% variation on the mean redshift $z = 0.50$, but with the same dispersion for the same fiducial cosmology as above.

5.5 Cosmological Parameter Dependence of the ISW signal

In this Section I describe the dependence of the ISW signal on the relationship between dark and luminous matter. I also describe degeneracy between dark energy and curvature which can both give rise to an ISW effect. Variation in the dark energy equation of state w is also detectable by cross-correlating tracers of LSS with the CMB. In Chapter 7 I discuss how I can break the degeneracy between both dark energy parameters w and Ω_Λ.

5.5.1 Galaxy Bias

In order to correctly model the ISW signal, it is necessary to know how biased the LSS is to the underlying matter distribution. The cross-correlation signal described in Equation 5.2 is linearly dependent on the galaxy bias b_g and is expected to change with redshift. It can be evaluated directly from the auto-correlation of the LSS survey. This self-calibration method means it is possible to predict the theoretical signal for a given data set and cosmological model, but also means it is difficult to speak of an *independent* detection of dark energy if its presence was priorly assumed in order to evaluate the bias. It is preferable to have independent inference of the bias, or to constrain both b_g and the dark energy density together.

5.5.2 Dark Energy vs. Curvature

In Section 5.2 I discussed that a positive ISW correlation between the CMB and LSS is expected in both a flat Universe with dark energy and in an open universe (with or without dark energy). In order to calculate the expected signal in non-flat geometry, it is necessary to use a non-Euclidean basis. This basis is given by the eigenfunctions of the Laplacian operator, which in a universe with a general geometry are $X_k^\ell(r)Y_{\ell m}(\theta,\phi)$ where $Y_{\ell m}$ are the spherical harmonics described in Section 3.3, r is the usual comoving distance and $X_k^\ell(r)$ is the radial eigenfunction called the hyperspherical Bessel function. In an open Universe these are given by (Kamionkowski 1996):

$$X_k^\ell(r) = (-1)^{\ell+1} N_\ell^{-1}(k)(k^2+1)^{\ell/2}\sinh^\ell(\mathrm{r})\frac{\mathrm{d}^{\ell+1}(\cos \mathrm{kr})}{\mathrm{d}(\cosh \mathrm{r})^{\ell+1}}\,, \tag{5.14}$$

where

$$N_\ell(k) = k^2(k^2+1)...(k^2+\ell^2)\,, \tag{5.15}$$

such that only the radial dependence is affected by the curvature constant. Kamionkowski & Spergel (1994) were the first to underline that the ISW signal in an open universe could be equal or greater in magnitude to that in a flat universe with similar matter content. The general form of the cross-correlation signal in an open universe is still given by Equation 5.2, but the temperature window function becomes:

$$W_\ell, T(k) = \frac{-3b_g\Omega_{m,0}H_0^2}{(k^2+4)c^3}\int drX^\ell(kr)HD[f-1]\,, \tag{5.16}$$

and the galaxy window function becomes:

$$W_{\ell,g}(k) = b_g\int dr\Theta(r)X^\ell(kr)D\,. \tag{5.17}$$

In the flat limit where $\Omega_k \to 0$ or when $k \gg 1$ and $\eta \ll 1$ then the hyperspherical Bessel functions reduce to the usual spherical Bessel functions and the (k^2+4) term in Equation 5.5.2 reduces to k^2 so that the expression reduces to that in flat space. In this Section I assume the flat limit holds and calculate the ISW galaxy-temperature correlation in the open case using Equation 5.12.

In Figure 5.8, I have plotted the expected ISW signal for an open universe with no dark energy (dashed lines) and in a flat universe with dark energy (solid lines) both with the same matter content. In both cases the signal increases with decreasing matter content, and is larger in the presence of curvature alone than in the flat universe with dark energy. The signal peaks at similar scales in all cases. The case where ($\Omega_m = 0.90$, $\Omega_\Lambda = 0$, $\Omega_k = 0.10$) is quasi-degenerate with the case where ($\Omega_m = 0.70$, $\Omega_\Lambda = 0.30$, $\Omega_k = 0$). The only way to differentiate which component is creating the ISW signal is by considering several redshift slices as the ISW signal's evolution will be different for $\Omega_k \neq 0$ than for $\Omega_\Lambda \neq 0$. This also requires independent knowledge of the redshift evolution of the galaxy bias b_g which is expected to increase with redshift. This can be simultaneously estimated from the galaxy-galaxy correlation function.

In Figure 5.9, I plot the ISW signal for a galaxy survey with mean redshift 0.30 and dispersion 0.06 for $\Omega_m = 0.15, 0.35, 0.55$ in a flat universe. The signal for $\Omega_m = 0.15$ is over four times larger than the signal for $\Omega_m = 0.55$.

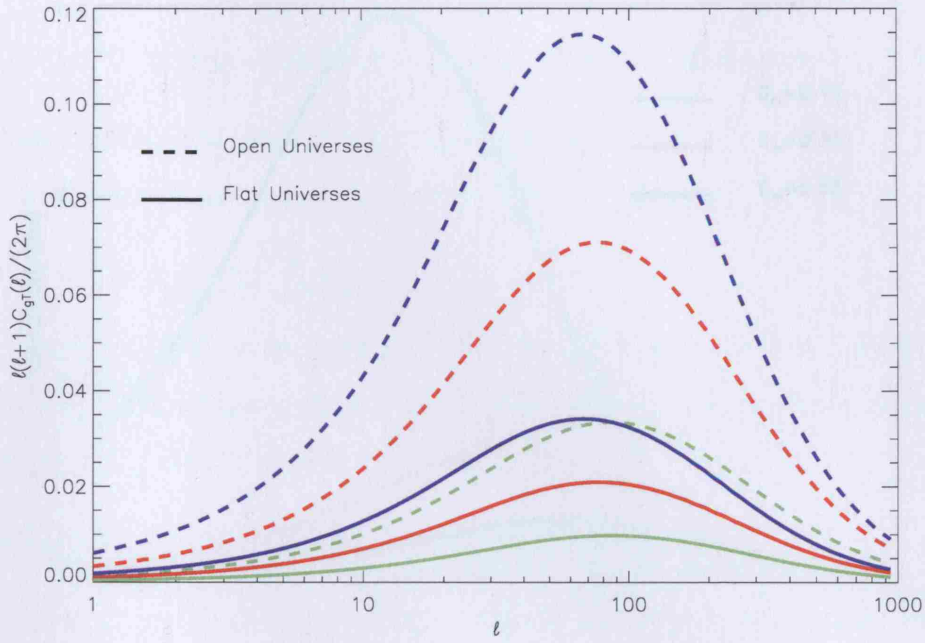

Figure 5.8: The ISW signal for open (with no dark energy) and flat (with dark energy) universes with the same matter content. Solid lines correspond to flat universes and dashed lines to open universes. The blue lines represent a universe with $\Omega_m^0 = 0.70$, the red lines $\Omega_m^0 = 0.80$, the green lines $\Omega_m^0 = 0.90$. The calculations are made assuming the curvature is small and that spherical Bessel functions are a good approximation of hyperspherical Bessel functions.

5.5.3 Dependence on w

When the equation of state of dark energy is given by $w \neq -1$, Ω_Λ no longer corresponds to the energy density of a cosmological constant but to a general form of dark energy or *quintessence* (Ratra & Peebles 1988). Contrarily to the cosmological constant, quintessence is a spatially inhomogeneous and time evolving cosmic fluid.

Quintessence will remain smooth on small scales (where $k \gg k_Q$), however on large scales ($k \ll k_Q$), it could cluster and therefore contribute to the energy density and pressure perturbations. Other quintessence models such as the Chaplygin gas do not necessarily cluster (Sen & Scherrer 2005), or can cluster on small scales only (Bilić *et al.* 2002). On linear scales, both the transfer function $T(k)$ and the growth factor $g(a) \equiv D/a$ will be affected by these. The general effect of the quintessence perturbations will be to increase large scale power in the CMB (Weller & Lewis 2003).

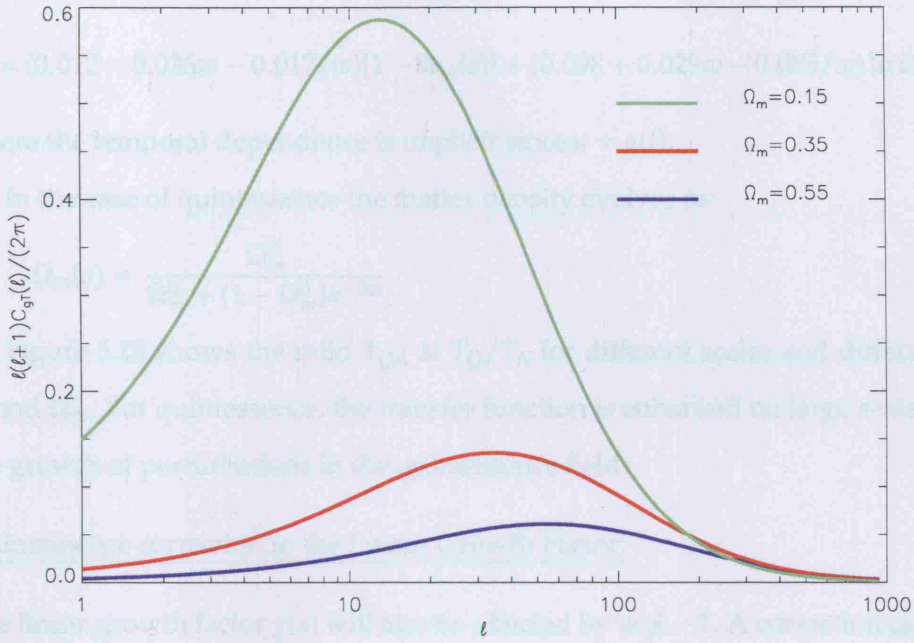

Figure 5.9: The ISW signal in a flat universe with matter content $\Omega_m^0 = 0.15$, $\Omega_m^0 = 0.35$, $\Omega_m^0 = 0.55$. The signal increases with decreasing matter content and is over four times larger for $\Omega_m^0 = 0.15$ than for $\Omega_m^0 = 0.55$.

Quintessence correction to the Transfer Function:

Ma *et al.* (1999) derived a general parameterisation to include the effect of quintessence in the transfer function and the growth function for a spatially flat Universe valid on ranges with $-1 < w < -0.2$. The transfer function for quintessence $T_Q(k,a)$ can be written as a function of the transfer function $T_\Lambda(k,a)$ for a cosmological constant, by:

$$T_Q(k,a) = \frac{\alpha + \alpha q^2}{1 + \alpha q^2} T_\Lambda(k,a) \,, \tag{5.18}$$

where

$$q = \frac{k}{\Gamma_Q h} \,. \tag{5.19}$$

The scale at which quintessence perturbations are non negligible is defined by:

$$k_Q = \Gamma_Q h = \frac{3H}{c}\sqrt{(1-w)[2+2w-w\Omega_m(a)]} \,. \tag{5.20}$$

The parameter α is a scale independent but time-dependent and is a function of the cosmology:

$$\alpha = (-w)^s \,, \tag{5.21}$$

where

$$s = (0.012 - 0.036w - 0.017/w)[1 - \Omega_m(a)] + (0.098 + 0.029w - 0.085/w)\ln\Omega_m(a)\,, \quad (5.22)$$

where the temporal dependence is implicit since $a = a(t)$.

In the case of quintessence the matter density evolves as:

$$\Omega_m(a) = \frac{\Omega_m^0}{\Omega_m^0 + (1 - \Omega_m^0)a^{-3w}}\,. \quad (5.23)$$

Figure 5.10 shows the ratio $T_{Q\Lambda} \equiv T_Q/T_\Lambda$ for different scales and different values of w and Ω_m. For quintessence, the transfer function is enhanced on large scales because of the growth of perturbations in the quintessence field.

Quintessence correction to the Linear Growth Factor:

The linear growth factor $g(a)$ will also be affected by $w \neq -1$. A correction can be applied to recover the growth for quintessence $g_Q(a)$ from the growth in the case of a cosmological constant $g_\Lambda(a)$ (Ma *et al.* 1999):

$$g_Q(a) = |w|^t g_\Lambda(a)\,, \quad (5.24)$$

where:

$$t = -(0.255 + 0.305w + 0.0027/w)[1 - \Omega_m(a)] - (0.366 + 0.266w - 0.07/w)\ln\Omega_m(a)\,. \quad (5.25)$$

Figure 5.11 shows the ratio of growth suppression $g_{Q\Lambda} \equiv g_Q/g_\Lambda$ for different values of w (bottom part of Figure) and its evolution with scale factor (top part of Figure).

In Figure 5.11 the solid and dashed lines are for $\Omega_m = 0.4$ and $\Omega_m = 0.6$ respectively. In the top panel, each set of curves corresponds to $w = -2/3, -1/2, -1/3, -1/6$ from the top down. Growth of structure becomes more important as $w \to -1$. In the bottom panel, it is clear that as $w \to -1$, $g_{Q\Lambda} \to 1$ or equivalently $g_Q \to g_\Lambda$, so that the quintessence correction becomes negligible for small departures from the cosmological constant.

Quintessence Correction to the Non-Linear Mapping:

Quintessence will also introduce a change in the mapping of the non-linear power spectrum, as described by Equations 1.20 and 1.21. Details of this can be seen in Ma *et al.* (1999). I only consider linear scales throughout this Thesis, so do not include this correction.

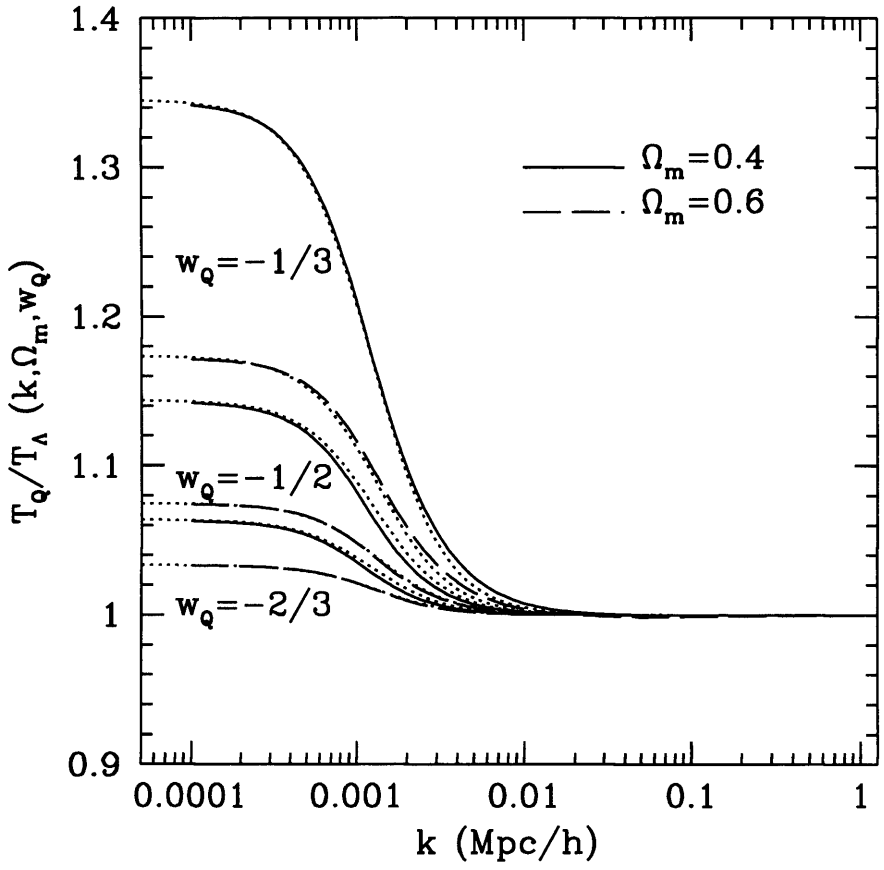

Figure 5.10: *from Ma* et al. *(1999)*: Ratio of the transfer functions $T_{Q\Lambda} \equiv T_Q/T_\Lambda$ as a function of scale k, where Q denotes a model with quintessence ($w \neq -1$) and Λ a model with cosmological constant ($w = -1$). Solid and dashed curves correspond to flat universe models with $\Omega_m = 0.4$ and $\Omega_m = 0.6$ respectively, where the transfer function has been calculated from the Boltzmann integrations. The transfer function ratio is plotted for three values of the equation of state parameter $w = -2/3, -1/2, -1/3$. For each cosmology, the dotted curves show the analytic approximation derived by Ma *et al.* (1999) and given by Equation 5.18. Quintessence affects the transfer function only on scales larger than $k \ll k_Q$. When $w \to -1$, $T_{Q\Lambda} \to 1$ so that the correction to the transfer function is negligible.

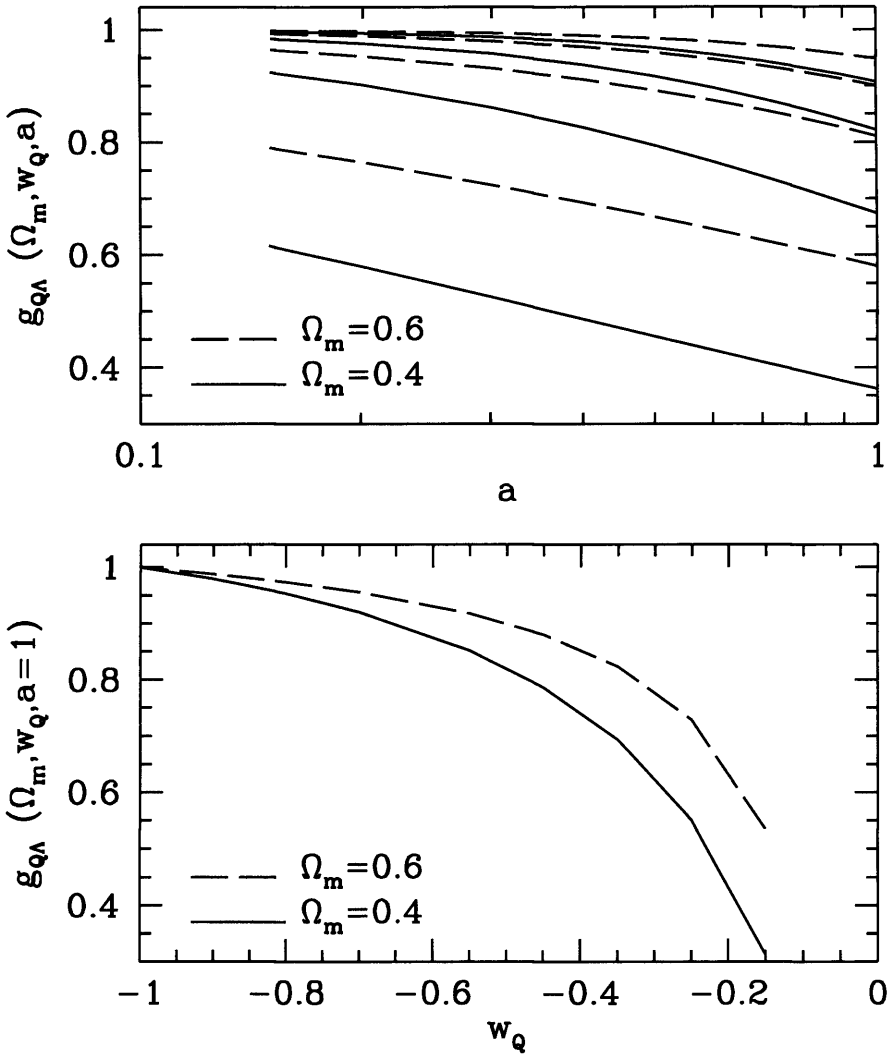

Figure 5.11: *from Ma* et al. *(1999)*: Ratio of the growth factor $g_{Q\Lambda} \equiv g_Q/g_\Lambda$ as a function of scale factor a (top) and equation of state parameter w (bottom) for various flat cosmologies. The term Q denotes a model with quintessence ($w \neq -1$) and Λ to a model with cosmological constant ($w = -1$). Solid and dashed lines are for $\Omega_m = 0.4$ and $\Omega_m = 0.6$ respectively. In the top panel, each set of curves corresponds to $w = -2/3, -1/2, -1/3, -1/6$ from the top down. Growth of structure becomes more important as $w \to -1$. In the bottom panel, it is clear that as $w \to -1$, $g_{Q\Lambda} \to 1$ or equivalently $g_Q \to g_\Lambda$, so that the quintessence correction becomes negligible.

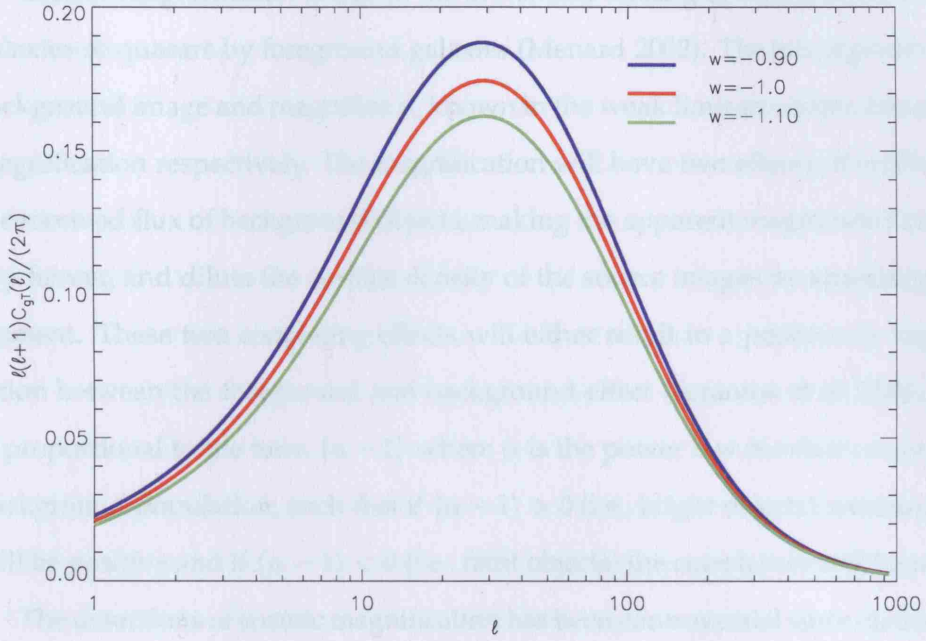

Figure 5.12: The ISW signal for varying values of w for a galaxy survey with a Gaussian redshift distribution with dispersion $\sigma = 0.06$ and mean redshift 0.30 .

Dependence of the ISW signal on w:

The dependence on the dark energy equation of state parameter w is shown in Figure 5.12. For values of $w > -1$ the ISW signal is amplified. It will eventually decrease as $w \to 0$, i.e. as the equation of state tends towards that of matter. The growth function f is given by $f(z) \equiv \frac{d \ln D(z)}{d \ln a(z)}$ which I derive numerically in this chapter and in Chapter 7. It can be seen that by changing w by 10%, the overall shape of the ISW effect is relatively unchanged, but the amplitude changes. This will introduce a degeneracy if measuring both w and Ω_Λ from the ISW signal.

5.6 Cosmic Magnification

It is often assumed that the ISW effect is the only large scale galaxy-temperature correlation expected, but another one called *cosmic magnification* or *magnification bias* can corrupt the ISW signal, leading to erroneous error bar calculations and parameter estimation if ignored.

Cosmic Magnification is due to the systematic lensing of background distribution of galaxies or quasars by foreground galaxies (Menard 2002). The lensing both distorts the background image and magnifies it, known in the weak limit as cosmic shear and cosmic magnification respectively. The magnification will have two effects: it will both increase the received flux of background objects, making the apparent magnitude limit of the survey fainter, and dilute the surface density of the source images by stretching the surface element. These two competing effects will either result in a positive or negative correlation between the foreground and background effect (Scranton *et al.* 2005). The signal is proportional to the term $\langle \alpha - 1 \rangle$ where α is the power law number count slope of the background population, such that if $\langle \alpha - 1 \rangle > 0$ (i.e., bright objects) resulting correlation will be positive and if $\langle \alpha - 1 \rangle < 0$ (i.e., faint objects) the correlation will be negative.

The detections of cosmic magnification has been controversial since claimed detection have either been in contradiction with each other or in disagreement with theoretical predictions The first detection to be in agreement with theoretical prediction with respects to the amplitude, angular dependence and change in sign of the signal were reported by Scranton *et al.* (2005). They cross-correlated 200,000 background quasars with 13 million foreground galaxies using 3800 deg^2 from the third data release of the SDSS, and found a 8σ detection, giving credibility to the importance of cosmic magnification.

If the ISW effect were the only large scale signal expected in the presence of dark energy (in a flat universe), correlating a high redshift population with the CMB would return zero correlation because most models predict $\Omega_m \simeq 1$ at high redshifts.. However, because of cosmic magnification, this correlation will no longer be null as the high redshift population will be affected by the low redshift matter and dark energy distribution, thus mimicking the presence of dark energy at high redshift. The cross-correlation of galaxies on large scales with the CMB will generally be the sum of two effects:

$$C_{gT}^{\rm Obs}(\ell, z) = C_{gT}^{\rm ISW}(\ell, z) + C_{gT}^{\rm CM}(\ell, z)\,, \tag{5.26}$$

where $C_{gT}^{\rm Obs}(\ell, z)$ is the total observed galaxy-temperature correlation, $C_{gT}^{\rm ISW}(\ell, z)$ is the correlation due to the ISW effect and $C_{gT}^{\rm CM}(\ell, z)$ the correlation due to cosmic magnification. The effect of cosmic magnification is to modify the amplitude and scale dependence of the galaxy-temperature correlation. There may exist another non-negligible term within

the temperature window function itself, due to cosmic magnification of the CMB with the foreground galaxies.

Loverde, Hui & Gaztañaga (2007) showed that the magnification-temperature effect (the galaxy-temperature correlation due to cosmic magnification) will dominate over the ISW signal at high redshifts ($z > 2$). This is due to the intrinsic decrease of the ISW signal with redshift, to the increase of the lensing efficiency with redshift and to the tendency of the number count slope α to increase with redshift. Figure 5.13 is taken from Loverde, Hui & Gaztañaga (2007) and compares existing galaxy-temperature correlation measurements from tracers of mass at increasing redshift (2MASS, APM, SDSS galaxies, NVSS, SDSS-LRGs, SDSS-QSOs) with the expected signal due to ISW alone (solid line) and with the effect of cosmic magnification (dotted line). The upper and lower lines correspond to values of $\alpha > 1$ (positive cosmic magnification correlation) and $\alpha < 1$ (negative cosmic magnification correlation), whilst the top and bottom plots correspond to respectively broad and narrow redshift distribution of the galaxy or QSO populations. In all cases, the cosmic magnification signal is negligible for redshifts smaller than ~ 1.

Figure 5.14 is also taken from Loverde, Hui & Gaztañaga (2007) and shows the simulated inferred value of the dark energy equation of state parameter w, inferred from galaxy-temperature correlations where the effect of cosmic magnification has been ignored. The value is inferred for fiducial galaxy surveys with increasing redshift and for which there exists either a negative cosmic magnification correlation (top, sample I) or a positive cosmic magnification correlation (bottom, sample II). The true value of the fiducial model is $w = -1$ and the inferred value deviates by more than 1σ from redshifts $1 - 3$ onwards (depending on the sign of the cosmic magnification correlation).

Because cosmic magnification is negligible for redshifts smaller than $\sim 1 - 2$, I do not include its effects in the parameter estimation from galaxy-temperature cross-correlations in Chapter 6, nor for the parameter forecasts from the DUNE and DES surveys in Chapter 7.

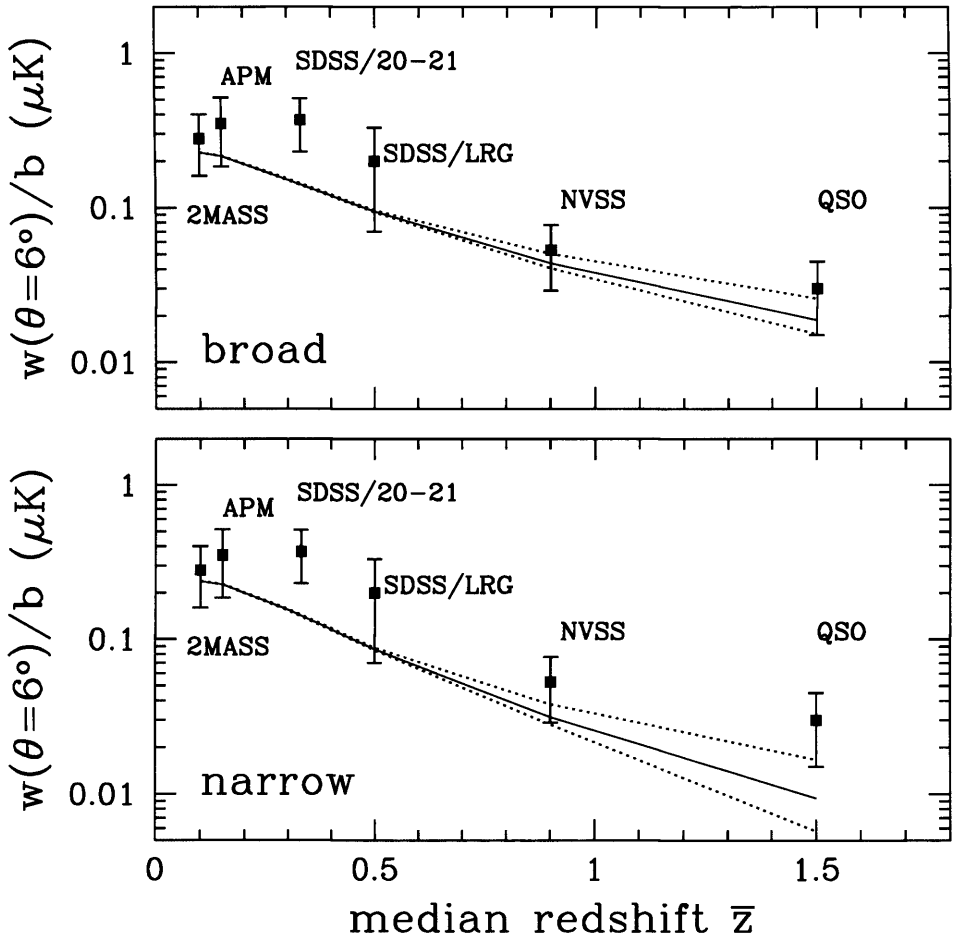

Figure 5.13: *From Loverde, Hui & Gaztañaga (2007)*: The galaxy-temperature correlation from different tracers of mass compared with the predicted ISW signal alone (solid line) and the ISW signal with the effect of cosmic magnification (dotted line). The upper dotted line corresponds to a number count slope which produces a positive cosmic magnification correlation, the lower dotted line a number count slope which produces a negative cosmic magnification correlation. In the top plot, Loverde, Hui & Gaztañaga (2007) have assumed a broad redshift distribution, in the bottom part a narrow redshift distribution.

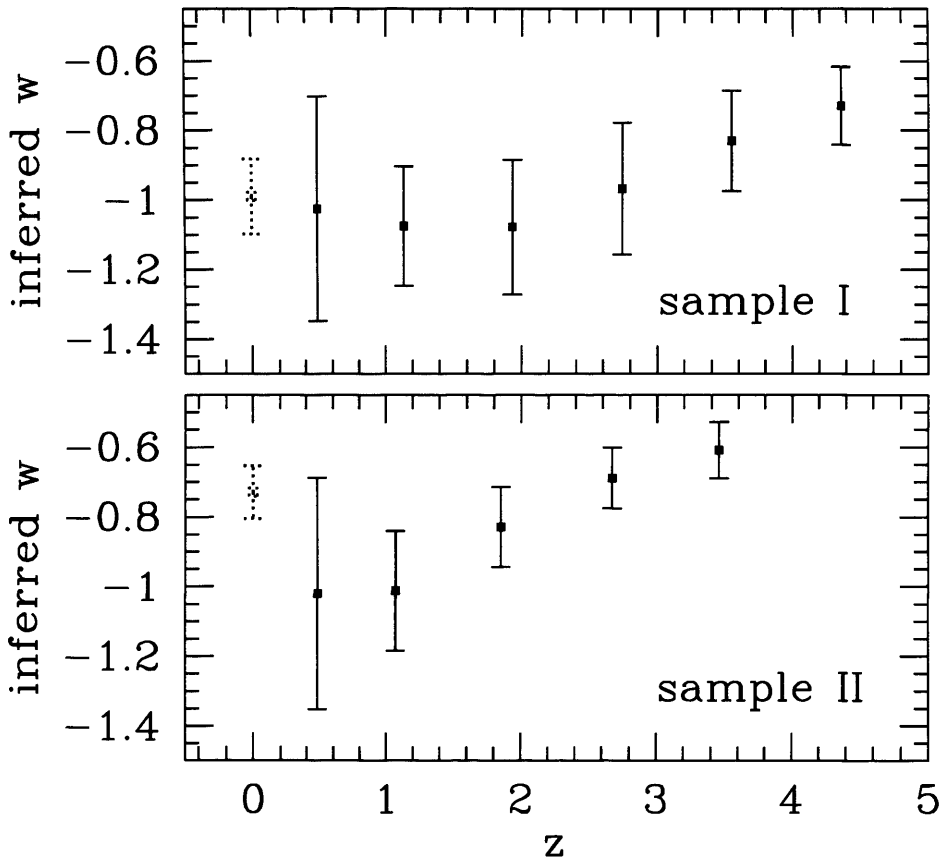

Figure 5.14: *From Loverde, Hui & Gaztañaga (2007)*: Inferred values of the dark energy equation of state parameter w from the galaxy-temperature correlation of a fiducial model, whilst ignoring the effects of cosmic magnification. The true value is $w = -1$. The value of w is inferred for galaxy surveys for which there exists a negative cosmic magnification correlation (top, sample I) or a positive cosmic magnification correlation (bottom, sample II).

5.7 Discussion

In this Chapter I described the late-time Integrated Sachs-Wolfe (ISW) effect, which can be used to probe the decay of large scale gravitational potential wells. This decay can be due to open geometry, the presence of dark energy or deviations from general relativity on large scales.

The ISW effect can be detected through cross-correlating a tracer of Large Scale Structure (LSS) with the Cosmic Microwave Background (CMB). The signal is strongest at low redshifts and in low matter universes. To date there are over 10 claimed detections, though all with low significance. In Chapter 6 I present work published in Rassat *et al.* (2007), in which I cross-correlated galaxies from 2MASS with the third year data of the Wilkinson Microwave Anisotropy Map (WMAP3). I discuss issues with the significance of this result in detail in Chapter 6.

There exists a strong degeneracy between Ω_Λ and the bias b_g. The bias can usually be estimated from the auto-correlation function of the large scale structure. However, this makes inference of the bias dependent on a cosmology, and so that any claimed ISW detection is dependent on the fiducial model. There is also a strong degeneracy in the (Ω_Λ, w) plane. I investigate whether this degeneracy can be broken with future surveys such as the Dark UNiverse Explorer (DUNE, Réfrégier *et al.* 2006) or the Dark Energy Survey (DES, Annis *et al.* 2005).

Finally, there is another large scale effect expected to produce a signal in the cross-correlation of LSS with the CMB. This is cosmic magnification (or magnification bias), and is expected to be negligible over the redshift ranges of all analyses in this Thesis.

CHAPTER 6

CROSS-CORRELATING 2MASS WITH WMAP3: IMPLICATIONS FOR THE INTEGRATED SACHS-WOLFE EFFECT

This work is also presented is Rassat, Land, Lahav & Abdalla (2007)

Summary

In this Chapter I perform a cross-correlation of the Cosmic Microwave Background (CMB) using the third year Wilkinson Microwave Anisotropy Probe (WMAP) data with the 2 Micron All Sky Survey (2MASS) galaxy map (about 828 000 galaxies with median redshift $z \approx 0.07$). One motivation is to detect the Integrated Sachs-Wolfe (ISW) effect, expected if the cosmic gravitational potential is time dependent; for example, as it is in a flat universe with a dark energy component. The measured spherical harmonic cross-correlation signal favours the ISW signal expected in the concordance ΛCDM model over that of zero correlation, although both are consistent with the data within 2σ. Within a flat ΛCDM model I find a best fit value of $\Omega_\Lambda = 0.85$ and $\Omega_\Lambda < 0.89$ (95% CL). The above limits assume a galaxy bias $b_g(\frac{\sigma_8}{0.75}) \approx 1.40 \pm 0.03$, which I derived directly from the 2MASS auto-correlation. Another goal is to test if previously reported anomalies in the WMAP data are related to the galaxy distribution (the so-called "Axis of Evil" - AoE). No such anomaly is observed in the 2MASS data nor are there any observed AoE correlations between the 2MASS and WMAP3 data.

6.1 Introduction

Our currently favoured ΛCDM cosmological model has received on-going confirmation and bolstering over recent years, especially from recent observations of the cosmic microwave background (CMB) by the Wilkinson Microwave Anisotropy Probe (WMAP, Spergel *et al.* 2003; Spergel *et al.* 2006). This model postulates that more than two thirds of the Universe is composed of 'dark energy', a mysterious energy with negative pressure. This dark energy has never been directly observed - only inferred. The case is compelling because of the very different types of observations that require its presence: acceleration of the Universe seen by supernovæ; joint analysis of the CMB with Large Scale Structure (LSS) requiring zero curvature (Hinshaw *et al.* 2006; Spergel *et al.* 2006) but a mass density today $\Omega_m \sim 0.25$. However, it would still be comforting to have a more direct and independent detection of the dark energy and its effects, especially in light of promising alternative theories based on inhomogeneous models which do not require dark energy (Alnes, Amarzguioui & Gron 2005, Moffat 2006, Vanderveld *et al.* 2006).

The Integrated Sachs-Wolfe (ISW) effect (Sachs & Wolfe 1967) provides us with one of the cleanest probes of dark energy, though it does require some assumptions about other cosmological parameters. In Chapter 5 I gave a detailed overview of the origin of the ISW effect and how it can be detected by cross-correlating tracers of Large Scale Structure (LSS) with the CMB. The ISW effect is predicted in flat universes with dark energy, as well as in universes with open geometries (Kamionkowski 1996; Kinkhabwala & Kamionkowski 1999). It is also predicted in some alternative gravity models (Carroll *et al.* 2005, Song, Sawicki & Hu 2006).

In the case of a flat universe described by the equations of general relativity, the detection of an ISW effect is a test for the presence of dark energy. To date there are over ten claimed detections of ISW effects (see Section 5.3.1). The tracers of large scale structure trace LSS up to a redshift of approximately $z \sim 1.5$. In this Chapter I cross-correlate the galaxies in the 2 Micron All-Sky Survey (2MASS) eXtended Source Catalogue (XSC) (see Chapter 2) with the third year data of the Wilkinson Microwave Anisotropy Probe (WMAP3) with the aim to detect a possible ISW effect.

A cross-correlation between LSS and the CMB can also probe the issue of foreground contamination in the CMB and LSS maps. Recent studies have highlighted anomalous features in CMB data that include alignments of the low-ℓ multipoles, and a North-South asymmetry (Land & Magueijo 2005*a*,*b*; Copi *et al.* 2006; Eriksen *et al.* 2004). Curiously these features align with the ecliptic plane, and possibly the Supergalactic Plane. Such alignments may, of course, be coincidental, or they may indicate the culprit behind these anomalies, such as contamination or some other more local secondary effect of the structure on CMB photons (Vale 2005, Rakic, Rasanen & Schwarz 2006).

2MASS as an infrared survey has the advantage of probing the older stellar populations in galaxies and is therefore a robust tracer of their mass. Since infrared light penetrates more easily through the Galaxy than optical light, 2MASS is nearly an all-sky extra-galactic survey. These two qualities of 2MASS make it one of the best available tracers of any large scale correlations, such as those expected by the ISW effect. However, even in the infrared, Galactic extinction and stellar contamination will produce a foreground contamination in the galaxy distribution which can be correlated with emission foregrounds that contaminate WMAP.

In this Chapter I perform a harmonic space cross-correlation of the CMB with LSS using the WMAP3 temperature maps (Spergel *et al.* 2006; Hinshaw *et al.* 2006) and the 2MASS galaxy survey (Jarrett *et al.* 2000; Jarrett 2004). I account for possible correlations from Galactic contamination using random simulations. This work updates the work of Afshordi *et al.* (2004), who cross-correlated WMAP1 with 2MASS. I also investigate correlations between another statistic, the so-called "Axis of Evil" (AoE) (Land & Magueijo 2005*a*).

In Section 6.2 I introduce the 2MASS and WMAP3 data that I use, and in Section 6.3 I outline the theory. In Section 6.4 I discuss the choice of fiducial model. In Section 6.5 I estimate the galaxy bias, b_g, from the galaxy auto-correlation function. In Section 6.6 I discuss the cross-correlation method. In Section 6.7 I present the results of the cross-correlation and discuss their statistical significance. In Section 6.8 I investigate "Axis of Evil" (AoE) type correlations and in Section 6.9 I present a discussion of these results.

6.2 The Data

In this section I summarize the two data sets used for the cross-correlation.

6.2.1 The Large-Scale Structure: 2MASS

I use the publicly available full-sky Extended Source Catalogue (XSC) of the Near-Infra Red (NIR) 2MASS (Jarrett *et al.* 2000). The 2MASS data is described in detail in Chapter 2, here I overview the selection criteria for this analysis.

Following Afshordi *et al.* (2004), I divide the galaxies into different magnitude bands depending on their K_s-band isophotal magnitude K_{20} ("k_m_i20c" - 20mag/arcsec^2 isophotal circular ap. magnitude). I correct these magnitudes for Galactic extinction using the IR reddening maps of Schlegel, Finkbeiner & Davis (1998)*:

$$K_{20} \rightarrow K_{20} - A_K \,, \tag{6.1}$$

where $A_K = 0.367 \times E(B-V)$ (Afshordi *et al.* 2004). I use the same extinction maps to create a mask that excludes regions of sky where the XSC is unreliable. Afshordi *et al.* (2004) find a limit of $A_k < 0.05$ for which 2MASS is seen to be 98% complete for $K_{20} < 13.85$. I adopt this method herein, and mask areas with $A_k > 0.05$, leaving 69% of the sky with approximately 828,000 galaxies for the analysis.

For the four K_{20} magnitude shells, I adopt the redshift distribution computed by Afshordi *et al.* (2004) (parameterised by their Equations 33 and 35). They fit the redshift distribution from the 2MASS K_{20} luminosity function (Kochanek *et al.* 2001) for a three parameter generalized gamma distribution which I use herein. I recall the number counts for the four K_{20} shells and the redshift z_0 at which the distributions peak, taken from Afshordi *et al.* (2004), in Table 6.2.1. In Figure 6.1 I plot the redshift distribution for each shell as well as for $12 < K_{20} < 14$. The 2MASS overdensity field for galaxies with galactic extinction $A_k < 0.05$ is plotted in Figures 6.2, where it is convolved with a Gaussian beam of Full Width Half Maximum (FWHM) 100′. The centre of the projection represents galactic coordinates $(l, b) = (0, 0)$ and the longitudinal coordinate increases leftwards and $l = 180°$ on both left and right edges of the projection.

*Corresponding reddening maps can be found at http://astro.berkeley.edu/davis/dust/index.html

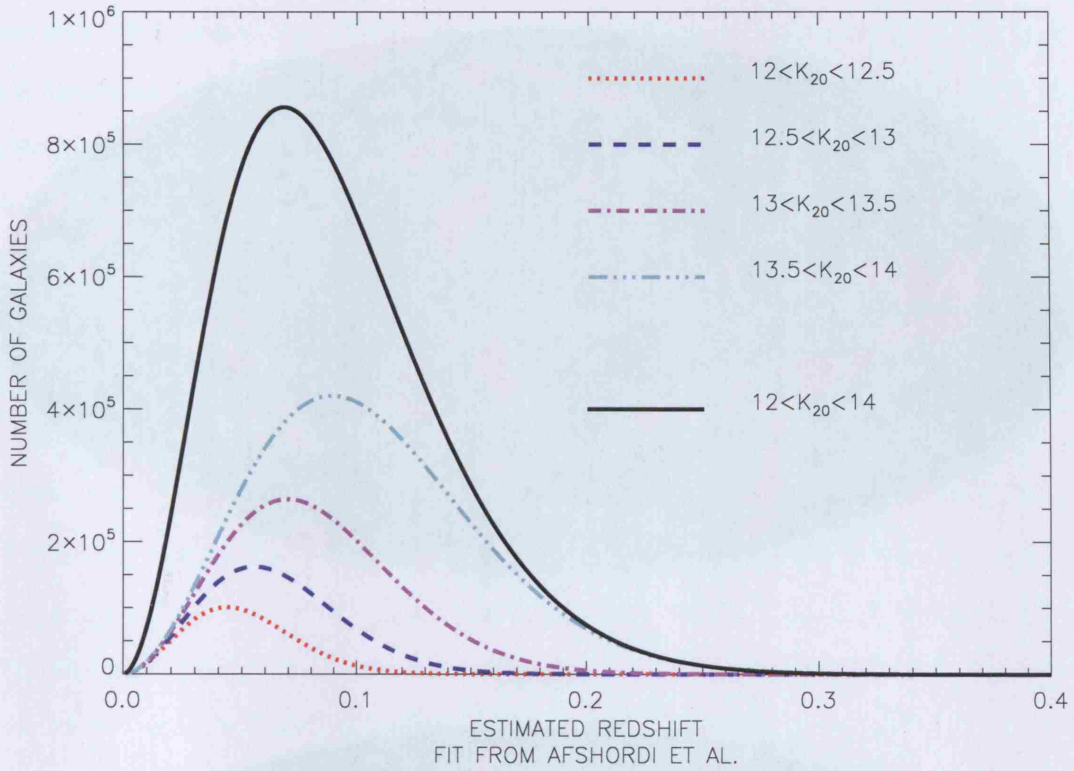

Figure 6.1: The redshift distribution for different magnitude cuts of 2MASS, estimated from the parameterisation in Afshordi et al (2004). The red (dotted) line corresponds to the closest shell $12 < K_{20} < 12.5$, the blue (dashed) to the $12.5 < K_{20} < 13$ shell, the magenta (dot-dashed) to the $13 < K_{20} < 13.5$ shell, the cyan (dot-dot-dashed) to the furthest $13.5 < K_{20} < 14$ shell. The solid (black) shows all four shells combined, i.e. $12 < K_{20} < 14$. The redshift, z_0, at which each distribution peaks and the number counts for the four K_{20} shells are reported in Table 6.2.1.

Magnitude	N_{tot}	z_0
$12.0 < K_{20} < 12.5$	49,902	0.043
$12.5 < K_{20} < 13.0$	102,947	0.054
$13.0 < K_{20} < 13.5$	217,831	0.067
$13.5 < K_{20} < 14.0$	457,267	0.084
$12.0 < K_{20} < 14.0$	827,947	0.073

Table 6.1: The number of galaxies for the four K_{20} shells and for all four shells combined. I also recall the peak redshift values for the distributions. These values are taken from Afshordi et al. (2004). The parameterisations of these distributions are shown in Figure 6.1.

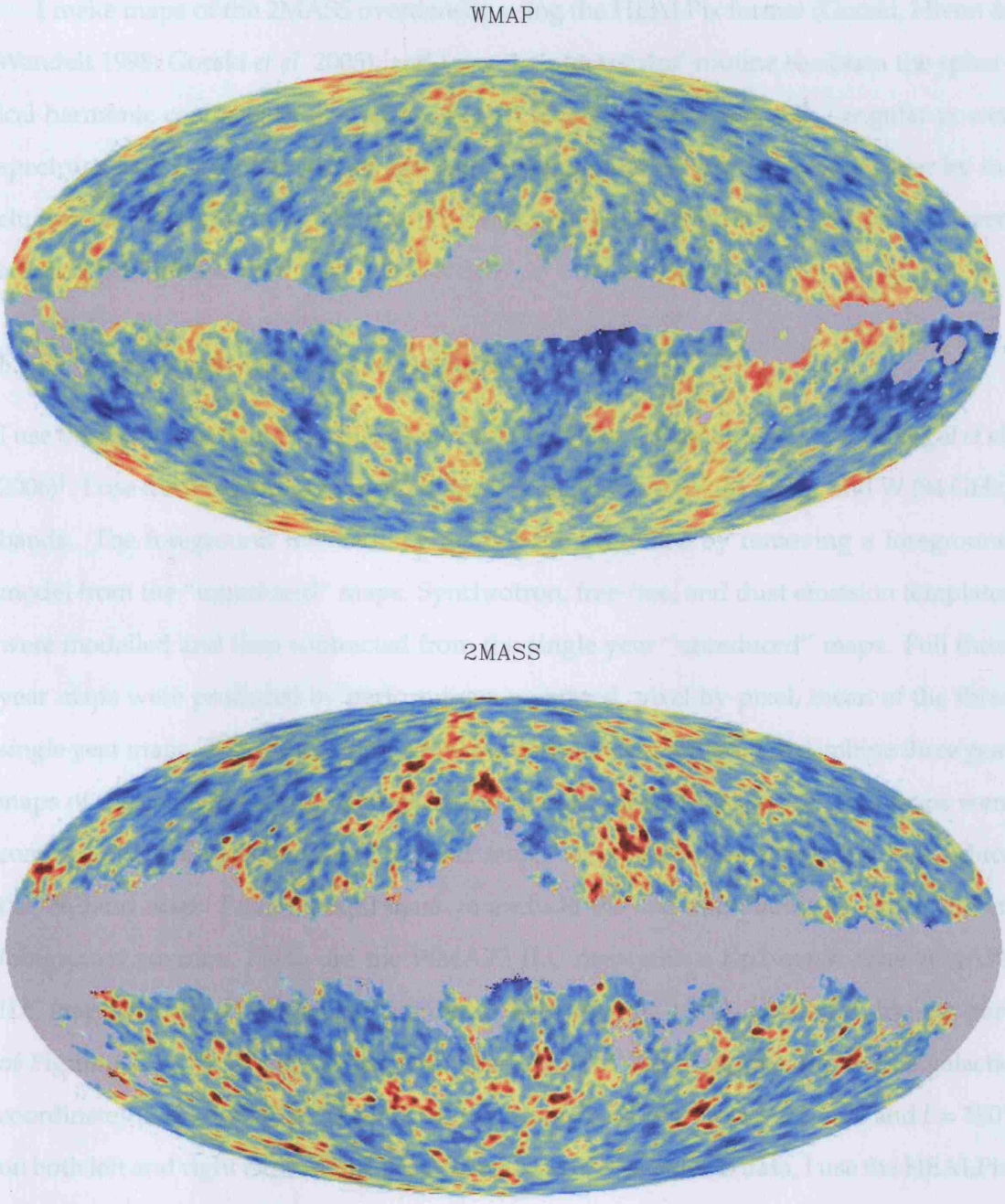

Figure 6.2: **Best viewed in colour.***Top:* The 3rd year WMAP (WMAP3) Internal Linear Combination (ILC) map, which maps temperature anisotropies in the Cosmic Microwave Background. *Bottom:* The 2 Micron All-Sky Survey (2MASS) overdensity field of 827,947 galaxies with magnitudes $12 < K_{20} < 14$. Red shading represents CMB hot spots and 2MASS overdensities and blue shading corresponds to CMB cold spots and 2MASS underdensities respectively. Grey shading corresponds to the K_p2 mask for the CMB and for the 2MASS map to galaxies with galactic extinction $A_k > 0.05$. The data are publicly available from http://lambda.gsfc.nasa.gov/ (WMAP3, see Hinshaw et al. 2006) and http://www.ipac.caltech.edu/2mass/ (2MASS, see Jarrett 2004).

I make maps of the 2MASS overdensity using the HEALPix format (Gorski, Hivon & Wandelt 1998; Gorski *et al.* 2005), and I use their '**map2alm**' routine to obtain the spherical harmonic coefficients. For an incomplete sky, the magnitude of the angular power spectrum scales with the survey area and I compensate for the loss of sky cover by including the factor f_{sky} in Equation 6.11. The sky cut will also induce correlations between adjacent multipoles.

6.2.2 The Cosmic Microwave Background: WMAP3

I use the third-year data from NASA's WMAP satellite (Hinshaw *et al.* 2006; Spergel *et al.* 2006)[†]. I use the foreground reduced maps of the Q (41 Ghz),V (61 GHz), and W (94 GHz) bands. The foreground reduced sky maps were produced by removing a foreground model from the "unreduced" maps. Synchrotron, free-free, and dust emission templates were modelled and then subtracted from the single year "unreduced" maps. Full three year maps were produced by performing a weighted, pixel-by-pixel, mean of the three single year maps. This same weighted mean method was then used to combine three year maps of the same frequency band into a single map for each frequency. Two maps were combined to produce the Q and V band maps; four maps were combined to produce the W band map. I use the Kp2 mask to exclude the Galactic plane and other known foreground sources. I also use the WMAP3 ILC map with a Kp2 mask. The WMAP3 ILC map convolved with a Gaussian beam with FWHM 100′ is plotted in the top part of Figure 6.2 in Mollweide projection. The centre of the projection represents galactic coordinates $(l, b) = (0, 0)$ and the longitudinal coordinate increases leftwards and $l = 180°$ on both left and right edges of the projection. As with the 2MASS data, I use the HEALPix routine '**map2alm**' to find the spherical harmonic coefficients.

I also return to the WMAP1 data and in Section 6.6 I compare the cross-correlation results for the V band (which is the least contaminated band with the best resolution). I use the first-year foreground cleaned maps, with the Kp2 mask, and inverse-noise co-add the two available V band maps.

[†]Available at http://lambda.gsfc.nasa.gov/

6.3 Auto- and Cross-Correlation Functions

The formalism for the linear theory calculation of the galaxy Auto-Correlation Function (ACF) is presented in Chapter 3, and I do not consider redshift distortions in this Chapter. In this case the ACF is give by:

$$C_{gg}(\ell) = 4\pi b_g^2 \int \mathrm{d}k \, \frac{\Delta^2(k)}{k} \left| W_g(k) \right|^2 . \tag{6.2}$$

The theory for the angular Cross-Correlation Function (CCF) is described in Chapter 5, and give by:

$$C_{gT}(\ell) = 4\pi b_g \int \mathrm{d}k \, \frac{\Delta^2(k)}{k} \, W_g(k) W_T(k) \, , \tag{6.3}$$

where as before:

$$\Delta^2(k) = \frac{4\pi}{(2\pi)^3} k^3 P(k) \tag{6.4}$$

$$W_g(k) = \int \mathrm{d}r \, \Theta(r) j_\ell(kr) D \tag{6.5}$$

$$W_T(k) = -\frac{3\Omega_{m,0} H_0^2}{k^2 c^3} \int_0^{z_L} \mathrm{d}r \, j_\ell(kr) H D(f-1) \tag{6.6}$$

$$\Theta(r) = \frac{r^2 n_c(r)}{\int \mathrm{d}r \, r^2 n_c(r)} \, . \tag{6.7}$$

All expressions are the same as those defined in Chapter 3 and 5. The selection function, $n_c(r)$, for each magnitude shell, is shown in Figure 6.2.1. These equations are exact in linear theory, and for $\ell > 10$ I replace them with the small angle approximation or *Limber* equation (Afshordi *et al.* 2004) and Section 5.3:

$$C_{gT}(\ell) = \frac{-3 b_g H_0^2 \Omega_{m,0}}{c^3 (\ell + 1/2)^2} \int \mathrm{d}r \, \Theta D^2 H [f-1] P\left(\frac{\ell + 1/2}{r} \right) , \tag{6.8}$$

$$C_{gg}(\ell) = b_g^2 \int \mathrm{d}r \, \frac{\Theta^2}{r^2} \, D^2 P\left(\frac{\ell + 1/2}{r} \right) . \tag{6.9}$$

In this Chapter I calculate the growth factor using the approximation $f \equiv \frac{\mathrm{dln}D}{\mathrm{dln}a} \simeq \Omega_m(z)^{0.6}$.

6.4 Choice of Fiducial Model and Priors

In this Chapter I focus on how to constrain dark energy from the ISW effect alone. This requires of course assumptions about the other cosmological parameters. To have the

ISW result independent of the CMB, I prefer to assume "round" cosmological parameters which are in accord with other cosmological measurements, rather than adopting exact values from another analysis, *e.g.*, the WMAP3 TT correlation function.

Based on inflation, I assume the Universe is flat, therefore $\Omega_\Lambda = 1 - \Omega_m$. I also assume the spectral index to have the Harrison-Zeldovich value $n = 1$ (although some inflationary models and the recent WMAP3 data suggest $n \approx 0.95$). Based on the HST key project, I take for the Hubble parameter $h = 0.7$ (the 1σ error bar is about 10%). For the matter density I take $\Omega_m = 0.30$, in accord with supernovæ Ia data combined with the flatness of the universe (I note however that the recent 2dFGRS data (Cole et al. 2005) and WMAP3 (Spergel *et al.* 2006) favour $\Omega_m \approx 0.25$). For the baryon density I assume $\Omega_b = 0.05$, based on Big Bang nucleosynthesis (Copi *et al.* 1995).

The normalization of the power spectrum, parameterised as σ_8, is still highly uncertain, with reported values in the range $\sigma_8 \approx 0.75$ (e.g. the recent WMAP3 result) to $\sigma_8 \approx 1.0$ (Massey *et al.* 2005). I fix $\sigma_8 = 0.75$, and I solve for the galaxy biasing b_g. I note that in linear theory I actually constrain the product $b_g\sigma_8$, so I can easily scale the result for any preferred value of σ_8.

In principle one should marginalise over the prior associated with each parameter. However, as I show in Section 6.7, the cross-correlation signal is very weak and is actually compatible with the null hypothesis of no correlation. Furthermore, these error bars do not take into consideration cosmic variance due of the galaxy field and so are underestimated.

By widening the priors on b_g and σ_8, I find this makes the signal even less significant. I are aware that widening priors for each parameter will reduce the significance of the result, but I chose to opt for a more optimistic view, and acknowledge that the significance of this result is tentative.

6.5 Galaxy Biasing from the Galaxy ACF

I compute the ACF of 2MASS, $C_{gg}(\ell)$, and use it to constrain the galaxy bias, b_g, in Equations 6.2 (and 6.9). Since I assume a constant bias across the magnitude shells I make the fit using all the galaxies at once, $12 < K_{20} < 14$. The redshift distribution for all of 2MASS

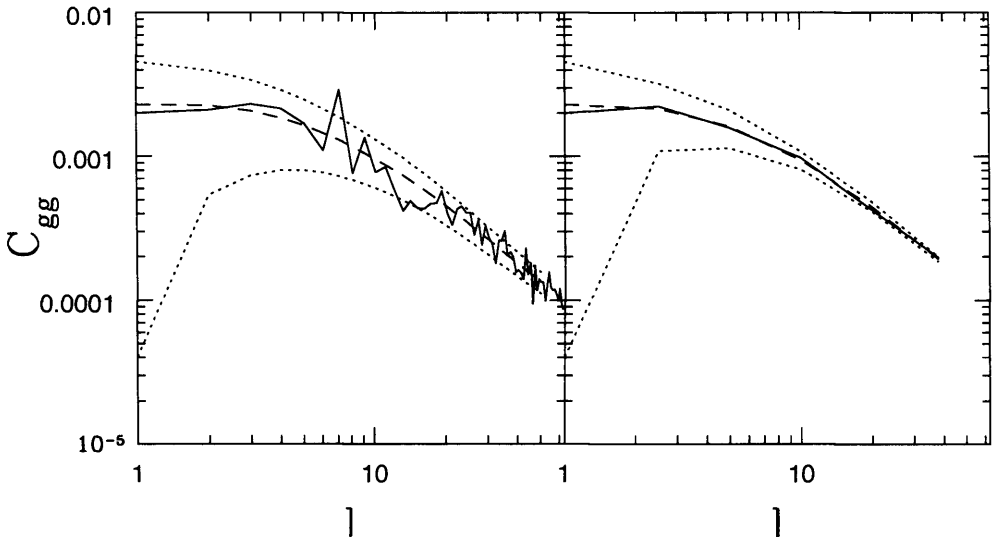

Figure 6.3: The raw (left) and binned (right) 2MASS angular power spectrum (solid line) for galaxies $12 < K_{20} < 14$, with theory (dashed) for the best fit bias $b_g = 1.40$, and 1σ Gaussian error bars (dotted). The expected Poisson noise has been subtracted from the data. I use $\Omega_m = 0.30$, $\Omega_b = 0.05$, $\sigma_8 = 0.75$, $h = 0.7$ as a fiducial model.

is plotted in Figure 6.1, and in Figure 6.3 I plot the results of the bias fitting.

Rigorously, Equations 6.3 and 6.2 (and 6.8 and 6.9) only hold for a *linear* matter power spectrum (calculated using CAMB Lewis *et al.* 2000), as I have assumed the redshift dependent power spectrum was separable: $P(k,z) = D^2(z)P_{lin}(k)$. I observe that using a linear power spectrum, one can fit the ACF well for linear scales, i.e. for $\ell < 30$. However I find that using a non-linear power spectrum (from Smith *et al.* (2003), as implemented in CAMB) provides a better fit to the data, and to higher ℓ, suggesting that using $P(k,z) = D^2(z)P_{\rm non-lin}(k)$ can be considered a valid approximation to about $\ell \sim 50$; since the bias does not change on the depth of the survey, I do not expect its scale-dependence to change much. This issue does not arise when considering the CCF, as the ISW effect should only arise on linear scales.

I therefore decide to fit the ACF using a non-linear power spectrum for $\ell \leq 50$ (to avoid highly non-linear scales), and I bin the data into 6 logarithmically spaced bins. This reduces correlation between different multipoles so that I can assume the bins are independent and have Gaussian error bars. Hence, scatter about the expected signal is

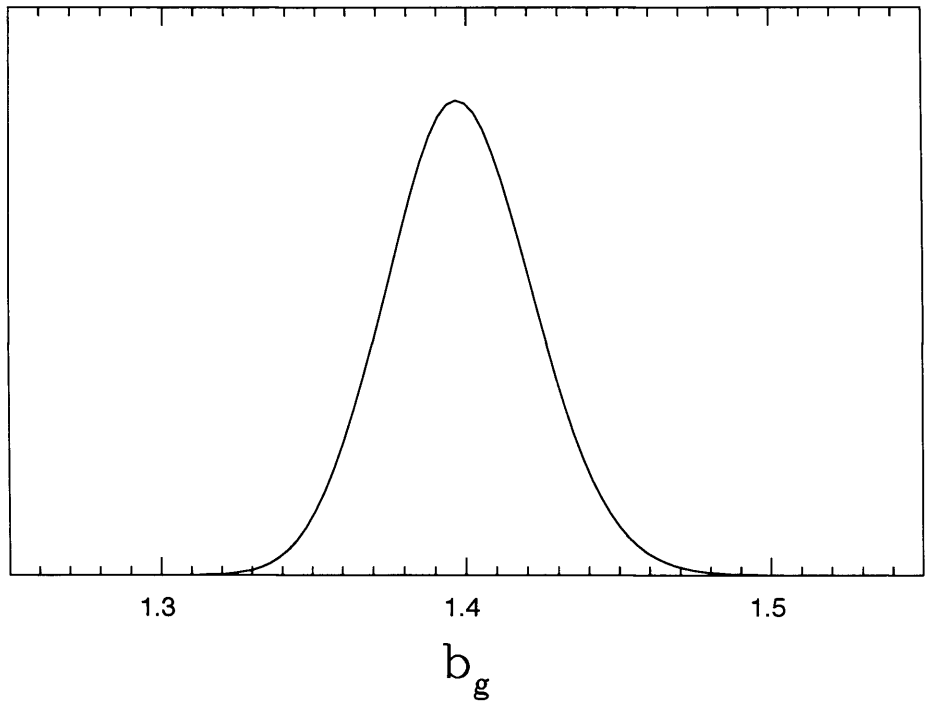

Figure 6.4: The (unnormalized) likelihood of b_g from fitting to the 2MASS galaxy autocorrelation function for a flat fiducial cosmology ($\Omega_m = 0.30$, $\Omega_b = 0.05$, $h = 0.7$, $\sigma_8 = 0.75$). The best fit bias is $b_g = 1.40 \pm 0.03$ from fitting for the multipole range $\ell = 1 - 50$. When fitting over a strict linear range ($\ell = 1 - 25$) the best fit bias changes slightly to $b_{g,lin} = 1.38 \pm 0.05$ which does not affect the χ^2 values reported in Table 6.2. The autocorrelation C_{gg} is shown in Figure 6.3 with the fit $b_g = 1.40$.

just due to cosmic variance, and the likelihood can be written:

$$-2 \ln \mathcal{L} = \det(\mathrm{M}) + \mathbf{d}^T \mathrm{M}^{-1} \mathbf{d} + const. , \tag{6.10}$$

Where the diagonal terms of M contain the variance of C_{gg} (e.g.: Dodelson (2003) or Appendix B for the full derivation),

$$\sigma^2(C_{gg}) \approx \frac{1}{f_{\rm sky}} \frac{2}{2\ell + 1} C_{gg}^2 , \tag{6.11}$$

and $\mathbf{d} = (\hat{C}_{gg} - C_{gg})$; $f_{\rm sky}$ is the fraction of sky observed; $\hat{C}_{gg}$ is the observed overdensity ACF after shot noise subtraction, given by $1/\bar{N}$ where $\bar{N}$ is the mean number of galaxies per steradian; C_{gg} is the theory (Equation 6.2 and 6.9). Note that the covariance matrix M, and its determinant, depend on b_g.

I fit for the bias using a fiducial model (flat universe with $\Omega_m = 0.30$, $\Omega_b = 0.05$, $h = 0.7$, $\sigma_8 = 0.75$) and I plot the resulting likelihood curve in Figure 6.4. The best fit value for

the multipole range $\ell = 1 - 50$ is $b_g = 1.40 \pm 0.03$ (to 2 d.p) at 1σ (fitting for a Gaussian). If I remove non-linear scales to the bias fitting, and consider only the multipole range $\ell = 1 - 25$, the error on the bias increases slightly while its value remains roughly the same ($b_{g,\rm lin} = 1.38 \pm 0.05$). I find the results in Section 6.7 do not differ significantly for these two values, and herein I take $b_g = 1.40 \pm 0.03$.

The determination of the bias is particularly sensitive to σ_8 because they both act as overall normalization factors, and in linear theory $C_{gg} \propto (b_g \sigma_8)^2$.

The above results are consistent with constraints I have derived from the 2MASS Redshift Survey (2MRS), which I have summarized in Table 4.2.

6.6 Cross-Correlation Method

I perform the cross-correlation in harmonic space. I have used masks on all the maps, and thus I cannot obtain true values of the multipole coefficients $a_{\ell m}$, as the power of the harmonic estimator will be reduced and correlations will be induced between multipoles. However, I scale for the loss of sky cover and use a full covariance matrix to account for the correlation between bins. I have obtained the spherical harmonic coefficients of the four 2MASS K_{20} shells, and the four WMAP3 maps, as outlined in Section 6.2. I perform the cross-correlation:

$$C_{gT}(\ell) = \frac{1}{(2\ell+1)} \sum_m \mathcal{R}_e(a^g_{\ell m} a^{T*}_{\ell m}) \,. \tag{6.12}$$

Taking the real part of the product ensures that $C_{gT} = C_{Tg}$.

I further bin the data, using logarithmically spaced bins and $\ell \geq 3$. I avoid $\ell = 2$ due to its anomalously low power in the CMB. For the analysis I use 5 bins $3 \leq \ell \leq 30$, as this is where the ISW signal is expected to dominate. In Figures 6.5 and 6.6 I plot the correlation using 6 bins with $3 \leq \ell \leq 200$.

In Figure 6.5 I compare the C_{gT} results of the WMAP1 and WMAP3 V-band data. Surprisingly I see a slight change, especially in the first point which corresponds to $\ell = 3 - 5$. The power in the WMAP3 maps has changed very little (see for example Figure 19 in Hinshaw *et al.* 2006), and thus the difference must be due to a slight change in the structure of these multipoles, perhaps due to the improved gain model (Jarosik *et al.*

2006). Note that although the reported power spectrum has changed at low-ℓ this is due to change in the likelihood analysis, rather than a change in the underlying data (Hinshaw *et al.* 2006).

I will be comparing two hypotheses: a null hypothesis of no cross-correlation, and that returned by Equation 6.3 (and 6.8) for a fiducial ΛCDM cosmology. To assess the fit I will compare the χ^2 values returned by the two hypotheses. Similarly I can compare the unnormalized evidence $\mathcal{E}$, where $-2\ln\mathcal{E} = \chi^2$ (if all parameters are fixed), or given by Equation 6.15 (if I marginalise over a parameter, where b_g in the equation can be replaced by any parameter). For this I use a covariance matrix, estimated from simulations, and thus I account for the correlation between ℓ bins and those between K-shells.

I make 500 simulations of a Gaussian CMB using the best fit theoretical C_{TT} from WMAP3. I apply the Kp2 mask, and correlate them with the four K-shell 2MASS maps. By not varying the 2MASS maps I have slightly underestimated the errors, because I have not accounted for the cosmic variance of the 2MASS data. I also note that the ISW signal in not inbuilt in the simulations; this should be inconsequential since this signal is negligible compared to the cosmic variance of the CMB.

I compute the χ^2 to find the favoured model and the improvement $\Delta(-2\ln\mathcal{E}) = \Delta(\chi^2)$. As usual I have $\chi^2 = \mathbf{d}^T M^{-1}\mathbf{d}$, $\mathbf{d} = (\hat{C}_{gT} - C_{gT})$, where C_{gT} is calculated for the two models, one with no correlation, i.e. $C_{gT} = 0$ and another with correlation due to ISW effect, given by equation 6.3 (and 6.8) for a fiducial cosmology. The covariance matrix is defined as:

$$M_{ij} \equiv \left\langle (\mathrm{d_i} - \langle \mathrm{d_i} \rangle)(\mathrm{d_j} - \langle \mathrm{d_j} \rangle) \right\rangle , \tag{6.13}$$

and is calculated from simulations in which the galaxies and the CMB are uncorrelated. I use 5 logarithmically spaced bins at low-ℓ where the expected signal dominates ($\ell = 3 - 30$), and I include all four K_{20} shells in the analysis, thus $i, j = 1, .., 20$. The fact that cosmic variance of 2MASS is not included suggests the simulations will *underestimate* the errors. I perform a consistency check on the covariance matrix by analytically estimating the diagonal elements of the covariance matrix:

$$M_{ii} = \sigma^2(C_{gT}) = \frac{1}{f_{sky}(2\ell+1)}\left(C_{gT}^2 + C_{gg}C_{TT}\right) , \tag{6.14}$$

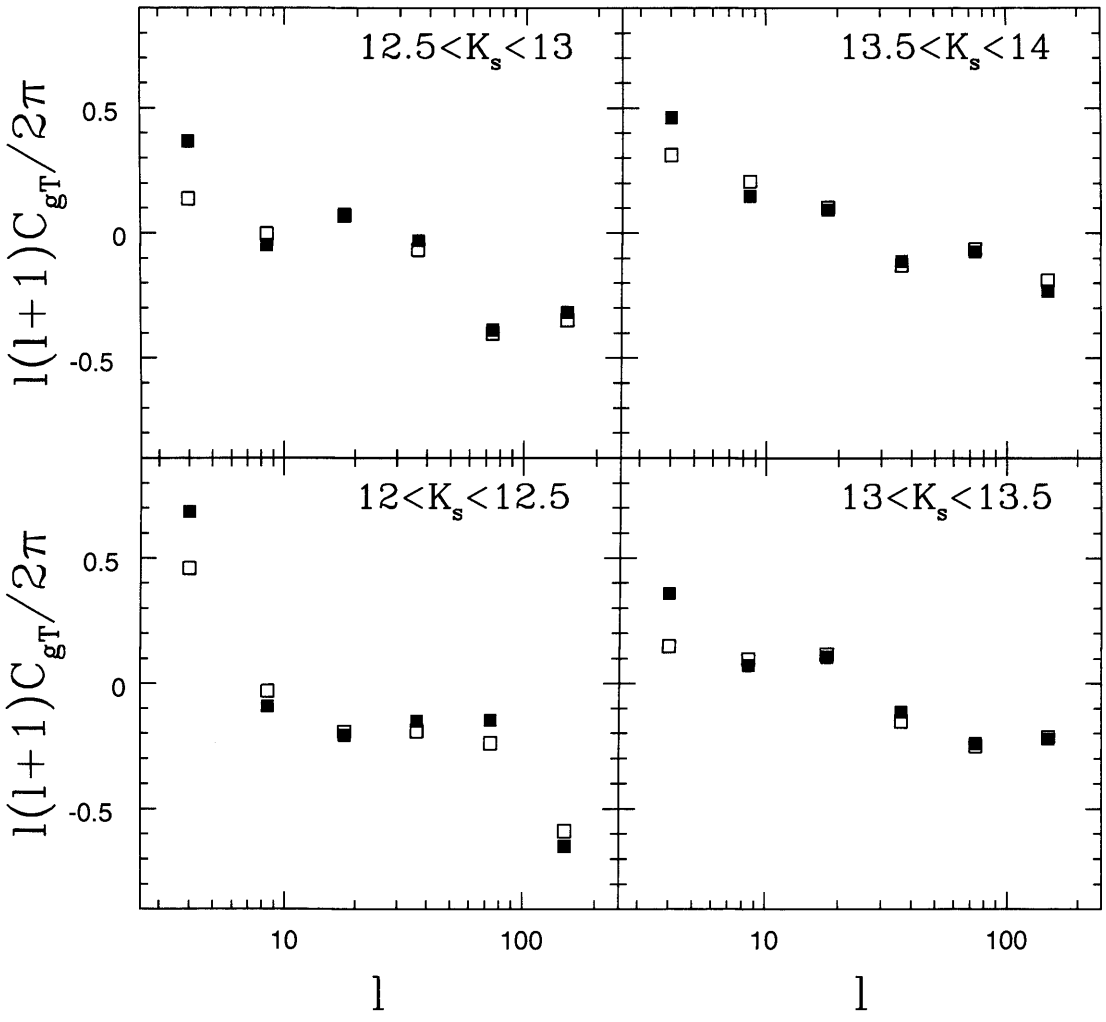

Figure 6.5: The cross-correlation C_{gT} (μK) of galaxies from the 2MASS catalogue, and the CMB from the V-band WMAP1 (open squares) and WMAP3 (filled squares) results. See Figure 6.6 for error bars. The power in the WMAP3 maps have changed very little (see for example Figure 19 in Hinshaw 2006), yet I see a slight change in the cross-correlations, especially in the first point which corresponds to $\ell = 3 - 5$. The difference may be due to a slight change in the structure of these multipoles, perhaps due to the improved gain model (Jarosik 2006).

	1	2	3	4	5
	Null Hypothesis of no correlation	ΛCDM $b_g = 1.40$	ΛCDM prior on b_g	ΛCDM $\Omega_\Lambda = 0.85$	ΛCDM marginalised over Ω_Λ
ILC	11.3	9.7	9.7	7.3	10.1
Q	12.1	10.4	10.4	8.1	10.9
V	11.0	9.5	9.5	7.4	10.0
W	10.8	9.1	9.1	6.9	9.6

Table 6.2: Log evidence ($-2\ln\mathcal{E}$) values for cross-correlation of each WMAP3 maps (V, W, Q and ILC) with four 2MASS magnitude shells, using different model assumptions and priors. In all cases σ_8 is taken to be 0.75. **Model 1** is the null hypothesis of no correlation. In **model 2**, I have considered a flat universe with $\Omega_m = 0.30$, $\Omega_b = 0.05$, $h = 0.7$ and $b_g = 1.40$ (for $b_g = 1.38$ only the W map result changes from 9.1 to 9.2). In **model 3**, I have widened the prior used on b_g to that which I obtained by fitting the 2MASS ACF on scales $\ell = 1 - 50$, i.e. $b_g = 1.40 \pm 0.03$ (the results are unchanged when using $b_{g,\rm lin} = 1.38 \pm 0.05$, the bias obtained from linear scales only, i.e., $\ell = 1 - 25$). **Model 4** is best fit $\Omega_\Lambda = 0.85$ in a universe with no curvature. In **model 5**, I have marginalised over Ω_Λ using the likelihood in Figure 6.8 assuming a flat geometry and a uniform prior on Ω_Λ in the range [0;0.95]. The evidence ratio for model 1 (null hypothesis) and 5 (marginalised ΛCDM) is $\Delta(-2\ln\mathcal{E}) \approx 1.1$ which means the data prefer a ΛCDM cosmology to the null hypothesis, but only marginally. For models 1, 2 and 4 the evidence is related to the χ^2 by $-2\ln\mathcal{E} = \chi^2$.

which is the general form of Equation 6.11 (see Appendix B for the full derivation). I find that error bars calculated using Equation 6.14 are larger than those estimated from simulations and so accounting for cosmic variance in the galaxy field would reduce the significance of these results.

6.7 Cross-Correlation Results

In this section I discuss the significance of the cross-correlation results and determine an upper limit on Ω_Λ.

6.7.1 Null Hypothesis

In Figure 6.6 I plot the results of the cross-correlation, for 6 logarithmically separated bins between ℓ=3-200, with 1σ error bars. The cross-correlation is *achromatic*, indicative of an ISW type cross-correlation. However the results appear completely compatible with the null hypothesis, and in fact scatter much less than expected.

I use five logarithmically separated bins between ℓ=3-30 to compute the $-2\ln\mathcal{E}$ values for the (ILC,Q,V,W) maps. These values can be found in Table 6.2 (model 1). By comparing to simulations, I find these values are low at the $\sim 95\%$ level.

6.7.2 ΛCDM Fiducial Model

To rule out the null hypothesis, at face value without considering a competing theory, I would actually need a high χ^2 value. However, I are comparing two theories and thus can ask the more subtle question of which the data prefer. To do this I can consider the ratio of the evidences, $\Delta(-2\ln\mathcal{E})$.

In Figure 6.7 I plot the results again for the two furthest redshift shells, which contain the most galaxies, for 5 bins at low-ℓ where the expected signal dominates. I also show the theoretical signal expected from the fiducial ΛCDM.

Using these bins and the four K_{20} shells, the $-2\ln\mathcal{E}$ values found for the ISW theory, using $b_g = 1.40$ and a fixed fiducial cosmology are reported in Table 6.2 (model 2). There is an improvement of $\Delta(-2\ln\mathcal{E}) \approx 1.5$, and thus I confirm that the data prefer the ISW theory to the null hypothesis (of no correlation, or equivalently Einstein-de Sitter). However rule of thumb has it that 'strong' evidence is $\Delta(-\ln\mathcal{E}) \geq 3$, and thus this improvement is not compelling.

I widen the uncertainty around the bias value, using the error bars from Section 6.5. There I found $P(b_g)$ was approximately a Gaussian with $(\mu, \sigma) = (1.40, 0.03)$, although I use the curve from Figure 6.4 for the marginalisation:

$$\mathcal{E} = \int P(\text{data}|\text{theory}, b_g) P(b_g) \mathrm{d}b_g \,, \tag{6.15}$$

where I have assumed uniform priors on the theory. In Table 6.2, I record the $-2\ln\mathcal{E}$ results for a ΛCDM with a prior on the bias (models 3), which are identical at 2 d.p. with

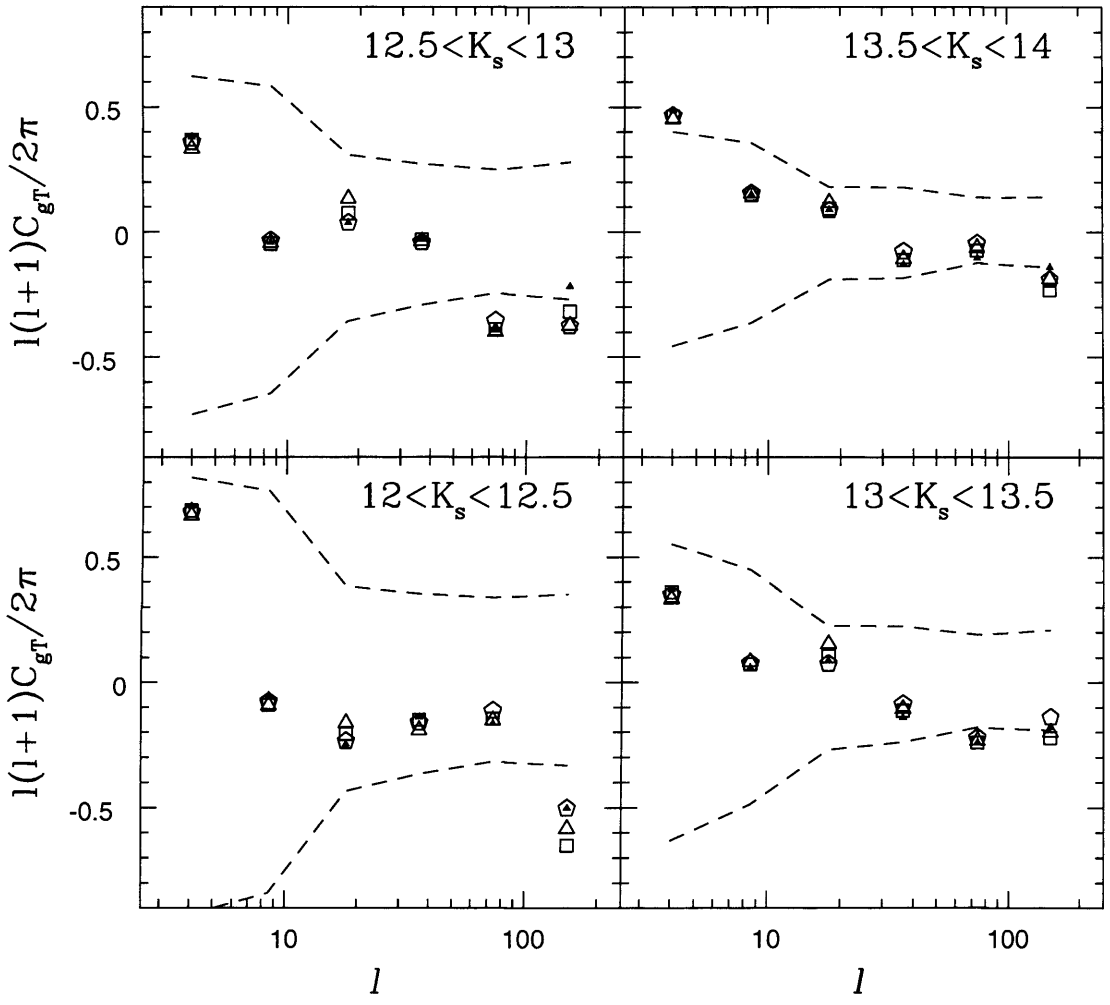

Figure 6.6: Cross-correlation $C_{gT}(\mu K)$ results for the ILC (small triangle) , Q (open triangle), V (open square), and W (open pentagon) CMB maps with different magnitude bins of the 2MASS galaxy surveys. The dashed lines are 1σ error bars about the null hypothesis, as evaluated from simulations. An ISW effect is expected to be *achromatic*, which is what I observe, but the null hypothesis is not ruled out.

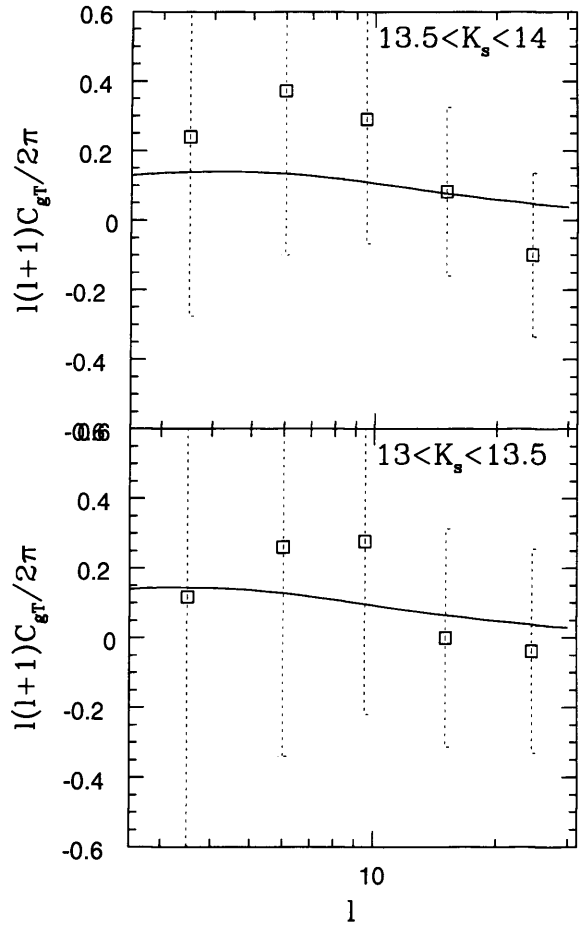

Figure 6.7: The observed C_{gT} (μK) (*squares*) from the V-band CMB map and the furthest magnitude shells of the 2MASS Survey ($13 < K_{20} < 13.5$ and $13.5 < K_{20} < 14$), with 1σ cosmic variance. These two shells contain the most galaxies. The solid line represents the theory for the fiducial model (flat universe with $\Omega_m = 0.30$, $\Omega_b = 0.05$, $h = 0.7$, $\sigma_8 = 0.75$) and $b_g = 1.40$. I have used 5 bins between $\ell = 3 - 30$ which corresponds to scales for which the ISW signal dominates.

those obtained from fixing $b_g = 1.40$. I get very similar results if I use the 2D probability distribution function $P(b_g, \sigma_8)$ and marginalise over both b_g and σ_8 (using a Gaussian with $\mu_{\sigma_8^2} = 0.56$ and $\sigma_{\sigma_8^2} = 0.08$). The results are also unchanged if I use the strictly linear bias $b_{g,lin} = 1.38 \pm 0.05$.

6.7.3 Assessing the goodness of fit

By comparing the χ^2 values to those obtained from simulations, I find that they are low to $\sim 95\%$, which is also evident from the lack of scatter in Figure 6.6. However, I are interested in maximising the evidence, or equivalently minimising the χ^2, and thus I find that moving from the null hypothesis to the ΛCDM model, the fit is improved (raising the interesting question: is minimising the χ^2 always appropriate?).

In the above analysis, I consider 20 correlated data points (five angular points in each of the four radial shells), and calculate the exact χ^2 using a full covariance matrix. I can also consider each magnitude shell separately and calculate the χ^2 for each one, as a consistency check. The χ^2 values obtained for the null hypothesis are (1.70, 0.67, 0.94, 2.36) going from the nearest to the furthest K_{20} shell, and for a fiducial model I find (1.72, 0.58, 0.83, 2.16). When the data are thus considered, a fiducial model is not always a better fit than the null hypothesis, and data in the closest shell prefer the null hypothesis.

6.7.4 Upper Limit on Ω_Λ and Marginalisation

Above I have compared a fiducial cosmology to the null hypothesis. Alternatively I can chose to consider only a fiducial ΛCDM model and use the cross-correlation to constrain its parameters. I vary Ω_Λ, and Ω_m keeping all other parameters fixed ($\Omega_m = 1 - \Omega_\Lambda$), and fit it to the measured correlation.

In Figure 6.8 I plot the resulting likelihood. I find a best fit of $\Omega_\Lambda = 0.85$, and upper limits of 0.87, 0.89, 0.90 at 1, 2, 3σ respectively. Corresponding $-2\ln\mathcal{L}$ values can be found in Table 6.2 (model 4).

This relatively high value for Ω_Λ is in good agreement with other studies of the ISW effect; Cabre *et al.* (2006) find $\Omega_\Lambda = 0.8 - 0.85$ at the 1σ level. As can be seen, the null hypothesis ($\Omega_\Lambda = 0$) is less than 2σ away from the best fit result, confirming that I cannot confidently rule it out.

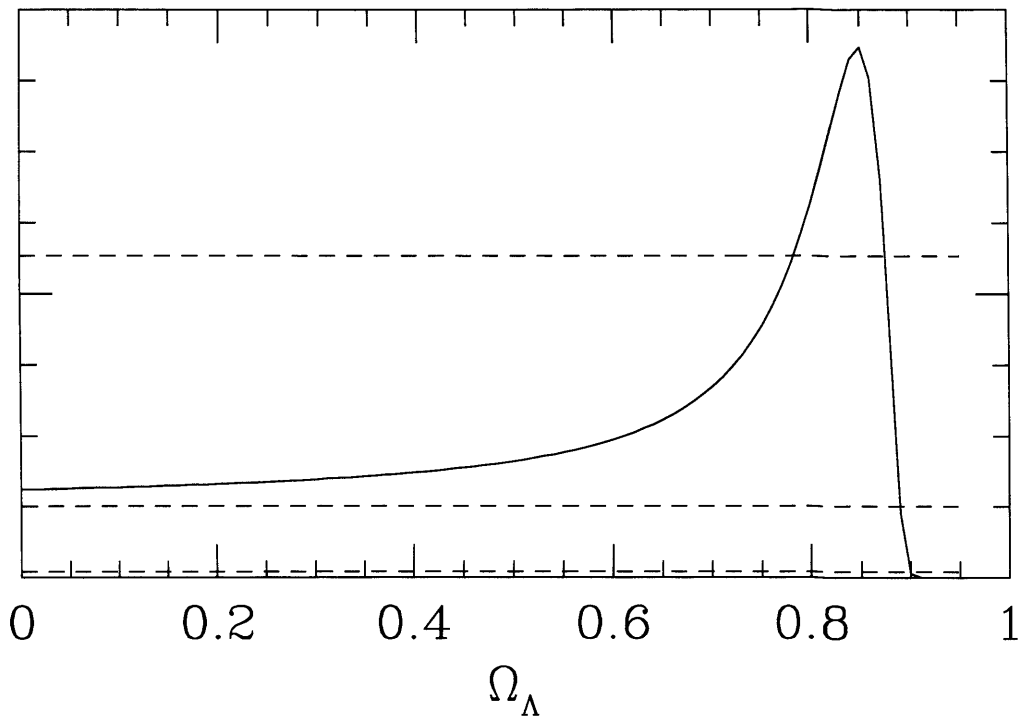

Figure 6.8: The (unnormalized) likelihood of Ω_Λ from fitting to the observed C_{gT} results (V band). The maximum is at $\Omega_\Lambda = 0.85$ Horizontal lines indicate the 1,2,3 σ levels, equivalent to the decrease in the likelihood value. I find the corresponding upper limits on Ω_Λ at 0.87, 0.89,0.90. Corresponding χ^2 values can be found in Table 6.2.

In the last column of Table 6.2, I present the marginalised evidence for a ΛCDM model (model 5), where the prior on the theory is flat over $\Omega_\Lambda = 0 - 0.95$, and the likelihood of the model is taken from Figure 6.8. For this model $\Delta(-2\ln\mathcal{E}) \approx 1.1$ on average, so the data prefers a ΛCDM model to the null hypothesis, but only marginally.

Bearing in mind this issue, and the fact that the χ^2 values are low for all models, any claim for an ISW detection using 2MASS and WMAP3 remains *tentative*, and indeed the results are also consistent with the null hypothesis of no correlation within the 2σ level.

6.8 Axis of Evil

I briefly consider other possible sources and statistics of a positive cross-correlation between the CMB and LSS. As discussed in Section 6.1, interesting anomalies dubbed the "Axis of Evil" (AoE) have been observed in the WMAP data of the CMB that indicate a possible departure from statistical isotropy (Land & Magueijo 2005*a*). Here I give a brief

description of the AoE anomaly, but the reader should refer to Land & Magueijo (2005*a*) for a detailed description.

In harmonic space, a statistically isotropic map is expected to have independent ℓ modes. For a given multipole ℓ, the power should also be distributed randomly among each m-mode, but it is possible to rotate any map so that the power in a given multipole is mostly in a given m-mode. However, if for a given frame, several multipoles have power mostly distributed in one m-mode, then the map can no longer be considered statistically isotropic. Land & Magueijo (2005*a*) found that there existed a set of nearly identical frames (with axis dubbed the "Axis of Evil") in which the multipoles of the WMAP1 maps showed phase correlations.

Possible sources of these anomalies are: foreground contamination; astrophysical effects (*e.g.*, lensing and moving cluster effect); alternative cosmological paradigms. If the AoE was in some way due to local inhomogeneities (*e.g.*, Vale 2005) then one might also expect a C_{gT} cross-correlation on these large scales. I investigate the AoE anomaly in two ways. Firstly, I rotate the 2MASS data to the frame of the WMAP AoE frame and search for anomalous phase correlations in 2MASS in that frame. Secondly, I rotate the 2MASS data in all possible directions, searching for an AoE type anomaly in all frames.

For the first test, I examine if the AoE signal observed in the CMB is also present in the 2MASS data. In Figure 6.9 I plot the power observed in each m-mode, for the AoE frames returned by the CMB. For each multipole, this is the frame where one m-mode dominates. I plot the power ratio $2|a_{\ell m}|^2/C_\ell$ (without the 2 factor for $m = 0$) evaluated in the AoE frames, for the 2MASS ($12 < K_{20} < 14$) as well as the CMB (using the cleaned ILC map of Tegmark, de Oliveira-Costa & Hamilton 2003). By definition, in these frames the CMB observes a pattern of one m significantly dominating each multipole. I do not observe a similar pattern in the 2MASS data, and thus conclude that if there exists a source responsible for the AoE features, then it is unlikely to be the same source of the C_{gT} correlation observed above.

For the second test, I looked at 2MASS independently over $\ell = 2 - 20$ and found no evidence for any AoE type structure (a correlation of multipole frames as defined above). Clearly the 2MASS catalogue is highly anisotropic, with structures such as the Supergalactic Plane visible by eye as well as the Galactic mask. Is it not strange that a statistic

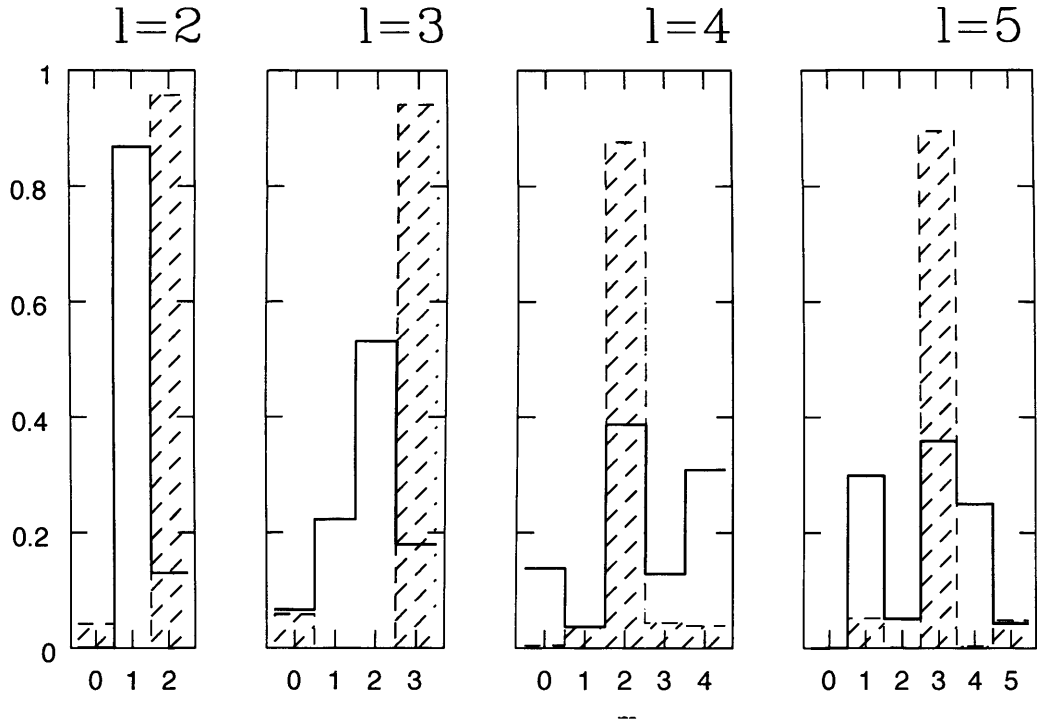

Figure 6.9: The fraction of power in each m-mode for multipoles $\ell = 2, 3, 4, 5$. The $a_{\ell m}$s are computed in the Axis of Evil (AoE) frames returned by the CMB. By definition the multipoles of the CMB are dominated by one m-mode in these frames (shaded). I do not observe a similar pattern in the 2MASS results (solid line). Negative values of m are not shown as $(-1)^m a_{\ell -m} = a^*_{\ell m}$.

that measures evidence for deviations from statistical isotropy in the CMB does not find any such feature in 2MASS? The AoE statistic highlights a very particular type of phase correlation, in harmonic space, and is by no means a conclusive test for general deviations from statistical isotropy. The fact that a clearly non-Gaussian and anisotropic map, such as 2MASS, does not return a anomalous AoE signal for $\ell = 2 - 20$ perhaps highlights the weakness of this statistic, and throws caution at how one defines and selects appropriate statistics. Perhaps the non-Gaussianity is 'washed out' by the depth of the survey - anomalies might be more significant in the shallowest part of the survey. However, there is currently no conclusive way to test a map for deviations from statistical isotropy.

6.9 Discussion

I calculate the cross-correlation between the 2MASS galaxy survey and the WMAP3 data. This updates the work of Afshordi *et al.* (2004) who cross-correlated 2MASS with WMAP1.

The cross-correlation signal expected in a ΛCDM Universe scales with the linear galaxy bias, b_g, and in linear theory with the product $(b_g\sigma_8)$. I fix $\sigma_8 = 0.75$, and use a flat fiducial cosmology (based on inflation). I use $\Omega_m = 0.30$ (based on supernovæ Ia data), $\Omega_b = 0.05$ (based on Big Bang nucleosynthesis), $h = 0.7$ (based on the HST key project), $n = 1$ (i.e., the Harrison-Zeldovich spectral index).

Fitting the fiducial cosmology to the angular auto-correlation function of the 2MASS galaxy survey for $12 < K_{20} < 14$, yields a linear bias value of $b_g = 1.40 \pm 0.03$, assessed from multipole scales $\ell = 1 - 50$ ($b_{g,\rm lin} = 1.38 \pm 0.05$ assessed from multipole scales $\ell = 1 - 25$). As the 2MASS galaxy survey is shallow, I assume b_g is constant with redshift over the depth of the survey.

The measured cross-correlations obtained from four different WMAP maps (V, W, Q, and ILC) and four different magnitude shells of 2MASS ($12 < K_{20} < 12.5$, $12.5 < K_{20} < 13$, $13 < K_{20} < 13.5$, and $13.5 < K_{20} < 14$) show an achromatic signal, as expected from an ISW effect. However, the observed signal is also within the 1σ error bars obtained from cross-correlating random simulations of the CMB with 2MASS data. This means the data are consistent with the null hypothesis of no correlation. Furthermore the error bars do not account for cosmic variance of the galaxy field and so should be larger.

I compare the observation with the ISW signal expected in a fiducial ΛCDM model, with a fixed bias and an uncertainty around the bias value which I found when fitting the auto-correlation function. The ΛCDM model finds a lower chi-squared, and thus is a better fit compared to the null hypothesis, but in both cases of treating the bias the evidence change is only $\Delta(-2\ln\mathcal{E}) \approx 1.5$. Whichever model is considered - the null hypothesis or a ΛCDM universe - the χ^2 values are low when compared to simulations.

Varying the dark energy density component of the ΛCDM model and assuming flatness, I find that the data prefer a high value of $\Omega_\Lambda = 0.85$, with $\Omega_\Lambda < 0.89$ (95% CL).

Thus, there is a higher correlation between WMAP3 and 2MASS than that expected

by a ΛCDM universe with $\Omega_\Lambda = 0.7$. However, the observed cross-correlation may not only be due to an ISW effect. Other signals might contribute to the correlation: positive curvature (even if very small) or cosmic magnification (higher redshift galaxies can contribute more than expected if they are lensed by the lower redshift galaxies and their luminosity function is such that the effect leads to a positive correlation).

When I marginalise over Ω_Λ, the evidence ratio between the null hypothesis and ΛCDM becomes $\Delta(-2\ln\mathcal{E}) \approx 1.1$ so I can say that the data prefer a ΛCDM universe, but only marginally. In any case, the correlation observed is consistent with both hypotheses within 2σ.

I also investigate "Axis of Evil" (AoE) type anomalies, which detect phase correlations between different multipoles in harmonic space. These phase correlations are not expected in a statistically isotropic map (Land & Magueijo 2005*a*). I do not observe an AoE type of structure in the 2MASS catalogue. As non-Gaussian features are expected in the LSS I feel this result raises issues about the use of the AoE statistic as a general test for statistic anisotropy.

I do not observe correlations between the CMB fractional power distribution as measured in its AoE frame and that of 2MASS, constraining the possible explanations of the low ℓ anomalies in the CMB.

Future spectroscopic and photometric galaxy redshift surveys (*e.g.*, the dark energy Survey, the Wide Field Multi-Object Spectrograph) will yield more galaxies out to higher redshifts. Afshordi (2004) showed that an all sky survey with 10 million galaxies and uniform sky coverage between $0 < z < 1$ would lead to a detection of the ISW effect at the 5σ level. It remains to be assessed what combination of depth and sky coverage is optimal for detecting the ISW effect.

I highlight that a claim for an ISW detection could be greatly weakened if one considers some of the uncertainty around the cosmological parameters as well as cosmic variance of the galaxy field which would widen the uncertainties on the measurement. For the 2MASS-WMAP3 correlation the signal-to-noise ratio is poor, however with a stronger data set a full Markov Chain Monte Carlo exploration of parameter space should be done.

CHAPTER 7

FORECASTS FROM ISW FOR THE NEXT GENERATION OF GALAXY SURVEYS

Summary

In this Chapter I review the method of using the Fisher Information Matrix for parameter forecasting. In Chapter 5 I showed how the amount (Ω_Λ) and equation of state (w) of dark energy affect the Integrated Sachs-Wolfe (ISW) signal. Since they have similar effects, if we try to simultaneously infer both parameters from data there will be a degeneracy. I use the ISW effect to forecast errors on Ω_Λ and w for the next generation of galaxy surveys, in particular from the Dark UNiverse Explorer (DUNE) and the Dark Energy Survey (DES). I find DES cannot break the (w, Ω_Λ) degeneracy mainly due to low sky coverage, though DUNE is able to. The constraints from DUNE improve if we use photometric redshift information to trace the characteristic evolution of the ISW signal with redshift. To probe how realistic the Fisher forecast method is, I compare forecasts with current constraints from SDSS and find they are in general agreement.

Finally, I investigate a general parameterisation of gravity modification, Minimalist Modified Gravity (MMG), which introduces a growth parameter γ in the linear growth function $f = \frac{d\ln D}{d\ln a} = \Omega_m^\gamma$. The goal of MMG is to pinpoint discrepancies between the expansion history and growth of structure for a given cosmology. I show it is possible to constrain γ using the ISW effect alone. DUNE may be able to measure γ to 12% in a low matter density universe.

7.1 Introduction

The ISW effect does not provide as tight constraints as weak lensing does due to the large error bars it is subject to, but can nonetheless be a very useful cosmological tool. It can be used as an independent probe to confirm the cosmological model constrained by other probes. In the context of general relativity and in a flat Universe, the existence of an ISW signal is a definite signature and confirmation of the presence of dark energy.

It can also be used to test for deviations of general relativity and there are several theories which predict the existence of an ISW signal on large scale without the need to resort to the presence of Dark Energy (Song, Sawicki & Hu 2006; Song, Hu & Sawicki 2007; Schmidt, Liguori & Dodelson 2007). In predicting the observed ISW signal, these theories correctly model the observed growth of structure, yet necessarily need to also explain the observed cosmic expansion history. The ISW can also be used to investigate general deviations from General Relativity, without probing a specific model, by looking for discrepancies between the growth of structure and the cosmic expansion history of the Universe, such as proposed by *Minimalist Modified Gravity*.

In Section 7.2, I overview the method for constraining parameter uncertainties from the Fisher Information Matrix (FIM). In Sections 7.3 and 7.4, I overview the next generation of large scale structure surveys, notably the Dark Energy Survey (DES) which is expected to have first light in 2010, and the Dark UNiverse Explorer (DUNE) which is a space mission expected to be launched in 2017. In Section 7.5, I use the ISW effect expected for DES and DUNE to forecast uncertainties on the dark energy parameters Ω_Λ and w. In Section 7.7, I introduce the *Minimalist Modified Gravity* (MMG) phenomenological parameterisation of the growth factor (Linder 2005) in order to search for deviations from general relativity on large scales. I use the ISW to predict constraints on the growth parameter γ for the DES and DUNE surveys. Finally, in Section 7.8, I present my conclusions on how well ISW can constrain cosmology with the next generation of large scale galaxy surveys.

7.2 The Fisher Information Matrix

It is possible to forecast the precision with which a future experiment will be able to constrain cosmological parameters, by using the Fisher Information Matrix (for a detailed derivation of the following see Tegmark, Taylor & Heavens 1997 or Dodelson 2003) . This method requires only three fundamental ingredients:

- A set of cosmological parameters $\vec{\theta}$ for which one wants to forecast errors, and assumed values of these for a 'true' underlying universe. For example, this could be a set of parameters $\vec{\theta} = (\Omega_\Lambda, w)$, for which one can assume: $\Omega_\Lambda^{\rm true} = 0.75, w^{\rm true} = -1$.
- A set of n measurements of the data $\vec{x} = (x_1, x_2, \ldots, x_n)$, say the galaxy-temperature angular power spectrum C_{gT} over a range $\ell = 1 \ldots n$, and a model for how the data depend on cosmological parameters, i.e.: $C_{gT}(\ell) = C_{gT}(\ell, \vec{\theta})$
- An estimate of the uncertainty on the data $\Delta(C_{gT})$, which may depend on the given experiment (instrument noise, shot noise, etc...) as well on the data estimator (e.g., cosmic variance).

The Fisher Information Matrix (FIM) is defined by:

$$F_{ij} = \left\langle \frac{\partial^2 \mathcal{L}}{\partial\theta_i \partial\theta_j} \right\rangle , \tag{7.1}$$

where $\mathcal{L} = -\ln L$ and $L = L(\vec{x}, \vec{\theta})$ is the likelihood function or the probability distribution of the data $\vec{x}$, which depends on some model parameter set $\vec{\theta}$. If the data are correlated, the Fisher matrix then this might instead be the inverse of the covariance matrix between data points. In this chapter, I only consider uncorrelated data points.

The uncertainty on the parameter θ_i can be estimated directly from the FIM and has been shown to obey:

$$\Delta\theta_i \geq \frac{1}{\sqrt{F_{ii}}} , \tag{7.2}$$

if all other parameters are known. This is known as the Cramér-Rao inequality. This is the key strength of the FIM forecast method, in that it places a solid lower limit on the parameter uncertainties, if the underlying probability distribution $L(\vec{x}, \vec{\theta})$ is Gaussian. If

the parameters $\vec{\theta}$ also have Gaussian distribution around the fiducial value, then:

$$\Delta\theta_i = \frac{1}{\sqrt{F_{ii}}}\,, \tag{7.3}$$

when all the other parameters are fixed.

If the vector of parameters $\vec{\theta}$ is allowed to vary, then the uncertainties for each parameter can still be obtained, and obey:

$$\Delta\theta_i \geq \sqrt{(F^{-1})_{ii}}\,, \tag{7.4}$$

where F^{-1} is the inverse of the FIM. In this case, the uncertainty for θ_i has been obtained by implicitly marginalizing over the other parameters. An unmarginalized estimate of the uncertainty of θ_i would be $1/\sqrt{F_{ii}}$.

By assuming the errors on the spherical harmonic estimator $C_{gT}(\ell)$ are Gaussian, then:

$$F = \left\langle \frac{\partial^2 \mathcal{L}}{\partial\theta_i \partial\theta_j} \right\rangle = \frac{1}{2}\left\langle \frac{\partial^2 \chi^2}{\partial\theta_i \partial\theta_j} \right\rangle\,, \tag{7.5}$$

since $\mathcal{L} = -\ln \mathrm{L} = \frac{1}{2}\chi^2$. Using the definition of χ^2:

$$\chi^2(\theta_i) = \sum_\ell \left[\frac{C_{gT}(\theta_i) - C_{gT}^{\mathrm{obs}}}{\Delta C_{gT}}\right]^2\,, \tag{7.6}$$

this gives:

$$F_{ij} = \sum_\ell \frac{1}{(\Delta C_{gT})^2}\left[\frac{\partial C_{gT}}{\partial\theta_i}\frac{\partial C_{gT}}{\partial\theta_j} + (C_{gT} - C_{gT}^{\mathrm{obs}})\frac{\partial^2 C_{gT}}{\partial\theta_i \partial\theta_j}\right] \tag{7.7}$$

$$\simeq \sum_\ell \frac{1}{(\Delta C_{gT})^2}\frac{\partial C_{gT}}{\partial\theta_i}\frac{\partial C_{gT}}{\partial\theta_j}\,, \tag{7.8}$$

where C_{gT} implicitly depends on ℓ, and where the last term in 7.7 can be neglected (Dodelson 2003).

The FIM is useful to forecast the minimum statistical uncertainty of a parameter for a given experiment, and is often used to rate the suitability of a given experiment to constrain desired parameters. If two experiments are independent, one can easily combine the information of two Fisher matrices F_1 and F_2, simply by adding them. The combined uncertainty on a parameter θ_i is then:

$$\Delta\theta_i \geq \sqrt{\left[(F_1 + F_2)^{-1}\right]_{ii}}\,. \tag{7.9}$$

7.3 The Dark UNiverse Explorer (DUNE)

DUNE (Réfrégier *et al.* 2006) is a European wide field space imager, intended to be launched circa 2017. Its principal aim is to provide an all-sky survey in the optical and NIR, which will be used to investigate the nature of Dark Energy and Dark Matter - the *Dark Universe* - through the study of weak gravitational lensing. It will also provide a wealth of information useful for the study of galaxy and star formation as well as for astrobiology. As this Thesis is being written, the outcome of the DUNE funding application to the European Space Agency's Cosmic Vision programme is not yet known; the decision should be made public in October 2007. In this Section, I give an overview of the scientific goals, requirements and planned data products of the DUNE mission and list the observable quantities which can be extracted from the DUNE Extragalactic survey in order to probe the dark Universe. The DUNE mission specifications are compared with those of the Dark Energy Survey (DES) in Table 7.1.

7.3.1 Scientific Goals & Requirements

The goals of DUNE are to solve the fundamental outstanding issues and questions in modern cosmology, which are:

- What is the nature of Dark Energy and Dark Matter?
- What are the seeds of structure formation and how do LSS and galaxies evolve with time and environment?
- Is Einstein's theory of gravity the most accurate and simplest way to describe cosmological observations?

In order to achieve these scientific goals, the main approach of DUNE will be to use the powerful tool of weak lensing which requires estimating redshifts and imaging the shapes of billions of galaxies. Spectroscopic redshift acquisition for such a large number of galaxies is expensive both logistically and time-wise, so that it is more efficient to estimate redshifts photometrically. The shape measurements are much more accurate in the absence of atmospheric turbulence, whilst photometric redshift estimation are vastly

improved with NIR photometry to depths that are not available from ground based telescopes. DUNE is therefore naturally being designed as a space telescope, ideal for using weak lensing as a cosmological tool.

The DUNE instrument will be composed of a 1.2m telescope with separate visible and NIR focal planes used simultaneously with a dichroic, each with a field of view covering 0.5deg^2. The visible band will be a broad band ($R + I + Z$; $550 - 920$nm) with a PSF of 0.23" (FWHM) and 0.10" sized pixels, enabling stable shape measurement. The three NIR bands (Y, J, H; 920-1600nm) are required for the redshift estimation.

7.3.2 Survey Strategy and Data Products

DUNE will survey the entire sky over a period of four years, and will provide four separate surveys, two of which (the extragalactic and the Galactic) will form the DUNE All-Sky Survey (DASS). The planned extragalactic data products are:

1. The wide extragalactic survey (DASS-EX) covering $20{,}000\text{deg}^2$ (the entire visible extragalactic sky) and cataloguing about 3 billion galaxies with a mean redshift of 1 over a period of three years (the mean galaxy surface density is predicted to be 35 galaxies per arcsecond). The predicted redshift distribution of DUNE-EX is shown in Figure 7.1 (dashed red line) and compared with the predicted DES distribution (blue histogram).

2. The DUNE Medium-Deep survey (DUNE-MD) will cover 100 deg^2 over a period of six months and probe extragalactic star-forming regions out to a redshift of $z \sim 12$.

By providing both wide and deep galaxy catalogues, the DASS-EX and the DUNE-MD will permit a detailed study of galaxy evolution and its relation to structure growth, as well as discovering higher redshift objects. The two planned Galactic surveys are:

3 The DUNE Galactic survey (DASS-G), which will compose the second half of the DASS and take three months to complete. It will probe Galactic structure, as well as heavily dust-obscured and low temperature objects in the Galactic plane and bulge.

4 The DUNE Micro-Lensing survey (DUNE-ML) will cover 4 deg^2 in the Galactic Bulge over a period of three months and catalogue Earth-mass extrasolar planets.

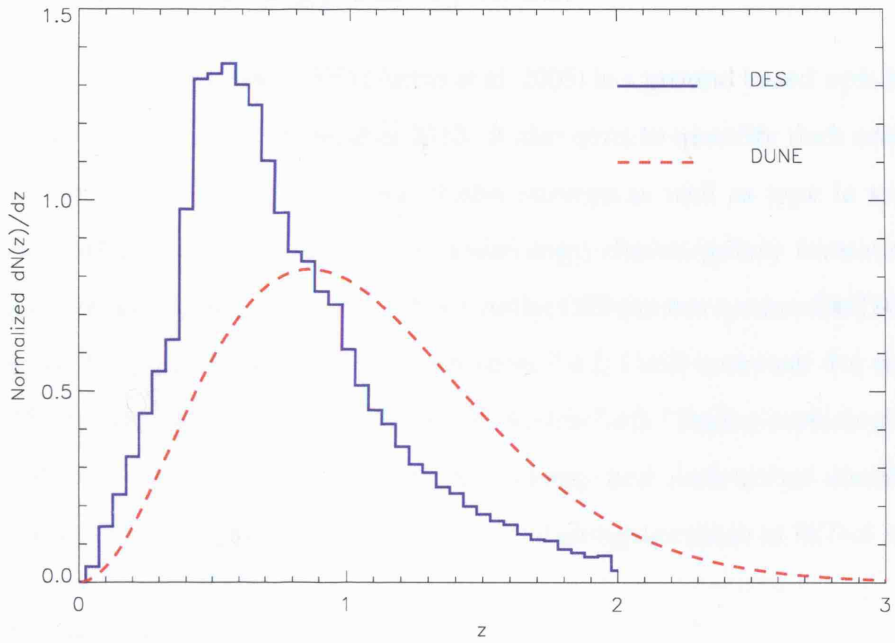

Figure 7.1: Comparison of the predicted redshift distributions for the Dark Energy Survey (DES, blue histogram, mean redshift $z \sim 0.8$) and for the Dark UNiverse Explorer (DUNE, red dashed line, mean redshift $z \sim 1$).

It will provide a reference map useful for astrobiological searches.

7.3.3 Cosmological Tools

The primary cosmological tool of DUNE will be to use galaxy shapes and their measured shear to quantify the weak lensing due to the inhomogeneous matter distribution in the Universe. However, the wealth of data provided by DUNE naturally leads to investigation of LSS using other observable statistics. These secondary cosmological tools include the Baryon Acoustic Oscillations (BAO) and Cluster Counts (CC) (see this Thesis' introduction). Another secondary tool will be the ISW effect which I have described in Chapter 5 and which I use to make forecasts of dark energy parameters in Sections 7.5 and 7.7.

7.4 The Dark Energy Survey (DES)

The Dark Energy Survey (DES) (Annis *et al.* 2005) is a ground based optical-NIR survey set to have first light in September 2010. It also aims to quantify dark energy and dark matter. It will provide galaxy and cluster surveys as well as type Ia supernovælight curves, making it a useful survey for cosmology, cluster/galaxy formation and stellar evolution studies. In Section 7.4.1, I describe the DES camera system (DeCAM) which will carry out the Dark Energy Survey. In Section 7.4.2, I will overview the survey strategy for DES and the planned data products. In Section 7.4.3, I list the cosmological probes the DES plans to use in order to quantify dark energy and dark matter distributions in the Universe. The DES specifications are presented alongside those of DUNE in Table 7.1.

7.4.1 DeCAM

DeCAM is a new instrument commissioned for the National Optical Astronomy Observatory (NOAO) designed as a wide field imager for the Blanco 4m telescope at the CTIO. It will be available to the entire astronomical community with 30% of its observing time dedicated to the Dark Energy Survey. The specifications of DeCAM are not yet finalized, but I give here an overview of current plans for DeCAM, as outlined in the White Paper of The Dark Energy Survey Collaboration (2005).

The imaging system consists of a 519 Megapixel optical CCD camera with 0.27″ pixels and a cryogenic cooling system maintaining the focal plane at 180K. The 1m wide field optical corrector has a 2.2 deg diameter field of view (3 deg^2 imaging area). The system will be fitted with the SDSS g, r, i, z filters and is planned to detect objects down to the limiting magnitudes of g=24.6, r=24.1, i=24.3, z=23.9. Additional filters might still be added to the system. These limits are the 10σ limits in 1.5″ aperture assuming 0.9″ seeing. They were derived from simulations which incorporate weather and seeing data at CTIO over 30 years (for the 5σ limit, the photometry limits are 1.5 mag fainter). The resulting wavelength sensitivity of DeCAM is 400-1100nm (this might change with the specifications).

Note: During the completion of this Thesis, the DES team have decided to add the Y filter.

7.4.2 Survey Strategy and Data Products

The DES will be carried out over 525 nights during September to February (when the mean seeing is 0.65") during 5 years. First light is expected at the earliest in September 2010 and the DES should be finished circa 2015.

Photometric redshifts will be acquired through a hybrid method incorporating e.g., an artificial neural networks technique developed by Collister & Lahav (2004) and template fitting techniques such as Hyperz (Bolzonella, Miralles & Pelló 2000) or Pégase (Le Borgne *et al.* 2004). This hybrid method was shown to return smaller photometric redshift errors than ANN, template and polynomial fitting techniques on their own.

The ANN technique requires at least $5.10^4 \sim 10^5$ galaxies with spectroscopic redshifts to train the network. The DES intentionally overlaps with existing spectroscopic redshift surveys in order to achieve this. For bright magnitudes, the DES will overlap with 70,000 galaxies in the SDSS Southern Equatorial Stripe down to r$\sim$ 20 and 90,000 galaxies in the 2 degree Field Galaxy Redshift Survey (2dFGRS) down to b_j=19.45 (Colless *et al.* 2003). For fainter magnitudes, the overlap will include 60,000 galaxies in the VIMOS VLT Deep Survey (VVDS) down to $I_{AB} = 24$ (Le Fèvre *et al.* 2005) and 30,000 galaxies in the Keck DEEP2 Survey (Davis, Gerke & Newman 2004). In total DES will have access to 250,000 spectroscopic redshifts which will be enough for the required training, validation and control sets necessary for the ANN technique.

Upon completion, DES will produce the following data products:

1. A galaxy survey covering 5,000 deg^2 ($1/8^{\text{th}}$ of the sky), including 300 million galaxies. The photometric redshift error, defined as $\sigma_z = \langle (z_{\text{spec}} - z_{\text{photo}})^2 \rangle^{1/2}$ is predicted to be $\sigma_z \leq 0.12$ for $z < 1$ and with mean redshift $z \sim 1$. By adding J, H and K bands from VISTA this can be reduced to $\sigma_z \leq 0.10$. Galaxy shapes will also be measured for over 200 million galaxies for the weak lensing measurement. The redshift distribution of a mock DES flux limited sample with $0 < z < 2$ and $20 < i < 24$ is plotted alongside the predicted DUNE DASS-EX distribution in Figure 7.1.

2. A 4,000 deg^2 cluster survey, consisting of tens of thousands of clusters south of $\delta = -30°$ with photometric redshift errors $\sigma_z \leq 0.02$ for $z < 1.3$. The cluster survey will overlap in totality with the South Pole Telescope (SPT) Sunyaev-Zel'dovich

Survey	DES	DUNE
Description	Ground Based First Light Sept. 2010	Space Mission Launch circa 2017
Galaxy Survey Sky Coverage	5000deg^2	20,000 deg^2
Filters	g, r, i, z, Y (400-1100nm) J, H, K from VHS VISTA	R, I, Z (550-920nm) Y,J,H (920-1600nm)
Cosmological Probes	BAO, CC, WL, SNæ Ia	BAO, CC WL, ISW

Table 7.1: Specifications of the Dark Energy Survey (DES) and Dark UNiverse Explorer (DUNE) missions. The cosmological probes include Baryon Acoustic Oscillations (BAO), Cluster Counts (CC), Weak Lensing (WL), Type Ia Supernoæ as well as the Integrated Sachs Wolfe Effect. The probes are described in Chapter 1 and 5.

(SZ) survey which will permit detection of high redshift clusters and mass estimates using the SZ effect. The overlap will also permit to statistically calibrate the SPT cluster mass estimates by using cluster masses obtained from DES weak lensing measurements. It will also permit calibration of the SPT cluster selection function by using clusters detected by DES that are below the SPT mass threshold.

3. DES will dedicate 10% of its observing time to repeat observing of 40 deg^2 area of the sky, aiming is to detect and measure the light curves of $\sim$2000 type Ia supernovæwith $0.3 < z < 0.75$.

7.4.3 Cosmological Tools

The DES will focus on the following cosmological probes: Weak gravitational lensing , Baryon Acoustic Oscillations (BAO), Cluster Counts (CC) and type Ia supernovæ(see Section 1.7). One of its secondary science drivers will be to use the ISW effect to search for departures from General Relativity, though the small sky coverage of DES does not make the ISW an ideal probe. I discuss this in Sections 7.5.4 and 7.7.

7.5 Forecasts for Dark Energy parameters from ISW alone

As I discussed in Section 7.2, the forecast of parameter uncertainties using the Fisher Information Matrix, requires only three ingredients. The first is a fiducial model along with a set of cosmological parameters values $\vec{\theta}$ for which forecasts are desired; I describe the one I chose in Section 7.5.1. The second ingredient is an observable quantity which I take in this Section to be the binned cross angular power spectrum of the galaxy and temperature fields (the ISW signal, C_{gT}), which I describe in Section 7.5.2. The final ingredient is an estimate of the error in measuring C_{gT}, which I quantify in Section 7.5.3. In Sections 7.5.4 and 7.5.6 I present forecasts for DUNE and DES for different cosmological parameters and using redshift binning of the data. In Section 7.5.5, I compare limits of current SDSS observations with limits from Fisher forecasts.

7.5.1 Fiducial Model

In this analysis, I take the following fiducial model: a flat ΛCDM universe with dark energy density $\Omega_\Lambda = 0.75$ and baryon density $\Omega_b = 0.05$. I set the equation of state parameter of Dark Energy to $w = -1$. I assume the Hubble parameter is $H_0 = 100\text{h kms}^{-1}\text{Mpc}^{-1}$ with $\text{h} = 0.7$. I take the spectral index of the primordial density fluctuations to have the Harrison Zel'dovich value of $n = 1$. I set $\sigma_8 = 0.75$ as the normalization of the power spectrum (see Section 1.6.2). I compute the linear transfer function of the dark matter power spectrum (see Section 1.6.1) from the approximation given by Eisenstein & Hu (1999).

I discussed in Chapter 5 (Section 5.5) how the ISW signal is proportional to the linear galaxy bias and is expected to evolve with redshift. In the following forecasts I assume the galaxy bias is well approximated by a linear scale-independent bias. For the fiducial model, I assume the bias at redshift zero is $b(z = 0) = 1.50$ for both the DES and DUNE galaxy surveys and that it evolves with redshift as (Fry 1996):

$$b(z) = 1 + \frac{b(z = 0) - 1}{D(z)}\,, \tag{7.10}$$

where $D(z)$ is the growth factor, normalized to 1 for $z = 0$ as in the rest of this Thesis.

7.5.2 Prediction of the ISW effect

As discussed in Section 3.5, the partial sky coverage of the DES and DUNE surveys will reduce the overall amount of power received by a factor of f_{sky}, as well as inducing correlations between adjacent multipoles. I account for power loss by defining:

$$C_{gT}(\ell) = \frac{1}{\sqrt{f_{sky}}} \langle \delta T^* \rangle \ , \tag{7.11}$$

and account for multipole correlation by binning the angular power spectrum in logarithmic bins. This reduces correlation between different multipoles so that I can assume the bins are independent and have Gaussian error bars.

For DES the correlation due to sky coverage should be negligible when considering bins over a multipole range $\Delta\ell > 10$. This value was estimated by Blake *et al.* (2007) for the SDSS sky coverage which is similar to that of DES. I bin the data logarithmically so as to maximize the error bar reduction at higher multipoles.

Because for each multipole ℓ there are $2\ell + 1$ harmonic coefficients which contribute to the cross-power, values of the power spectrum for higher multipoles should be given more weight than for lower multipoles when binning. The following formulæ are used when binning:

$$\ell_{\rm bin} = \sum_{\ell_{\rm min}}^{\ell_{\rm max}} \frac{(2\ell+1)\ell}{(\ell_{\rm max} - \ell_{\rm min} + 1)(\ell_{\rm max} + \ell_{\rm min} + 1)} \ , \tag{7.12}$$

where $\ell_{\rm min}$ and $\ell_{\rm max}$ correspond to the minimum and maximum ℓ in the range corresponding to $\ell_{\rm bin}$. The power spectrum is binned similarly:

$$C(\ell_{\rm bin}) = \sum_{\ell_{\rm min}}^{\ell_{\rm max}} \frac{(2\ell+1)C(\ell)}{(\ell_{\rm max} - \ell_{\rm min} + 1)(\ell_{\rm max} + \ell_{\rm min} + 1)} \ . \tag{7.13}$$

The minimum and maximum ℓ's for each logarithmic bin in this analysis are given in Table 7.2. The lowest multipole range covers $\Delta\ell = 6$ and so underestimates the range over which multipoles are correlated for DES, but for all the others $\Delta\ell > 10$. For DUNE (50% sky coverage) I assume that the correlation is always contained within the range $\Delta\ell \leq 6$. This is probably reasonable given that I showed in Chapter 3 that the multipoles for the 2MRS mask (90% sky coverage) were correlated at less than 1% over $\Delta\ell > 1$.

$\ell_{\rm min}$	$\ell_{\rm max}$	$\sim \ell_{\rm bin}$
2	7	5
8	28	20
29	106	75
107	400	282

Table 7.2: Minimum and maximum multipoles and the approximate corresponding $\ell_{\rm bin}$ for logarithmic binning of the ISW signal.

7.5.3 Calculation of $C_{gT}(\ell)$ Error Bars

The variance for the cross-correlation is given by (see Appendix B for the derivation):

$$\sigma^2_{C_{gT}}(\ell) = \frac{1}{(2\ell+1)f_{\rm sky}}\left[C^2_{gT} + (C_{gg}+\mathcal{N}_g)(C_{TT}+\mathcal{N}_T)\right] , \tag{7.14}$$

which is derived from the assumption that the galaxy and temperature anisotropy fields behave as Gaussian random fields. The galaxy-galaxy overdensity auto-correlation C_{gg} is calculated using linear theory prediction (Equation 5.13) and $\mathcal{N}_g$ is the Poisson galaxy shot noise given by $\frac{\Delta\Omega}{N_g}$. An estimate of C_{TT} is taken from the measured third year WMAP temperature-temperature power spectrum [†] (it could be taken from the theoretical prediction, but here we keep the temperature cosmic variance contribution model-independent). I do not include the detector noise $\mathcal{N}_T$ which is negligible compared to cosmic variance on scales larger than $\ell \simeq 400$ (Spergel *et al.* 2006).

7.5.4 Forecasts for DES and DUNE

The predicted redshift distributions of the DES and the DUNE surveys are given in Figure 7.1. The DES redshift range covers $z = [0:2]$, whilst the DUNE survey will be slightly deeper with $z = [0:3]$. The predicted ISW signal for both surveys are shown in Figure 7.3 (*top two plots*). The ISW signal is logarithmically binned following Equation 7.13. This reduces correlation between multipoles which arises from the surveys' partial sky coverage so that I can assume the bins are independent. The DES ISW signal is shown in the top left plot (blue solid line) and the DUNE signal in the top right plot (red dashed line),

[†]http://lambda.gsfc.nasa.gov/product/map/dr2/pow_tt_spec_get.cfm

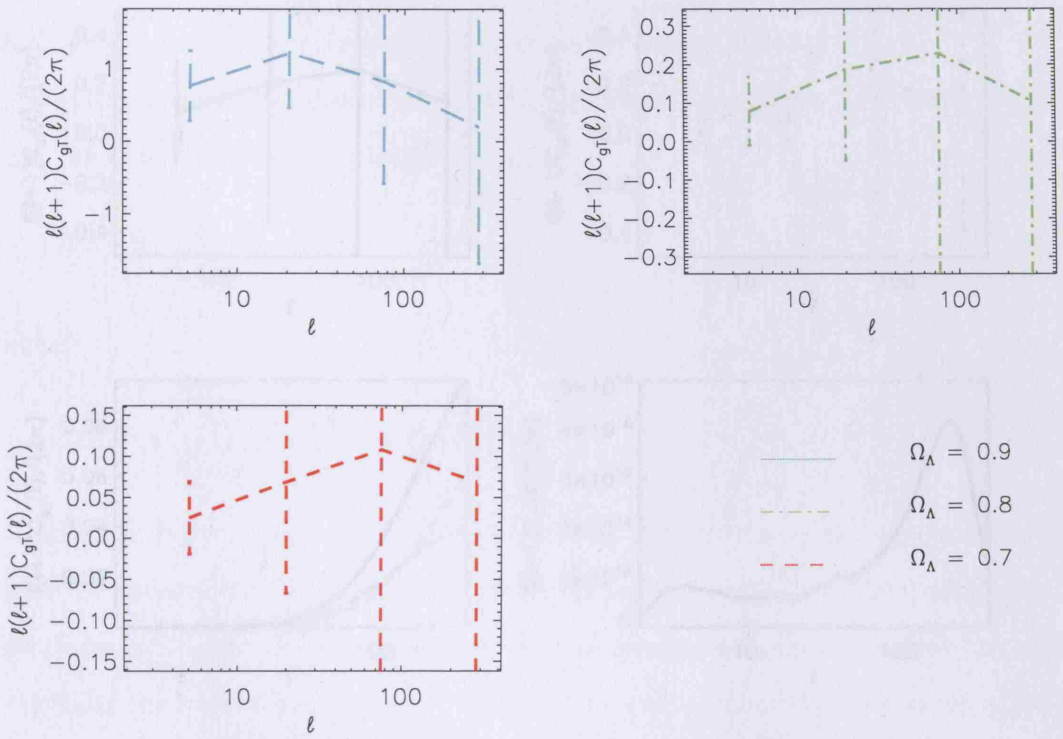

Figure 7.2: Predicted ISW cross-correlation for all of DUNE using fiducial models with $\Omega_m = 0.1$ (light blue, long dashed), 0.2 (green, dot-dashed), 0.3 (red, dashed). The strength of the signal increases with decreasing matter density, whilst the relative size of the error bars decreases with decreasing matter density. This makes it more likely to detect the ISW effect in a low matter density universe, and make the ISW effect a useful probes in universes with high dark energy density.

both for the same fiducial model described in 7.5.1.

The ISW signal is comparable in shape and strength whichever survey is considered. The main difference between the two ISW signals lies in the error bar predictions, give by Equation 7.14. There are three factors which will make DES and DUNE error bars different. The first is the shot noise due to the number of galaxies per steradian on the sky, in the $(C_{gg} + \mathcal{N}_g)C_{TT}$ term. Since for both surveys $C_{gg} \gg \mathcal{N}_g$ and $C_{TT} \gg \mathcal{N}_g$, the change due to shot noise is negligible.

The second contribution to the error bars which changes from DES to DUNE is the strength and the location of the peak of the galaxy auto-correlation function (ACF). This is plotted in the second row left panel of Figure 7.3. The DES galaxy ACF is plotted as a blue solid line and the DES ACF as the red dashed line. The dot-dashed black line shows

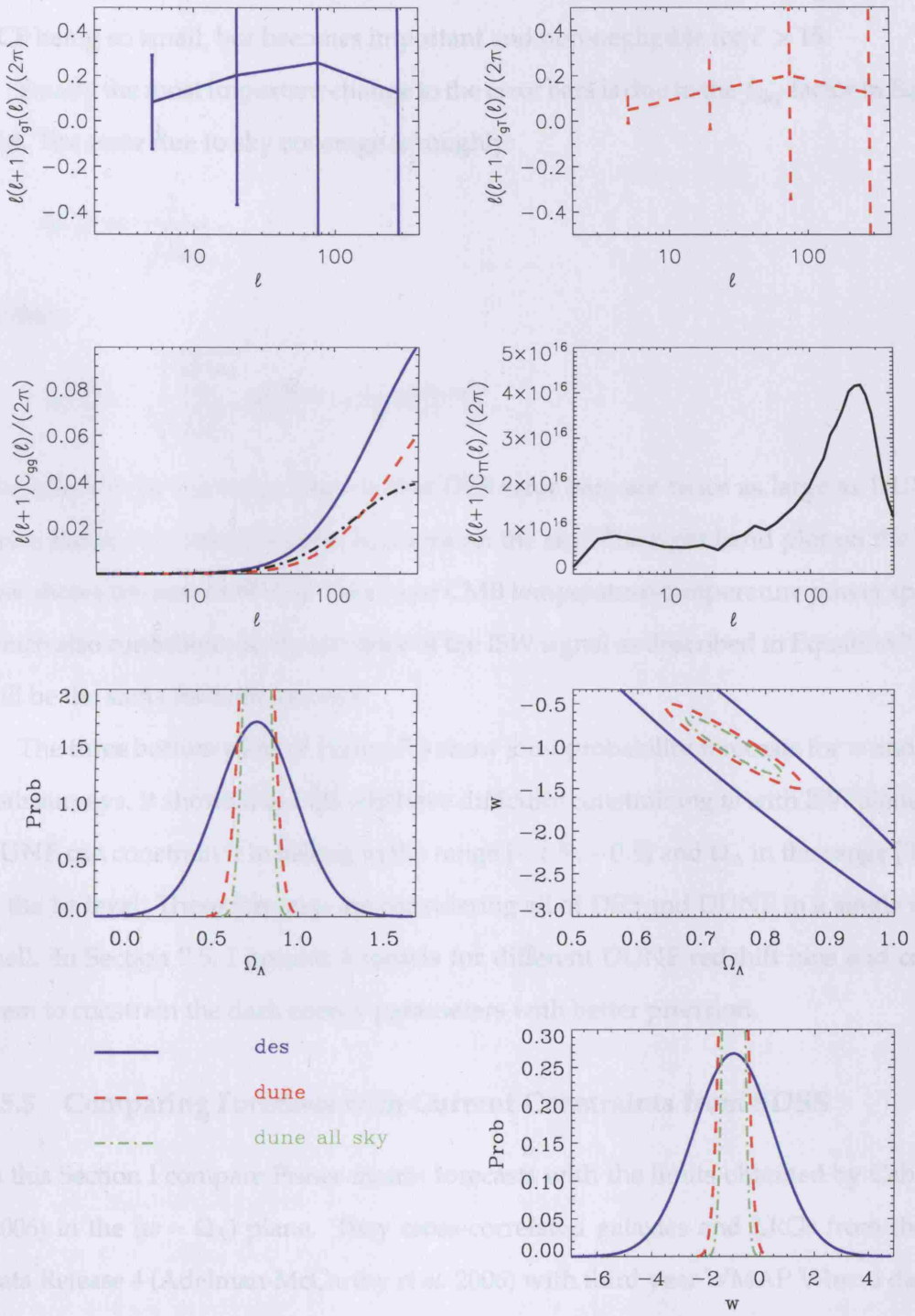

Figure 7.3: Predicted ISW signal (top) for the DES survey (solid blue line) and DUNE (dashed red line). The signal is similar in amplitude and shape for both surveys. The variance $\sigma(C_{gT})$ (Equation 7.14) depends on $f_{\rm sky}$ as well as the galaxy ACF and CMB T-T power spectrum (second row). The black dot-dashed line is the absolute difference between the ACFs for DES and DUNE. The bottom three plots show the Fisher forecasts for parameters describing the dark energy density Ω_Λ and equation of state w around $\Omega_\Lambda = 0.75$ and $w = -1$. The green contour is for a fiducial all-sky DUNE.

the absolute difference between the two. At low ℓ this difference is negligible due to the ACF being so small, but becomes important and non-negligible for $\ell > 15$.

Finally the most important change to the error bars is due to the $f_{\rm sky}$ factor in Equation 7.14. The error due to sky coverage is roughly:

$$\Delta C_{gT} \propto \frac{1}{\sqrt{f_{\rm sky}}}, \tag{7.15}$$

so that:

$$\Delta C_{gT}^{\rm Des} \propto \sqrt{\frac{f_{\rm sky}^{\rm Dune}}{f_{\rm sky}^{\rm Des}}} \Delta C_{gT}^{\rm Dune} = 2\left(\Delta C_{gT}^{\rm Dune}\right). \tag{7.16}$$

The effect is sky coverage alone is that DES error bars are twice as large as DUNE because the survey covers 4 times less area on the sky. The right hand plot on the second row shows the best fit WMAP third year CMB temperature-temperature power spectrum which also contributes to the variance of the ISW signal as described in Equation 7.14, but will be the same for both surveys.

The three bottom plots of Figure 7.3 show joint probability forecasts for w and Ω_Λ for both surveys. It shows that DES will have difficulty constraining w with ISW alone, while DUNE can constrain it to belong to the range $[-1.5 : -0.5]$ and Ω_Λ in the range $[0.6 : 0.9]$ at the 1σ level. These forecasts are considering all of DES and DUNE in a single redshift shell. In Section 7.5, I present forecasts for different DUNE redshift bins and combine them to constrain the dark energy parameters with better precision.

7.5.5 Comparing Forecasts with Current Constraints from SDSS

In this Section I compare Fisher matrix forecasts with the limits obtained by Cabre *et al.* (2006) in the $(w - \Omega_\Lambda)$ plane. They cross-correlated galaxies and LRGs from the SDSS Data Release 4 (Adelman-McCarthy *et al.* 2006) with third year WMAP V-band data. The analysis focused on the North Galactic Cap where SDSS data are concentrated on a contiguous area covering 13% of the sky.

The galaxy sample they used is broadly distributed over $z = [0, 1.2]$ and selected using a cut in the r band ($20 < r < 21$). The higher redshift LRG sample was colour selected using the following cuts: $17 < r < 21, (r - i) > (g - r)/4 + 0.36$ and $(g - r) >$

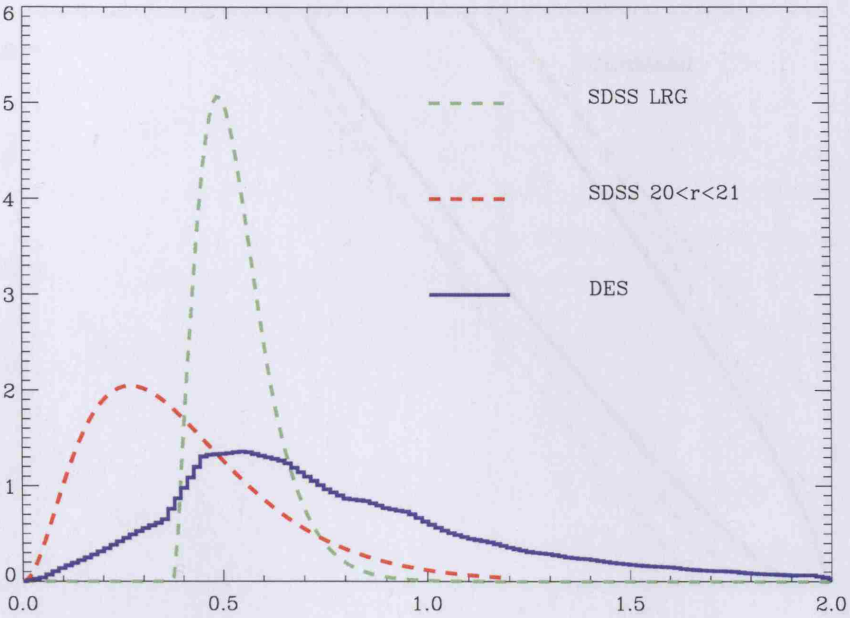

Figure 7.4: The parameterised redshift distribution of SDSS DR4 galaxies ($20 < r < 21$) and LRGs compared with the prediction for DES (blue histogram).

$0.72(r-i)+1.7$. This ensures few galaxies with $z < 0.40$ are selected and that only red galaxies with old stellar populations are chosen. Both samples were parameterised by Cabre *et al.* (2006) using:

$$\frac{dN(z)}{dz} \propto (z-z_c)^2\Big[\exp\Big(-\frac{z-z_c}{z_0-z_c}\Big)\Big]^{1.5}, \quad \text{for } z > z_c\,, \tag{7.17}$$

and $\frac{dN(z)}{dz} = 0$ for $z < z_c$. The parameters for the galaxy and LRG samples as fitted by Cabre *et al.* (2006) are shown in Table 7.3. The number of galaxies per sample is estimated to be 5.10^6. I plot the normalized redshift distribution of the $20 < r < 21$ galaxy and the SDSS LRG samples alongside the DES distribution in Figure 7.4.

Cabre *et al.* (2006) use the following fiducial model: a flat Universe with $w = -1$, $h = 0.71$ and $\Omega_b = 0.022/h^2$ (i.e.: $\Omega_b \simeq 0.044$), $n_s = 0.938$ and the best fit normalization from WMAP3 data $\sigma_8 = 0.75^{+0.03}_{-0.04}$ (Spergel *et al.* 2006). Using this fiducial model they fit the linear galaxy bias to the galaxy and LRG ACFs. The linear bias values they found are reported in Table 7.3.

Cabre *et al.* (2006) fit the dark energy density from the measured galaxy /LRG and temperature cross-correlation and find $\Omega_\Lambda = 0.83^{+0.02}_{-0.03}$. This result is for whichever pre-

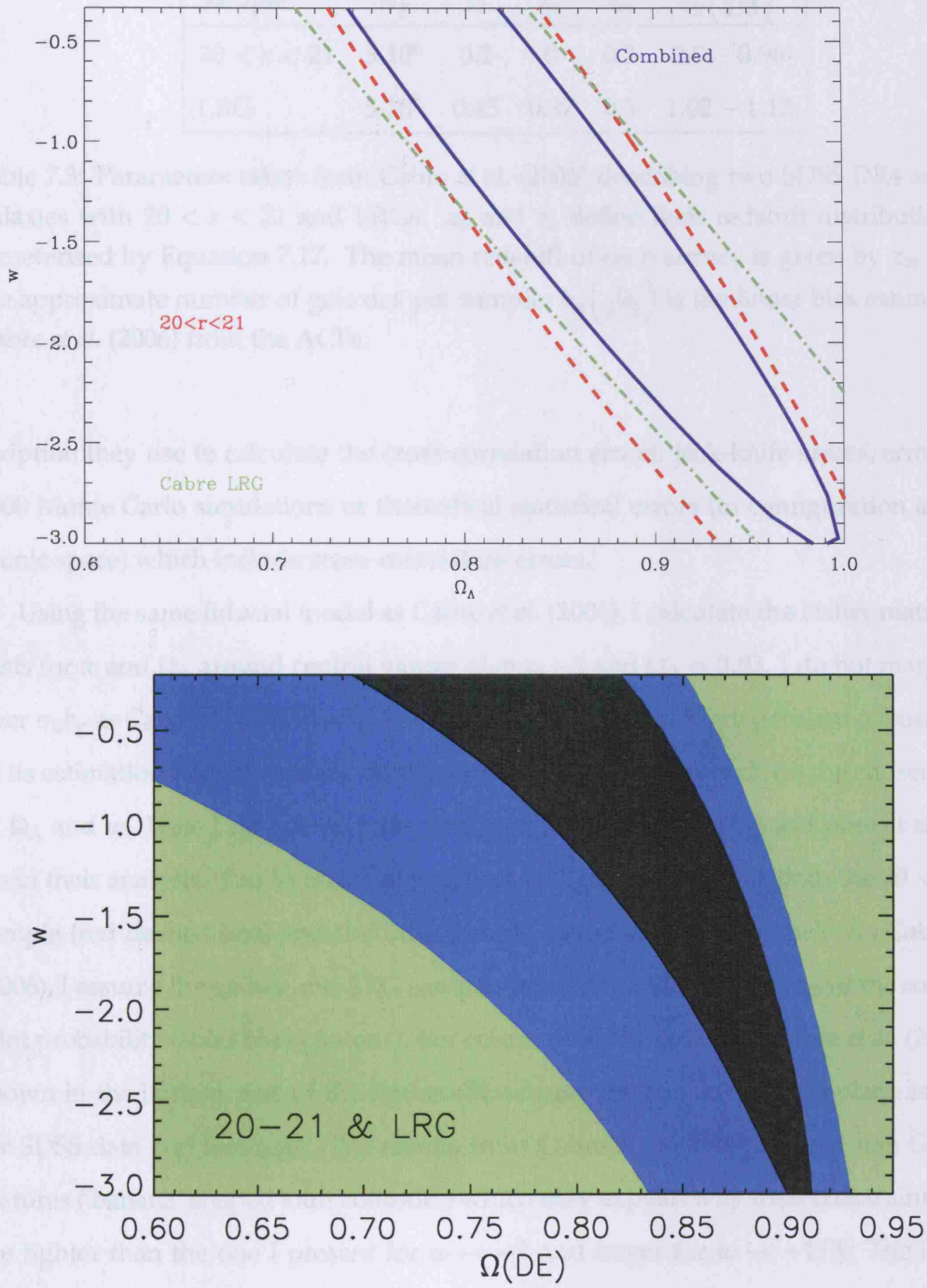

Figure 7.5: Fisher forecasts (*top*) for (w, Ω_Λ) compared with contours from SDSS DR4 cross-correlation with WMAP3 (*bottom, from Cabre* et al. *2006*). The degeneracy is similar, though the contours I have forecasted are larger than those predicted by Cabre *et al.* (2006) which might be due to non-Gaussianities in the data and in the parameter space. This might also indicate that the covariance between the galaxy and LRG sample is not negligible.

Sample	N_g	z_0	z_c	z_m	$b_g\left(\frac{\sigma_8}{0.75}\right)$
$20 < r < 21$	5.10^6	0.2	0	0.3	$0.9 - 0.96$
LRG	5.10^6	0.45	0.37	0.5	$1.02 - 1.12$

Table 7.3: Parameters taken from Cabre *et al.* (2006) describing two SDSS DR4 samples: galaxies with $20 < r < 21$ and LRGs. z_0 and z_c define their redshift distributions parameterised by Equation 7.17. The mean redshift of each survey is given by z_m and N_g the approximate number of galaxies per sample. $b_g\left(\frac{\sigma_8}{0.75}\right)$ is the linear bias estimated by Cabre *et al.* (2006) from the ACFs.

scription they use to calculate the cross-correlation errors: jack-knife errors, errors from 2000 Monte Carlo simulations or theoretical statistical errors (in configuration and harmonic space) which include cross-correlation errors.

Using the same fiducial model as Cabre *et al.* (2006), I calculate the Fisher matrix forecasts for w and Ω_Λ around central values of $w = -1$ and $\Omega_\Lambda = 0.83$. I do not marginalize over $\sigma_8 b_g$ as Cabre *et al.* (2006) do. In principle the bias is not independent of cosmology, as its estimation from the galaxy auto-correlation function depends on the chosen values of Ω_Λ and w. Here I do not vary the bias as a function of (w, Ω_Λ) as Cabre *et al.* (2006) do in their analysis. The forecasts are plotted in Figure 7.5 (*top*) for both the $20 < r < 21$ sample (red dashed line) and the LRG sample (dot-dashed green line). As Cabre *et al.* (2006), I assume the galaxy and LRG samples are independent and present the combined joint probability (solid blue contour). For comparison the results of Cabre *et al.* (2006) are shown in the bottom part of the figure. The degeneracy in the (w, Ω_Λ) plane is similar for SDSS data and forecasts. The results from Cabre *et al.* (2006) present non Gaussian features ('banana' shaped joint contours) which may explain why their constraints on Ω_Λ are tighter than the one I present for $w \to -3$ and larger for $w \to -1/3$. The fact that their contours are smaller than forecasts may also indicate that the two galaxy and LRG samples are not physically independent. If this is the case, neglecting the covariance between the shells can artificially reduce contours. The direction of the degeneracy is the same. While my forecasts show the marginalized 1σ constraint is $\Omega_\Lambda = [0.74; 1.0]$, the constraints from SDSS-WMAP3 give $\Omega_\Lambda = [0.69; 0.91]$.

Because SDSS and DES have very similar sky coverage, the main source of cross-

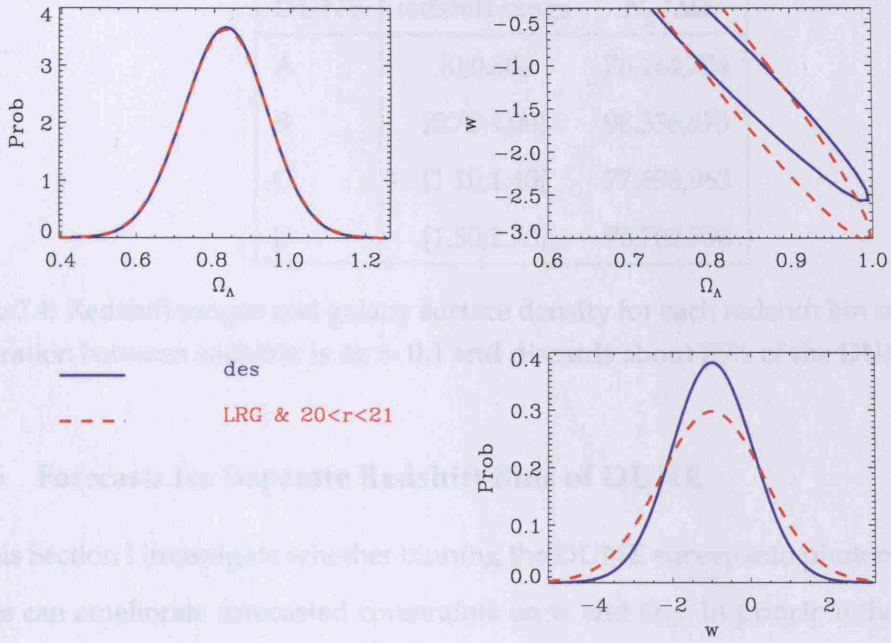

Figure 7.6: Fisher forecasts for combined LRG & $20 < r < 21$ galaxies from SDSS DR4 (red dashed contour), compared with DES forecasts (blue solid contour). The statistical error due to sky coverage is the same in both cases; the difference arises due to shot noise and change in ACFs at higher redshifts.

correlation variance due to sky coverage will similar in both cases. I compare forecasts for both surveys for the original fiducial model described in 7.5.1. For SDSS data I take the (assumed independent) $20 < r < 21$ galaxies and LRGs with distribution as above. Their combined forecasts is compared to DES forecasts in Figure 7.6.

Marginalized constraints on Ω_Λ are almost exactly similar. Whereas neither survey can break the (w, Ω_Λ) degeneracy below $w \simeq -2.5$, constraints on w from DES are better than from SDSS.

This may result from the smaller variance on the ISW signal of DES. DES will have 30 times more galaxies than the SDSS DR4 samples used here, which will reduce the shot noise term in the variance. DES will also have a higher mean redshift, so that its ACF will have less power, again reducing error bars.

DUNE	redshift range	$N_g/\Delta\Omega$
A	[0;0.60]	76,144,734
B	[0.70;1.00]	98,336,475
C	[1.10;1.40]	77,698,963
D	[1.50;2.70]	76,702,798

Table 7.4: Redshift ranges and galaxy surface density for each redshift bin of DUNE. The separation between each bin is $\Delta z = 0.1$ and discards about 25% of the DUNE data.

7.5.6 Forecasts for Separate Redshift Bins of DUNE

In this Section I investigate whether binning the DUNE survey into photometric redshift shells can ameliorate forecasted constraints on w and Ω_Λ. In principle the photometric redshift shells can be chosen to overlap, in which case it is necessary to calculate the covariance between each shell, as I did in Chapter 3 for the redshift shells of the 2MASS Redshift Survey. Here I chose a simpler approach as a mean of illustrating redshift binning. I separate each redshift bin by a 'buffer' zone which corresponds to a pessimistic overlap due to errors in photometric redshifts. In this way I can consider each redshift shell to be independent, i.e. with no physical overlap. Obviously even with pessimistic buffer zones, there will still be catastrophic failures in the photometric redshift estimation, but in any case, these are difficult to take into account.

The method of creating buffer zones between the redshift shells has the disadvantage of discarding large amounts of data and so it is more advantageous to calculate the full covariance.

I bin the DUNE survey into four redshift bins so that each bin has roughly the same galaxy surface density. Each bin is separated by a pessimistic buffer zone of Δz=0.1, corresponding to the possible photometric redshift error of DUNE. This is to ensure that adjacent redshift bins do not physically overlap. These three redshift buffers remove over 80 million galaxies per steradian from this analysis (SDSS DR4 samples have roughly 3 million galaxies per steradian). If the bins are physically separate, then it is not necessary to calculate correlations between the bins. The four redshift bins (DUNE A, DUNE B, DUNE C, DUNE D) used in this analysis are shown in Figure 7.7. The redshift ranges

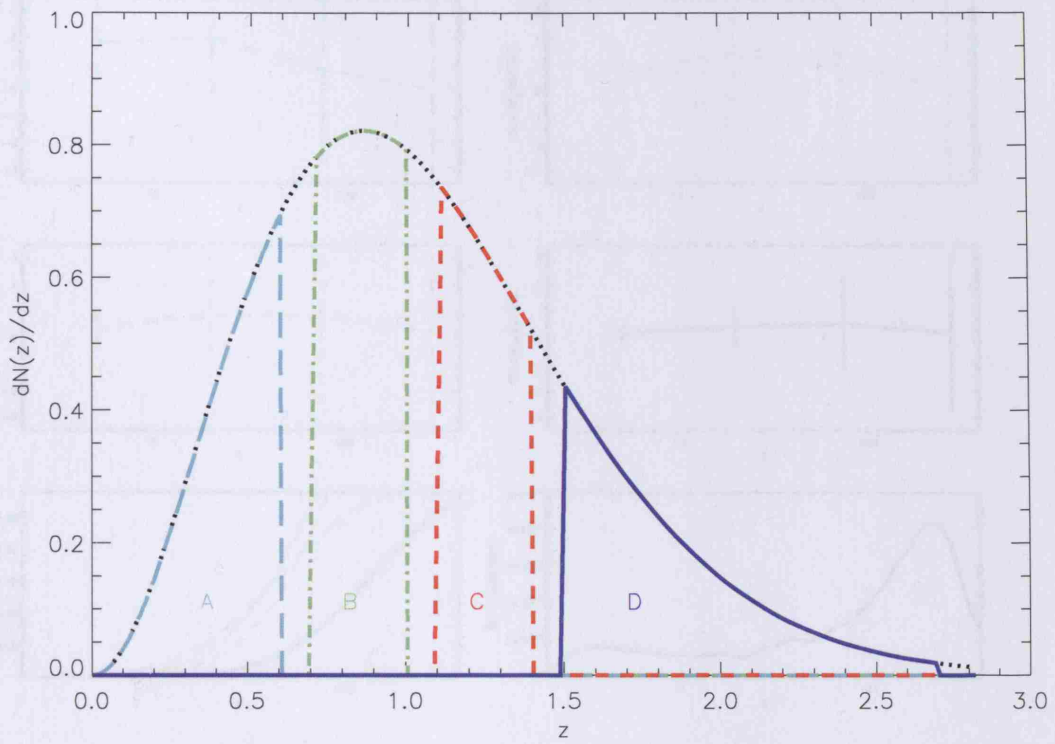

Figure 7.7: DUNE redshift distribution binned into four redshift bins: A, B, C and D, each containing approximately the same number of galaxies per steradian. The separation between each bin is $\Delta z = 0.1$ and discards about 25% of the DUNE data. See Table 7.4 for details.

and number of galaxy for each bin are shown in Table 7.4.

In Figures 7.8, 7.9, I consider the fiducial model described in Section 7.5.1 with either $\Omega_\Lambda = 0.75$ (Figure 7.9) or $\Omega_\Lambda = 0.90$ (Figure 7.8). The top four plots of each Figure are the expected ISW signal for each redshift bin (see Key). The third row plots are the predicted galaxy ACF signal (*left*) and the binned best fit WMAP3 temperature ACF (*right*). These are plotted to help understand how statistical errors due to cosmic variance of the galaxy and temperature fields affect the ISW variance on different scales.

It is interesting to note that high redshift bins tend to benefit from low variance of the galaxy field, making the ISW variance smaller than at lower redshifts where the signal is stronger.

In the bottom panel of Figures 7.8 and 7.9, I have plotted the joint and marginalized probabilities for each redshift bin.

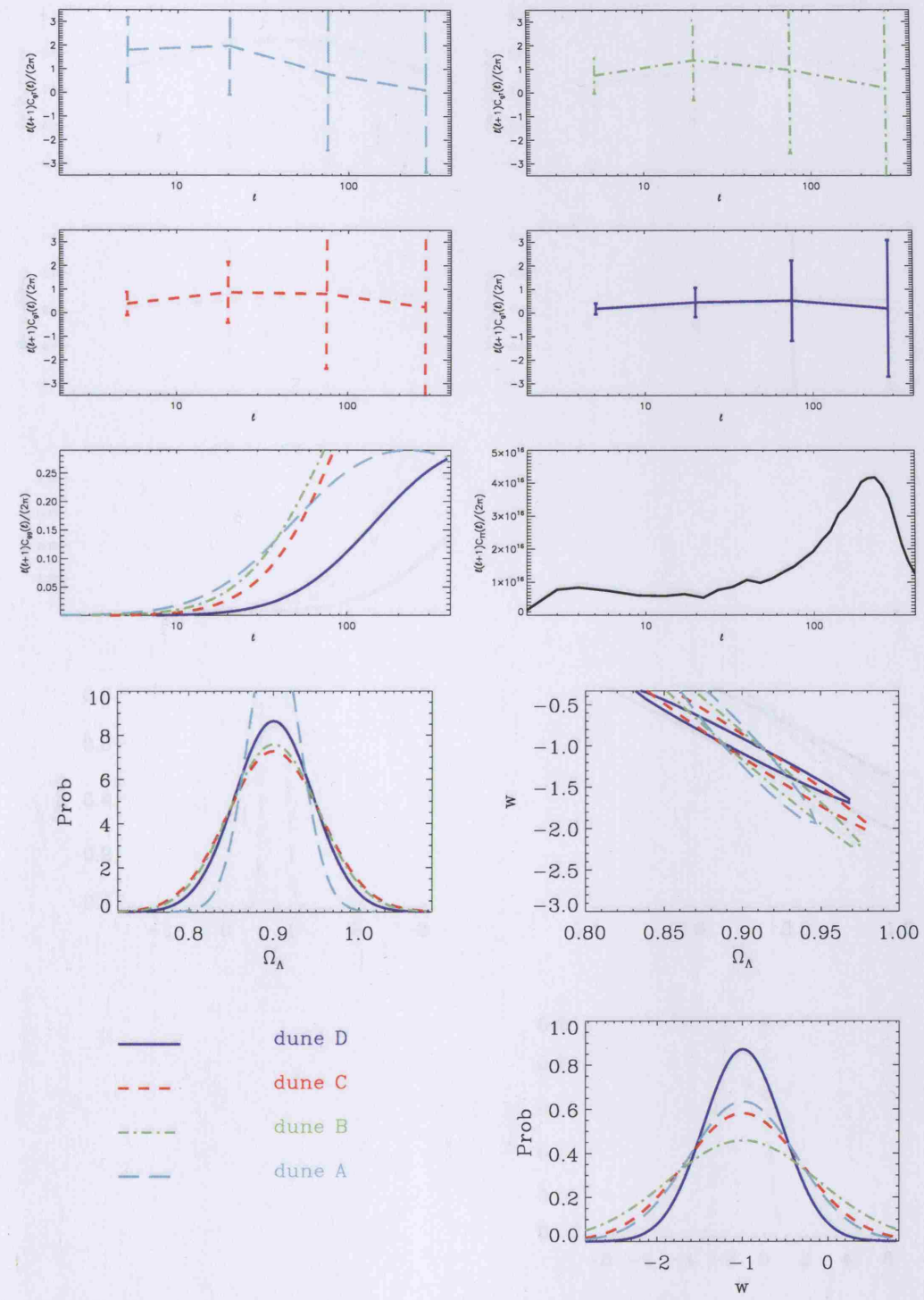

Figure 7.8: Predictions and Forecasts for the four DUNE redshift bins around a central value $\Omega_\Lambda = 0.90$. *Top 4 plots*: ISW predictions. *3rd row*: Predicted galaxy ACFs and best fit WMAP3 temperature ACF (see text for the impact of these on the ISW variance). *Bottom*: Joint and marginalized forecasted contours for (w, Ω_Λ) for each redshift bin separately. The combined joint contours are shown in Figure 7.11.

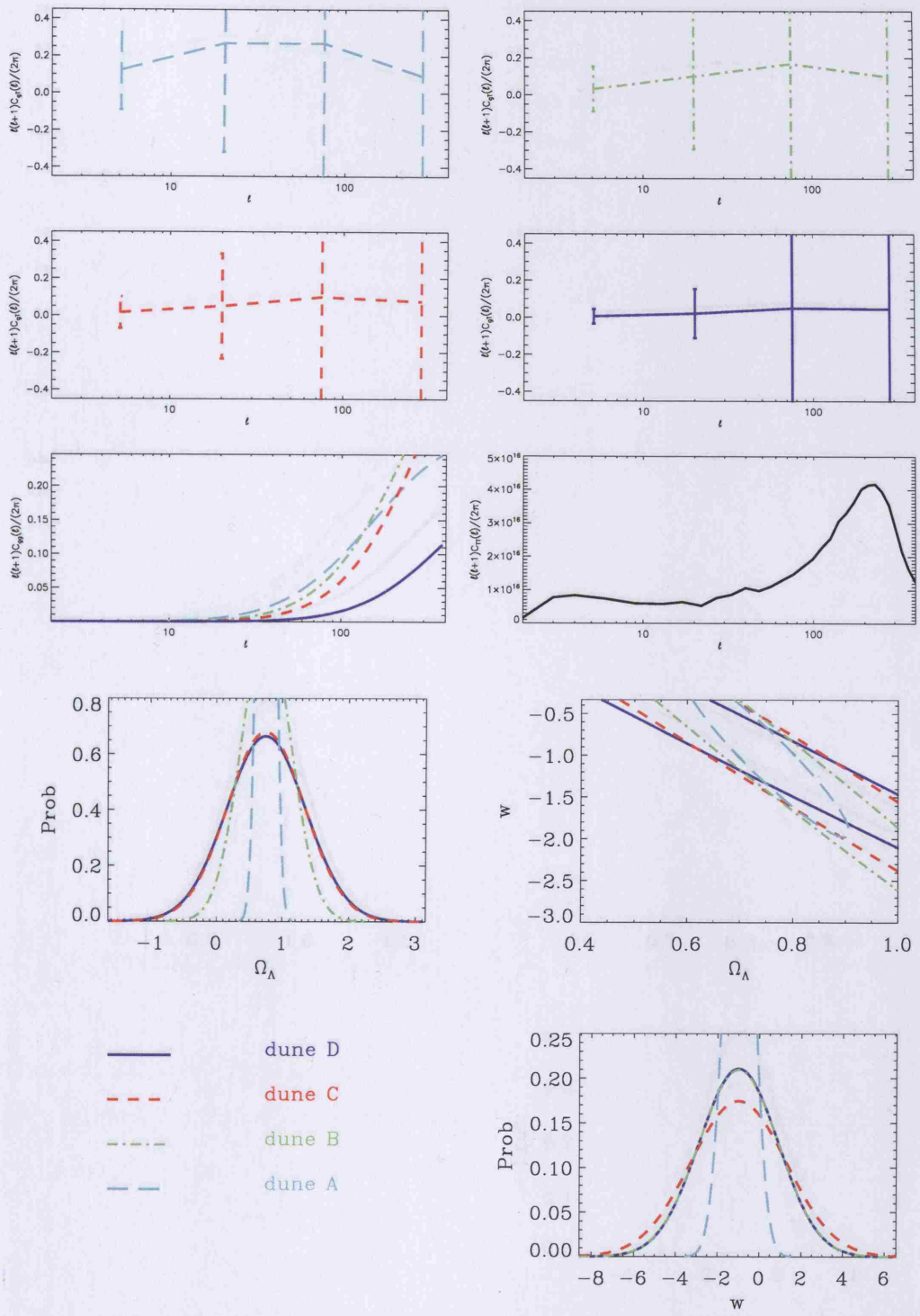

Figure 7.9: Predictions and Forecasts for the four DUNE redshift bins around a central value $\Omega_\Lambda = 0.75$. *Top 4 plots*: ISW predictions. *3rd row*: Predicted galaxy ACFs and best fit WMAP3 temperature ACF (see text for the impact of these on the ISW variance). *Bottom*: Joint and marginalized forecasted contours for (w, Ω_Λ) for each redshift bin separately. The combined joint contours are shown in Figure 7.11.

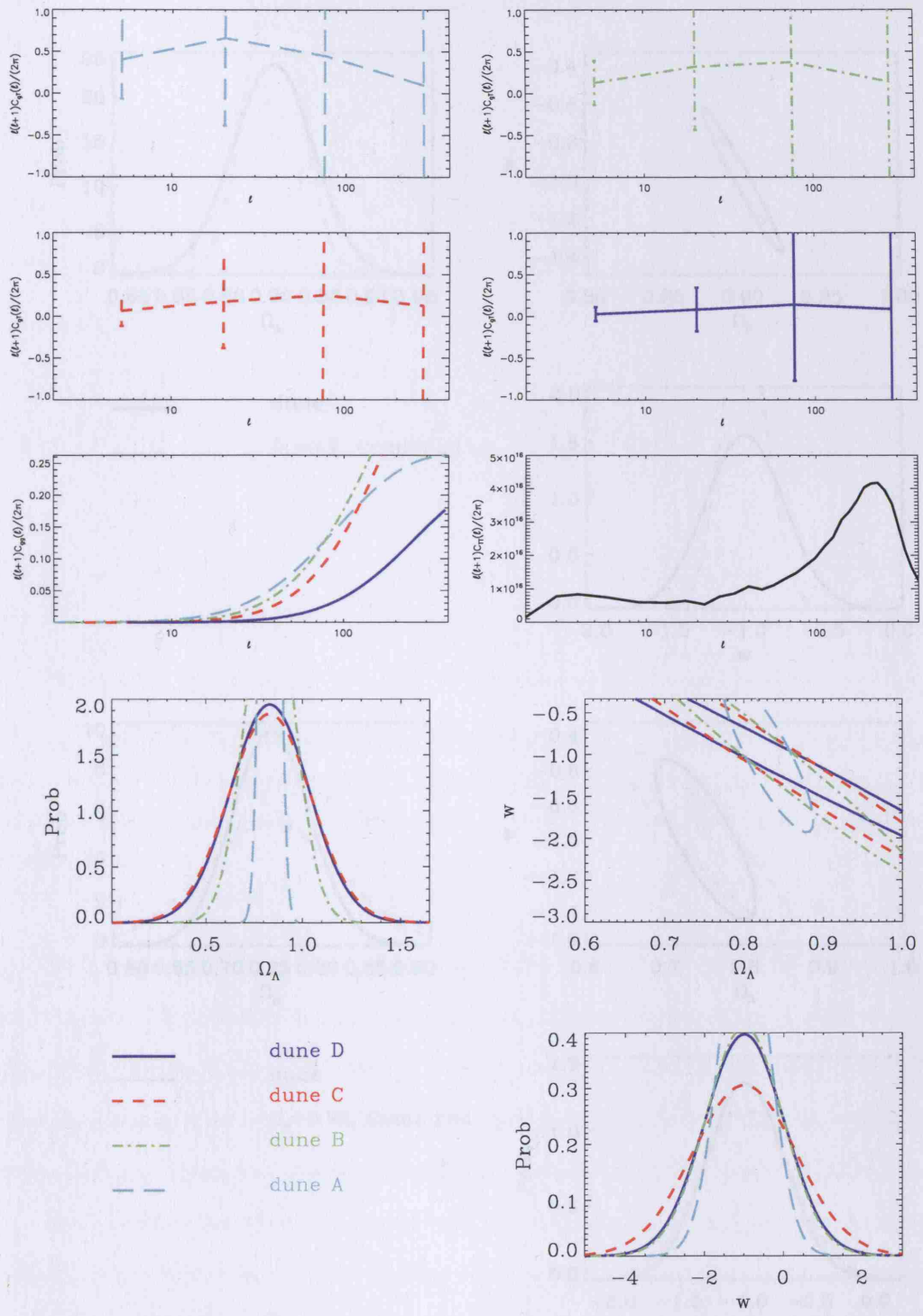

Figure 7.10: Predictions and Forecasts for the four DUNE redshift bins around a central value $\Omega_\Lambda = 0.83$ and the fiducial model used by Cabre *et al.* (2006). *Top 4 plots*: ISW predictions. *3rd row*: Predicted galaxy ACFs and best fit WMAP3 temperature ACF (see text for the impact of these on the ISW variance). *Bottom*: Joint and marginalized forecasted contours for (w, Ω_Λ) for each redshift bin separately. The combined joint contours are shown in Figure 7.12.

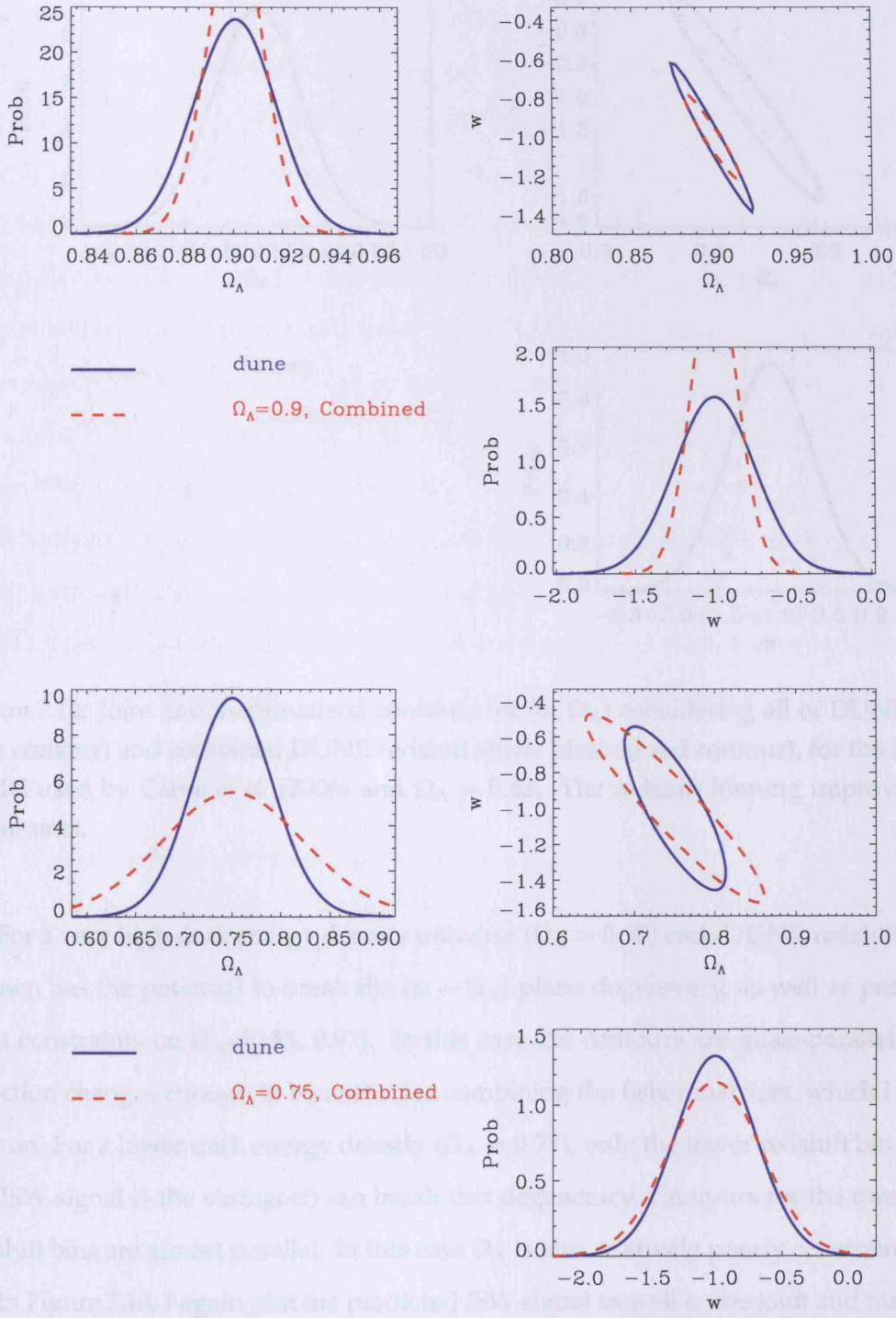

Figure 7.11: Joint and marginalized contours for (w, Ω_Λ) considering all of DUNE (solid blue contour) and combined DUNE redshift shells (dashed red contour). *Top:* $\Omega_\Lambda = 0.90$, redshift binning improves constraints. *Bottom:* $\Omega_\Lambda = 0.75$, redshift binning gives worse constraints, probably due to the discarded data at low redshift.

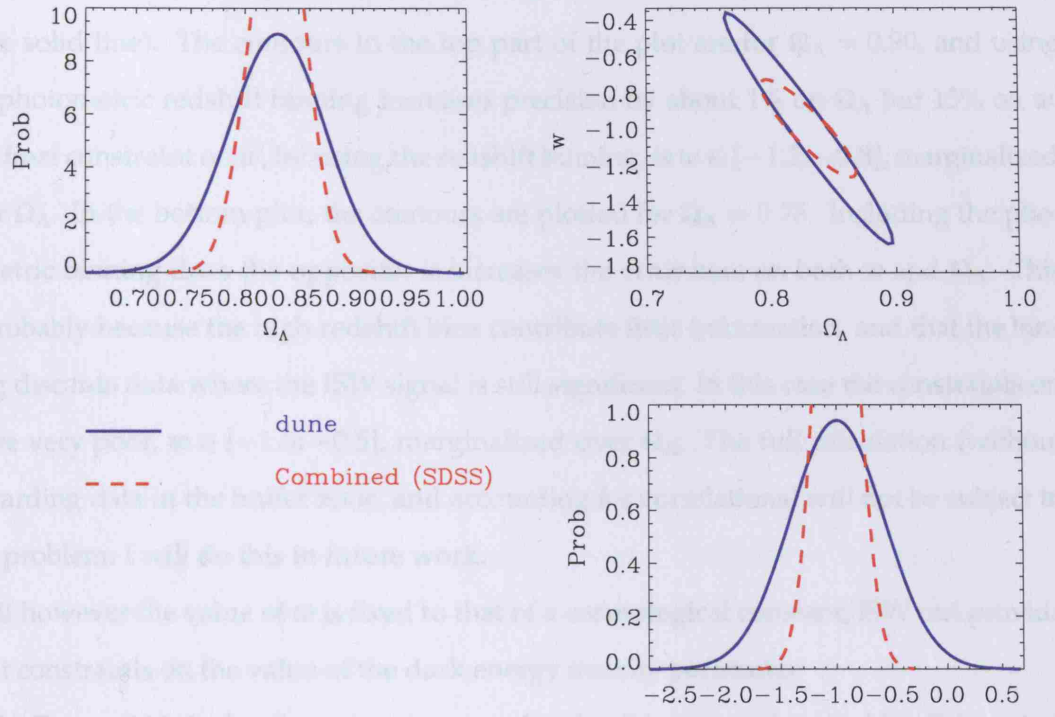

Figure 7.12: Joint and marginalized contours for (w, Ω_Λ) considering all of DUNE (solid blue contour) and combined DUNE redshift shells (dashed red contour), for the fiducial model used by Cabre *et al.* (2006) and $\Omega_\Lambda = 0.83$. The redshift binning improves joint constraints.

For a very high dark energy density universe ($\Omega_\Lambda = 0.90$) each DUNE redshift bin on its own has the potential to break the $(w - \Omega_\Lambda)$ plane degeneracy, as well as producing tight constraints on Ω_Λ=[0.83, 0.97]. In this case the contours are quasi-parallel. Their direction changes enough to be useful for combining the fisher matrices, which I do further on. For a lower dark energy density ($\Omega_\Lambda = 0.75$), only the lower redshift bin (where the ISW signal is the strongest) can break this degeneracy. Contours for the three other redshift bins are almost parallel. In this case Ω_Λ is also relatively poorly constrained.

In Figure 7.10, I again plot the predicted ISW signal as well as the joint and marginalized probabilities for w and Ω_Λ using the fiducial model used by Cabre *et al.* (2006). In this case, only the lowest redshift bin can break the (w, Ω_Λ) degeneracy. Its contours are orthogonal to the contours from other redshift bins.

In Figure 7.11, I plot the combined contours for (w, Ω_Λ) assuming the redshift bins of

DUNE are independent (red dashed contours) and for all of DUNE in one redshift shell (blue solid line). The contours in the top part of the plot are for $\Omega_\Lambda = 0.90$, and using the photometric redshift binning increases precision by about 1% on Ω_Λ but 15% on w. The final constraint on w, by using the redshift binning, is $w \in [-1.2; -0.8]$, marginalized over Ω_Λ. In the bottom plot, the contours are plotted for $\Omega_\Lambda = 0.75$. Including the photometric binning does the opposite: it increases the error bars on both w and Ω_Λ. This is probably because the high redshift bins contribute little information, and that the binning discards data where the ISW signal is still significant. In this case the constraints on w are very poor, $w \in [-1.5; -0.5]$, marginalized over Ω_Λ. The full calculation (without discarding data in the buffer zone, and accounting for correlations) will not be subject to this problem. I will do this in future work.

If however the value of w is fixed to that of a cosmological constant, ISW can provide tight constraints on the value of the dark energy density parameter.

In Figure 7.12, I plot the same contours for the fiducial model used by Cabre *et al.* (2006) and find that including the redshift binning decreases error bars on Ω_Λ by about 4% and by 40% on w.

7.6 Discussion of Forecasts

In this Section I overview the results of Section 7.5. The goal of Section 7.5 was to determine if the ISW effect could be used independently to confirm the presence of dark energy using the next generation of galaxy surveys. To do this I considered a fiducial model which was geometrically flat and agreed with general relativity. In such a universe, an ISW effect can only be due to the presence of dark energy.

In Section 7.5.4 I compared constraints in the (w, Ω_Λ) plane, forecasted for the next generation of galaxy surveys, in particular Dark Energy Survey (DES) and for the Dark UNiverse Explorer (DUNE). The expected ISW signal is similar for both surveys, the main difference is the variance of the signal, which is dominated by the effect of sky coverage. DUNE covers four times the area of sky as DES. For this reason, DES cannot break the (w, Ω_Λ) degeneracy, though DUNE can.

In Section 7.5.5 I compare if the forecasting method provides similar constraints to

results from data, by investigation the ISW detection of Cabre *et al.* (2006). They used third year WMAP (WMAP3) data and the fourth data release (DR4) of the Sloan Digital Sky Survey (SDSS). The forecasts in the (w, Ω_Λ) plane are very similar to the constraints from the SDSS-WMAP3 cross-correlation. The direction of the degeneracy is the same. While the forecasts show the marginalized 1σ constraint is $\Omega_\Lambda = [0.74; 1.0]$, the constraints from SDSS-WMAP3 give $\Omega_\Lambda = [0.69; 0.91]$. The similitude of the constraints confirms the Fisher Information Matrix is a reliable way to forecast parameter constraints.

In Section 7.5.6 I investigate whether photometric redshift binning of DUNE data can improve constraints on (w, Ω_Λ). In principle the photometric redshift shells can be chosen to overlap, in which case it is necessary to calculate the covariance between each shell. Here I chose a simpler approach as a mean of illustrating redshift binning. I separate each redshift bin by a 'buffer' zone so that I can consider each redshift shell to be independent, i.e. with no physical overlap. I separate the DUNE data into four redshift shells, each with approximately the same galaxy density. The width of the buffer zones are chosen as Δz=0.10, which discards about 25% of the DUNE data. The width of the buffer zones were chosen to be pessimistic values of the photometric errors expected from DUNE. In a fiducial low matter universe ($\Omega_m = 0.10$), the redshift binning improves the constraints by 15% for w. In this case DUNE would be able to constrain $w = [-1.2; -0.8]$.

The amplitude of the ISW signal decreases with decreasing dark energy density. Since most cosmologies predict $\Omega_\Lambda \to 0$ at high redshifts, the signal is also weaker at high redshifts for the same reason. So for a universe where $\Omega_\Lambda = 0.75$ the constraints from ISW alone are worse than for a universe where $\Omega_\Lambda = 0.90$. In this case where Ω_Λ the redshift binning method actually provides poorer constraints than using all of DUNE in one redshift shell. This is the price we pay for discarding data at low redshifts where the ISW signal is strongest.

If the equation of state parameter is fixed to $w = -1$, so the dark energy component corresponds to a cosmological constant, the ISW effect can provide tight constraints on Ω_Λ. In a low matter density universe ($\Omega_m = 0.10$) the constraints are $\Omega_\Lambda = 0.90 \pm 0.02$. For a universe where $\Omega_m = 0.25$, the constraints are $\Omega_\Lambda = 0.75 \pm 0.04$.

7.7 Minimalist Modified Gravity (MMG)

Probing cosmology with the ISW effect is far from being the pinnacle of precision cosmology and it is undoubtedly wiser to design future surveys with more decisive tools like weak lensing and cluster counts in mind. However, if an output of such surveys includes a galaxy catalogue - and obviously it will - it would be short-sighted to totally discard the ISW probe and omit it as a consistency check of the otherwise determined best fit cosmology. This is especially true given the relative simplicity of an ISW measurement: it does not require difficult shape measurements or mass estimates and the measurement of a cross-correlation signal is itself model independent.

In fact, the ISW effect might be more useful to investigate departures from general relativity, rather than weakly confirm a set of standard cosmological parameters. Linder (2005) proposed a model independent, phenomenological parameterisation of the growth factor, which can be used to measure any general departure from general relativity, and dubbed *Minimal(ist) Modified Gravity* (MMG). MMG checks for consistency between the cosmic expansion history and the measured growth of structure for a given cosmological model, and does not require the framework of a specific alternative gravity model. I describe the parameterisation of MMG in Section 7.7.1 and present forecasts on its parameter γ in Section 7.7.3 from future galaxy surveys DUNE and DES.

7.7.1 Parameterisation of the Growth Function with γ

The idea behind MMG is to look for consistency checks between the expansion history and the growth of structure for a given cosmology. MMG operates within the framework of general relativity, and works as a model independent phenomenological parameterisation of a general gravity modification. It does this by parameterising the growth factor:

$$f \equiv \frac{d\mathrm{lnD}}{d\mathrm{lna}} \simeq \Omega_m^{\gamma}(z) \,. \tag{7.18}$$

This parameterisation was previously suggested by Peebles (1980). It was revisited by Lahav *et al.* (1991) who showed it was still valid even when $\Omega_\Lambda \neq 0$ and Wang & Steinhardt (1998) generalized the parameterisation for quintessence. Recently Kiakotou, Elgaroy & Lahav (2007) generalized this parameterisation to cases where the neutrinos have mass.

For a given expansion history, the parameter γ can be determined for a universe behaving as predicted by general relativity. The Vanilla Model predicts $\gamma_{GR}^{\Lambda CDM} = 0.55$ (Linder 2005) in the framework of general relativity. For MMG, the goal of the parameterisation is not to provide a useful analytic equation for the growth function but to add an extra freedom. By letting γ be a free parameter, it is possible to investigate departures from general relativity without testing a specific alternative model. In this sense, MMG is general, though not complete: it will *not* detect a departure from general relativity if the true underlying model mimics both the expansion history and growth of structure expected in general relativity.

Huterer & Linder (2007) showed that ignoring this freedom can strongly bias constraints on the dark energy equation of state w, if the universe actually obeys a modified version of general relativity.

The advantage of parameterising the growth function using Equation 7.18 is that γ is relatively stable with redshift even in the case of dynamical dark energy (Wang & Steinhardt 1998; Linder & Cahn 2007). In the context of general relativity, γ can be determined to be (for a constant w):

$$\gamma = \frac{3(1-w_\infty)}{5-6w_\infty}\,, \tag{7.19}$$

where $w_\infty = \lim_{a\to 0} w(a)$. For dynamical dark energy, parameterised by:

$$w(a) = w_0 + w_a(1-a) = w_\infty - w_a a\,. \tag{7.20}$$

The parameter γ is given by (Linder & Cahn 2007):

$$\gamma = \frac{3(1-w_\infty)}{5-6w_\infty} + \frac{3w_a a}{(5-6w_\infty)(5-6w_\infty+2)}\,, \tag{7.21}$$

where the second correction term is always small, i.e. γ is still stable with redshift for dynamical dark energy.

7.7.2 Limitations of MMG

In this Section I briefly overview the main limitations of MMG.

Lack of Physical Motivation

Minimalist Modified Gravity can probe deviations from general relativity, and does not require the framework of a specific alternative gravity model. This is one of its benefits. It can be applied in a general way, using the framework of general relativity.

For the same reason, it is very limited. It is not at all physically motivated. To predict what the expected value of γ should be, one needs to focus on a specific model. However it is an ideal way to probe an *unknown* modification of gravity, by searching for self-consistencies.

MMG in the context of ISW

For some specific alternative gravity model, e.g. DGP (Dvali, Gabadadze & Porrati 2000), it is possible to predict what the value of γ should be (Linder & Cahn 2007). In this case constraining γ could rule out certain models, and draw attention to others. In the context of the ISW effect though, there is a drawback because the ISW effect probes scales beyond the horizon (Huterer & Linder 2007), where metric perturbations are difficult to calculate.

Sawicki, Song & Hu (2006) found an ansatz which allows solutions to the linear evolution of the gravitational potential for DGP models. In this case it should be possible to relate the model to a specific value of γ.

Furthermore, the parameterisation of γ might be scale dependent, i.e. have a value $\gamma_{\rm ISW}$ on large scales probed by ISW and a value $\gamma_{\rm WL}$ on smaller scales probed by weak lensing for example, making the MMG parameterisation an even more powerful tool for probing alternative gravitational theories.

7.7.3 Forecasts for γ from DUNE and DES

In order to visualize how a change in the MMG growth parameter γ affects the ISW signal, I plot in Figure 7.13 the ISW signal for $\gamma = 0.55$ and for $\pm 20\%$ deviations from it. The signal is that predicted for the DUNE galaxy survey, in a universe with dark energy density $\Omega_\Lambda = 0.90$ (*top*) and $\Omega_\Lambda = 0.80$ (*bottom*).

Because the ISW signal is much stronger in a high dark energy density universe, it will be easier to use the ISW to measure a deviation from $\gamma_{\rm GR}^{\Lambda{\rm CDM}} = 0.55$. I estimate what the

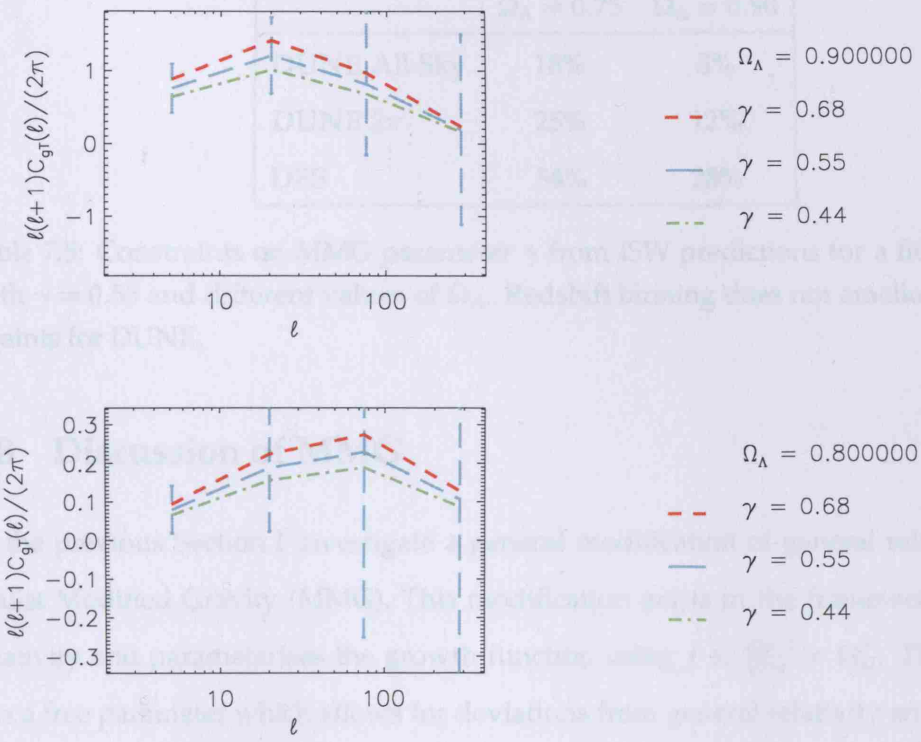

Figure 7.13: The effect of a 20% change in the MMG growth parameter γ on the ISW signal for the DUNE survey, in a universe with dark energy density $\Omega_\Lambda = 0.90$ (*top*), and $\Omega_\Lambda = 0.80$ (*bottom*).

minimum error bars on γ are given the fiducial model described in 7.5.1 and an assumed value of $\gamma = 0.55$, corresponding to what is expected in standard general relativity. The constraints on $\frac{\Delta\gamma}{\gamma}$ are given in Table 7.5 for DES, DUNE (covering 2π) and an ideal all-sky DUNE survey.

If the dark energy density in the Universe is very high, it may be possible to detect departures from γ equal or greater to 12% using a 2π DUNE survey, and equal or greater to 28% using DES. The penalty for having a lower dark energy density ($\Omega_\Lambda = 0.75$) is great, and makes it difficult for the DES to detect any departure that is smaller than 54% of $\gamma_{GR}^{\Lambda CDM}$. In such a case, even an all sky DUNE galaxy survey, could only constrain departures equal or greater to 18%. The results are shown considering the whole redshift distribution for the DUNE survey; considering redshift bins does unfortunately not ameliorate the constraints on γ.

	$\Omega_\Lambda = 0.75$	$\Omega_\Lambda = 0.90$
DUNE All-Sky	18%	8%
DUNE 2π	25%	12%
DES	54%	28%

Table 7.5: Constraints on MMG parameter γ from ISW predictions for a fiducial model with $\gamma = 0.55$ and different values of Ω_Λ. Redshift binning does not ameliorate the constraints for DUNE.

7.8 Discussion of MMG

In the previous Section I investigate a general modification of general relativity, Minimalist Modified Gravity (MMG). This modification exists in the framework of general relativity and parameterises the growth function using $f \equiv \frac{d\ln D}{d\ln a} = \Omega_m^\gamma$. The parameter γ is a free parameter which allows for deviations from general relativity and specifically checks for consistency between the expansion history of the Universe and the growth of structure. The main problem with MMG is that it is not physically motivated, but this is also one of its advantages, as it permits investigations of general deviations of gravity.

Constraining the value of the parameter γ can rule out certain modified models and draw attention to others. In the case of ISW, the prediction of the ISW effect and the value of γ requires careful attention to the metric perturbation calculation.

Using Fisher forecasts with the ISW alone, I show that in a high dark energy universe ($\Omega_\Lambda = 0.90$), DES can constrain γ to 28% and DUNE to 12%. If $\Omega_\Lambda = 0.75$, DES can constrain γ to 54% and DUNE to 25%.

The parameterisation may also be scale dependent in which case $\gamma_{\rm ISW}$ will probe deviations on large scales and can be complementary to a measure deviations on smaller scales, with weak lensing for example. In future work I will investigate modified DGP models and how well they can be constrained from DUNE using the ISW effect alone and combined with weak lensing measurements.

CHAPTER 8

CONCLUSIONS

This Thesis is concerned with two cosmological probes of linear gravity. The first relates to Large Scale Structure (LSS) in the Universe, probed by galaxy surveys. The second to temperature anisotropies of the Cosmic Microwave Background (CMB), probed by the Wilkinson Microwave Anisotropy Map (WMAP). Both probe the matter and dark energy distributions in the Universe and can be used to test general relativity. The first part of this Thesis (Chapters 2 to 4) is concerned with the analysis of galaxy clustering in redshift space. The second part (Chapters 5 to 7) is concerned with the Integrated Sachs-Wolfe (ISW) effect using LSS-CMB cross-correlations.

The conclusions of this Thesis are as follows:

- Quantifying galaxy clustering in redshift space is an exact way to describe redshift distortions within linear theory. I use a maximum likelihood method to determine the matter density Ω_m and the linear galaxy bias b_g from the 2 Micron all-sky Redshift Survey (2MRS), which probes over 32,000 galaxies with mean redshift $z \simeq 0.03$ and covers 90% of the sky. I find performing the analysis in redshift space rather than in projection improves uncertainties on Ω_m by a factor of 5 and on b_g by a factor of 2. The joint constraints for the near infrared galaxy bias in the local Universe is b_g and Ω_m are $b_g = \left(\frac{\sigma_8}{0.75}\right) = 1.06^{+0.06}_{-0.05}$, $\Omega_m = 0.23 \pm 0.06$. This is equivalent to a distortion parameter $\beta \simeq \Omega_m^{0.6}/b_g = 0.39 \pm 0.08$, in agreement with results in the literature.

- The above results assume the galaxy field is well described by a Gaussian random field, though non-Gaussianity is detected in several redshift shells of the 2MRS. Including the data which shows signs of non-Gaussianity does not affect the above results significantly (4% for b_g and 10% for Ω_m).

- I separately analyse the clustering of early (elliptical and lenticular) and late (spiral) type galaxies in the 2MRS. In agreement with other studies on smaller scales, and find early type galaxies preferentially reside in dense areas, whereas late types are found in the field. As expected from many previous studies, this suggests that early types are more clustered than late types. A redshift space analysis confirm that the early type bias $b_g^{\rm early}$ is larger than the late type bias $b_g^{\rm late}$ and that $b_g^{\rm early}/b_g^{\rm late} \simeq 1.30 \pm 0.11$. This is in agreement with recent studies of galaxy per morphological type which use the Halo model.

- I revisit current claims of a detection of the Integrated Sachs Wolfe (ISW) effect using galaxies in the 2 Micron All-Sky Survey (2MASS) and the third year Wilkinson Microwave Anisotropy Map (WMAP3). I find that when using a model dependent interpretation of the data (i.e., one which assumes a ΛCDM concordance cosmology) the data is consistent with a 2σ detection of the ISW effect. This detection is lower than previously claims and prefers a high value of the dark energy density $\Omega_\Lambda < 0.89$ at the 95% confidence level. A model independent approach confirms the data is compatible with no detection.

- Recent analyses claim there is a preferred direction in WMAP data ('Axis of Evil'). I investigate whether this direction could be due to foreground Large Scale Structure (LSS) by performing a test of statistical isotropy on the 2MASS data. The analysis does not show the LSS data has a preferred axis, nor is there a correlation with the preferred axis of the CMB. As the LSS data presents non-Gaussianity and a preferred direction (the supergalactic plane) this lack of detection suggests limitations in the test used.

- The amplitude of the ISW signal is highly dependent on both the dark energy density Ω_Λ and equation of state w. Estimating both simultaneously from data will be

subject to degeneracies. Using a forecasting method with a Fisher Information Matrix, I show that future large scales surveys such as the Dark Energy Survey can difficultly use the ISW effect to probe dark energy parameters with precision, mainly due to the limited sky coverage. Surveys like the Dark UNiverse Explorer (DUNE) can break the degeneracy in the (w, Ω_Λ) plane. Photometric redshift binning of the data improves the constraints. In a high redshift universe ($\Omega_m = 0.90$) and using photometric redshift binning, DUNE constrain $w \in [-1.2; -0.8]$ using ISW alone, where these are 1σ constraints been marginalised over Ω_Λ. In the case of a cosmological constant, DUNE could constrain $\Omega_\Lambda = 0.90 \pm 0.02$ using ISW alone in a higher dark energy density universe, or $\Omega_\Lambda = 0.75 \pm 0.04$ for a universe with less dark energy density.

- I also investigate a general modification of general relativity, Minimalist Modified Gravity (MMG). This modification exists in the framework of general relativity and parameterises the growth function using $f \equiv \frac{\mathrm{dln}D}{\mathrm{dln}a} = \Omega_m^\gamma$. The parameter γ is a free parameter which allows for deviations from general relativity and specifically checks for consistency between the expansion history of the Universe and the growth of structure. Constraining the value of γ can rule out certain modified models and draw attention to others. I show that in a high dark energy universe ($\Omega_\Lambda = 0.90$), DES can constrain γ to 28% and DUNE to 12%. If $\Omega_\Lambda = 0.75$, DES can constrain γ to 54% and DUNE to 25%.

CHAPTER 9

FUTURE WORK

This Thesis focuses on cosmological probes of linear gravity. The two main observational tools are the galaxy redshift space Auto-Correlation Function (ACF) and the Cross-Correlation Function between Large Scale Structure (LSS) and the Cosmic Microwave Background (CMB).

Here I list future directions and possible extensions which could benefit the analyses presented in this Thesis:

9.1 Testing Non-Gaussianity

In Chapter 3, I use a simple test of non-Gaussianity which searches for anomalies in the spherical harmonic phase distribution. This test showed that certain redshift shells in the 2 Micron all-sky Redshift Survey (2MRS) were non-Gaussian. In general , the Large Scale Structure (LSS) distribution tends to a lognormal distribution (Cole *et al.* 2001, Kayo, Taruya & Suto 2001), and preliminary tests show this is true for 2MRS. In future work it would be promising to test on which scales this is true for 2MRS and to use a lognormal maximum likelihood method to constrain cosmological parameters.

In Chapter 3 I tested the effects of applying a non-Gaussian likelihood to a Gaussian Random Field (GRF) and showed this method was faulty. To quantify the effects of log-normality described above, one can apply a Gaussian maximum likelihood to a N-body simulations, which I intend to do in future work.

9.2 Halo Model

In Chapters 3 and 4 I assume the bias linearly traces the matter distribution in the Universe. In Chapter 4 I show that there is a definite galaxy morphology dependence on the density and the early type galaxies are more biased than late type galaxies. This suggests that the bias cannot be considered as scale independent. In future work, I intend to repeat the analysis of the clustering of 2MRS galaxies in the context of the Halo Model.

9.3 ISW and Redshift Binning

In Chapter 7 I made Fisher matrix forecasts using the ISW and the Dark UNiverse Explorer (DUNE, Réfrégier *et al.* 2006). I investigate whether binning the DUNE galaxy survey into redshift bins could ameliorate constraints. To do this I consider redshift bins which I separate by buffer zones to minimize correlations between the shells. In some cases binning did not improve constraints mainly due to the data that was discarded in between shells. In the future I will calculate the full covariance between the shells. This will avoid discarding precious data and the covariance between the shells also contains cosmological information. I will also investigate what the optimum number of redshift bins is in order to minimise the forecasted uncertainties.

9.4 Shear-Temperature Cross-Correlation

In Chapter 5 I overview the method of cross-correlating tracers of mass with the CMB in order to detect the Integrated Sachs-Wolfe (ISW) effect. Throughout this Thesis, I always consider the tracer of mass to be luminous, though the ISW effect is related to the change in gravitational potential. This would be better traced by density contour maps as those reconstructed using weak lensing shear measurements. Cross-correlating the CMB directly with the shear measurement is a more direct way to measure the ISW effect, and using this statistic it is no longer necessary to estimate the bias (Cooray 2002). With Planck it may also be possible to use the Sunyaev-Zel'dovich effect to trace high redshift clusters, which should also induce an ISW effect in the CMB (Cooray 2002).

I will investigate how combining these probes can ameliorate constraints on cosmological parameters for the Dark UNiverse Explorer (DUNE, Réfrégier *et al.* 2006).

9.5 Cosmic Magnification

In Chapter 5 I discussed cosmic magnification (magnification bias) as a 'nuisance' signal on large scales which could be confused with the ISW effect. The cosmic magnification signal depends strongly on cosmology and is the dominant large scale signal when correlating high redshift tracers of mass with the CMB. In future work, I intend to estimate dark energy parameters using both the ISW effect and cosmic magnification simultaneously taking into account the covariance between the signals.

9.6 Minimalist Modified Gravity and mDGP Models

For specific alternative gravity models, it is possible to predict an 'effective' value of the growth function parameter γ. This parameter may vary with scale in which case it will be a useful handle with which to discriminate specific alternative models. In future work I intend to predict what the effective γ is for modified DGP models (mDPG, Dvali, Gabadadze & Porrati 2000). The effective γ can be predicted for scales relating to the ISW effect and scales relating to weak lensing.

APPENDIX A

INTEGRATION BY PARTS OF THE GALAXY ACF WITH REDSHIFT DISTORTIONS

Here, I derive Equation 3.19. For reference this is Equation (27) in Padmanabhan *et al.* (2006).

I start from considering the galaxy window function which arises due to redshift distortions, i.e. Equation 3.18.

$$W_\delta^z(k) = \frac{1}{k}\int \mathrm{d}r \frac{\mathrm{d}\left[\phi(r)f(r)\right]}{\mathrm{d}r} j'_\ell(kr) \,. \tag{A.1}$$

For simplicity we consider $F(r) = \phi(r)f(r)$, i.e.:

$$W_\delta^z(k) = \frac{1}{k}\int \mathrm{d}r \frac{\mathrm{d}\left[F(r)\right]}{\mathrm{d}r} j'_\ell(kr) \,, \tag{A.2}$$

where

$$j'_\ell(kr) \equiv \frac{\mathrm{d}j_\ell(kr)}{\mathrm{d}kr} \,. \tag{A.3}$$

First, we change the variable of integration to from $r \rightarrow kr$, using:

$$\mathrm{d}r\frac{\mathrm{d}F}{\mathrm{d}r} = \mathrm{d}(kr)\frac{\mathrm{d}F}{\mathrm{d}(kr)} \,. \tag{A.4}$$

This makes A.2 equal to:

$$W_\delta^z(k) = \frac{1}{k}\int_0^\infty \mathrm{d}(kr)\frac{\mathrm{d}F}{\mathrm{d}(kr)} j'_\ell(kr) \,. \tag{A.5}$$

Integrating by parts:

$$W_\ell^z(k) = \frac{1}{k}\left[\left[Fj'_\ell(kr)\right]_0^\infty - \int_0^\infty \mathrm{d}(kr)Fj''_\ell(kr)\right] . \tag{A.6}$$

The first term vanishes as for $\ell > 1$:

$$\lim_{kr\to\infty} j'_\ell(kr) = \lim_{kr\to\infty} j'_\ell(kr) = 0 , \tag{A.7}$$

$$\text{and} \quad \lim_{\mathrm{r}\to\infty} \mathrm{F(r)} = 0 . \tag{A.8}$$

Giving:

$$W_\ell^z(k) = -\frac{1}{k}\int \mathrm{d}(kr)Fj''_\ell(kr) = -\frac{1}{k}\int \mathrm{d}rkFj''_\ell(kr) = -\int \mathrm{d}rFj''_\ell(kr) . \tag{A.9}$$

The following recurrence relations for the spherical Bessel function:

$$(2\ell+1)j'_\ell = \ell j_{\ell-1} - (\ell+1)j_{\ell+1} , \tag{A.10}$$

$$(2\ell-1)j'_{\ell-1} = (\ell-1)j_{\ell-2} - \ell j_\ell , \tag{A.11}$$

$$(2\ell+3)j'_{\ell+1} = (\ell+1)j_\ell - (\ell+2)j_{\ell+2} . \tag{A.12}$$

Differentiating Equation A.10 with respects to kr and then using A.11 and A.12 provides the following recurrence relation for the second derivative of the spherical Bessel function:

$$j''_\ell(kr) = \frac{-(2\ell^2+2\ell-1)}{(2\ell+3)(2\ell+1)}j_\ell(kr) + \frac{\ell(\ell-1)}{(2\ell+1)(2\ell-1)}j_{\ell-2}(kr) + \frac{(\ell+1)(\ell+2)}{(2\ell+1)(2\ell+3)}j_{\ell+2}(kr) . \tag{A.13}$$

Equation A.9 can then be written in the same form as Equation 3.19:

$$W_\ell^z(k) = -\int \mathrm{d}rFj''_\ell(kr) , \tag{A.14}$$

$$= \int \mathrm{d}rF(r)\Big(A_\ell j_\ell(kr) - B_\ell j_{\ell-2}(kr) - D_\ell j_{\ell+2}(kr)\Big) , \tag{A.15}$$

where:

$$A_\ell = \frac{(2\ell^2+2\ell-1)}{(2\ell+3)(2\ell+1)} , \tag{A.16}$$

$$B_\ell = \frac{\ell(\ell-1)}{(2\ell+1)(2\ell-1)} , \tag{A.17}$$

$$D_\ell = \frac{(\ell+1)(\ell+2)}{(2\ell+1)(2\ell+3)} , \tag{A.18}$$

which concludes the derivation.

APPENDIX B

DERIVATION OF THE VARIANCE OF A CROSS- OR AUTO-CORRELATION SIGNAL

I derive analytically the variance for a harmonic cross- or auto-correlation for two *gaussian random fields* A and B, for a survey covering $\Delta\Omega$ in area. The variance is derived assuming there is no correlation between adjacent multipoles ℓ. For partial sky coverage, this can be acheived by binning both the correlation function and its variance using Equations 7.12 and 7.13.

The nearly all-sky correlator of the fields A and B, is given by:

$$C_{AB}(\ell) = \frac{1}{f_{\rm sky}} \langle AB^* \rangle = \frac{1}{f_{\rm sky}(2\ell+1)} \sum_{m=-\ell}^{\ell} A_{\ell m} B^*_{\ell m} \,, \tag{B.1}$$

where $f_{\rm sky} = \Delta\Omega/(4\pi)$. Because C_{AB} is a real quantity, we have the following relations:

$$C_{AB}(\ell) = C_{BA}(\ell) = \frac{1}{f_{\rm sky}} \langle AB^* \rangle = \frac{1}{f_{\rm sky}} \langle B^* A \rangle \,, \tag{B.2}$$

$$A^*_{\ell m} = (-1)^m A_{\ell -m} \,. \tag{B.3}$$

Using Equation B.1, the variance of C_{AB} is equal to:

$$\sigma^2_{C_{AB}} = \frac{1}{f_{\rm sky}} \sigma^2_{\langle AB^* \rangle} = \frac{1}{f_{\rm sky}} \frac{\sigma^2_{AB^*}}{(2\ell+1)} \,. \tag{B.4}$$

Now the variance of a quantity x is given by:

$$\sigma^2_x = \left\langle x^2 \right\rangle - \langle x \rangle^2 \,, \tag{B.5}$$

so:

$$\sigma^2_{AB^*} = \left\langle (AB^*)^2 \right\rangle - \langle AB^* \rangle^2 \ , \tag{B.6}$$

$$= \langle AB^* BA^* \rangle - \langle AB^* \rangle \ . \tag{B.7}$$

Wicks's theorem shows that the four point correlator of four gaussian random fields can be written as the sum of their two point correlation functions, i.e.:

$$\langle ABCD \rangle = \langle AB \rangle \langle CD \rangle + \langle AC \rangle \langle BD \rangle + \langle AD \rangle \langle BC \rangle \ . \tag{B.8}$$

The first term in Equation B.7 becomes:

$$\langle AB^* BA^* \rangle = \langle AB^* \rangle \langle BA^* \rangle + \langle AB \rangle \langle B^* A^* \rangle + \langle AA^* \rangle \langle B^* B \rangle \ . \tag{B.9}$$

Equation B.3 implies that:

$$\langle AB \rangle \langle B^* A^* \rangle = \langle AB \rangle \langle A^* B^* \rangle = \langle AB^* \rangle^2 \ . \tag{B.10}$$

So that, combining Equations B.7 and B.9:

$$\sigma^2_{AB^*} = \langle AB^* \rangle^2 + \langle AA^* \rangle \langle B^* B \rangle \ . \tag{B.11}$$

Remembering that $\sigma^2_{AB^*}$ is related to $\sigma^2_{C_{AB}}$ by Equation B.4, and explicitely showing the multipole dependence, then:

$$\sigma^2_{C_{AB}}(\ell) = \frac{1}{f_{\rm sky}(2\ell+1)} \left[C^2_{AB}(\ell) + C_{AA}(\ell) C_{BB}(\ell) \right] \ . \tag{B.12}$$

If the fields considered are the galaxy overdensity field (g) and the CMB temperature anisotropy field (T), then the variance for the integrated Sachs-Wolfe effect (ISW) signal is:

$$\sigma^2_{C_{gT}}(\ell) = \frac{1}{f_{\rm sky}(2\ell+1)} \left[C^2_{gT}(\ell) + C_{gg}(\ell) C_{TT}(\ell) \right] \ , \tag{B.13}$$

where:

$$C_{gg} = \overline{C}_{gg} + \mathcal{N}_g \ , \tag{B.14}$$

$$C_{TT} = \overline{C}_{TT} + \mathcal{N}_T \ . \tag{B.15}$$

The intrinsic (cosmic) variance of the galaxy and temperature fields are give by $\overline{C}_{gg}$ and $\overline{C}_{TT}$ respectively. The galaxy shot noise is given by $\mathcal{N}_g$, the CMB instrumental noise is given by $\mathcal{N}_T$. For the case of the auto-correlation functions, we recover:

$$\sigma^2_{C_{gg}} = \frac{2}{f_{\rm sky}(2\ell+1)}\left[C^2_{gg}\right] , \tag{B.16}$$

$$\sigma^2_{C_{TT}} = \frac{2}{f_{\rm sky}(2\ell+1)}\left[C^2_{TT}\right] . \tag{B.17}$$

The actual values of C_{gg}, C_{TT} and C_{gT} can be taken from either observational measurements (which therefore intrinsincally include shot noise, etc ...), or theoretical predictions, the latter making the variance model dependent. These expressions can easily be checked by creating gaussian random simulation for two fields and directly calculating the variance of their auto- and cross-correlations.

Bibliography

Adelman-McCarthy, J. K., Agüeros, M. A., Allam, S. S., Anderson, K. S. J., Anderson, S. F., Annis, J., Bahcall, N. A., Baldry, I. K., Barentine, J. C., Berlind, A., Bernardi, M., Blanton, M. R., Boroski, W. N., Brewington, H. J., Brinchmann, J., Brinkmann, J., Brunner, R. J., Budavári, T., Carey, L. N., Carr, M. A., Castander, F. J., Connolly, A. J., Csabai, I., Czarapata, P. C., Dalcanton, J. J., Doi, M., Dong, F., Eisenstein, D. J., Evans, M. L., Fan, X., Finkbeiner, D. P., Friedman, S. D., Frieman, J. A., Fukugita, M., Gillespie, B., Glazebrook, K., Gray, J., Grebel, E. K., Gunn, J. E., Gurbani, V. K., de Haas, E., Hall, P. B., Harris, F. H., Harvanek, M., Hawley, S. L., Hayes, J., Hendry, J. S., Hennessy, G. S., Hindsley, R. B., Hirata, C. M., Hogan, C. J., Hogg, D. W., Holmgren, D. J., Holtzman, J. A., Ichikawa, S.-i., Ivezić, Ž., Jester, S., Johnston, D. E., Jorgensen, A. M., Jurić, M., Kent, S. M., Kleinman, S. J., Knapp, G. R., Kniazev, A. Y., Kron, R. G., Krzesinski, J., Kuropatkin, N., Lamb, D. Q., Lampeitl, H., Lee, B. C., Leger, R. F., Lin, H., Long, D. C., Loveday, J., Lupton, R. H., Margon, B., Martínez-Delgado, D., Mandelbaum, R., Matsubara, T., McGehee, P. M., McKay, T. A., Meiksin, A., Munn, J. A., Nakajima, R., Nash, T., Neilsen, Jr., E. H., Newberg, H. J., Newman, P. R., Nichol, R. C., Nicinski, T., Nieto-Santisteban, M., Nitta, A., O'Mullane, W., Okamura, S., Owen, R., Padmanabhan, N., Pauls, G., Peoples, J. J., Pier, J. R., Pope, A. C., Pourbaix, D., Quinn, T. R., Richards, G. T., Richmond, M. W., Rockosi, C. M., Schlegel, D. J., Schneider, D. P., Schroeder, J., Scranton, R., Seljak, U., Sheldon, E., Shimasaku, K., Smith, J. A., Smolčić, V., Snedden, S. A., Stoughton, C., Strauss, M. A., SubbaRao, M., Szalay, A. S., Szapudi, I., Szkody, P., Tegmark, M., Thakar, A. R., Tucker, D. L., Uomoto, A., Vanden Berk, D. E., Vandenberg, J., Vogeley, M. S., Voges, W., Vogt, N. P., Walkowicz, L. M., Weinberg, D. H., West, A. A., White, S. D. M., Xu, Y., Yanny, B., Yocum, D. R., York, D. G., Zehavi, I., Zibetti, S.

& Zucker, D. B., 2006, *ApJS*, **162**, 38

Afshordi, N., 2004, *Phys. Rev.*, **D70**, 083536

Afshordi, N., Loh, Y.-S. & Strauss, M. A., 2004, *Phys. Rev.*, **D69**, 083524

Allgood, B., Blumenthal, G. & Primack, J. R., 2001, *ArXiv Astrophysics e-prints*

Alnes, H., Amarzguioui, M. & Gron, O., 2005

Annis, J., Bridle, S., Castander, F. J., Evrard, A. E., Fosalba, P., Frieman, J. A., Gaztanaga, E., Jain, B., Kravtsov, A. V., Lahav, O., Lin, H., Mohr, J., Stebbins, A., Walker, T. P., Wechsler, R. H., Weinberg, D. H. & Weller, J., 2005, *ArXiv Astrophysics e-prints*

Bacon, D. J., Refregier, A. R. & Ellis, R. S., 2000, *mnras*, **318**, 625

Bennett, C. L., Halpern, M., Hinshaw, G., Jarosik, N., Kogut, A., Limon, M., Meyer, S. S., Page, L., Spergel, D. N., Tucker, G. S., Wollack, E., Wright, E. L., Barnes, C., Greason, M. R., Hill, R. S., Komatsu, E., Nolta, M. R., Odegard, N., Peiris, H. V., Verde, L. & Weiland, J. L., 2003, *ApJS*, **148**, 1

Bennett, C. L., Smoot, G. F. & Kogut, A., 1990, in *Bulletin of the American Astronomical Society*, volume 22 of *Bulletin of the American Astronomical Society*, pp. 1336–+

Bilić, N., Tupper, G. B. & Viollier, R. D., 2002, *Physics Letters B*, **535**, 17

Birkinshaw, M., 1999, *physrep*, **310**, 97

Blake, C., Collister, A., Bridle, S. & Lahav, O., 2007, *mnras*, **374**, 1527

Bolzonella, M., Miralles, J.-M. & Pelló, R., 2000, *A&A*, **363**, 476

Boughn, S. & Crittenden, R., 2004, *Nature*, **427**, 45

Boughn, S. P. & Crittenden, R. G., 2002, *Physical Review Letters*, **88**(2), 021302

Boughn, S. P. & Crittenden, R. G., 2003, in S. H. Holt & C. S. Reynolds (eds.), *AIP Conf. Proc. 666: The Emergence of Cosmic Structure.*, pp. 67–70

Boughn, S. P. & Crittenden, R. G., 2005, *New Astron. Rev.*, **49**, 75

Bucher, M., Moodley, K. & Turok, N., 2002, *prd*, **66**(2), 023528

Cabre, A., Gaztañaga, E., Manera, M., Fosalba, P. & Castander, F., 2006

Caillerie, S., Lachièze-Rey, M., Luminet, J. ., Lehoucq, R., Riazuelo, A. & Weeks, J., 2007, *ArXiv e-prints*, **705**

Carroll, S. M. *et al.*, 2005, *Phys. Rev.*, **D71**, 063513

Chiang, L.-Y., Naselsky, P. D. & Coles, P., 2006, *ArXiv Astrophysics e-prints*

Clowe, D., Bradač, M., Gonzalez, A. H., Markevitch, M., Randall, S. W., Jones, C. & Zaritsky, D., 2006, *ApJL*, **648**, L109

Clowe, D., Gonzalez, A. & Markevitch, M., 2004, *ApJ*, **604**, 596

Cole, S., Norberg, P., Baugh, C. M., Frenk, C. S., Bland-Hawthorn, J., Bridges, T., Cannon, R., Colless, M., Collins, C., Couch, W., Cross, N., Dalton, G., De Propris, R., Driver, S. P., Efstathiou, G., Ellis, R. S., Glazebrook, K., Jackson, C., Lahav, O., Lewis, I., Lumsden, S., Maddox, S., Madgwick, D., Peacock, J. A., Peterson, B. A., Sutherland, W. & Taylor, K., 2001, *MNRAS*, **326**, 255

Cole, S., Percival, W. J., Peacock, J. A., Norberg, P., Baugh, C. M., Frenk, C. S., Baldry, I., Bland-Hawthorn, J., Bridges, T., Cannon, R., Colless, M., Collins, C., Couch, W., Cross, N. J. G., Dalton, G., Eke, V. R., De Propris, R., Driver, S. P., Efstathiou, G., Ellis, R. S., Glazebrook, K., Jackson, C., Jenkins, A., Lahav, O., Lewis, I., Lumsden, S., Maddox, S., Madgwick, D., Peterson, B. A., Sutherland, W. & Taylor, K., 2005, *MNRAS*, **362**, 505

Colless, M., Peterson, B. A., Jackson, C., Peacock, J. A., Cole, S., Norberg, P., Baldry, I. K., Baugh, C. M., Bland-Hawthorn, J., Bridges, T., Cannon, R., Collins, C., Couch, W., Cross, N., Dalton, G., De Propris, R., Driver, S. P., Efstathiou, G., Ellis, R. S., Frenk, C. S., Glazebrook, K., Lahav, O., Lewis, I., Lumsden, S., Maddox, S., Madgwick, D., Sutherland, W. & Taylor, K., 2003, *ArXiv Astrophysics e-prints*

Collister, A. A. & Lahav, O., 2004, *PASP*, **116**, 345

Collister, A. A. & Lahav, O., 2005, *MNRAS*, **361**, 415

Cooray, A., 2002, *prd*, **65**(10), 103510

Cooray, A. & Sheth, R., 2002, *physrep*, **372**, 1

Copi, C. J., Huterer, D., Schwarz, D. J. & Starkman, G. D., 2006, *Mon. Not. Roy. Astron. Soc.*, **367**, 79

Copi, C. J., Schramm, D. N. & Turner, M. S., 1995, *Science*, **267**, 192

Cowie, L. L., Songaila, A., Hu, E. M. & Cohen, J. G., 1996, *AJ*, **112**, 839

Crittenden, R. G. & Turok, N., 1996, *Phys. Rev. Lett.*, **76**, 575

Davis, M., Gerke, B. F. & Newman, J. A., 2004, *ArXiv Astrophysics e-prints*

de Vaucouleurs, G., de Vaucouleurs, A. & Corwin, H. G., 1976, *2nd reference catalogue of bright galaxies containing information on 4364 galaxies with reference to papers published between 1964 and 1975* (University of Texas Monographs in Astronomy, Austin: University of Texas Press, 1976)

Deligny, O., Armengaud, E., Beau, T., Da Silva, P., Hamilton, J.-C., Lachaud, C., Letessier-Selvon, A. & Revenu, B., 2004, *Journal of Cosmology and Astro-Particle Physics*, **10**, 8

Dicke, R. H., Peebles, P. J. E., Roll, P. G. & Wilkinson, D. T., 1965, *ApJ*, **142**, 414

Dodelson, S., 2003, *Modern cosmology* (Modern cosmology / Scott Dodelson. Amsterdam (Netherlands): Academic Press. ISBN 0-12-219141-2, 2003, XIII + 440 p.)

Dressler, A., 1980, *ApJ*, **236**, 351

Dvali, G., Gabadadze, G. & Porrati, M., 2000, *Physics Letters B*, **485**, 208

Efstathiou, G., 2004, *MNRAS*, **348**, 885

Efstathiou, G., Sutherland, W. J. & Maddox, S. J., 1990, *Nature*, **348**, 705

Eisenstein, D. J. & Hu, W., 1999, *ApJ*, **511**, 5

Eisenstein, D. J., Zehavi, I., Hogg, D. W., Scoccimarro, R., Blanton, M. R., Nichol, R. C., Scranton, R., Seo, H.-J., Tegmark, M., Zheng, Z., Anderson, S. F., Annis, J., Bahcall, N.,

Brinkmann, J., Burles, S., Castander, F. J., Connolly, A., Csabai, I., Doi, M., Fukugita, M., Frieman, J. A., Glazebrook, K., Gunn, J. E., Hendry, J. S., Hennessy, G., Ivezić, Z., Kent, S., Knapp, G. R., Lin, H., Loh, Y.-S., Lupton, R. H., Margon, B., McKay, T. A., Meiksin, A., Munn, J. A., Pope, A., Richmond, M. W., Schlegel, D., Schneider, D. P., Shimasaku, K., Stoughton, C., Strauss, M. A., SubbaRao, M., Szalay, A. S., Szapudi, I., Tucker, D. L., Yanny, B. & York, D. G., 2005, *apj*, **633**, 560

Elgarøy, Ø. & Lahav, O., 2006, *Physica Scripta Volume T*, **127**, 105

Erdoğdu (a), P. *et al.*, 2006, *Mon. Not. Roy. Astron. Soc.*, **368**, 1515

Erdoğdu (b), P., Lahav, O., Huchra, J. P., Colless, M., Cutri, R. M., Falco, E., George, T., Jarrett, T., Jones, D. H., Macri, L. M., Mader, J., Martimbeau, N., Pahre, M. A., Parker, Q. A., Rassat, A. & Saunders, W., 2006, *MNRAS*, **373**, 45

Eriksen, H. K., Hansen, F. K., Banday, A. J., Gorski, K. M. & Lilje, P. B., 2004, *Astrophys. J.*, **605**, 14

Falco, E. E., Kurtz, M. J., Geller, M. J., Huchra, J. P., Peters, J., Berlind, P., Mink, D. J., Tokarz, S. P. & Elwell, B., 1999, *VizieR Online Data Catalog*, **611**, 10438

Fay, S., Nesseris, S. & Perivolaropoulos, L., 2007, *prd*, **76**(6), 063504

Fisher, K. B., Davis, M., Strauss, M. A., Yahil, A. & Huchra, J., 1994*a*, *MNRAS*, **266**, 50

Fisher, K. B., Lahav, O., Hoffman, Y., Lynden-Bell, D. & Zaroubi, S., 1995, *MNRAS*, **272**, 885

Fisher, K. B. & Nusser, A., 1996, *MNRAS*, **279**, L1

Fisher, K. B., Scharf, C. A. & Lahav, O., 1994*b*, *MNRAS*, **266**, 219

Fort, B. & Mellier, Y., 1994, *aapr*, **5**, 239

Fosalba, P. & Gaztañaga, E., 2004, *MNRAS*, **350**, L37

Fosalba, P., Gaztañaga, E. & Castander, F., 2003, *Astrophys. J.*, **597**, L89

Frith, W., 2005, *Ph.D.*

Fry, J. N., 1996, *apjl*, **461**, L65+

Gaztañaga, E., Manera, M. & Multamaki, T., 2006, *Mon. Not. Roy. Astron. Soc.*, **365**, 171

Geller, M. J. & Huchra, J. P., 1989, *Science*, **246**, 897

Giannantonio, T., Crittenden, R. G., Nichol, R. C., Scranton, R., Richards, G. T., Myers, A. D., Brunner, R. J., Gray, A. G., Connolly, A. J. & Schneider, D. P., 2006, *ArXiv Astrophysics e-prints*

Gorski, K. M. *et al.*, 2005, *Astrophys. J.*, **622**, 759

Gorski, K. M., Hivon, E. & Wandelt, B. D., 1998

Gramann, M., Cen, R. & Gott, J. R. I., 1994, *ApJ*, **425**, 382

Groth, E. J. & Peebles, P. J. E., 1977, *ApJ*, **217**, 385

Guth, A. H., 1981, *prd*, **23**, 347

Guth, A. H. & Tye, S.-H. H., 1980, *Physical Review Letters*, **44**, 631

Hamilton, A. J. S., 1995, in S. Maurogordato, C. Balkowski, C. Tao & J. Tran Thanh van (eds.), *Clustering in the Universe*, pp. 143–+

Hamilton, A. J. S., 1998, in D. Hamilton (ed.), *The Evolving Universe*, volume 231 of *Astrophysics and Space Science Library*, pp. 185–+

Heavens, A. F. & Taylor, A. N., 1995, *mnras*, **275**, 483

Hinshaw, G. *et al.*, 2006

Hivon, E., Górski, K. M., Netterfield, C. B., Crill, B. P., Prunet, S. & Hansen, F., 2002, *ApJ*, **567**, 2

Hoekstra, H., Mellier, Y., van Waerbeke, L., Semboloni, E., Fu, L., Hudson, M. J., Parker, L. C., Tereno, I. & Benabed, K., 2006, *ApJ*, **647**, 116

Hubble, E., 1925, *Contributions from the Mount Wilson Observatory / Carnegie Institution of Washington*, **304**, 1

Hubble, E. & Humason, M. L., 1931, *Contributions from the Mount Wilson Observatory / Carnegie Institution of Washington*, **427**, 1

Hubble, E. P., 1936, *Yale University Press*

Huchra, J., Jarrett, T., Skrutskie, M., Cutri, R., Schneider, S., Macri, L., Steining, R., Mader, J., Martimbeau, N. & George, T., 2005, in A. P. Fairall & P. A. Woudt (eds.), *Nearby Large-Scale Structures and the Zone of Avoidance*, volume 329 of *Astronomical Society of the Pacific Conference Series*, pp. 135–+

Huchra, J. P., Geller, M. J., Clemens, C. M., Tokarz, S. P. & Michel, A., 1992, *Bulletin d'Information du Centre de Donnees Stellaires*, **41**, 31

Huterer, D. & Linder, E. V., 2007, *prd*, **75**(2), 023519

Ishibashi, A. & Wald, R. M., 2006, *Classical and Quantum Gravity*, **23**, 235

Jarosik, N. *et al.*, 2006

Jarrett, T., 2004, *Publications of the Astronomical Society of Australia*, **21**, 396

Jarrett, T. H. *et al.*, 2000, *Astron. J.*, **119**, 2498

Jones, D. H., Saunders, W., Read, M. & Colless, M., 2005, *Publications of the Astronomical Society of Australia*, **22**, 277

Kaiser, N., Wilson, G. & Luppino, G. A., 2000, *ArXiv Astrophysics e-prints*

Kamionkowski, M., 1996, *Phys. Rev.*, **D54**, 4169

Kamionkowski, M. & Spergel, D. N., 1994, *apj*, **432**, 7

Kayo, I., Taruya, A. & Suto, Y., 2001, *apj*, **561**, 22

Kennicutt, Jr., R. C., 1992, *ApJ*, **388**, 310

Kiakotou, A., Elgaroy, O. & Lahav, O., 2007, *ArXiv e-prints*, **709**

Kinkhabwala, A. & Kamionkowski, M., 1999, *Physical Review Letters*, **82**, 4172

Kneib, J.-P., Ellis, R. S., Smail, I., Couch, W. J. & Sharples, R. M., 1996, *ApJ*, **471**, 643

Kochanek, C. S. *et al.*, 2001, *Astrophys. J.*, **560**, 566

Kunz, M., Aghanim, N., Cayon, L., Forni, O., Riazuelo, A. & Uzan, J. P., 2006, *prd*, **73**(2), 023511

Lahav, O., 2000, in S. Courteau & J. Willick (eds.), *Cosmic Flows Workshop*, volume 201 of *Astronomical Society of the Pacific Conference Series*, pp. 377–+

Lahav, O. & Liddle, A. R., 2004, *ArXiv Astrophysics e-prints*

Lahav, O., Lilje, P. B., Primack, J. R. & Rees, M. J., 1991, *MNRAS*, **251**, 128

Lahav, O., Naim, A., Buta, R. J., Corwin, H. G., de Vaucouleurs, G., Dressler, A., Huchra, J. P., van den Bergh, S., Raychaudhury, S., Sodre, Jr., L. & Storrie-Lombardi, M. C., 1995, *Science*, **267**, 859

Land, K. & Magueijo, J., 2005*a*, *Phys. Rev. Lett.*, **95**, 071301

Land, K. & Magueijo, J., 2005*b*, *Mon. Not. Roy. Astron. Soc.*, **357**, 994

Le Borgne, D., Rocca-Volmerange, B., Prugniel, P., Lançon, A., Fioc, M. & Soubiran, C., 2004, *A&A*, **425**, 881

Le Fèvre, O., Vettolani, G., Garilli, B., Tresse, L., Bottini, D., Le Brun, V., Maccagni, D., Picat, J. P., Scaramella, R., Scodeggio, M., Zanichelli, A., Adami, C., Arnaboldi, M., Arnouts, S., Bardelli, S., Bolzonella, M., Cappi, A., Charlot, S., Ciliegi, P., Contini, T., Foucaud, S., Franzetti, P., Gavignaud, I., Guzzo, L., Ilbert, O., Iovino, A., McCracken, H. J., Marano, B., Marinoni, C., Mathez, G., Mazure, A., Meneux, B., Merighi, R., Paltani, S., Pellò, R., Pollo, A., Pozzetti, L., Radovich, M., Zamorani, G., Zucca, E., Bondi, M., Bongiorno, A., Busarello, G., Lamareille, F., Mellier, Y., Merluzzi, P., Ripepi, V. & Rizzo, D., 2005, *A&A*, **439**, 845

Lesgourgues, J. & Pastor, S., 2006, *physrep*, **429**, 307

Lewis, A., Challinor, A. & Lasenby, A., 2000, *Astrophys. J.*, **538**, 473

Linder, E. V., 2005, *prd*, **72**(4), 5+

Linder, E. V. & Cahn, R. N., 2007, *ArXiv Astrophysics e-prints*

Loverde, M., Hui, L. & Gaztañaga, E., 2007, *prd*, **75**(4), 043519

Ma, C.-P., Caldwell, R. R., Bode, P. & Wang, L., 1999, *ApJL*, **521**, L1

Maddox, S. J., Efstathiou, G. & Sutherland, W. J., 1990*a*, *MNRAS*, **246**, 433

Maddox, S. J., Efstathiou, G., Sutherland, W. J. & Loveday, J., 1990*b*, *MNRAS*, **243**, 692

Madgwick, D. S., Hawkins, E., Lahav, O., Maddox, S., Norberg, P., Peacock, J. A., Baldry, I. K., Baugh, C. M., Bland-Hawthorn, J., Bridges, T., Cannon, R., Cole, S., Colless, M., Collins, C., Couch, W., Dalton, G., De Propris, R., Driver, S. P., Efstathiou, G., Ellis, R. S., Frenk, C. S., Glazebrook, K., Jackson, C., Lewis, I., Lumsden, S., Peterson, B. A., Sutherland, W. & Taylor, K., 2003, *MNRAS*, **344**, 847

Magliocchetti, M., Bagla, J. S., Maddox, S. J. & Lahav, O., 2000, *MNRAS*, **314**, 546

Maller, A. H., McIntosh, D. H., Katz, N. & Weinberg, M. D., 2003, *ApJL*, **598**, L1

Maller, A. H., McIntosh, D. H., Katz, N. & Weinberg, M. D., 2005, *ApJ*, **619**, 147

Massey, R., Refregier, A., Bacon, D. J., Ellis, R. & Brown, M. L., 2005, *MNRAS*, **359**, 1277

Massey, R., Rhodes, J., Leauthaud, A., Capak, P., Ellis, R., Koekemoer, A., Réfrégier, A., Scoville, N., Taylor, J. E., Albert, J., Bergé, J., Heymans, C., Johnston, D., Kneib, J.-P., Mellier, Y., Mobasher, B., Semboloni, E., Shopbell, P., Tasca, L. & Van Waerbeke, L., 2007, *ApJS*, **172**, 239

McEwen, J. D., Vielva, P., Hobson, M. P., Martinez-Gonzalez, E. & Lasenby, A. N., 2006

Menard, B., 2002, in F. Combes & D. Barret (eds.), *SF2A-2002: Semaine de l'Astrophysique Francaise*, pp. 57–+

Moffat, J. W., 2006, *ArXiv Astrophysics e-prints*

Naim, A., Lahav, O., Sodre, Jr., L. & Storrie-Lombardi, M. C., 1995, *MNRAS*, **275**, 567

Neugebauer, G. & Leighton, R. B., 1969, *Two-micron sky survey. A preliminary catalogue* (NASA SP, Washington: NASA, 1969)

Nolta, M. R. *et al.*, 2004, *Astrophys. J.*, **608**, 10

Padmanabhan, N. *et al.*, 2005, *Phys. Rev.*, **D72**, 043525

Padmanabhan, N., Schlegel, D. J., Seljak, U. & Makarov, A. e. a., 2006, *ArXiv Astrophysics e-prints*

Peacock, J. A. & Dodds, S. J., 1994, *MNRAS*, **267**, 1020

Peacock, J. A. & Smith, R. E., 2000, *mnras*, **318**, 1144

Peebles, P. J. E., 1976, *ApSS*, **45**, 3

Peebles, P. J. E., 1980, *The large-scale structure of the universe* (Research supported by the National Science Foundation. Princeton, N.J., Princeton University Press, 1980. 435 p.)

Peebles, P. J. E., 1993, *Principles of physical cosmology* (Princeton Series in Physics, Princeton, NJ: Princeton University Press, —c1993)

Perlmutter, S., Aldering, G., della Valle, M., Deustua, S., Ellis, R. S., Fabbro, S., Fruchter, A., Goldhaber, G., Groom, D. E., Hook, I. M., Kim, A. G., Kim, M. Y., Knop, R. A., Lidman, C., McMahon, R. G., Nugent, P., Pain, R., Panagia, N., Pennypacker, C. R., Ruiz-Lapuente, P., Schaefer, B. & Walton, N., 1998, *Nature*, **391**, 51

Pigott, E., 1785, *Philosophical Transactions Series I*, **75**, 127

Pike, R. W. & Hudson, M. J., 2005, *ApJ*, **635**, 11

Press, W. H., Teukolsky, S. A., Vetterling, W. T. & Flannery, B. P., 1992, *Numerical recipes in FORTRAN. The art of scientific computing* (Cambridge: University Press, —c1992, 2nd ed.)

Rakic, A., Rasanen, S. & Schwarz, D. J., 2006

Ramella, M., Geller, M. J. & Huchra, J. P., 1989, *ApJ*, **344**, 57

Rassat, A., Land, K., Lahav, O. & Abdalla, F. B., 2007, *MNRAS*, **377**, 1085

Ratra, B. & Peebles, P. J. E., 1988, *prd*, **37**, 3406

Réfrégier, A., Boulade, O., Mellier, Y., Milliard, B., Pain, R., Michaud, J., Safa, F., Amara, A., Astier, P., Barrelet, E., Bertin, E., Boulade, S., Cara, C., Claret, A., Georges, L.,

Grange, R., Guy, J., Koeck, C., Kroely, L., Magneville, C., Palanque-Delabrouille, N., Regnault, N., Smadja, G., Schimd, C. & Sun, Z., 2006, in *Space Telescopes and Instrumentation I: Optical, Infrared, and Millimeter. Edited by Mather, John C.; MacEwen, Howard A.; de Graauw, Mattheus W. M.. Proceedings of the SPIE, Volume 6265, pp. 62651Y (2006).*, volume 6265 of *Presented at the Society of Photo-Optical Instrumentation Engineers (SPIE) Conference*

Riess, A. G., Filippenko, A. V., Challis, P., Clocchiatti, A., Diercks, A., Garnavich, P. M., Gilliland, R. L., Hogan, C. J., Jha, S., Kirshner, R. P., Leibundgut, B., Phillips, M. M., Reiss, D., Schmidt, B. P., Schommer, R. A., Smith, R. C., Spyromilio, J., Stubbs, C., Suntzeff, N. B. & Tonry, J., 1998, *AJ*, **116**, 1009

Rowan-Robinson, M., Sharpe, J., Oliver, S. J., Keeble, O., Canavezes, A., Saunders, W., Taylor, A. N., Valentine, H., Frenk, C. S., Efstathiou, G. P., McMahon, R. G., White, S. D. M., Sutherland, W., Tadros, H. & Maddox, S., 2000, *MNRAS*, **314**, 375

Rubin, V. C., Burstein, D., Ford, Jr., W. K. & Thonnard, N., 1985, *ApJ*, **289**, 81

Sachs, R. K. & Wolfe, A. M., 1967, *Astrophys. J.*, **147**, 73

Sawicki, I., Song, Y.-S. & Hu, W., 2006, *ArXiv Astrophysics e-prints*

Scharf, C., 1993, in F. Bouchet & M. Lachieze-Rey (eds.), *Cosmic Velocity Fields*, pp. 575–+

Scharf, C., Hoffman, Y., Lahav, O. & Lynden-Bell, D., 1992, *MNRAS*, **256**, 229

Schlegel, D. J., Finkbeiner, D. P. & Davis, M., 1998, *Astrophys. J.*, **500**, 525

Schmidt, B. P., Suntzeff, N. B., Phillips, M. M., Schommer, R. A., Clocchiatti, A., Kirshner, R. P., Garnavich, P., Challis, P., Leibundgut, B., Spyromilio, J., Riess, A. G., Filippenko, A. V., Hamuy, M., Smith, R. C., Hogan, C., Stubbs, C., Diercks, A., Reiss, D., Gilliland, R., Tonry, J., Maza, J., Dressler, A., Walsh, J. & Ciardullo, R., 1998, *ApJ*, **507**, 46

Schmidt, F., Liguori, M. & Dodelson, S., 2007, *ArXiv e-prints*, **706**

Scranton, R., Ménard, B., Richards, G. T., Nichol, R. C., Myers, A. D., Jain, B., Gray, A., Bartelmann, M., Brunner, R. J., Connolly, A. J., Gunn, J. E., Sheth, R. K., Bahcall, N. A., Brinkman, J., Loveday, J., Schneider, D. P., Thakar, A. & York, D. G., 2005, *ApJ*, **633**, 589

Seljak, U., 2000, *mnras*, **318**, 203

Seljak, U., Slosar, A. & McDonald, P., 2006, *Journal of Cosmology and Astro-Particle Physics*, **10**, 14

Semboloni, E., Mellier, Y., van Waerbeke, L., Hoekstra, H., Tereno, I., Benabed, K., Gwyn, S. D. J., Fu, L., Hudson, M. J., Maoli, R. & Parker, L. C., 2006, *A&A*, **452**, 51

Sen, A. A. & Scherrer, R. J., 2005, *ArXiv Astrophysics e-prints*

Silk, J., 1967, *Nature*, **215**, 1155

Smith, K. M., Zahn, O. & Doré, O., 2007, *prd*, **76**(4), 043510

Smith, R. E., Peacock, J. A., Jenkins, A., White, S. D. M., Frenk, C. S., Pearce, F. R., Thomas, P. A., Efstathiou, G. & Couchman, H. M. P., 2003, *MNRAS*, **341**, 1311

Sodré, Jr., L. & Cuevas, H., 1994, *Vistas in Astronomy*, **38**, 287

Song, Y.-S., Hu, W. & Sawicki, I., 2007, *prd*, **75**(4), 044004

Song, Y.-S., Sawicki, I. & Hu, W., 2006, *ArXiv Astrophysics e-prints*

Spergel, D. N. *et al.*, 2003, *Astrophys. J. Suppl.*, **148**, 175

Spergel, D. N. *et al.*, 2006, *ArXiv Astrophysics e-prints*

Sunyaev, R. A. & Zeldovich, I. B., 1980, *mnras*, **190**, 413

Tang, J.-Y., Weller, J. & Zablocki, A., 2006, *ArXiv Astrophysics e-prints*

Taylor, A. N., Bacon, D. J., Gray, M. E., Wolf, C., Meisenheimer, K., Dye, S., Borch, A., Kleinheinrich, M., Kovacs, Z. & Wisotzki, L., 2004, *MNRAS*, **353**, 1176

Taylor, A. N. & Hamilton, A. J. S., 1996, *MNRAS*, **282**, 767

Tegmark, M., de Oliveira-Costa, A. & Hamilton, A., 2003, *Phys. Rev.*, **D68**, 123523

Tegmark, M., Taylor, A. N. & Heavens, A. F., 1997, *apj*, **480**, 22

The Dark Energy Survey Collaboration, 2005, *ArXiv Astrophysics e-prints*

Totsuka, Y. & The Super-KAMIOKANDE Collaboration, 1998, in J. Paul, T. Montmerle & E. Aubourg (eds.), *Abstracts of the 19th Texas Symposium on Relativistic Astrophysics and Cosmology, held in Paris, France, Dec. 14-18, 1998. Eds.: J. Paul, T. Montmerle, and E. Aubourg (CEA Saclay), meeting abstract.*

Vale, C., 2005, *ArXiv Astrophysics e-prints*

Van Waerbeke, L., Mellier, Y., Erben, T., Cuillandre, J. C., Bernardeau, F., Maoli, R., Bertin, E., Mc Cracken, H. J., Le Fèvre, O., Fort, B., Dantel-Fort, M., Jain, B. & Schneider, P., 2000, *A&A*, **358**, 30

Vanderveld, R. A., Flanagan, E. E. & Wasserman, I., 2006

Wagoner, R. V., Fowler, W. A. & Hoyle, F., 1967, *ApJ*, **148**, 3

Wall, J. & Jenkins, C., 2004, *Practical statistics for astronomers. Cambridge Observing Handbooks for Research Astronomers, Vol. 3. Cambridge, Cambridge University Press, 2003, XV+277 pp., ISBN 0-521-45416-6*, **62**, 36

Wang, L. & Steinhardt, P. J., 1998, *APJ*, **508**, 483

Webster, M., Lahav, O. & Fisher, K., 1997, *MNRAS*, **287**, 425

Weller, J. & Lewis, A. M., 2003, *mnras*, **346**, 987

Wittman, D. M., Tyson, J. A., Kirkman, D., Dell'Antonio, I. & Bernstein, G., 2000, *Nature*, **405**, 143

Wu, K., Lahav, O. & Rees, M., 1999, *Nature*, **397**, 225

Zehavi, I., Weinberg, D. H., Zheng, Z., Berlind, A. A., Frieman, J. A., Scoccimarro, R., Sheth, R. K., Blanton, M. R., Tegmark, M., Mo, H. J., Bahcall, N. A., Brinkmann, J., Burles, S., Csabai, I., Fukugita, M., Gunn, J. E., Lamb, D. Q., Loveday, J., Lupton, R. H., Meiksin, A., Munn, J. A., Nichol, R. C., Schlegel, D., Schneider, D. P., SubbaRao, M., Szalay, A. S., Uomoto, A. & York, D. G., 2004, *ApJ*, **608**, 16

Zwicky, F., 1933, *Helvetica Physica Acta*, **6**, 110